



Third United States Microgravity Payload: One Year Report

P.A. Curreri, Editor

Marshall Space Flight Center, Marshall Space Flight Center, Alabama

D. McCauley, Editor

University of Alabama in Huntsville, Huntsville, Alabama

C. Walker, Editor

Universities Space Research Association, Huntsville, Alabama

The NASA STI Program Office...in Profile

Since its founding, NASA has been dedicated to the advancement of aeronautics and space science. The NASA Scientific and Technical Information (STI) Program Office plays a key part in helping NASA maintain this important role.

The NASA STI Program Office is operated by Langley Research Center, the lead center for NASA's scientific and technical information. The NASA STI Program Office provides access to the NASA STI Database, the largest collection of aeronautical and space science STI in the world. The Program Office is also NASA's institutional mechanism for disseminating the results of its research and development activities. These results are published by NASA in the NASA STI Report Series, which includes the following report types:

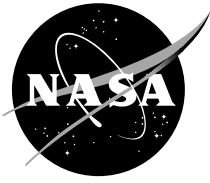
- **TECHNICAL PUBLICATION.** Reports of completed research or a major significant phase of research that present the results of NASA programs and include extensive data or theoretical analysis. Includes compilations of significant scientific and technical data and information deemed to be of continuing reference value. NASA's counterpart of peer-reviewed formal professional papers but has less stringent limitations on manuscript length and extent of graphic presentations.
- **TECHNICAL MEMORANDUM.** Scientific and technical findings that are preliminary or of specialized interest, e.g., quick release reports, working papers, and bibliographies that contain minimal annotation. Does not contain extensive analysis.
- **CONTRACTOR REPORT.** Scientific and technical findings by NASA-sponsored contractors and grantees.

- **CONFERENCE PUBLICATION.** Collected papers from scientific and technical conferences, symposia, seminars, or other meetings sponsored or cosponsored by NASA.
- **SPECIAL PUBLICATION.** Scientific, technical, or historical information from NASA programs, projects, and mission, often concerned with subjects having substantial public interest.
- **TECHNICAL TRANSLATION.** English-language translations of foreign scientific and technical material pertinent to NASA's mission.

Specialized services that complement the STI Program Office's diverse offerings include creating custom thesauri, building customized databases, organizing and publishing research results...even providing videos.

For more information about the NASA STI Program Office, see the following:

- Access the NASA STI Program Home Page at <http://www.sti.nasa.gov>
- E-mail your question via the Internet to help@sti.nasa.gov
- Fax your question to the NASA Access Help Desk at (301) 621-0134
- Telephone the NASA Access Help Desk at (301) 621-0390
- Write to:
NASA Access Help Desk
NASA Center for AeroSpace Information
800 Elkridge Landing Road
Linthicum Heights, MD 21090-2934



Third United States Microgravity Payload: One Year Report

P.A. Curreri, Editor

Marshall Space Flight Center, Marshall Space Flight Center, Alabama

D. McCauley, Editor

University of Alabama in Huntsville, Huntsville, Alabama

C. Walker, Editor

Universities Space Research Association, Huntsville, Alabama

National Aeronautics and
Space Administration

Marshall Space Flight Center

Acknowledgments

The untiring efforts and dedication of the STS-75 payload and orbiter crews, the mission and program managers, and mission operations personnel were critical to the completion of the missions' objectives and are sincerely appreciated. The editors wish to thank the Office of Life and Microgravity Science and Applications (OLMSA) and the Microgravity Research Division (MRD) at NASA Headquarters for their support and encouragement. The editors also wish to thank the NASA Marshall Space Flight Center's Public Affairs Office for their help in publicizing the results of the USMP-3 mission, as well as all of the investigators for contributing to this document.

Available from:

NASA Center for AeroSpace Information
800 Elkridge Landing Road
Linthicum Heights, MD 21090-2934
(301) 621-0390

National Technical Information Service
5285 Port Royal Road
Springfield, VA 22161
(703) 487-4650

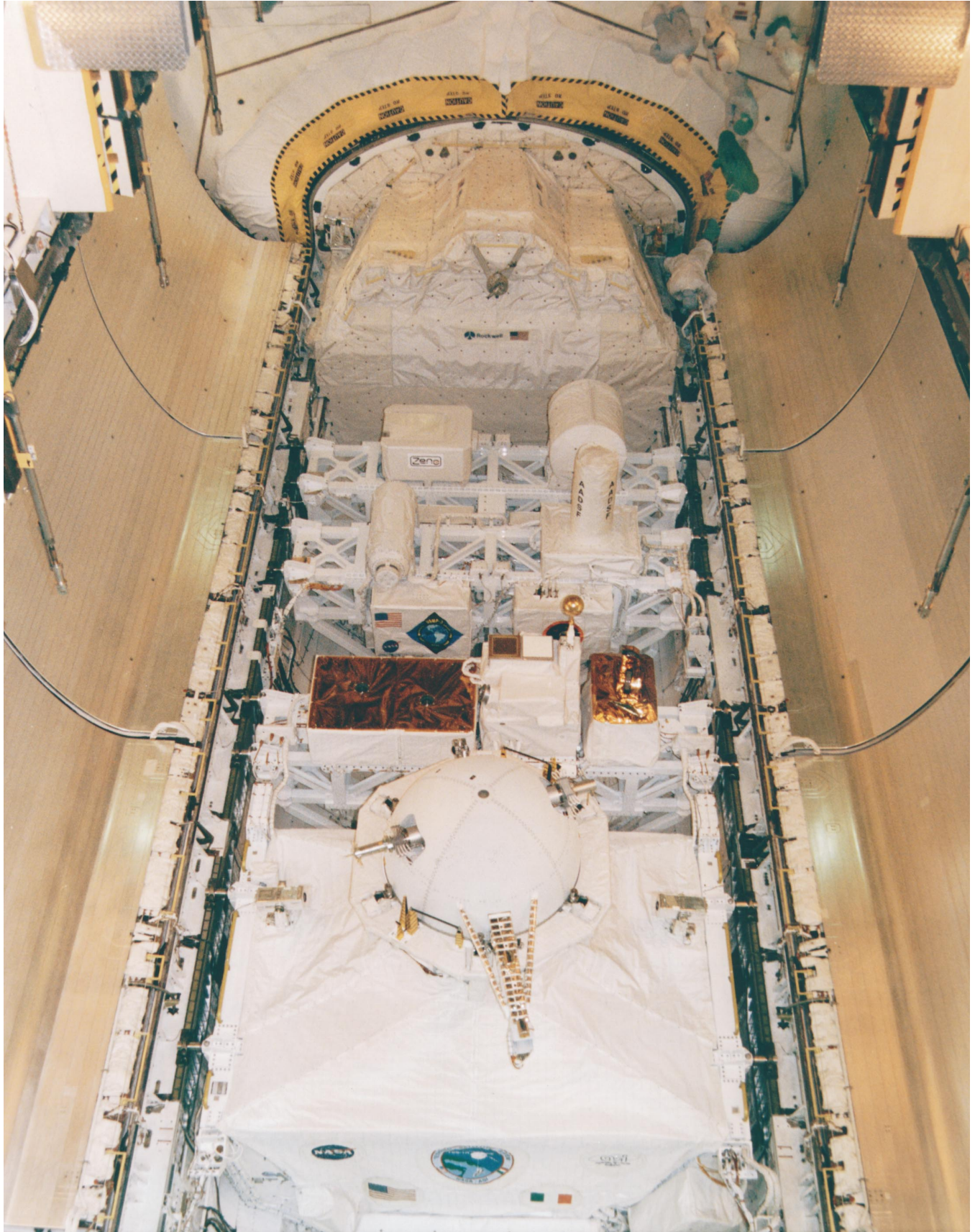




TABLE OF CONTENTS

	Page
INTRODUCTION	xxi
USMP-3 EXPERIMENTS	
SECTION I: Study of Interesting Solidification Phenomena on the Ground and in Space (MEPHISTO) Jean-Jacques Favier, CENG (Grenoble, France)	1-1
SECTION II: Second Flight of the Zeno Experiment on USMP-3 Robert W. Gammon, University of Maryland at College Park	2-11
SECTION III: The Isothermal Dendritic Growth Experiment Martin E. Glicksman, Rensselaer Polytechnic Institute (Troy, New York)	3-39
SECTION IV: The Effect of Microgravity Direction on the Growth of PbSnTe Archibald L. Fripp, NASA Langley Research Center (Hampton, Virginia)	4-55
GLOVEBOX INVESTIGATIONS (USMP-3—MGBX)	
SECTION V: Forced Flow Flamespreading Test: Preliminary Findings From the USMP-3 Shuttle Mission Kurt R. Sacksteder, NASA Lewis Research Center (Cleveland, Ohio)	5-85
SECTION VI: Forced Flow Flamespreading Test: Preliminary Findings From the USMP-3 Shuttle Mission Radiative Ignition and Transition to Spread Investigation (RITSI) Takashi Kashiwagi, National Institute of Standards and Technology (Gaithersburg, Maryland)	6-105
SECTION VII: Comparative Soot Diagnostics: One Year Report David L. Urban, NASA Lewis Research Center (Cleveland, Ohio)	7-133

ACCELERATION MEASUREMENT FACILITIES

SECTION VIII: Principal Investigator Microgravity Services—USMP-3	8-157
Melissa J.B. Rogers (USMP-3), Tal-Cut/NASA Lewis Research Center (Cleveland, Ohio)	

SECTION IX: AUTHOR INDEX	xxi, xxii
--------------------------------	-----------

LIST OF FIGURES

Figure	Title	Page
STS-75	Onboard Photo: Shuttle Cargo Bay	iii
	USMP-3 Payload	iv
Figure 1-1.	(a) Acceleration versus time for the OMS burn recorded on USMP-1 and the associated Seebeck signal, $E_s(t)$ [1]. (b) OMS engine alignment with the orbiter. ..	1-8
Figure 1-2.	The MEPHISTO set-up (bottom-left), temperature profile (top left) and computational model (right). T_m denotes the melting temperature.	1-9
Figure 1-3.	(a) Actual and (b) predicted Seebeck signal for a 25-sec and 15-sec burn oriented parallel to the crystal-melt interface.	1-10
Figure 2-1.	Zeno optical layout. Components: He-Ne Laser, Mirrors M 1-4, Beam Splitter B 1, Shutters S 1-2, Filters F 1-2, Photodiodes PD 1-2, Lenses L 1-4, Apertures A 1-4, Photomultipliers PMT 1-2, and Thermostat TH . The sample cell is in the center of the three-shell thermostat. The scattering angles are approximately 12° and 168° for either beam path chosen by shutter.	2-22
Figure 2-2.	Cross section of the Zeno sample cell. Cylindrical sample wall flange is copper and is in mechanical/thermal contact with the copper window holders. The seals are crushed knife edges machined on the wall flange. The filling and sealing valve is built into the cell wall. The spacing of the inner window surfaces is 110 ± 1 mm in the central region. The outside dimensions are 3.8-cm diameter by 4.3-cm long.	2-23
Figure 2-3.	The temperature timeline for the second Zeno flight. Notice that the sample did not cross into the two-phase region until the last day of the mission.	2-24
Figure 2-4.	Scattering intensity (photon count rate) versus MET. At MET day 10, hour 7:00, the laser path was switched and the power lowered from $17 \mu\text{W}$ to $1.7 \mu\text{W}$. The path change means that this detector began looking at backscattered light after this time.	2-24
Figure 2-5.	Turbidity measurements over the mission. This is actually the turbidity-path-length . product calculated from the natural log of the transmission T_x . A change of 0.01 in “turbidity” corresponds to a 1 percent change in T_x . Notice the dramatic response of this signal at the time of the path change/laser power change at MET day 10, hour 7:00 and the indication of phase separation on MET day 15.	2-25

Figure 2-6.	Turbidity during large temperature scan, far from T_c , showing the interference fringes from the cell windows. By stopping the temperature scan near positions of maximum fringe slope, high sensitivity to local density changes could be realized. The horizontal sections are at times when the scanning was stopped to verify the equilibrium of the local density.	2-26
Figure 2-7.	Density transients during and following temperature step ramps during the mission. Approximately MET days 4 to 8.	2-27
Figure 2-8.	Comparison of calculated and measured density perturbations due to a temperature ramp applied to sample cell wall. The ramp was from 500 mK to 300 mK from T_c , occurring at MET day 3, hour 11:22. This event appears in figure 2-6 as the last event and shows a large overshoot. The ramp consisted of 10 steps of 20 mK each over an hour interval. The comparison is absolute, without any scaling. The smooth curve is calculated based on the adiabatic equations for a hypercompressible fluid. The noisy curve gives the measurements.	2-28
Figure 2-9.	Correlogram computed and recorded by the ALV correlator in the Zeno instrument during the second flight. Laser power 1.7 mW. The round data symbols are from forward scattering and the + symbols are from back scattering. Temperature “2 mK” above T_c . The forward scattering has the slower decay rate so it drops down to the background correlation at longer times. The “faster” fluctuations are seen in backscattering. Notice the clear presence of forward scattering dynamics in the backscattering correlogram from the window reflection.	2-29
Figure 2-10.	Set of forward-scattering correlograms recorded at temperatures from 2 mK to 100 mK during the second flight (USMP-3). The legend distinguishes the curves based on labels are not accurate expressions of the approach to T_c (see discussion).	2-30
Figure 2-11.	Log-log plot of fluctuation decay rates for forward scattering (11.465° angle, in the fluid) versus temperature-distance to T_c . Symbols: squares, 17 μ W scattering, flight 2; circles, 1.7 μ W scattering, flight 2; triangles pointed up, 17 μ W scattering, postflight 2; triangles pointed down, 1.7 μ W scattering, postflight 2. The solid curve is a prediction based on equations of Burstyn, Sengers, Ferrell and Bhattacharjee.	2-31
Figure 2-12.	Log-log plot of fluctuation decay rates for backscattering (169.546° angle, in the fluid) versus temperature-to T_c . Symbols: squares, 17 μ W scattering, flight 2; circles, 1.7 μ W scattering, flight 2; triangles pointed up, 17 μ W scattering, postflight 2; triangles pointed down, 1.7 μ W scattering, postflight 2. The solid curve is a prediction based on equations of Burstyn, Sengers, Ferrell and Bhattacharjee.	2-32

Figure 2-13.	Log-log plot of fluctuation decay rates for forward scattering from the first Zeno flight. Symbols: diamonds are the flight data, plusses are the ground data. The solid curve is a prediction based on equations of Burstyn, Sengers, Ferrell and Bhattacharjee. Notice that the flight data show limiting behavior almost 2 times below the ground data.	2-33
Figure 2-14.	Log-log plot of fluctuation decay rates for forward scattering (11.465° angle, in the fluid) versus a correlation-range corrected temperature distance to T_c . Symbols: squares, $17\ \mu\text{W}$ scattering, flight 2; circles, $1.7\ \mu\text{W}$ scattering, flight 2; triangles pointed up, $17\ \mu\text{W}$ scattering, postflight 2; triangles pointed down, $1.7\ \mu\text{W}$ scattering, postflight 2. The solid curve is a prediction based on equations of Burstyn, Sengers, Ferrell and Bhattacharjee.	2-34
Figure 2-15.	Log-log plot of fluctuation decay rates for backscattering (169.546° angle, in the fluid) versus a correlation-range corrected temperature distance to T_c . Symbols: squares, $17\ \mu\text{W}$ scattering, flight 2; circles, $1.7\ \mu\text{W}$ scattering, flight 2; triangles pointed up, $17\ \mu\text{W}$ scattering, postflight 2; triangles pointed down, $1.7\ \mu\text{W}$ scattering, postflight 2. The solid curve is a prediction based on equations of Burstyn, Sengers, Ferrell and Bhattacharjee.	2-35
Figure 2-16.	Microgravity slow-scan search for the liquid-vapor phase-coexistence phase boundary. Scan rate was $-100\ \text{mK/hr}$. This was done in the last day of the mission. Data are marked with the $+$ symbol while the straight lines are least-squares fitted to the data with the intersection a fitting parameter, T_0 . The transition observed is much sharper than observed on Earth.	2-36
Figure 2-17.	Postflight ($1\ \text{g}$), slow-scan search for the liquid-vapor phase boundary. Scan rate was $-100\ \mu\text{K/hr}$, as in Figure 16. Data are marked with a $+$ symbol.	2-37
Figure 3-1.	In situ dendritic growth velocity measurements from IDGE on USMP-3 during STS-75.	3-51
Figure 3-2.	There is no clear correlation between steady-state dendrite velocity and the microgravity vector.	3-52
Figure 3-3.	Variation in the quasi-static microgravity vector obscures any possible correlation with dendrite velocity.	3-52
Figure 3-4.	Noise in the dendritic growth does not appear to correlate with noise in the microgravity vector.	3-53
Figure 3-5.	An abrupt change in the microgravity vector does not seem to affect the dendrite.	3-53

Figure 4-1.	Axial composition of Earth-grown PbSnTe crystal. The solid line is from the analytical equation for totally mixed melt. This crystal was grown in a low gradient furnace, hence the first-to-freeze region is larger than that of crystals grown in the AADSF.	4-68
Figure 4-2.	Schematic of the geometric, thermal, and concentration boundary conditions used in the computational fluid dynamical calculations in this study.	4-69
Figure 4-3.	The three-dimensional flow field in the liquid region with constant acceleration magnitude and direction. (a) Acceleration is aligned with ampoule axis at 10^{-5} Earth gravity. (b) Acceleration is aligned with ampoule axis at 10^{-4} Earth gravity. (c) Acceleration is misaligned with ampoule axis by 5° with magnitude of 10^{-5} Earth gravity.	4-70
Figure 4-4.	The two-dimensional flow field near the melt solid interface when the acceleration vector (magnitude of 10^{-5} Earth gravity) is undergoing a 10° time-dependent tilt variation at a frequency of one cycle per hour.	4-71
Figure 4-5.	A typical segmented ampoule showing the three cells, and the location of the sample thermocouples.	4-72
Figure 4-6.	Temperature response of the recalescence in cell No. 1. The response did not show a sharp peak as in Earth-grown events, but showed a rounded temperature change. The event was repeated (upper curve displaced by 10°C for clarity) to verify the observation.	4-73
Figure 4-7.	The acceleration magnitudes, at the AADSF freeze zone, for each of the three primary directions. The z acceleration is along the AADSF furnace bore and in such direction that more dense fluid would move from the hot zone toward the cold zone, This time slice shows the acceleration during the free drift period that occurred at approximately MET 8/06:30 (198.6 hours on the graph).	4-74
Figure 4-8.	Vertical slices of the three USMP-3 PbSnTe crystals. These scans were made from the integrated results of CAT scans. Each crystal is positioned with the first to freeze end down. The insert at the upper left shows the position of the vertical slice for each crystal.	4-75
Figure 4-9.	Successive CAT, horizontal, slices of cell No. 1. The first to freeze end is at upper left. The first 13 slices were taken at 1-mm steps and the remaining slices at 3-mm steps. Images were made with 420 KV x rays.	4-76

Figure 4-10.	Successive CAT, horizontal, slices of cell No. 2. The first to freeze end is at upper left. The 13 slices were taken at 1-mm steps and the remaining slices at 3-mm steps. Images were made with 420 KV x rays. The first scan was taken approximately 8 mm above the base of the crystal hence it shows the beginning of the void formation.	4-76
Figure 4-11.	Successive CAT, horizontal, slices of cell No. 3. The first to freeze end is at upper left. The first 26 slices were taken at 1-mm steps and the remaining slices at 3-mm steps. Images were made with 420 KV x rays.	4-77
Figure 4-12.	Graphs of the one-dimensional analytical solutions for the profiles for both fully mixed and mixing via diffusion only during the directional solidification of PbSnTe.	4-77
Figure 4-13.	Axial composition scan of cell No. 1. The data scan was made 2 mm from the center line. Also shown are the analytical curves for a totally mixed sample and the start of one grown with diffusion mixing only. The anticipated composition spike of SnTe shows at the recalescence area at the left side of the plot, then the data flattens for what may be growth during thermal stabilization after the release of the latent heat. At 5 mm of growth the composition shows signs of trying to go to diffusion-controlled growth. At approximately 25 mm of growth the curve closely approximates the fully mixed case.	4-78
Figure 4-14.	Axial compositional profile of the crystal in cell No. 2. The nominally hot on bottom orientation follows the completely mixed curve for the first 45 mm of growth and then exhibits deviations that are, as yet, unexplained.	4-79
Figure 4-15.	Axial compositional profile of the crystal grown in cell No. 3. This crystal shows similar deviations from totally mixed as the crystal in cell No. 2 but over a longer section.	4-80
Figure 4-16.	Photomicrograph of the first to freeze region of cell No. 1. The first to freeze region clearly shows random patterns of sub-millimeter pores which were not visible on the CAT scans.	4-81
Figure 4-17.	A few pores were seen at the very base of the crystal from cell No. 2, but the defects are not clearly visible in the photograph.	4-82
Figure 4-18.	Photomicrograph of the first-to-freeze region of cell No. 3. The first-to-freeze region clearly shows random patterns of sub-millimeter pores which were not visible on the CAT scans.	4-83

Figure 5-1.	Schematic concept of the SIBALS experiment concept.	5-97
Figure 5-2.	Forced Flow Flame Spread Test (FFFT) Flight hardware including the 2 FFFT wind tunnel modules, 1 of 11 flat samples, 1 of 5 cylindrical samples, 2 of the 16 exit screens and the FFFT control box.	5-98
Figure 5-3.	FFFT Flat cellulose sample. Ignitor wire is shown on the right end of the sample and the thermocouple array is positioned along the sample centerline. During combustion the air flows from right to left to obtain concurrent flow flame spreading.	5-99
Figure 5-4.	FFFT cylindrical cellulose sample. Fuel materials is cast over a cylindrical heater rod. Ignitor wire is located on right hand end of fuel sample and thermocouple array positioned in the plane of the sample mounting card. During combustion the airflow is from right to left to obtain concurrent flow flame spreading.	5-100
Figure 5-5.	Position of flame features versus time during the burn of FFFT sample six, ashless filter paper, burning in air at normal pressure at approximately 1 cm/sec.	5-101
Figure 5-6	Comparison of a flame image from FFFT test six with reaction rate contours from the numerical simulation of concurrent-flow flame spreading.	5-102
Figure 5-7.	Time history of temperature at a point on the fuel surface for a flame spreading over ashless filter paper in a purely forced concurrent flow of 21 percent oxygen/ 79 percent nitrogen in an indicated free stream velocity of approximately 1 cm/sec.	5-102
Figure 5-8.	Comparison of a flame lengths for FFFT cylindrical samples in various air flow velocities and initial fuel temperatures.	5-103
Figure 6-1.	RITSI hardware. Two modules, two sample/holder storage containers, one sample/holder, electronic control, and outputs display.	6-119
Figure 6-2.	Schematic cross section view of hardware.	6-120
Figure 6-3.	Sample card with 1 cm by 1 cm grid.	6-121
Figure 6-4.	Flame spread at three different flow velocities in two-dimensional configuration (flow from right).	6-122
Figure 6-5.	Char growth patterns at three different flow velocities in two-dimensional configuration (flow from right).	6-123
Figure 6-6.	Temperature histories in two-dimensional configuration, 5 cm/sec.	6-124

Figure 6-7.	Upstream char front location histories in two-dimensional configuration.	6-125
Figure 6-8.	Flame spread patterns at three different flow velocities in three-dimensional configuration (flow from right).	6-126
Figure 6-9.	Char growth patterns in the three-dimensional configuration (flow from right).	6-127
Figure 6-10.	Temperature histories in three-dimensional configuration, 5 cm/sec.	6-128
Figure 6-11.	Upstream char front location histories in three-dimensional configuration.	6-129
Figure 6-12.	Char upstream spread rate versus external flow velocity.	6-130
Figure 6-13.	Flame spread patterns along open edges (ignition was initiated at the center, flow from right).	6-131
Figure 6-14.	Smoldering char growth patterns at different flow velocities (flow from right).	6-132
Figure 7-1.	Photograph of the detector used in the orbiter (STS) fleet and on Spacelab. The air enters from the right and is exhausted out the port under the small plate on the top left.	7-146
Figure 7-2.	Photograph of an engineering model of the <i>ISS</i> smoke detector. The lasers and other electronics are in the black enclosure below and the laser beam passes through the space enclosed by the framework on the top, reflecting off of turning mirrors at the top.	7-147
Figure 7-3.	Schematic showing installation of the CSD near-field module inside the glovebox and far-field module outside the glovebox.	7-148
Figure 7-4.	Photograph of the near-field module. The soot sampler assembly (probes extended) is on the left, and is installed in a hole in the center of the near-field module. A sample card with a candle installed is on the right.	7-149
Figure 7-5.	Photograph of the inside of the far-field box. The STS detector is the aluminum module in the center of the duct and the <i>ISS</i> detector is the black module on the right.	7-150
Figure 7-6.	Traces of smoke detector signals as a function of time for a candle test No. 16. Initial peak on both detectors is wax vapor released by the ignition process. The units on the vertical axis are arbitrary, the smoke detector data have been scaled so their dynamic ranges have similar vertical extent.	7-151

Figure 7-7.	Traces of smoke detector signals as a function of time for a candle test No. 6. Initial peak both detectors is wax vapor released by the ignition process. The units on the vertical axis are arbitrary; the smoke detector data have been scaled so their dynamic ranges have similar vertical extent.	7-152
Figure 7-8.	Traces of smoke detector signals as a function of time for a silicone rubber test No. 7. The units on the vertical axis are arbitrary; the smoke detector data have been scaled so their dynamic ranges have similar vertical extent.	7-153
Figure 7-9.	Traces of smoke detector signals as a function of time for a Kapton™ test No. 14. The units on the vertical axis are arbitrary; the smoke detector data have been scaled so their dynamic ranges have similar vertical extent.	7-154
Figure 7-10.	(From left to right) Images of microgravity particulate from overheated Teflon™ and Kapton™ and Candle soot.	7-155
Figure 8-1.	Approximate OARE instrument location on STS–75.....	8-172
Figure 8-2.	Orbiter body and structural coordinate systems.	8-173
Figure 8-3.	Approximate location of SAMS sensors on the USMP–3 MPESSE carriers, STS–75.....	8-174
Figure 8-4.	SAMS Unit F TSH 1B data, 10-sec interval average, showing use of F5L and F5R VRCS jets for attitude maintenance. Simultaneous F5L and F5R jet firings indicated by + markers; individual events indicated by o markers. MET start 010/04:00.	8-175
Figure 8-5.	SAMS Unit F TSH 1B data from MEPHISTO PRCS 5D ($-z_b$) event. MET start 012/12:24:45.	8-176
Figure 8-6.	SAMS Unit F TSH 1B data from MEPHISTO PRCS 5C1 ($+y_b$) event. MET start 012/14:24:45	8-177
Figure 8-7.	SAMS Unit F TSH 1B data from MEPHISTO PRCS 5C2 ($-y_b$) event. MET start 012/14:27:45.	8-178
Figure 8-8.	SAMS Unit F TSH 1B data from MEPHISTO PRCS 5D ($-z_b$) event, z_o axis of data shown. PRCS jet usage indicate on top section of plot. MET start 012/12:24:45.	8-179
Figure 8-9.	SAMS Unit F TSH 1B spectrogram showing data collected during Ku band antenna reposition. MET start 007/13:00:12. Note interruption of 17-Hz signal at 007/13:05:25 for 17 sec.	8-180

Figure 8-10.	SAMS Unit G TSH 2A spectrogram showing data collected during flight control system checkout. MET start 013/15:00:00. Note change in signal character upon activation of auxiliary power unit one at 013/15:03.	8-181
Figure 8-11.	OARE data representing the microgravity environment at the OARE location during TSS-1R deploy operations. MET start at 003/00:00. Note TSS flyaway occurred at 003/00:27. Transient accelerations seen in the plot are due to PRCS activity to compensate for tether dynamics.	8-182
Figure 8-12.	SAMS Unit F TSH 1A data representing the microgravity environment during TSS-1R deploy operations. MET start at 003/00:00. Note TSS flyaway occurred at 003/00:27. Transient accelerations seen in the plot are due to PRCS activity to compensate for tether dynamics.	8-183
Figure 8-13.	SAMS Unit F TSH 1A spectrogram showing data collected during TSS-1R deploy operations. MET start at 003/00:00. Note TSS flyaway occurred at 003/00:27. Transient accelerations seen in the plot as vertical stripes are due to PRCS activity to compensate for tether dynamics. Variable frequency traces are related to tether pulley rotations during tether deploy.	8-184
Figure 8-14.	SAMS Unit F TSH 1A data from time of TSS-1R break. Note ringing of orbiter structure at about 9 Hz.	8-185
Figure 8-15.	Orbiter venting locations.	8-186
Figure 8-16.	OARE data representing the microgravity environment at the OARE location during the STS-75 mission. MET start at 000/00:27.	8-187
Figure 8-17.	OARE data representing the microgravity environment at the OARE location while Columbia was in the nominal USMP-3 attitude. MET start at 011/00:00:26.	8-188
Figure 8-18.	OARE data representing the microgravity environment at the OARE location while Columbia was in the AADSF 1 attitude. MET start at 008/07:15:13.	8-189
Figure 8-19.	Three-dimensional projection of OARE data representing the microgravity environment at the OARE location while Columbia was in the AADSF 1 attitude. MET start at 008/02:00:47.	8-190
Figure 8-20.	OARE data representing the microgravity environment at the OARE location while Columbia was in the AADSF 2 attitude. MET start at 009/07:00:03.	8-191
Figure 8-21.	Three-dimensional projection of the OARE data representing the microgravity environment at the OARE location while Columbia was in the AADSF 2 attitude. MET start at 009/02:02:00.	8-192

Figure 8-22.	OARE data representing the microgravity environment at the OARE location while Columbia was in the AADSF 3 attitude. MET start at 010/07:00:24.	8-193
Figure 8-23.	Three-dimensional projection of the OARE data representing the microgravity environment at the OARE location while Columbia was in the AADSF 3 attitude. MET start at 010/02:00:13.	8-194

LIST OF TABLES

Table	Title	Page
Table 6-1	Test Matrix	6-118
Table 7-1	Detector signals from CSD flight tests (<i>ISS</i> values are scaled to flight detector sensitivity)	7-144
Table 7-2	TEM results	7-145
Table 8-1	STS-75 OARE head location and orientation	8-170
Table 8-2	STS-75 SAMS head location and orientation	8-170, 171
Table 8-3	Accelerations associated with PRCS activity	8-171

USMP–3 Acronyms

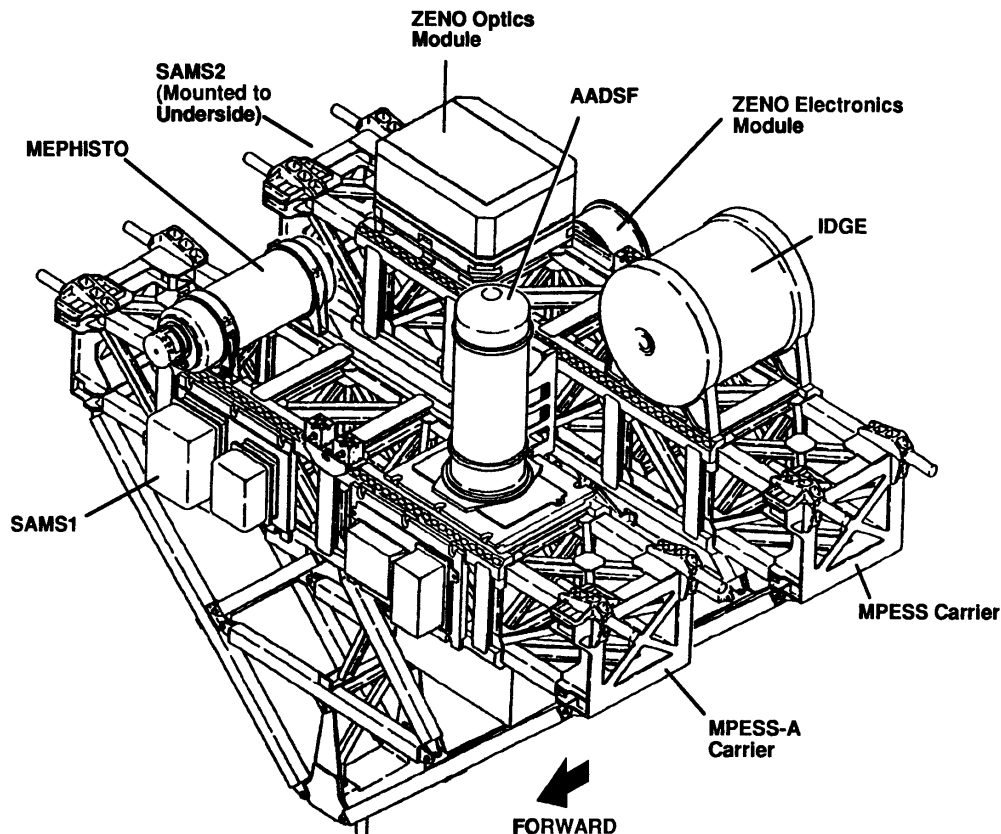
AADSF	Advanced Automated Directional Solidification Furnace (USMP–2, USMP–3)
ARC	NASA Ames Research Center (Moffett Field, CA)
CCD	Charge-Coupled Device
CENG	Centre d’Etudes Nuclaires National de Grenoble (Grenoble, France)
CFD	Computational Fluid Dynamics
CMC	Center for Macromolecular Crystallography (UAB)
CMDS	Consortium for Materials Development in Space (UAH)
CMMR	Center for Microgravity and Materials Research (UAH)
CNES	Centre Nationale d’Études Spatiales (“National Center for Space Studies,” French space agency)
CNRS	Centre National de la Recherche Scientifique (France)
CSD	Comparative Soot Diagnostics (experiment)
DARA	Deutsche Agentur für Raumfahrtangelegenheiten (“German Agency for Space Affairs,” German Space Agency)
DLS	Dynamic Light Scattering
ESA	European Space Agency
FFFT	Forced Flow Flamespreading Test
GBX	Glovebox
GCEL	Ground Control Experiments Laboratory (NASA MSFC)
IDGE	Isothermal Dendritic Growth Experiment
JPL	Jet Propulsion Laboratory (Pasadena, CA, managed by the California Institute of Technology)
JSC	NASA Johnson Space Center (Houston, TX)
KSC	NASA Kennedy Space Center (Cape Canaveral, FL)
LaRC	NASA Langley Research Center
LeRC	NASA Lewis Research Center (Cleveland, OH)
LOS	Loss of Signal
MEPHISTO	Matériel pour l’Étude des Phenomènes Intéressants de la Solidification sur Terre et en Orbite (“Apparatus for the Study of Interesting Phenomena of Solidification on Earth and in Orbit”)
MET	Mission Elapsed Time

MGBX	Middeck Glovebox
MPESS	Mission Peculiar Experiment Support Structure (Shuttle)
MSAD	Microgravity Science and Applications Division (NASA MSFC, also used to be the acronym for an OLMSA division at NASA Headquarters before name was changed to “Microgravity Research Division” (still Code UG))
MSFC	NASA Marshall Space Flight Center (Huntsville, AL)
NASA	National Aeronautics and Space Administration
NRC	National Research Council
OARE	Orbital Acceleration Research Experiment
PI	Principal Investigator
PIMS	Principal Investigator Microgravity Services (NASA LeRC)
POCC	Payload Operations and Control Center (NASA MSFC)
RITSI	Radiative Ignition and Transition to Spread Investigation
RPI	Rensselaer Polytechnic Institute (Troy, NY)
SAMS	Space Acceleration Measurement System
SEM	Scanning Electron Microscope
STS	Space Transportation System (Shuttle/external tank/solid rocket booster system, also a Shuttle mission designation)
TBE	Teledyne Brown Engineering
TEM	Transmission Electron Microscope
UAB	University of Alabama in Birmingham
UAH	University of Alabama in Huntsville
USMP–1	First United States Microgravity Payload (STS–52 Shuttle mission, launched in October 1992)
USMP–2	Second United States Microgravity Payload (STS–62 Shuttle mission, launched in March 1994)
USMP–3	Third United States Microgravity Payload (STS–75 Shuttle mission, launched in February 1996)
USMP–4	Fourth United States Microgravity Payload (STS–87 Shuttle mission, scheduled for launch in November 1997)
ZENO	Critical Fluid Light Scattering Experiment

USMP-3 Mission Information

Mission Designation: STS-75 (75th Shuttle mission)
Orbiter: *Columbia* (19th flight for this Shuttle)
Orbit Inclination: 28.45 degrees
Orbit Altitude: 160 nautical miles (184 statute miles)
Number of Orbits: 251 (6.5 million miles)
Major Payloads: USMP-3 and TSS-1R
Launch: February 22, 1996 @ 3:18 p.m. EST
Landing: March 9, 1996 @ 8:58 a.m. EST at KSC
Mission Duration: 15 days, 17 hours, 41 minutes, 25 seconds (15/17:41:25)
Crew:

Commander: Lt. Col. Andrew M. Allen, U.S. Marine Corps (3rd mission)
Pilot: Lt. Col. Scott J. Horowitz, U.S. Air Force (1st mission)
Payload Commander: Dr. Franklin R. Chang-Diaz, Ph.D. (5th mission)
Mission Specialist: Maurizio Cheli, ESA (1st mission)
Mission Specialist: Claude Nicollier, ESA (3rd mission)
Mission Specialist: Dr. Jeffrey A. Hoffman, Ph.D. (5th mission)
Payload Specialist: Dr. Umberto Guidoni, Ph.D., Italian Space Agency (1st mission)



AUTHOR INDEX

	Page
Alexander, J.I.D.	1-3
Boukari, H.	2-13
Briggs, M.E.	2-13
Debnam, W.J.	4-57
DeLombard, R.	8-159
Favier, J.J.	1-3
Ferkul, P.V.	5-87
Fripp, A.L.	4-57
Gammon, R.W.	2-13
Garandet, J.P.	1-3
Gard, M.Y.	7-135
Gent, D.	2-13
Glicksman, M.E.	3-41
Greenberg, P.S.	5-87
Griffin, D.W.	7-135
Hrovat, K.	8-159
Kashiwagi, T.	6-107
Koss, M.B.	3-41
Malarik, D.C.	3-41

McPherson, K.M.	8-159
Moskowitz, M.E.	8-159
Narayanan, R.	4-57
Olson, S.L.	6-107
Pettegrew, R.D.	5-87
Reckart, T.A.	8-159
Rogers, M.J.B.	8-159
Rosch, W.R.	4-57
Sacksteder, K.R.	5-87
Shaumeyer, J.N.	2-13
Shih, H.Y.	5-87
T'ien, J.S.	5-87
Urban, D.L.	7-135
Wilkinson, R.A.	2-13

TECHNICAL MEMORANDUM

THIRD UNITED STATES MICROGRAVITY PAYLOAD: ONE YEAR REPORT

Peter Curreri

USMP-3 Mission Scientist

George C. Marshall Space Flight Center, MSFC, Alabama 35812

Overview

The Third United States Microgravity Payload (USMP-3) Space Shuttle mission was launched February 22, 1996, and landed March 9, 1996. It lasted 15 days and the Shuttle crew performed extensive microgravity science research during that time. The principal investigators (PI's) for the mission submitted science reports of their research findings to the USMP-3 mission scientist, and those reports were compiled into the USMP-3 One Year Report. The purpose of the report is to inform the microgravity science community and the public of the results of the experiments flown on the Shuttle mission.

The USMP-3 One Year Report represents the culmination of many years of sustained effort on the part of the investigators, mission management, and support personnel and is intended not only for the scientific community, but also for general public awareness and education. This mission gave the microgravity science community outstanding research opportunities not only to report and verify results obtained in previous flights, but to perform new experiments which contributed substantially and uniquely to the technological and commercial knowledge of the United States and its international partners. The results obtained and the lessons learned from this and future missions will lead us into a new era of microgravity research—to the Space Station and beyond.

USMP-3

The USMP-3 mission was launched on the 19th flight of the Space Shuttle Columbia, STS-75, on February 22, 1996. It carried four major microgravity experiments as well as the SAMS and OARE accelerometer systems. The USMP-3 experiments utilized microgravity to increase the fundamental understanding of materials processes. Three studied formation of solid from the melt and one studied the critical point of a noble gas. The science payload also included three middeck glovebox investigations which studied the effect of microgravity on combustion processes. While the glovebox investigations required intense crew involvement, the major USMP-3 experiments were controlled almost completely by telepresence.

USMP-3 utilized two Mission-Peculiar Experiment Support Structures (MPES) which were connected together and mounted behind the other STS-75 primary payload, the Tethered Satellite System (TSS). Opportunities for science by the USMP investigations were achieved during the TSS operations. After the TSS was lost on flight day 4, the USMP investigations went on to receive about 10 days of microgravity as the primary payload. The TSS safety requirements mandated that the Shuttle crew operate with dual shifts. Thus, unlike previous USMP missions, there were no “quiet periods” (where the total crew was asleep).

which would have allowed the microgravity investigations to perform the most sensitive microgravity experiments without crew-induced disturbances. In order to provide quiet periods for the USMP experiments, a concept for a crew display to monitor accelerations and provide real-time crew feedback was developed with Payload Commander Dr. Franklin Chang-Diaz, and was implemented during the mission. The results, as will be presented in the SAMS section of this report, were comparable to “quiet time” accelerations during crew sleep. Thus, one lesson learned was that the crew acceleration feedback display could be quite effective and should be considered for use on future microgravity missions.

The major USMP-3 experiments were the Advanced Automated Directional Solidification Furnace (AADSf), the Isothermal Dendritic Growth Experiment (IDGE), Matériel pour l’Etude des Phénomènes Intéressants de la Solidification sur Terre et en Orbite (MEPHISTO), and the Critical Fluid Light Scattering Experiment (Zeno).

The AADSf experiment was involved in gaining new understanding of both fundamental crystal growth and its interaction with gravity. The furnace operated superbly. As the first crystal started to form, the temperature signature of the crystal nucleation was much more subdued than observed in Earth-based experiments. The telescience capability built into the AADSf was used to remelt and save the crystal. Postflight x-ray measurements showed void, or large pore, formation in the crystals, which has not been observed in Earth-grown crystals.

The IDGE experiment examined the formation of dendrites, which are tiny, pine tree-shaped crystals that commonly form as molten materials solidify. Dendrites are a concern in the production of most commercially important metal alloys because their structure has a strong influence on the mechanical properties of the material. Previous studies on USMP-2 indicated that small deviations from theory in the growth rate and tip radius of the dendrites were due to the microgravity environment. USMP-3 results during the varying gravity resulting from the TSS being reeled out found that the variations are instead due to specimen size.

The MEPHISTO experiment studied how small disturbances in gravity can affect the production of alloys and metals by firing the Shuttle primary control jets and observing the impact. The experiment demonstrated that when the angle of the growing metal relative to the accelerations was carefully controlled, the damage to the crystals by the resulting fluid flow could be eliminated. This and other solidification experiments from the USMP-3 provided unique data that is being applied to improve processes for making products ranging from alloys for airplane turbine blades to electronic materials.

The Zeno experiment used its exquisite temperature control of ± 3 microdegrees to explore the behavior of xenon near its critical point. On USMP-3 the investigators were able to control the density changes by changing the temperature, which, although its impact is very small on Earth, became a major factor in the low gravity of the Shuttle. This allowed the investigators to achieve their goal of getting stable, equilibrium measurements of the microscopic hydrodynamic fluctuations in the sample. At the end of the flight they were able to record and observe the sharpest phase transition ever observed near room temperature; the phase boundary was observed with a precision of ± 20 microdegrees.

The glovebox experiments consisted of three combustion processes investigations—

- The Comparative Soot Diagnostics (CSD). The CSD investigation attempted to understand the

soot production processes from flames burning in microgravity. NASA has flown fire detectors on Skylab and the Space Shuttle and has included them in the design for the *International Space Station (ISS)*. CSD data will help improve their design by determining soot morphology in low gravity.

- The Radiative Ignition and Transition to Spread Investigation (RITSI). The RITSI investigation found that the flame spread behavior with the external flow velocity in microgravity showed a completely opposite trend from that found in normal gravity. The investigators also observed surprisingly complex smoldering growth patterns in microgravity.
- The Forced Flow Flamespread Test (FFFT). The FFFT investigation studied the effects of flow speed and paper thickness for the flat paper samples, as well as the effect of flow speed, flow direction, and initial fuel temperature for the cylindrical fuels.

KEY USMP–4 PERSONNEL

Stephen Davison
Universities Space Research Association/NASA Headquarters
USMP–3 Program Scientist

Sherwood Anderson
NASA Marshall Space Flight Center
USMP–3 Mission Manager

Rose Cramer
NASA Marshall Space Flight Center
USMP–3 Payload Operations Lead

SECTION I.

STUDY OF INTERESTING SOLIDIFICATION PHENOMENA ON THE GROUND AND IN SPACE (MEPHISTO)

Acknowledgments

This work was carried out within the framework of the GRAMME agreement between CNES and the CEA, and was supported by NASA through Grant NAG3-1740 and by the State of Alabama through the Center for Microgravity and Materials Research and the Alabama Research and Education Network.

SECTION I. STUDY OF INTERESTING SOLIDIFICATION PHENOMENA ON THE GROUND AND IN SPACE (MEPHISTO)

J. J. Favier, J. Iwan D. Alexander[†], J. P. Garandet

Comissariat à l'Energie Atomique
DTA/CEREM/DEM/SPCM
17 Rue des Martyrs
Grenoble Cedex 9
FRANCE

[†]Center for Microgravity and Materials Research
University of Alabama in Huntsville
Huntsville, Alabama 35899, USA

ABSTRACT

Real-time Seebeck voltage variations in a Sn-Bi melt, during directional solidification in the MEPHISTO (*Material por l'Etude des Phenomenes Intéressants de la Solidification sur Terre et en Orbite*) space flight experiment flown on the Third United States Microgravity Payload (USMP-3) mission can be correlated with well-characterized thruster firings and an Orbiter Main System (OMS) burn. The Seebeck voltage measurement is related to the response of the instantaneous average melt composition at the melt-crystal interface. This allowed us to make a direct comparison of numerical simulations with the experimentally obtained Seebeck signals. Based on the results of preflight and real-time computations, several well-defined thruster firing events were programmed to occur at specific times during the experiment. In particular, we simulated the effects of the thruster firings on melt and crystal composition in a directionally solidifying Sn-Bi alloy. The relative accelerations produced by the firings were simulated by impulsive accelerations of the same magnitude, duration and orientation as the requested firings. A comparison of the simulation results with the Seebeck signal indicates that there is a good agreement between the two. This unique opportunity allows us, for the first time, to quantitatively characterize actual g-jitter effects on an actual crystal growth experiment and to properly calibrate our models of g-jitter effects on crystal growth.

1.1 INTRODUCTION

The MEPHISTO program is the result of a cooperative effort that involves the French nuclear and space agencies, Commissariat à l'Energie Atomique (CEA)—Centre National d'Etudes Spatiales (CNES), and the National Aeronautics and Space Administration (NASA). Six space flights on the USMP carrier were initially planned, with odd-numbered missions being the responsibility of the French scientific teams and the even-numbered missions being the responsibility of the U.S. During the first flight of MEPHISTO in October 1992, bismuth-doped tin samples (Sn:0.5 percent at. Bi) were used and experiments were carried out both below and above the morphological stability threshold. Exciting results were obtained¹ that opened new perspectives for research.

The first scientific objective of the USMP-3 flight was to investigate the g-jitter induced solutal segregation in planar front solidification. To do so, we requested well controlled gravity perturbations, mainly in the form of primary remote control system (PRCS) burns. The other main scientific objective was to track the morphological stability threshold (i.e., the instability where the growth front goes from planar to cellular) with the finest accuracy possible. In comparison with the first flight, the USMP-3 alloys were slightly more concentrated (1.5 percent at. Bi), in order to check a possible soluto-convective effect. It should be noted that, in contrast, both the USMP-2 and USMP-4 MEPHISTO flights (Professor Abbaschian, University of Florida, principal investigator) featured bismuth-based alloys with low tin concentrations. MEPHISTO is basically a directional solidification furnace, where three samples are simultaneously processed. An original point is that there are in fact two heating/cooling subsystems;^{2,3} one of them is maintained at a fixed position to provide a reference interface, whereas the other is allowed to move for solidification and melting of the alloy. Sample No. 1 is dedicated to a measurement of the Seebeck voltage between the two ends, meaning that the system acts as its own thermocouple, with a “cold” and a “hot” reference junction (respectively the moving and fixed interfaces). The Seebeck voltage is then a measure of the undercooling at the growth front, a key feature being that the signal is obtained in real time. It is thus possible to run many experimental cycles on the same sample, which in turn allows checking of the reproducibility of the process and ensuring a better accuracy of the results. On sample No. 2, the position and the velocity of the moving interface are obtained from an one line resistance measurement. At the end of the experimental cycle, a quench freezes the structure of the solid-liquid front. Peltier pulse marking performed on sample No. 3 allow the determination of the shape of the interface at given time intervals. Moreover, thermocouples present in the liquid phase for both samples No. 2 and No. 3 are used to determine the temperature gradient and possible thermal fluctuations. The MEPHISTO facility ran for 312 hr, including 216 hr dedicated to scientific operation. During that time period, 24 solidification/fusion cycles were carried out. Five growth rates were preprogrammed (1.7, 3.7, 5.7, 12 and 24 mm/hr) before the flight, but, thanks to teleoperation, we were able to use different growth rates to track the morphological stability threshold. For controlled gravity perturbations, we obtained nine PRCS burns, ranging in duration from 10 to 25 sec. In addition, an OMS burn and a 360° *x*-axis roll were also performed. Last but not least, it should be noted that no anomalies were detected during the mission.

During the first flight of the MEPHISTO directional solidification experiment on NASA's USMP-1 mission in 1992, the impact of sudden effective gravity perturbations was clearly evidenced.¹ Real-time Seebeck voltage variations across an Sn-Bi melt showed a distinct variation that can be correlated with thruster firings (fig. 1-1).¹ The Seebeck voltage measurement is related to the response of the instantaneous average melt composition at the melt-solid interface.⁴ This permitted a direct comparison of numerical simulations (and acceleration data) with the Seebeck signals obtained on USMP-1. Motivated by the results of the comparison, we used numerical simulations to predict the response of the Seebeck signal to thruster firings of various magnitudes and durations. The behavior of the signal is directly related to changes in interfacial composition caused by thruster-induced convective disturbances. Motivated by the observations made on USMP-1, one of the objectives of the USMP-3 MEPHISTO experiments was to quantitatively characterize g-jitter effects on an actual crystal growth experiment. To plan the USMP-3 MEPHISTO experiments, simulations were carried out for different solidification rates and g-jitter scenarios.

There were several differences between the USMP-3 and USMP-1 experiments. First, a more concentrated alloy was solidified on USMP-3, and second, PRCS thruster burns were requested at particular times during four separate growth runs. The Seebeck signal was recorded continuously and downlinked in

real time to the MEPHISTO experiment team at NASA's Marshall Space Flight Center. This allowed for quantification of the effects of g-jitter on convective-diffusive transport in the melt through the changes in average interfacial composition obtained from the Seebeck measurement. In addition, guided by Space Acceleration and Measurement System (SAMS) acceleration data, we carried out simulations for comparison with the recorded Seebeck signals. The effects of thruster firings on the average composition were monitored in 6 separate experiments and for 11 separate acceleration disturbance events. Selected results from our ongoing postflight analysis are described below.

1.2 APPROACH

A sketch of the experiment setup is shown in figure 1–2. There are two furnaces: one is fixed and the other translated. The applied temperature profile shown in figure 1–2 leads to a central cylindrical melt volume bounded by a moving and a stationary (or reference) solid-liquid interface. The melt composition at the moving and the stationary reference interfaces is not the same. For Sn-Bi there is a dependence of melting temperature on concentration. Thus, it follows that the melting temperature at the two interfaces will also be different. The Seebeck effect gives rise to a small but measurable voltage difference between these two interfaces. Measurement of this voltage difference allows us to determine the average temperature and, thus, the average composition of the growing interface. The MEPHISTO setup and the Seebeck measurements are discussed in more detail in reference 4.

The numerical model used to simulate the response of the tin-bismuth melt to particular types of g-jitter has been described elsewhere.^{5–7} The essential features are outlined below. Solidification takes place as the furnace is translated along the ampoule (fig. 1–2). Directional solidification due to the furnace translation is simulated by supplying a two-component melt of bulk composition c_∞ at a constant velocity Vg at the top of the computational space (inlet), and withdrawing a solid of composition $c_s = c_s(x, t)$ from the bottom (fig. 1–2). The crystal-melt interface is located at a distance L from the inlet; the width of the ampoule is W . The temperature at the interface is taken to be T_m , the melting temperature of the crystal, while the upper boundary is held at a higher temperature T_h . In the actual experiment, the temperature gradient along the ampoule wall ahead of the growing interface was essentially linear (195 K cm⁻¹). Thus, we set a linear temperature gradient along the wall in the simulations. Furthermore, since we wish to confine our attention to compositional nonuniformities caused by buoyancy-driven convection, rather than variations resulting from nonplanar crystal-melt interfaces, the interface is held flat. We expect that, given the large temperature gradient, changes in melting temperature due to compositional nonuniformity will not lead to significant changes in interface shape due to interfacial compositional inhomogeneity. Furthermore, because of the melt's low Prandtl number and the low-magnitude accelerations, convection does not lead to significant deviations of the temperature from the conductive state. Thus, changes in the interface shape due to changes in the thermal field will be negligible. In an actual experiment, owing to the finite length of the ampoule, there is a gradual decrease in length of the melt zone during growth. In this model, transient effects related to the change in melt length are ignored. Since the MEPHISTO experiments involve melt lengths that far exceed the ampoule diameter, this does not preclude us from calculating the compositional transient. That is, we can start the calculations by solidifying from an initially uniform composition melt.

The dimensionless equations governing coupled convective-diffusive heat mass and species transfer in the melt were assumed to be those for a Boussinesq fluid with a linear dependence of density on temperature

and composition. The boundary conditions imposed were those corresponding to plane front directional solidification at a translation rate V_g with a linear temperature gradient applied to the ampoule walls. Solute was preferentially rejected at the crystal-melt interface ($k=0.27$ for this Sn-Bi alloy). The equations were solved using a Chebyshev spectral method.

1.3 RESULTS

The PRCS firings produced an impulse acceleration with the largest component parallel to the solid liquid interface. Figure 1–3 shows the actual (uncorrected for drift) and predicted Seebeck signal for an experiment subject to two thruster burns (25 sec and 10 sec in duration) that produced an acceleration oriented parallel to the crystal-melt interface (i.e., perpendicular to the ampoule axis). Before the first burn, the Seebeck signal decreased monotonically. Immediately following the burn, the signal increased rapidly and reached a maximum about 100 sec after the termination of the burn. The signal then decreased slowly and eventually took on almost the same slope that it had before the burn. The same behavior occurred following the second burn after translation of the furnace was stopped. Solidification then ceased and the Seebeck signal increased as the average interfacial concentration decreased. Note that the actual Seebeck measurement shown was not corrected for drift and, thus, the voltage did not return to its original value. For the response of the Seebeck signal predicted by computer simulation, there was an immediate rapid response to each of the firings. In addition, we see that the time taken for the Seebeck signal to reach a maximum value was approximately the same for the computed and measured signals.

1.4 DISCUSSION

There is considerable interest in the effects of spacecraft residual acceleration, or g-jitter, on experiments conducted in the low-gravity environment of a spacecraft, particularly since the objective of conducting many of the experiments in low gravity is to avoid the effects of gravitational acceleration on Earth. Understanding these effects is important when considering the design of orbital experiment facilities, the choice of orbital attitude for space laboratories and platforms, the optimal choice of experiment operating conditions and materials, as well as the scheduling of crew activities, quiet periods, pointing maneuvers and thruster firings used for attitude control.

The USMP–3 MEPHISTO experiments permitted a quantitative correlation between well-characterized g-jitter recorded by spacecraft accelerometers and the response of a directionally solidifying alloy. Furthermore, the comparison of the results of the experiment with the predictions of numerical simulations carried out on the Alabama Research and Education Network's C–90 Supercomputer will allow us to verify the degree to which such simulations can accurately predict experiment sensitivity to g-jitter accelerations. Without quantitative experimental verification, such predictions are of limited use and could lead to unnecessary design restrictions, an undesirable low-gravity environment, or unsuitable experiment operating conditions.

Ongoing work involves corrections of the raw Seebeck data, analysis of residual acceleration data measured by NASA's SAMS, and refinement of the computational simulations. This unique experiment showed that use of simulations to assist in changes in experiment strategy greatly enhances the scientific return from limited opportunity space flight experiments. It is expected that ongoing work will yield benchmark comparisons between measured and predicted residual acceleration effects.

1.5 REFERENCES

1. Favier, J.J.; Garandet, J.P.; Rouzaud, A.; and Camel, D.: *J. Crystal Growth*, Vol. 140, p. 237, 1994.
2. Rouzaud, A.; Comera, J.; Contamin, P.; Angelier, B.; Herbillon, F.; and Favier, J.J.: *J. Crystal Growth*, Vol. 129, p. 173, 1993.
3. Rouzaud, A.; Favier, J.J.; and Thevenard, D.: *Adv. Space Res.*, Vol. 8, p. 49, 1988.
4. Favier, J.J.; Garandet, J.P.; Rouaud, A.; and Camel, D.: *J. Crystal Growth*, Vol. 113, p. 21, 1991.
5. Favier, J.J.; and Rouzaud, A.: *Revue Phys. Appl.*, Vol. 22, p. 713, 1987.
6. Alexander, J.I.D.; Ouazzani, J.; and Rosenberger, F.: *J. Crystal Growth*, Vol. 97, p. 285, 1989.
7. Alexander, J.I.D.; Amiroudine, S.; Ouazzani, J.; and Rosenberger, F.: *J. Crystal Growth*, Vol. 113, p. 21, 1991.
8. Alexander, J.I.D.: "Materials and Fluids Under Low Gravity," (Ratke, L.; Walter, H.; and Feuerbacher, B., eds. Springer, Berlin), pp. 95–102, 1995.
9. Alexander, J.I.D.; Garandet, J.P.; Favier, J.J.; and Lizée, A.: "G-jitter Effects on Segregation During Directional Solidification of Tin-Bismuth in the MEPHISTO Furnace Facility," *J. Crystal Growth*, pp. 97–02, 1997, in press.

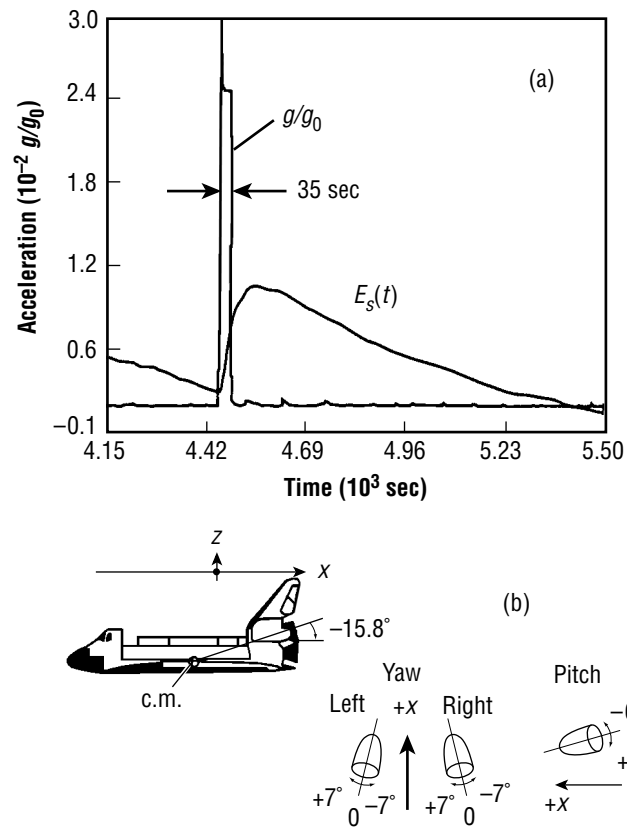


Figure 1-1. (a) Acceleration versus time for the OMS burn recorded on USMP-1 and the associated Seebeck signal, $E_s(t)$ [1]. (b) OMS engine alignment with the orbiter.

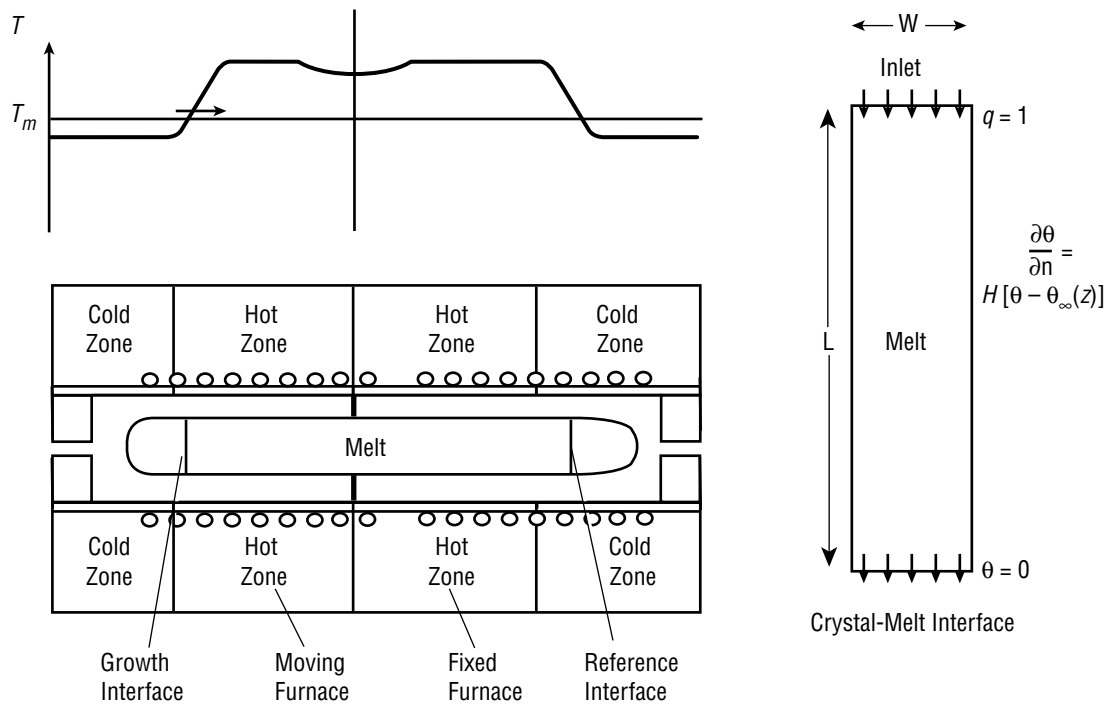


Figure 1-2. The MEPHISTO set-up (bottom-left), temperature profile (top left) and computational model (right). T_m denotes the melting temperature.

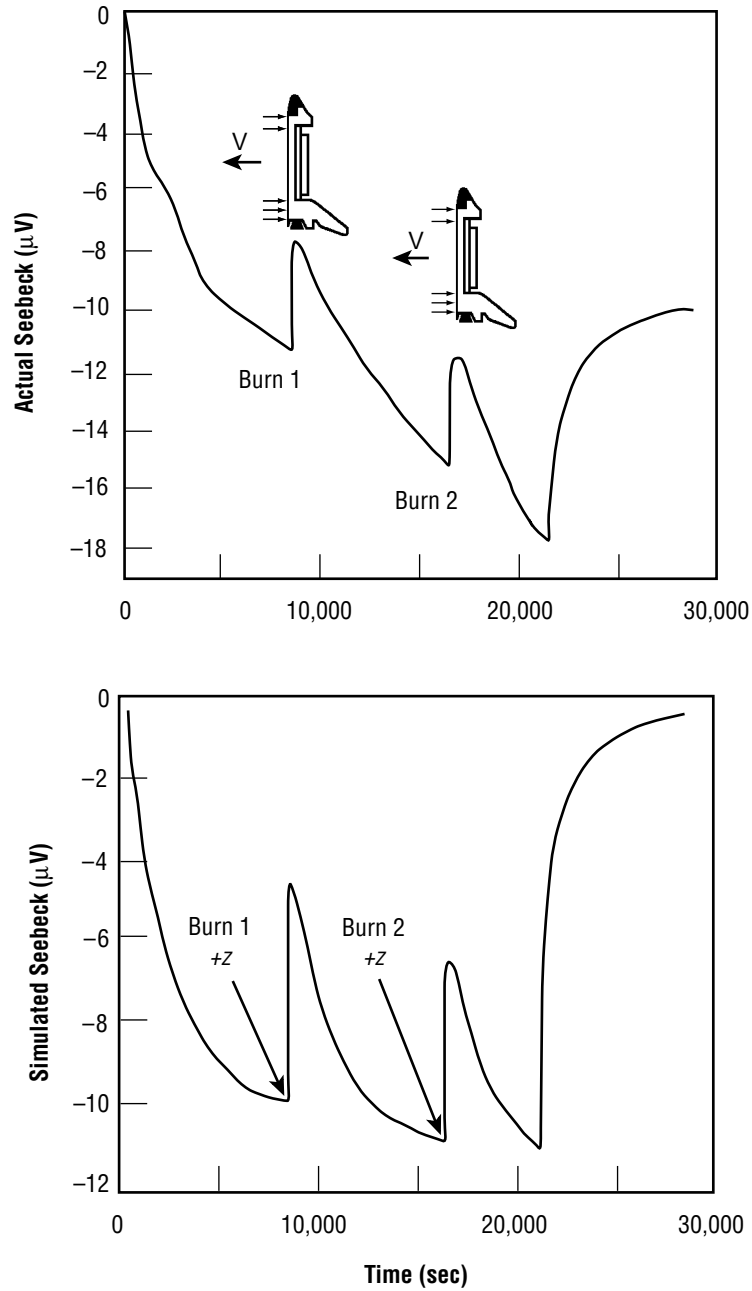


Figure 1-3. (a) Actual and (b) predicted Seebeck signal for a 25-sec and 15-sec burn oriented parallel to the crystal-melt interface.

SECTION II.

SECOND FLIGHT OF THE ZENO EXPERIMENT ON USMP-3

Acknowledgements

This work was sponsored by the Microgravity Applications and Science Division of NASA through NASA-Lewis under contract NAG3–25370. We wish to acknowledge the tireless efforts of our project managers, John Borden at the University of Maryland, Richard Lauver at Lewis Research Center, NASA, and Richard Reinker at Ball Aerospace, who kept all the parts of this project moving to the end. Robert Stack of Ball Aerospace worked energetically to get the instrument checked out and tested for the reflight, and prepared himself to be an expert at commanding. Mark Sienkiewicz got the flight software modified so that we could run under all TFL's and added a new calculated turbidity function that corrected an old offset problem. Robert Berg and Michael Moldover were always sympathetic and helpful as they helped us and worked to get their related experiment on the viscosity of xenon, CVX, designed and built. Richard Ferrell and Jan Sengers have offered much stimulation and guidance over many years on the importance and subtle issues of critical transport coefficients. Finally, thanks go to the rest of our POCC team, Greg Zimmerli, Andrew Peddie, and Klaus Gumpo, for working so hard to avoid making a false move or missing any data during the rather risky timeline of the second flight.

SECOND FLIGHT OF THE ZENO EXPERIMENT ON USMP-3

Robert W. Gammon, J. N. Shaumeyer, Matthew E. Briggs,

Hacène Boukari, David Gent,

Institute for Physical Science and Technology, University of Maryland, College Park

and

R. Allen Wilkinson

NASA Lewis Research Center, Cleveland, Ohio

Gammon

Phone: 301-405-4791

Fax: 301-314-9404

E-mail: rg2@umail.umd.edu

Shaumeyer

Phone: 301-805-4545

Fax: 301-805-4538

E-mail: jeff.sha@jnt.com

Briggs

Phone: 301-801-581-9990

Fax: 801-581-4801

E-mail: meb@mail.physics.utah.edu

Boukari

Phone: 301-405-4792

Fax: 301-314-9404

E-mail: hb@roissy.umd.edu

Wilkinson

Phone: (216)-433-2075

Fax: (216)-433-8660

E-mail: aw@lerc.nasa.gov

2.1 ABSTRACT

The second flight of the Zeno experiment in the USMP-3 flight has shown successful control of density perturbations near the window surfaces. These density changes were demonstrated to be arising from the rate of temperature change in the sample cell during the flight. These effects could be controlled by using decreasing ramp rates as the critical point (T_c) was approached. The cell window interference was carefully recorded to provide data about the phase of the interference close to the critical point and the effective window reflectivity. Correlograms were recorded from 500 μ K down to 2 μ K at 24 temperatures, 383 correlograms in all. The efforts to get closer were prevented by a long (>2 -week time constant) decay of a 1.3 percent density error caused by local heating from the 17 μ W laser beam. The phase boundary was located with unprecedented precision of ± 20 μ K. The complete experiment sequence was done with ground commanding and uploaded script files, bypassing the original autonomous-mode program sequence. More details of the experiment science requirements, the personnel, apparatus, and results are displayed on the Zeno home page at <http://www.zeno.umd.edu>.

2.2 INTRODUCTION

All fluids exhibit universal, anomalous behavior in their thermodynamic and transport properties in the region of their liquid-vapor critical point. This is most dramatic when one looks at a critical fluid in an optical cell and sees the sample become opaque with opalescence. This cloudiness is the consequence of the enormous thermodynamic fluctuations occurring in the fluid. The renormalization group calculations about critical thermodynamics have shown how to calculate the equilibrium divergences and how to relate different critical systems into universality classes. The theoretical calculation of transport processes such as thermal conductivity and viscosity in critical systems is much less developed.

The goal of the Zeno experiment is to measure the decay rate of critical fluctuations in xenon close enough to the critical point to determine the limiting behavior. The experiment uses photon-correlation light-scattering spectroscopy to measure the characteristics of the density fluctuations as the critical point is approached. (Critical properties of xenon are: $T_c=17.57^\circ\text{C}$, $P_c=58.4\text{ atm}$, critical density= 1.110 gm/cc.) The primary measurements are photon correlation functions, digitally processed in real time from the detected scattered-photon pulse stream. We also monitor the sample transmission which provides data about the local density and the sample turbidity when we get close to the critical point.

In this second flight we followed a timeline with only cooling steps of decreasing size and cooling rate in order to avoid problems found in the first flight with the locally perturbed density near the sample cell windows. We also took enough data far from T_c to characterize the sample cell reflectivity and thus provide a way to extract an accurate correlation range from the measured intensities. This data should allow the analysis of the first flight data despite its density uncertainties.

In the following report we will give an overview of the apparatus, review the problems found in the first flight, describe the plan for the second flight, and look at the second flight performance. This performance is summarized by the timeline plots of temperature, scattering intensity, and turbidity data. We show the improved control of density errors, the correlogram data, and our efforts so far to extract the correlation range. The surprise of a large density error from laser heating is discussed. Finally we show plots resulting from the slow temperature scan to locate the phase boundary (phase transition temperature). The reader is urged to look at the USMP-2 One Year Report to see a discussion of the first Zeno flight and a bibliography of the field.

2.3 THE APPARATUS

The optical layout is shown in figure 2-1. The sample cell sat at the center of a three-concentric-cylinder thermostat (*TH*). This thermostat could be set with $1\text{-}\mu\text{K}$ resolution and it gave control of $1.5\text{-}\mu\text{K}$ RMS for periods of 4 hours (sampling 2/min with 5-sec time constant). The shutters *S* 1–2 were used with one open and one closed to give two paths through the sample for the He-Ne laser beam (633 nm), split by *B* 1. Together with the filters *F* 1–2, two different intensities were available for the light scattering: $17\text{ }\mu\text{W}$ and $1.7\text{ }\mu\text{W}$. The lenses *L* 1–2 focused the laser waist into the sample. The lenses *L* 2–4 imaged the scattering volume onto the pinhole field stops *A* 2–4. The *PD* 1–2 are photodiodes used to measure the laser intensity before and after the sample by sampling behind the partial mirrors *M* 2–3. The photon counting detectors

were the photomultipliers *PMT* 1–2. All these optical components were mounted on a 10-cm-thick optical-honeycomb table and placed inside a temperature controlled (± 0.1 K on orbit), dry nitrogen filled, aluminum box. Overall external dimensions of the optics module were 102 by 84 by 56 cm³. The box had a radiation panel on the top through which heat energy flowed to allow active control of the box temperature. The remaining outside surfaces were covered with multilayer insulating blankets.

The sample cell was of unique design. A cross-sectional view is shown in figure 2-2. It featured stepped (“top-hat”) windows which allowed a large sample volume (0.7 cm) while allowing the beams down the axis to pass through only a thin, 100- μ m sheet of the fluid sample. The thin section limits the multiple scattering from the sample to less than 1 percent in our experiments. In the cell flown, the windows were an epoxied stack of a larger sapphire window and a smaller fused quartz window with AR coatings on the outer surfaces and no coatings on the inner surfaces next to the sample. All surfaces were superpolished. The fluid seals (to 70 bar) were crushed copper knife edges machined on the copper flanges. The remaining body parts were copper with some indium used to assure good thermal mating of the parts. The cell was filled to within 0.1 percent of the critical density, estimated by the symmetry of the sample volume and the centering of the meniscus when 2 mK below T_c . The filling and sealing valve is built into the cell wall.

The temperature control and measurement is based on using AC bridges which compare a thermistor and stable resistor (1 ppm/K) ratio with the ratio from a computer controlled inductive voltage divider. There are three nested, controlled aluminum cylinders providing the temperature control and setting a final gradient across the sample cell of <1 μ K/cm. A fourth transformer is switched between five different half bridges, on command, to monitor the temperatures of the sample, the three controlled shells and a Pt calibration thermometer on the sample cell. The least count (digitization) resolution of the measurements is 1 μ K and the measured RMS is 1.5 μ K, just larger than the least count.

2.4 LESSONS FROM THE FIRST FLIGHT

The first flight featured an active timeline, mostly run by the autonomous mode of flight computer. Three scanned searches for T_c were performed as well as one very long “zig-zag” search.²⁻¹ A temperature of 1 K from T_c was used for sample density homogenization. Temperature steps were done as fast as the thermostat would allow (up to 4.6 K/hr) or accelerated up to 60 mK/hr for steps less than 10 mK. During the flight we were puzzled and troubled by the fact that the transmission of the sample seemed to be drifting. There were also very strong density over-shoot transients during temperature changes. Postflight measurements showed that the instrument was reporting real sample property drifts. Further measurement and analysis showed that the interference effects from the inner cell windows were providing an extremely sensitive and useful check of the deviations in local sample density; we could see density changes less than 0.01 percent. We eventually concluded that we had managed to get the local density of the sample at the laser beam off by 1 to 2 percent from the critical density by our aggressive timeline and incomplete homogenization following the crossings to the two-phase region.

2.5 PLAN FOR THE SECOND FLIGHT

Thus we made our plans for the second flight on the basis of testing for equilibration when 4 K from T_c (“mixing”), making sure that we did not cross into the two-phase region until the end of the experiment, a slow scan search for the phase boundary, and to limit the rate of temperature change so that we kept the

density errors from lagging window surface temperatures to <0.1 percent. This required using controlled ramps between temperature points with ever lower slopes. In the course of preflight testing we found that we could use much slower scanning rates during T_c searches and we eventually settled on rates of $-100 \mu\text{K/hr}$ as a compromise rate for the search.

2.6 SECOND FLIGHT TIMELINE

During the second flight we operated with the flight computer in a paused state and controlled the sequence with a combination of uploaded sequence scripts and ground commanding. We actually carried out the planned timeline. The only changes from the ground baseline were that we waited until the drifts in the transmission (turbidity) signal corresponded to <0.1 percent/hr before taking data or moving to the next temperature. We equilibrated and took measurements at: 4 K, 1.4 K, 750 mK, 300 mK, 200 mK, 100 mK, 56 mK, 30 mK, 18 mK, 10 mK, 5.6 mK, 3 mK, 1.8 mK, 1.0 mK, 560 μK , 300 μK , and 180 μK . These temperatures are temperature distance above the nominal value of T_c . During the mission we used the data in hand to refine our estimate of the location of T_c on our temperature scale.

The timeline and experiment history are well illustrated by the flight data in figures 2-3, 2-4, and 2-5. Figure 2-3 shows the sequence of temperatures seen by the sample over the course of the mission. In this log plot, the temperature steps and slopes all look the same but they are logarithmically decreasing. Figure 4 shows the forward scattered intensity over the mission sequence. The sudden jump in count rate at Mission Elapsed Time day 10, hour 7:00 (MET 10/7:00) comes from the scheduled laser intensity change made at that point (sitting at 1 mK from T_c). The intensities following this change show very little drift. Figure 5 shows that after the laser power was lowered from 17 μW to 1.7 μW , the turbidity jumped up and then began a strong, uncontrollable drift downward. We have concluded that this drift was real (though it has never been seen on the ground at a power change)! and due to a low-density region that had developed from laser heating of the inner window surfaces. When the laser power was changed, the density began moving back towards the average (critical) density. By that time the sample temperature was so close to T_c that it was going to take weeks to relax away. Unfortunately there were only 4 days of the mission left so we plunged on, taking the planned data. We were also making needed adjustments in our estimate of the T_c location based on the data in hand (turbidity, intensity and decay rates).

2.7 DENSITY MONITORING

Figure 2-6 shows a magnified section of the turbidity data from MET day 2. This plot shows the interference fringes from the windows. It also shows how the temperature scanning was stopped at positions of maximum slope so that the sensitivity of the interference was maximized for local density changes. In the first 10 days of the mission, with the laser power fixed at 17 μW , we could routinely achieve our goal of turbidity drifts of $\leq 0.001/\text{hr}$. After the power change, there was only a steady drift of the signal indicating a fairly large density error with very long time constant.

Figure 2-7 is another section of turbidity data from MET days 4 to 8 that shows a phenomenon which is accentuated in low gravity. The figure shows the fairly large density transients occurring during and following controlled ramps between temperatures. These transients are much smaller on the ground. The ramps used did not completely avoid density transients but they were small enough at each step that, within a few hours, the turbidity signal would again become stable (defined as equilibrium).

We made a quantitative study of the density transients observed on some temperature changes during the mission. An example is shown in figure 2-8. Here the thermal expansion contribution has been subtracted and the residual phase interpreted as due to density changes. Thus we can plot $\delta\rho/\rho_c$ during and following a temperature change, in this case from 500 mK to 300 mK. This change was done with a sequence of 10 steps, 6 minutes apart. Notice that each step can be distinctly seen in the response of the fluid fluctuations. This is a striking demonstration of the effect of the surface film density changes occurring during the temperature changes; the laser beam crosses essentially only fluid which is in such a film. We were delighted to see the good agreement between the calculated density dynamics, modeled with numerical solutions of the adiabatic effect equations for a critical fluid.³ The inputs to the model are the dimensions of the sample volume, the properties of critical xenon, and the measured temperature of the cell wall during the ramp. The comparison is absolute, without scaling. Attempts to model this effect for terrestrial measurements have so far failed because of convective flows which quickly smear the wall-induced density changes in the adiabatic expansion layers.

With this background in using our “window-interferometer,” we are certain of the interpretation of the drifting turbidity signals following dropping the laser power. We have looked carefully at our baseline data taken before and after the mission. There is no indication of this local heating. Thus we were surprised to see this strong effect during the mission. We believe that the buildup of low density around the window hot spots is hidden on the ground by convective flows in the vertical sheet of the thin fluid sample. We estimate the temperature rise from the 48-ppm surface absorption from the two surfaces to be about 1.9 μ K. Unfortunately, this small temperature change can produce more than 1.3 percent local density error in the part of the sample being probed by the laser scattering when the temperature reaches 1 mK from T_c .

2.8 MEASURED CORRELATION FUNCTIONS

Precision measurements of the fluctuation decay rates, G , for two supplementary scattering angles were made. A total of 383 valid correlograms were recorded at 24 temperatures from 500 mK down to 2 mK. They were recorded in groups of 15 or more at each temperature point and were recorded in the dual mode allowing both the forward and backward correlograms to be recorded simultaneously. An example of the correlograms produced by our flight-adapted, ALV-digital correlator is shown in figure 9. The figure shows both forward and backward scattering correlograms which were computed and recorded simultaneously using 1.7 μ W of laser power at a temperature of “2 mK” (see below) from T_c . Notice the clear presence of forward scattering dynamics in the backscattering correlogram. This is due to window reflections and is accounted for carefully in the fitting analysis. There is also a small amount of backscattering in the forward scattering correlogram which is also treated in the fitting functions. The signal-to-noise is good, even with this low laser power, due to the very strong scattering close to T_c .

Figure 2-10 shows a set of forward scattering correlograms from the second flight covering the total range of temperatures. At temperatures above 100 mK the noise increases as expected due to shot-noise limitations at the 17 μ W power used. The fluctuation lifetimes (inverse of the decay rates) are approximately at the time where the correlogram falls from 2 to 1. Notice the wide range of lifetimes covered in the experiment and shown in this semi-logarithmic plot.

After least-squares fitting, the correlogram sets recorded at each temperature are used to produce an average fluid critical fluctuation decay rate and its statistical error bar. The average decay rates are shown

in figure 2-11 and figure 2-12 for forward and backward scattering angles (11.465° and 169.546° angles, in the fluid) as plots versus temperature-distance from T_c . These are all from the second flight. The ground (1 g) points are from immediate postflight testing at the Kennedy Space Center. The error bars are usually smaller than the plotting symbols here, except for the low-power, backscattering correlograms.

The solid curve is an estimate based on the work of Burstyn, Sengers, Ferrell and Bhattacharjee for a sample of critical density. They showed that the critical part of the fluctuation decay rate for a fluctuation spatial wavevector q was given by

$$\Gamma(q, \xi) = R \frac{kT}{6\pi\nu\xi} \frac{\Omega(x)}{x^3} q^3 (1 + (B_1 x)^2)^{x\eta/2}, \quad (1)$$

with R a dimensionless amplitude taken = 1.00, k Boltzman's constant, T the absolute temperature, ν the viscosity, ξ the correlation range, $x = q\xi$ the reduced wavevector, the Kawasaki function,

$$\Omega(x) = \frac{3}{4} (1 + x^2 + (x^3 - 1/x) \cdot \text{atn}(x)) , \quad (2)$$

with B_1 a dimensionless constant taken as 0.5, and the viscosity exponent x_η anomaly taken as $x_\eta = 0.054$. The viscosity function used is from refitting the data of Strump et al. with the asymptotic-limit form from Burstyn, Sengers, Ferrell and Bhattacharjee²⁻⁴ The curve is shown here before serious fitting is attempted to show that the data appear to be in reasonable agreement with expectations. There are greatly improved xenon viscosity measurements and a corrected and tested exponent x_η available from Berg and Moldover.⁵ These cannot be used until they are refitted with the correct correlation range amplitude and exponent. The same calculated decay rate curve is used in all the figures, figures 2-11 to 2-15.

The postflight ground data are shown for comparison. The very strong effect of density stratification from Earth's gravity gives a limiting value of the decay rate almost 2 times larger on the ground. On the ground we never saw decay rates smaller than 70 rad/sec while the first flight saw rates down to 38 rad/sec and the second, down to 42 rad/sec for the forward angle. This was clearer in the first flight data² where there were more points close to T_c . Here the ground postflight baseline data was taken as if T_c was the preflight value and so ended up with points too far from the critical point. Figure 2-13 shows the data from the first flight for forward scattering fluctuation decay rates.

We now know that the local density was slightly off critical due to local heating by the laser. Thus a better comparison to theory involves determining the correlation range from the measured intensities, since the correlation range is directly related to the "distance" to the thermodynamic critical point. Eventually these will best be determined from some global least-squares fitting. For now we have estimated the correlation ranges by correcting for a 2.5 percent reflection in the forward/backward intensity ratios to arrive at simple Ornstein-Zernike ratios. From these ratios and the known scattering wavevectors, we can estimate the correlation range of the fluctuations at each temperature-density point.

We can use the Cannell determination²⁻⁷ of the correlation range, ξ , for xenon at the critical density,

$$\xi(\rho_c, T) = 1.78 \times 10^{-8} \left(\frac{T - T_c}{T_c} \right)^{-\nu} \text{ (cm)} , \quad (3)$$

refitted with a renormalization group exponent, $\nu=0.63$, to convert the measured correlation ranges to equivalent $(T-T_c)$ at the critical density and replot the decay rates in figures 2-14 and 2-15. The new temperature scale in these figures indicates the possibility that the density errors prevented a close approach to the critical in the second flight. The data plan called for measurements down to 100 μK while staying within 0.1 percent of critical density. This we now see was impossible with the sample used in the two Zeno flights. Though we did not reach the limiting behavior desired in the second flight, the experience gained with the “window density-interferometer” will allow a reanalysis of the first flight data using ξ . Many of the first flight correlograms had lower decay rates and so were closer to the critical point and its limiting decay rate. Thus the data from the two flights should meet the goals of the Zeno experiment.

2.9 LOCATING THE PHASE BOUNDARY NEAR T_c

It is a common experience for critical point experiments that have been carried on the Shuttle to experience a shift in temperature calibration from the launch stresses. Zeno has also seen this. Even though the drift rate of the repeated measurement of T_c over 3 years has shown the drift to be <1 mK/year, the USMP-3 launch caused a -2.2 mK shift in the location of T_c on the instrument temperature scale. Thus we needed to adjust our estimate of the location of T_c during the data collection. Then based on our last estimate we set up the final scanned search for the phase boundary. The forward scattering intensity seen by the photomultiplier PMT-1 is plotted versus temperature in figure 2-16. This data was fitted as two straight lines with the intersection at T_o . This T_o we take as the phase separation temperature at the local density probed. The fit gave a best fit value for T_o with error estimate of ± 10 μK . The backscattering data was fitted in the same way. The two fit parameters for T_o agreed to within ± 20 μK . For comparison, figure 2-17 shows the postflight search conducted in 1 g with all instrument settings the same as flight. Here the forward scattering intensity is plotted versus time rather than temperature, but the conversion is simple: 1 hour is equivalent to -100 μK .

One can see that the maximum intensity reached is 30 times lower on Earth and the peak is broader. The plot in figure 2-17 covers twice the temperature span as that in figure 2-16. The precision found in locating the phase boundary (about 0.6 mK below the T_c) in low gravity is almost a decade better than the best terrestrial measurements. The transition is much sharper in microgravity, probably due to the lack of convection and sedimentation, which smear the transition. We believe this to be the sharpest critical transition ever seen except for the helium lambda transition.

2.10 CONCLUSIONS

The second flight of the Zeno experiment provided a surprise in the discovery of detectable laser local heating even though the laser power was only 17 μW . We took time to characterize the “window interferometer” during the flight. Thus it was possible to use the interferometer to ensure good local density stability until late in the mission when the laser power was changed. We have illustrated how the intensity ratios, corrected for window reflections, can determine the correlation range, ξ , at each correlogram collection point. This method will enable calculation of the limiting decay rates close to the critical point from the combined flight data sets.

This experiment has reached the limits of the particular sample flown. The only way to lower the amount of local heating is to use a cell with all sapphire windows (14 times higher conduction makes the local temperature rise 14 times smaller). We have produced a flight qualified version of such a cell but it was made too late for integration into the Zeno experiment. One could lower the laser power, but only if detectors with much higher quantum efficiency were used: the laser powers used in the Zeno flights were at the shot-noise limits for recording precise correlograms in the time available. Finally, it would be good to know why the window surface absorption was 24 times higher than the expected losses from superpolished surfaces (1 ppm). It seems that the greatest challenge turns out to be not the approach to equilibrium, but rather the tiny temperature nonuniformities in the sample fluid, which make themselves strongly felt only in microgravity.

Finally, we have found the best, detailed confirmation of the adiabatic effects occurring in critical fluids in response to wall temperature changes. The successful modeling of the temperature-step-induced density changes during the second mission was only possible because of the data from the low-gravity measurements in the unique Zeno sample cell.

2.11 REFERENCES

1. Gammon, R.W.; and Shaumeyer, J.N.: "Science Requirements Document for Zeno," NASA, Microgravity Science and Applications Division (MSAD), Washington, D.C., 1988.
2. Gammon, R.W.; Shaumeyer, J.N.; Briggs, M.E.; Boukari, H.; Gent, D.A; and Wilkinson, R.A.: Highlights of the Zeno Results from the USMP-2 Mission," *NASA Technical Memorandum 4737*, NASA, Marshall Space Flight Center, Huntsville, AL, pp. 5-135, 1996.
3. Boukari, H.; Shaumeyer, J.N.; Briggs, M.E.; and Gammon, R.W.: "Critical Speeding Up in Pure Fluids," *Phys. Rev.*, A 41, 2260-2263, 1990; Boukari, H.; Shaumeyer, J.N.; Briggs, M.E.; and Gammon, R.W.: Critical Speeding Up Observed," *Phys. Rev. Letters* 65, 2654-2657, and references therein, 1990.
4. Burstyn, H.C.; Sengers, J.V.; Bhattacharjee, J.K.; and Ferrell, R.A.: "Dynamic Scaling Function for "Critical Fluctuations in Classical Fluids," *Phys. Rev.*, A 28, 1567, 1983.
5. Berg, R.F.; and Moldover, M.R.: "Critical Exponent for the Viscosity of Carbon Dioxide and Xenon," *J. Chem. Phys.*, 93, 1926, 1991.
6. Strumpf, H.J.; Collings, A.F. and Pings, C.J.: *J. Chem. Phys.* 60, 3109, 1974.
7. Cannell, D.S.: Experimental Study of the Liquid Phase of SF₆ Near Its Critical Point," *Phys. Rev.*, A 15, 2053, 1977; Gütter, H.; and Cannell, D.S.: "Correlation Range and Rayleigh Linewidths of Xenon Near the Critical Point," *Phys. Rev.*, A 22, 285, 1980.

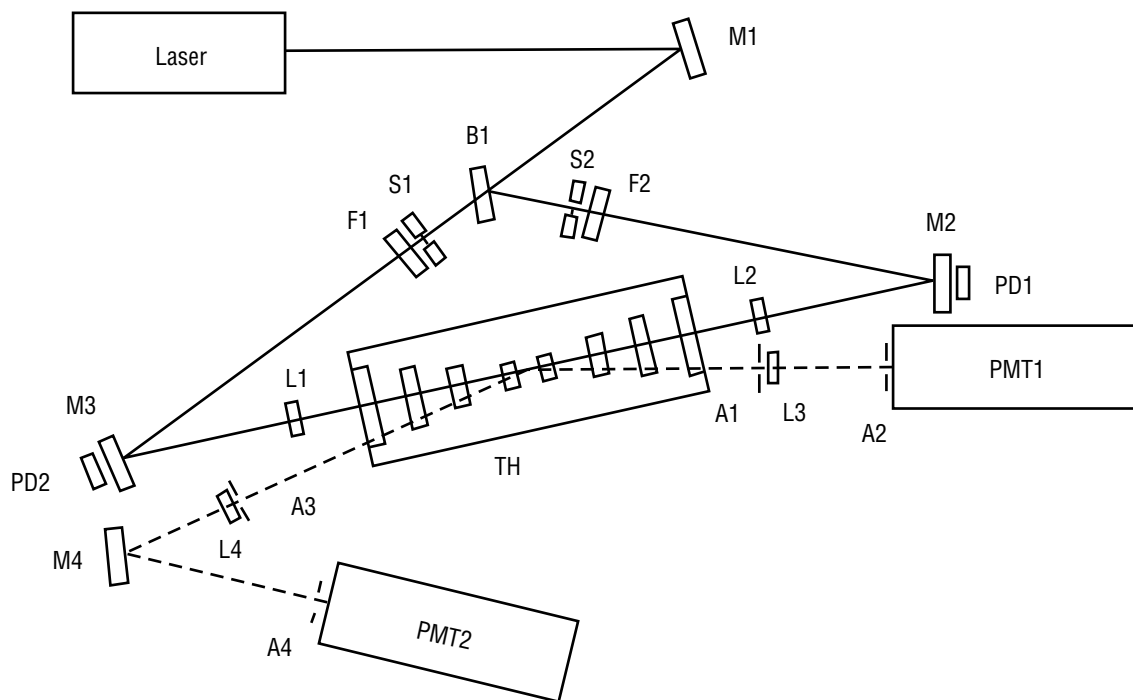


Figure 2-1. Zeno optical layout. Components: He-Ne Laser, Mirrors M 1–4, Beam Splitter B 1, Shutters S 1–2, Filters F 1–2, Photodiodes PD 1–2, Lenses L 1–4, Apertures A 1–4, Photomultipliers PMT 1–2, and Thermostat TH . The sample cell is in the center of the three-shell thermostat. The scattering angles are approximately 12° and 168° for either beam path chosen by shutter.

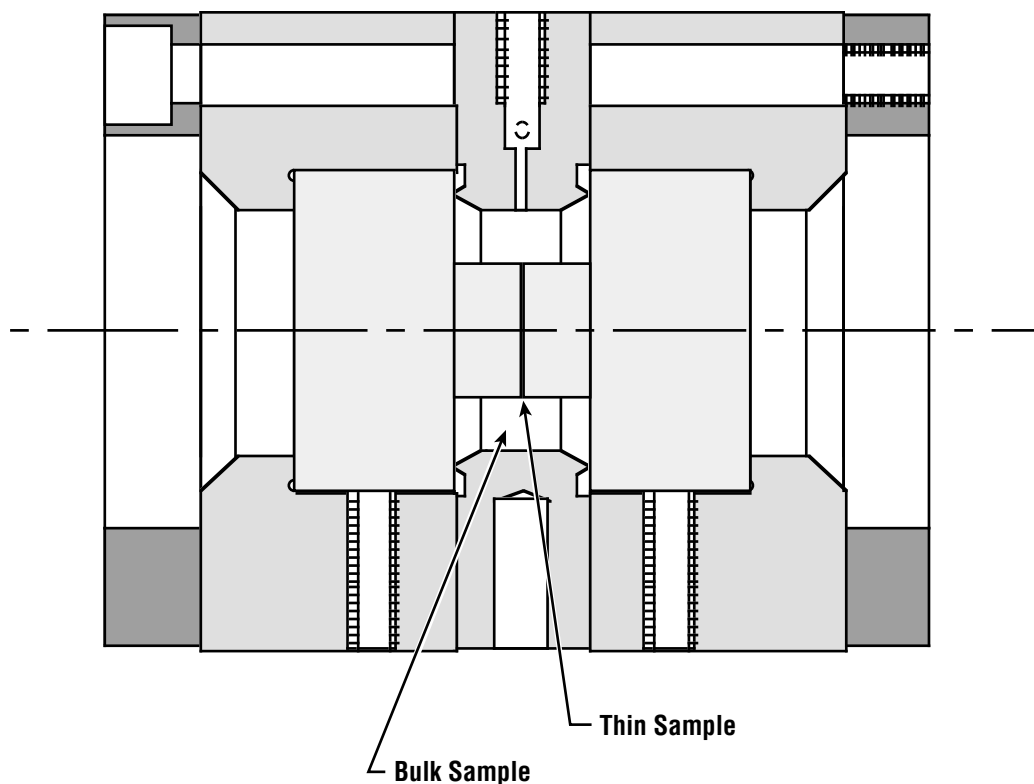


Figure 2-2. Cross section of the Zeno sample cell. Cylindrical sample wall flange is copper and is in mechanical/thermal contact with the copper window holders. The seals are crushed knife edges machined on the wall flange. The filling and sealing valve is built into the cell wall. The spacing of the inner window surfaces is $110 \pm 1 \mu\text{m}$ in the central region. The outside dimensions are 3.8 cm diameter by 4.3 cm long.

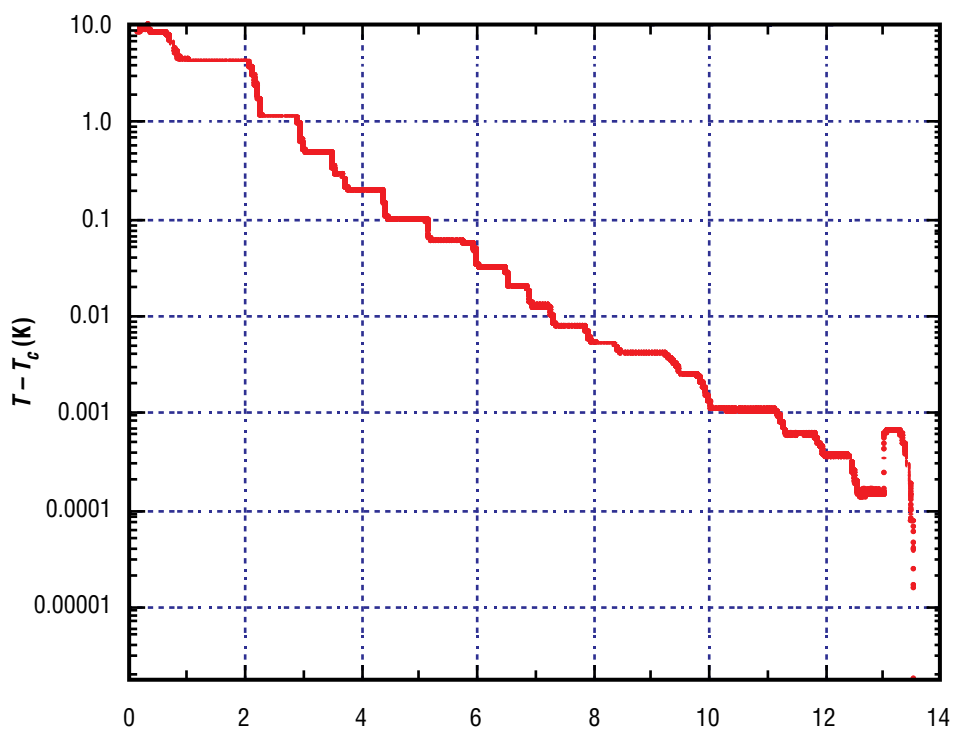


Figure 2-3. The temperature timeline for the second Zeno flight. Notice that the sample did not cross into the two-phase region until the last day of the mission.

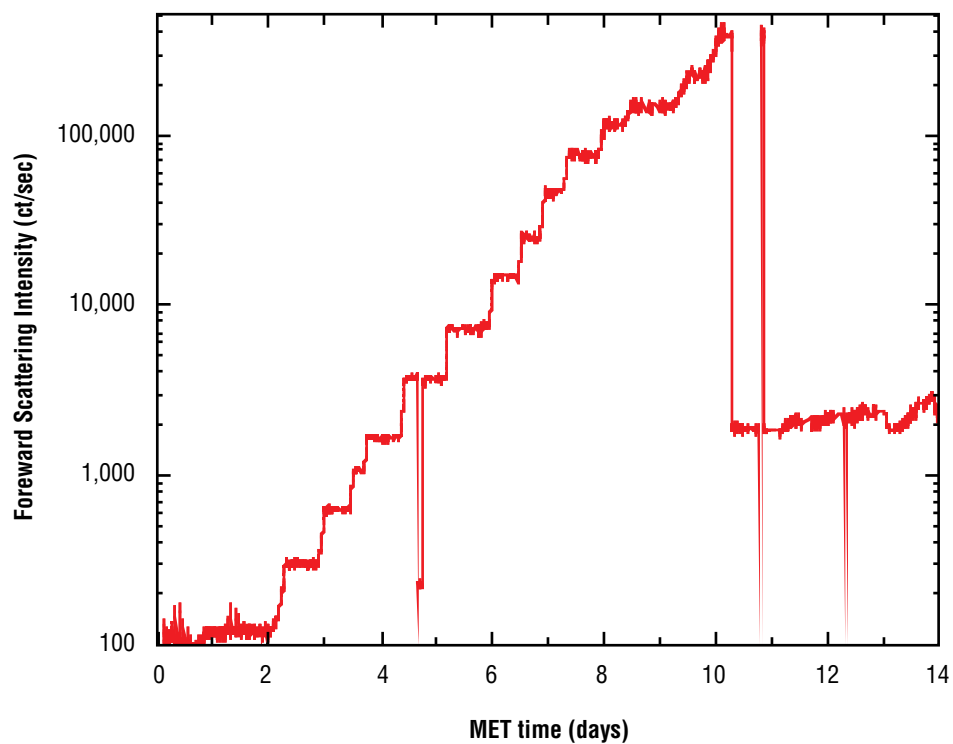


Figure 2-4. Scattering intensity (photon count rate) versus MET. At MET day 10, hour 7:00, the laser path was switched and the power lowered from $17\ \mu\text{W}$ to $1.7\ \mu\text{W}$. The path change means that this detector began looking at backscattered light after this time.

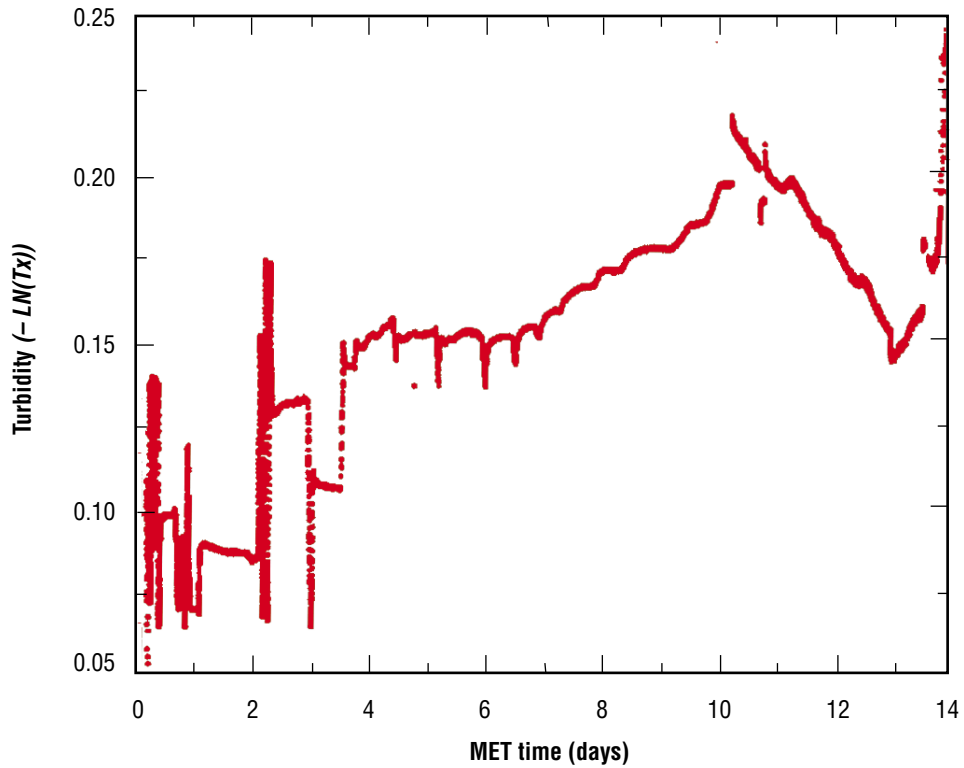


Figure 2-5. Turbidity measurements over the mission. This is actually the turbidity-path-length product calculated from the natural log of the transmission T_x . A change of 0.01 in “turbidity” corresponds to a 1 percent change in T_x . Notice the dramatic response of this signal at the time of the path change/laser power change at MET day 10, hour 7:00 and the indication of phase separation on MET day 15.

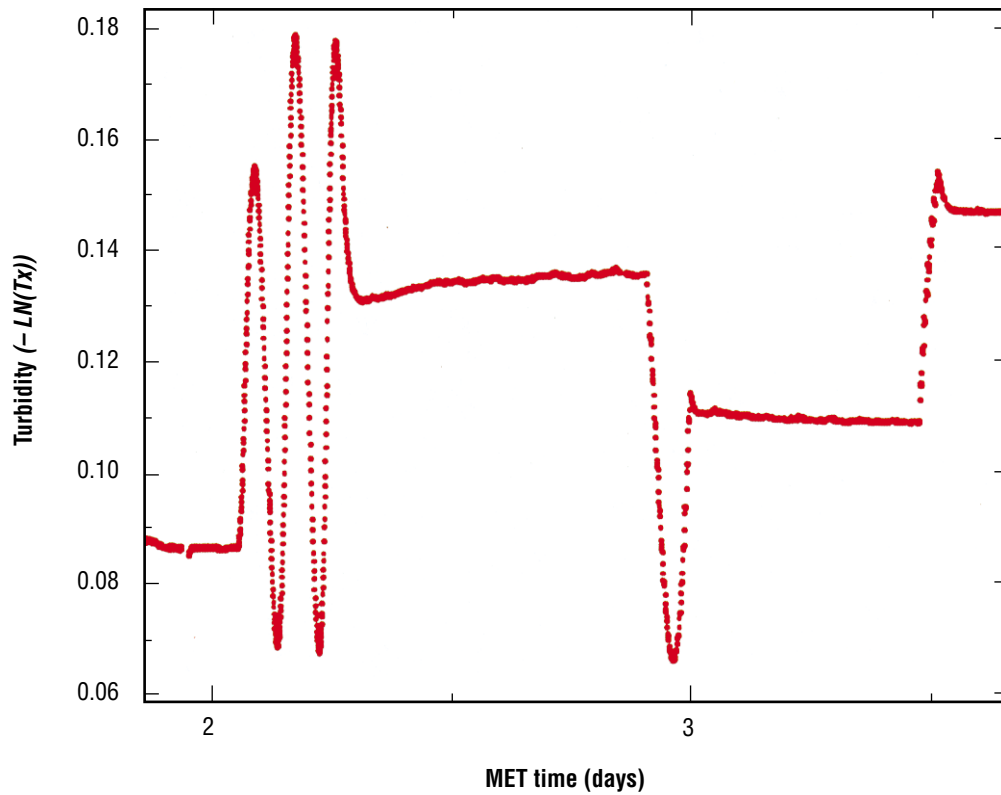


Figure 2-6. Turbidity during large temperature scan, far from T_c , showing the interference fringes from the cell windows. By stopping the temperature scan near positions of maximum fringe slope, high-sensitivity to local density changes could be realized. The horizontal sections are at times when the scanning was stopped to verify the equilibrium of the local density.

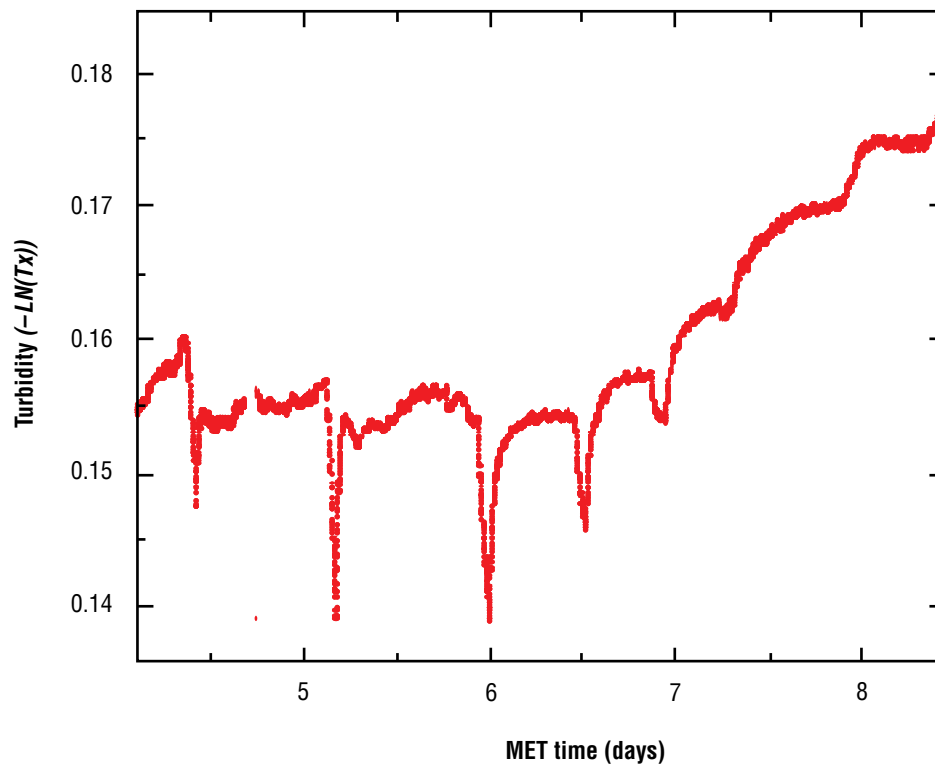


Figure 2-7. Density transients during and following temperature step ramps during the mission. Approximately MET days 4 to 8.

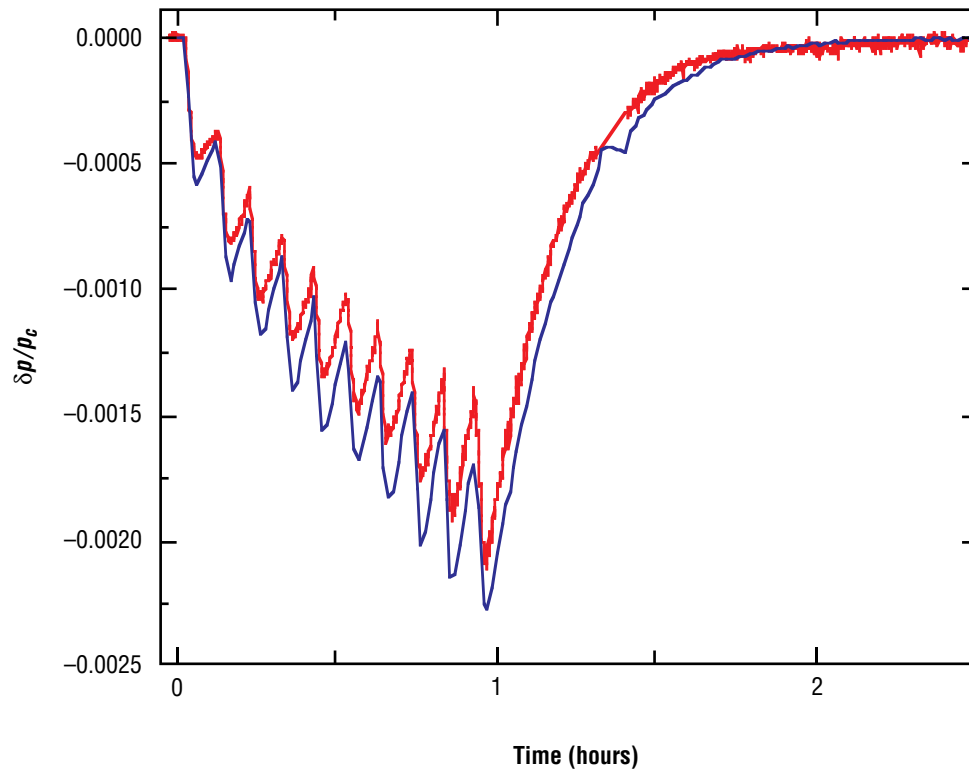


Figure 2-8. Comparison of calculated and measured density perturbations due to a temperature ramp applied to sample cell wall. The ramp was from 500 mK to 300 mK from T_c , occurring at MET day 3, hour 11:22. This event appears in figure 2-6 as the last event and shows a large over shoot. The ramp consisted of 10 steps of 20 mK each over an hour interval. The comparison is absolute, without any scaling. The smooth curve is calculated based on the adiabatic equations for a hypercompressible fluid. The noisy curve gives the measurements.

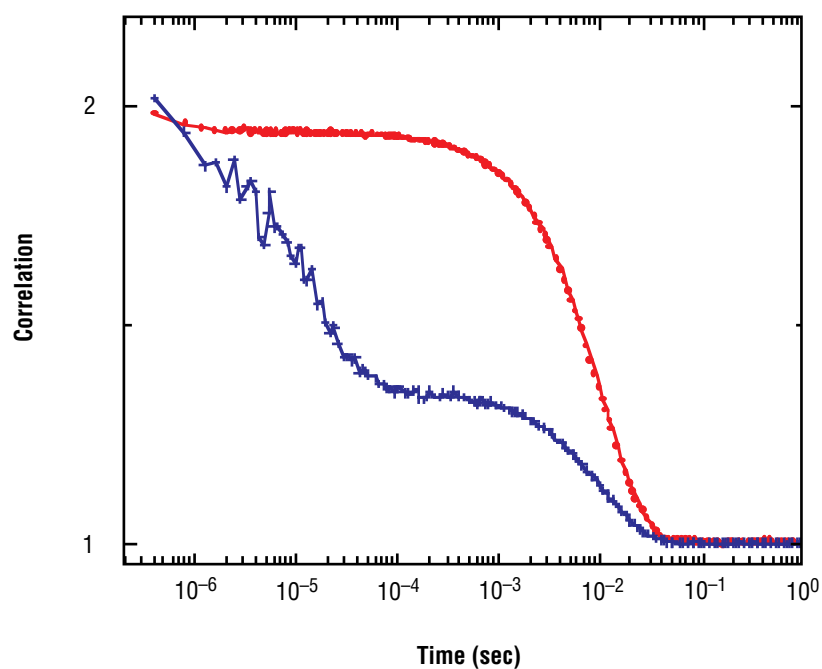


Figure 2-9. Correlogram computed and recorded by the ALV correlator in the Zeno instrument during the second flight. Laser power 1.7 mW. The round data symbols are from forward scattering and the + symbols are from backscattering. Temperature “2 mK” above T_c . The forward scattering has the slower decay rate so it drops down to the background correlation at longer times. The “faster” fluctuations are seen in backscattering. Notice the clear presence of forward scattering dynamics in the backscattering correlogram from the window reflection.

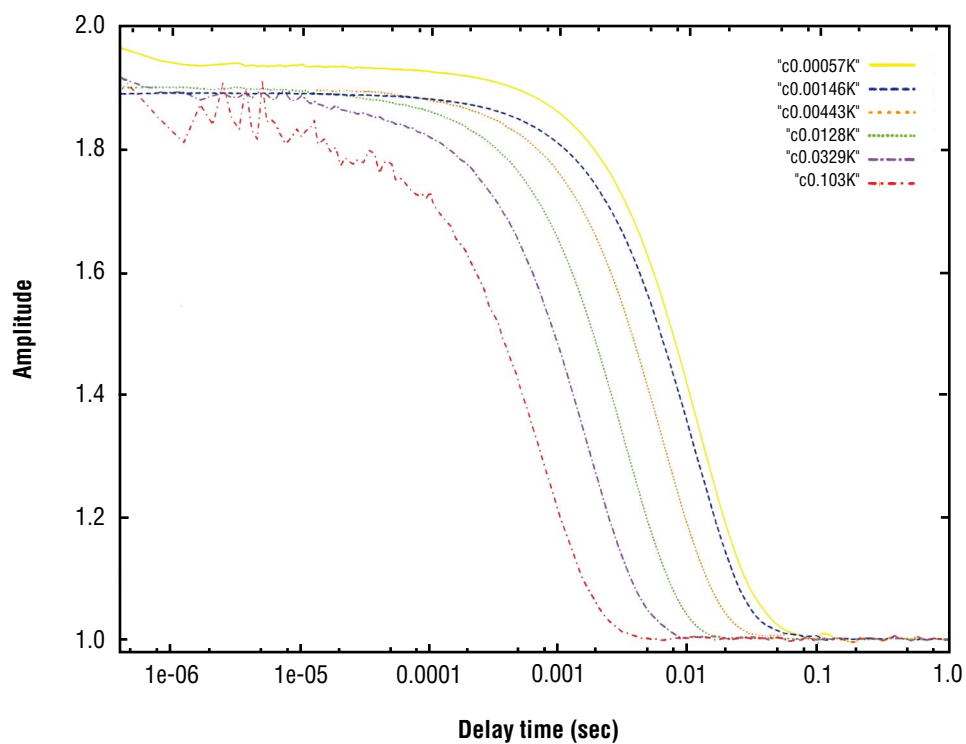


Figure 2-10. Set of forward scattering correlograms recorded at temperatures from 2 mK to 100 mK during the second flight (USMP-3). The legend distinguishes the curves based on approach to T_c . The curves are correctly sorted but the labels are not accurate expressions of the approach to T_c (see discussion).

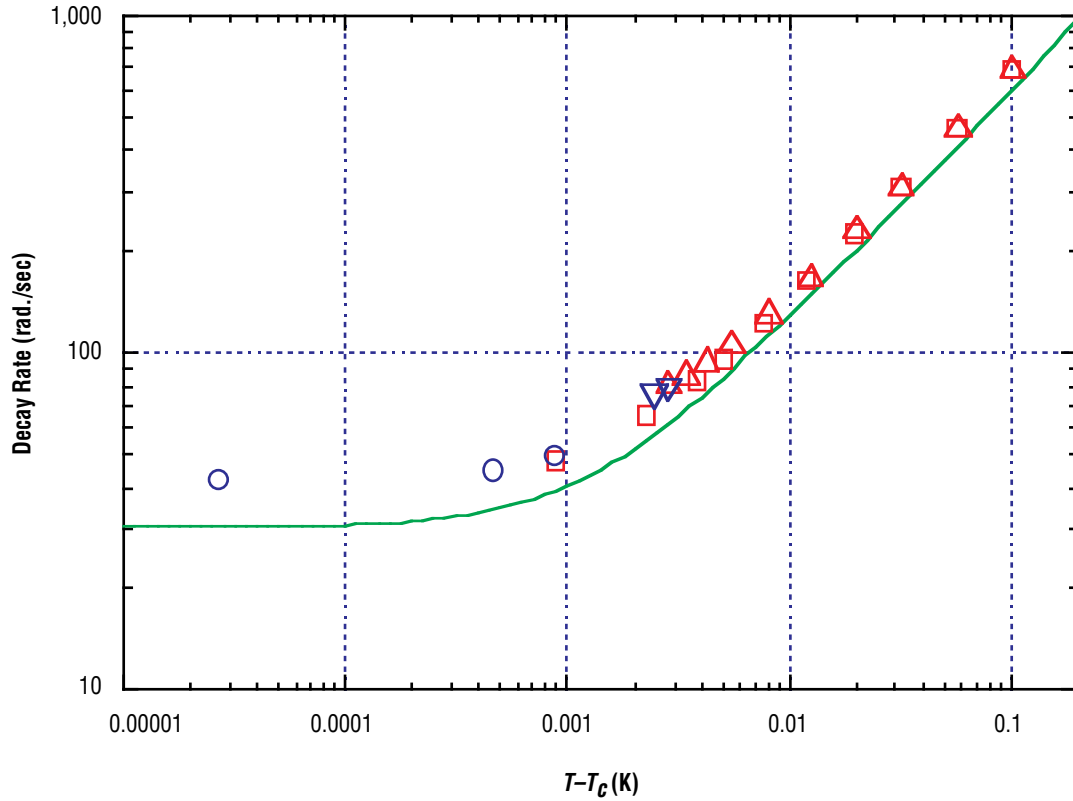


Figure 2-11. Log-log plot of fluctuation decay rates for forward scattering (11.465° angle, in the fluid) versus temperature-distance to T_c . Symbols: squares, 17 μ W scattering, flight 2; circles, 1.7 μ W scattering, flight 2; triangles pointed up, 17 μ W scattering, postflight 2; triangles pointed down, 1.7 μ W scattering, postflight 2. The solid curve is a prediction based on equations of Burstyn, Sengers, Ferrell and Bhattacharjee.

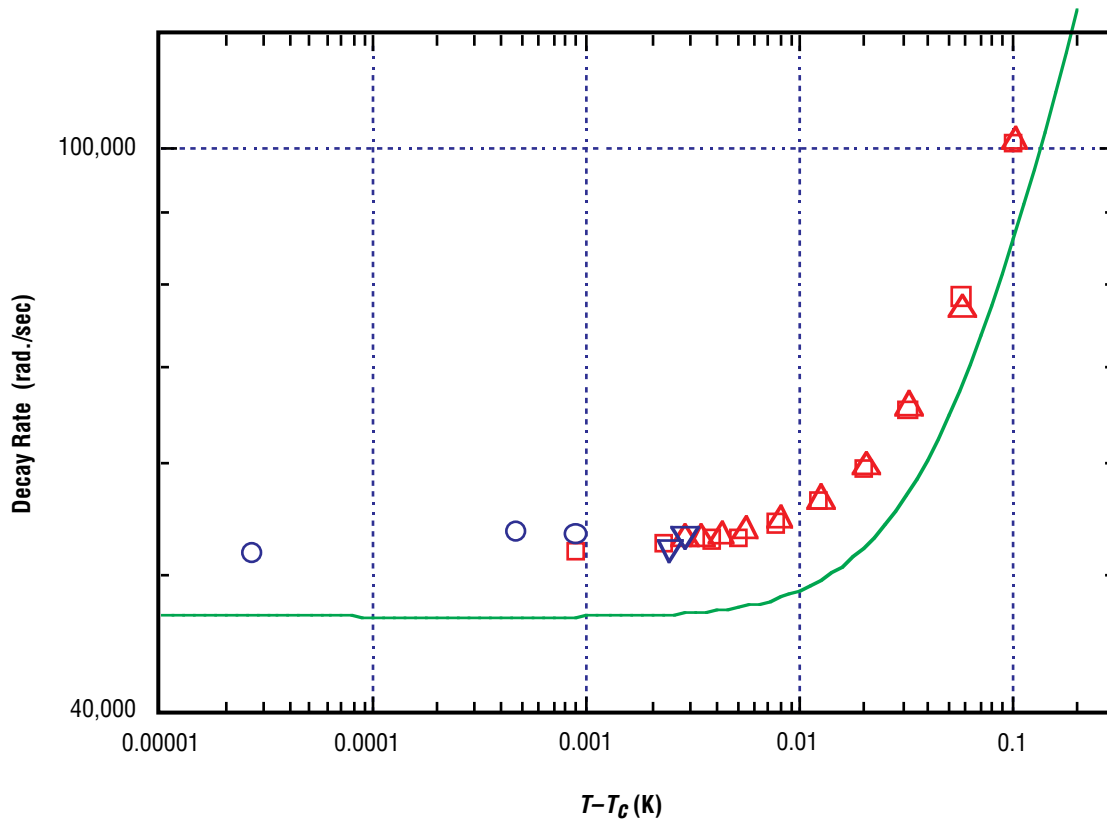


Figure 2-12. Log-log plot of fluctuation decay rates for backscattering (169.546° angle, in the fluid) versus temperature-to T_c . Symbols: squares, 17 μ W scattering, flight 2; circles, 1.7 μ W scattering, flight 2; triangles pointed up, 17 μ W scattering, postflight 2; triangles pointed down, 1.7 μ W scattering, postflight 2. The solid curve is a prediction based on equations of Burstyn, Sengers, Ferrell and Bhattacharjee.

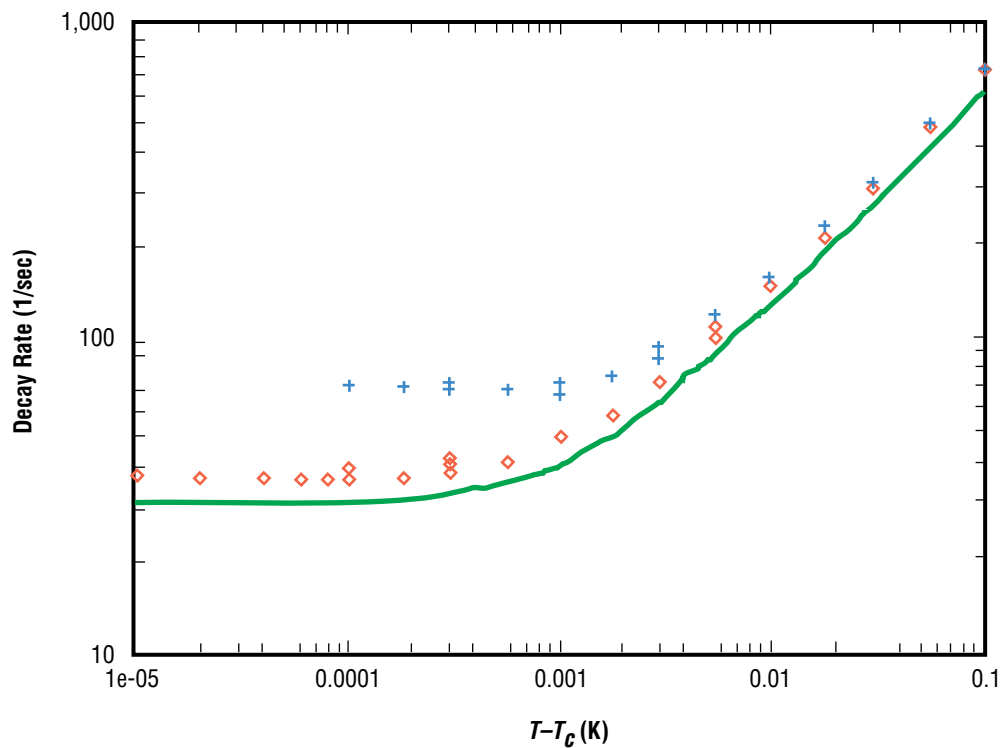


Figure 2-13. Log-log plot of fluctuation decay rates for forward scattering from the first Zeno flight. Symbols: diamonds are the flight data, plusses are the ground data. The solid curve is a prediction based on equations of Burstyn, Sengers, Ferrell and Bhattacharjee. Notice that the flight data show limiting behavior almost 2 times below the ground data.

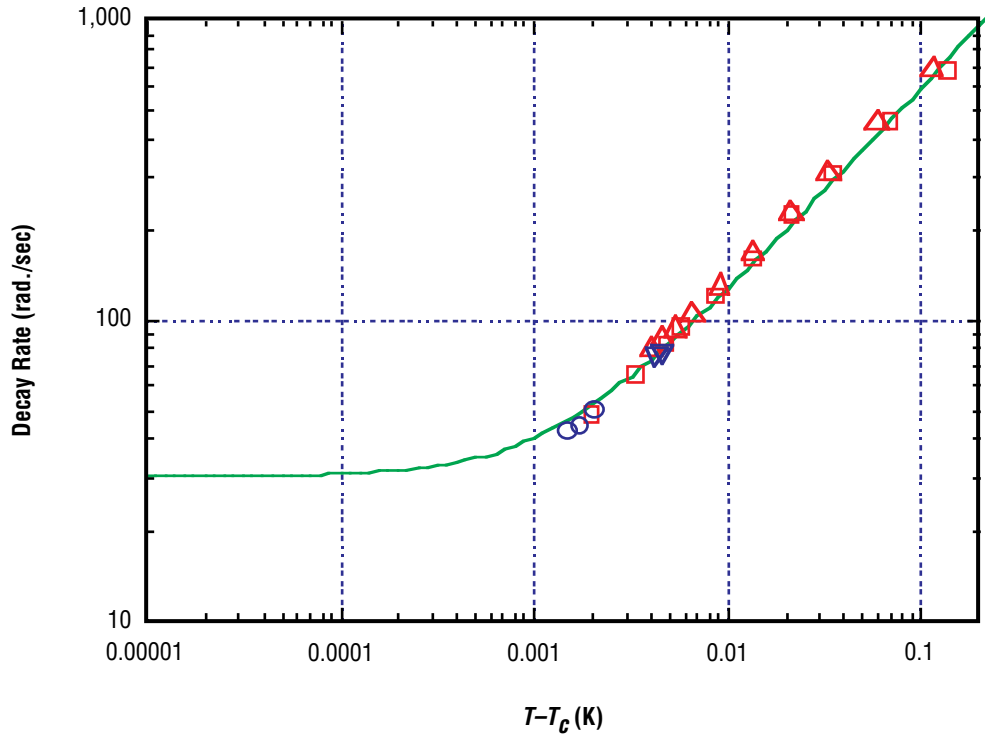


Figure 2-14. Log-log plot of fluctuation decay rates for forward scattering (11.465° angle, in the fluid) versus a correlation-range corrected temperature distance to T_c . Symbols: squares, 17 μ W scattering, flight 2; circles, 1.7 μ W scattering, flight 2; triangles pointed up, 17 μ W scattering, postflight 2; triangles pointed down, 1.7 μ W scattering, postflight 2. The solid curve is a prediction based on equations of Burstyn, Sengers, Ferrell and Bhattacharjee.

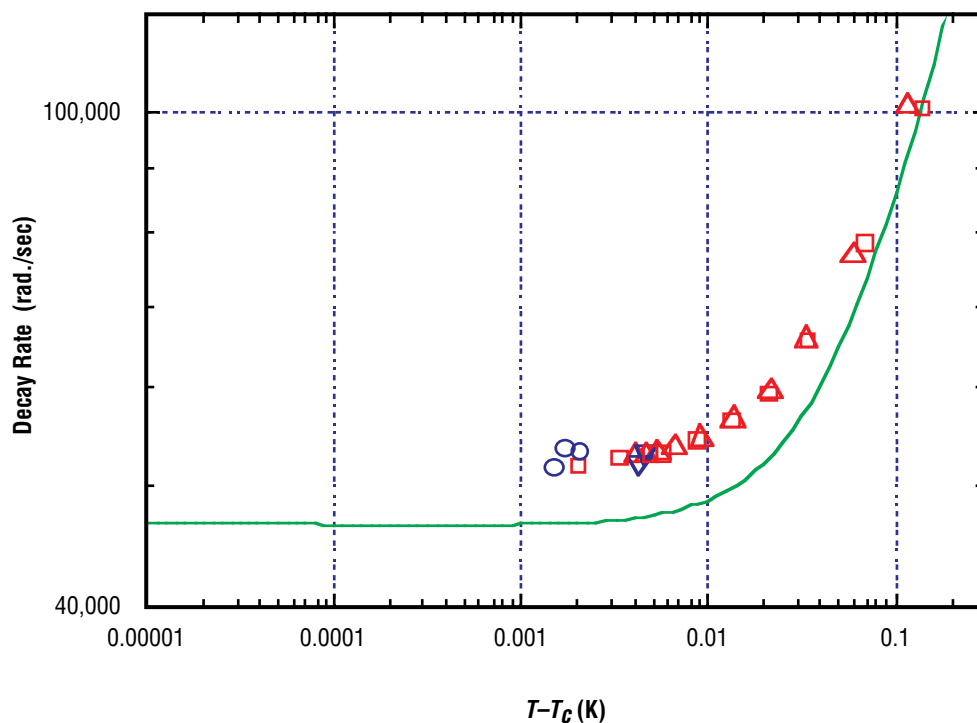


Figure 2-15. Log-log plot of fluctuation decay rates for backscattering (169.546° angle, in the fluid) versus a correlation-range corrected temperature distance to T_c . Symbols: squares, 17 μ W scattering, flight 2; circles, 1.7 μ W scattering, flight 2; triangles pointed up, 17 μ W scattering, postflight 2; triangles pointed down, 1.7 μ W scattering, postflight 2. The solid curve is a prediction based on equations of Burstyn, Sengers, Ferrell and Bhattacharjee.

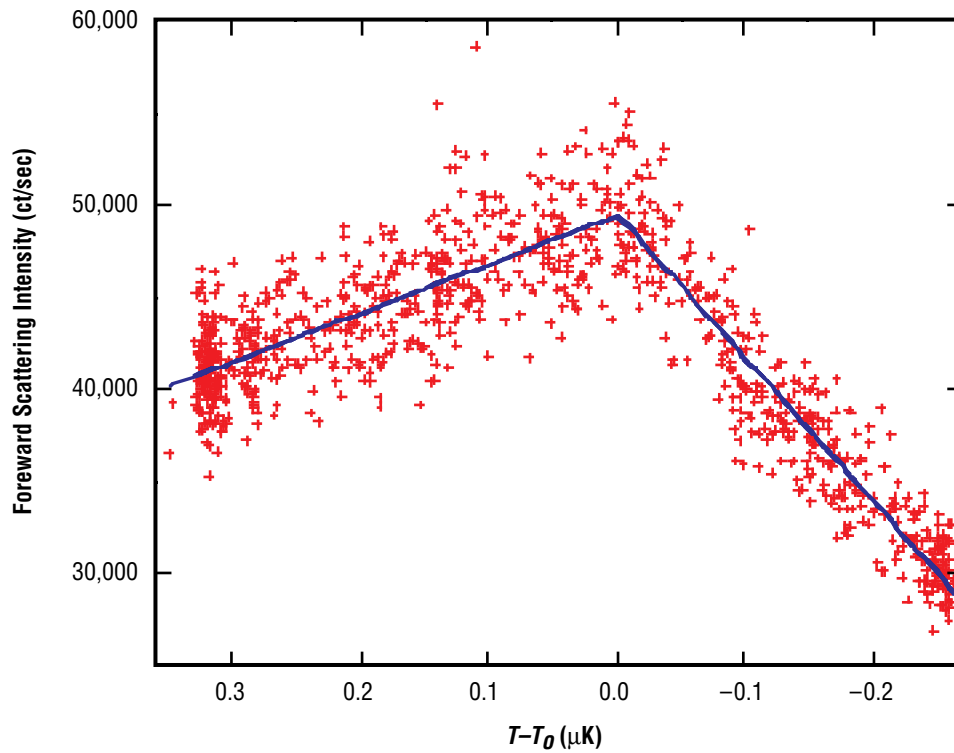


Figure 2-16. Microgravity slow-scan search for the liquid-vapor phase-coexistence phase boundary. Scan rate was $-100 \mu\text{K/hr}$. This was done in the last day of the mission. Data are marked with the + symbol while the straight lines are least-squares fitted to the data with the intersection a fitting parameter, T_0 . The transition observed is much sharper than observed on Earth.

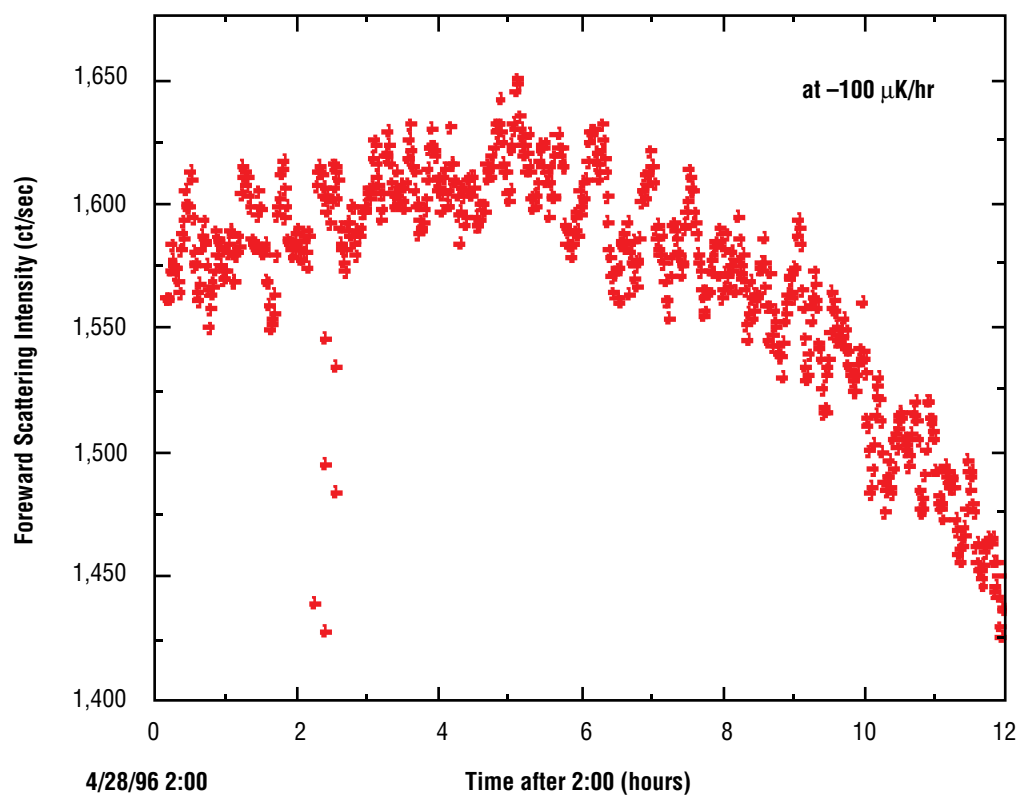


Figure 2-17. Postflight (1 g), slow-scan search for the liquid-vapor phase boundary. Scan rate was $-100\text{ }\mu\text{K/hr}$, as in figure 2-16. Data are marked with a + symbol.

SECTION III.

THE ISOTHERMAL DENDRITIC GROWTH EXPERIMENT

Acknowledgments

For their continuing interest and financial support, we would like to thank the NASA Microgravity Research Division (MRD—Code UG), NASA Headquarters, Washington, D.C., under Contract NAS3–25368, with liaison provided through the NASA Lewis Research Center in Cleveland, Ohio. We would also like to thank the flight crews of STS–62 and STS–75, the payload cadres for USMP–2 and USMP–3, the Rensselaer Operations and Control Center (ROCC) cadre, the IDGE engineering team at or associated with the Microgravity Science Division at the NASA Lewis Research Center, Rensselaer Administrative Secretary T. Geren, graduate students L.A. Tennenhouse and J.C. LaCombe, and Post-doctoral Research Associate A. Lupulescu.

THE ISOTHERMAL DENDRITIC GROWTH EXPERIMENT

M.E. Glicksman

Materials Science & Engineering Department
Rensselaer Polytechnic Institute
Troy, NY 12180–3590, U.S.
Phone: 518–276–6721
E-mail: glickm@rpi.edu

M.B. Koss

Materials Science & Engineering Department
Rensselaer Polytechnic Institute
Troy, NY 12180–3590, U.S.
Phone: 518–276–2844
E-mail: kossm@rpi.edu

D.C. Malarik

Microgravity Science Division
NASA Lewis Research Center
Cleveland, OH 44135, U.S.
Phone: 216–433–3203
E-mail: diane.malarik@lerc.nasa.gov

3.1 INTRODUCTION

The growth of dendrites is one of the commonly observed forms of solidification encountered when metals and alloys freeze under low thermal gradients, as occurs in most casting and welding processes. In engineering alloys, the details of the dendritic morphology directly relates to important material responses and properties. Of more generic interest, dendritic growth is also an archetypal problem in morphogenesis, where a complex pattern evolves from simple starting conditions. Thus, the physical understanding and mathematical description of how dendritic patterns emerge during the growth process are of interest to both scientists and engineers.¹

The Isothermal Dendritic Growth Experiment (IDGE) is a basic science experiment designed to measure, for a fundamental test of theory, the kinetics and morphology of dendritic growth without complications induced by gravity-driven convection. The IDGE, a collaboration between Rensselaer Polytechnic Institute (Troy, New York) and NASA's Lewis Research Center (Cleveland, Ohio), was developed over a 10-year period from a ground-based research program into a space flight experiment.^{2,3} Important to the success of this flight experiment was provision of in situ near real-time teleoperations during the space flight experiment.⁴

3.2 BACKGROUND ON DENDRITIC GROWTH THEORY AND EXPERIMENT

A number of theories of dendritic crystal growth, based on various transport mechanisms, physical assumptions, and mathematical approximations, have been developed over the last 50 years. These theories attempt to predict a dendrite's tip velocity, V , and radius of curvature, R , as a function of the supercooling, ΔT (see the review by one of the authors).¹ The growth of dendrites in pure melts is known to be controlled by the transport of latent heat from the moving crystal-melt interface as it advances into its supercooled melt. Ivantsov, in 1947, provided the first mathematical solution to the dendritic heat conduction problem⁵ and modeled the steady-state dendrite as a paraboloidal body of revolution, growing at a constant velocity, V . The resultant thermal conduction field can be expressed exactly in paraboloidal coordinates moving with the dendritic tip. The temperature field solution is known as the Ivantsov, or "diffusion-limited" transport solution. This solution is, however, incomplete, insofar as it only specifies the dendritic tip growth Péclet number, $Pe=VR/2\alpha$, (here Pe is the growth Péclet number, and α is the thermal diffusivity of the molten phase) as a function of the initial supercooling, and not the unique dynamic operating state, V and R . The Péclet number obtained from the Ivantsov solution for each supercooling yields instead an infinite range of V and R values that satisfy the diffusion-limited solution at that particular value of ΔT .

In the early 70's, succinonitrile (SCN), a body centered cubic (BCC) organic plastic crystal, was developed as a model metal analog system for studying dendritic growth.⁶ SCN solidifies like the cubic metals (i.e., with an atomically "rough" solid-liquid interface) yet retains advantages because SCN displays convenient properties for solidification experiments, such as a low melting temperature, optical transparency, and accurate characterization of its thermophysical properties. The use of SCN greatly facilitated dendritic growth studies over the past 20 years, where, because of its use, dendritic tip velocities could be accurately measured and used as a critical test of theory.^{6,7}

Theoretical efforts have concentrated on trying to discover an additional equation or length scale, which, when combined with the Ivantsov conduction solution, "selects" the observed operating states (see references within reference 1). Although the underlying physical mechanisms for these "theories of the second length scale" are quite different, their results are invariably expressed through a scaling constant, $\sigma^*=2\alpha d_0/(VR^2)$, where d_0 is the capillary length scale, a materials parameter defined from the equilibrium temperature of the crystal-melt interface, the solid-liquid interface energy, and the specific and latent heats. Although some theories predict the value of this scaling constant, in practice the scaling constant is used as an adjustable parameter to describe dendritic growth data in various materials.

Subsequent experiments with SCN showed that gravity-induced convection dominates dendritic growth in the lower supercooling range typical of metal alloy castings.⁸ Convection unfortunately confounds any straightforward analysis of dendritic solidification based on conductive heat transfer. There have been a few attempts to estimate the effect of natural or forced convection on dendritic growth,⁹ but these calculations are themselves based on yet unproven elements of dendritic growth theory, and consequently cannot provide an independent test of the theory. In the higher supercooling range, where thermal convective influences diminish in comparison to thermal conduction, the morphological scale of dendrites becomes too small to be resolved optically at the high growth speeds encountered. The experimental situation prior to the

microgravity experiment reported here, was that there appeared to be too narrow a range of supercoolings in any crystal-melt system studied terrestrially that remains both free of convection effects, and also permits an accurate determination of the dendrite tip radius of curvature.

3.3 THE ISOTHERMAL DENDRITIC GROWTH EXPERIMENT

The IDGE, a NASA-sponsored series of Space Shuttle microgravity experiments, was designed to grow and photograph dendrites in the absence of convective heat transfer for a fundamental test of dendritic growth theories. The data and subsequent analysis on the dendritic tip growth speed and size from the first flight of the IDGE on the Second United States Microgravity Payload (USMP-2/STS-62) mission in March of 1994, has demonstrated that although the theory can make predictions which are in reasonable agreement with the results of the experiment, there are several important areas of disagreement.¹⁰⁻¹³

3.4 REVIEW OF RESULTS FROM THE IDGE ON USMP-2

We measured the dendritic growth velocities and tip radii of curvature of succinonitrile in microgravity using the IDGE instrument flown on the USMP-2 platform in the payload bay of the Space Shuttle Columbia (STS-62). The on-orbit microgravity data, when compared to terrestrial dendritic growth data, demonstrate that:

1. Convective effects under terrestrial conditions remain significant even up to values as high as $\Delta T = 1.7$ K supercooling;
2. In the supercooling range from 0.47 K to 1.7 K, the data remain virtually free of convective or non-Ivantsov conditions, and may be used reliably for examining diffusion-limited, infinite boundary dendritic growth theories;
3. A diffusion solution to the dendrite problem, combined with a unique (measured) scaling constant, σ^* , does not yield individual growth velocity and radius predictions consistent with the observed dendritic growth velocities and radii as a function of supercooling;
4. The failure of this conventional formulation is currently attributed to small departures from the Ivantsov thermal diffusion solution, which is formulated for paraboloidal dendrites. Ivantsov's theory describes the overall dependence of Péclet number on supercooling, but predicts a value higher (5 to 15 percent) than the data we observed in microgravity in the diffusion-limited regime;
5. The scaling parameter σ^* does not appear to be a constant over a range of supercoolings; and finally,
6. The average σ^* measurements from the terrestrial and microgravity data are in good agreement, despite a difference of over six orders-of-magnitude in the quasi-static acceleration environment of low-Earth orbit and terrestrial conditions.¹⁰⁻¹³

Before the IDGE, it was not possible to test separately the Ivantsov transport solution and the interface scaling hypothesis. To our knowledge, the IDGE provides the first solid evidence that Ivantsov's formulation for paraboloidal dendritic growth does not accurately describe dendritic growth in SCN. The approximate

agreement achieved between the transport theory and the microgravity data indicates that dendritic growth is indeed most likely governed by the conduction of latent heat from the crystal-melt interface, but the detailed Ivantsov formulation to describe that conduction process is in need of some modification.

One of the key assumptions in the Ivantsov model that we are actively investigating is whether a dendrite can be modeled as a parabolic body of revolution. Early observations of dendrite morphologies lead researchers to approximate the tip shape with a paraboloid. The notion that dendrites are actually not paraboloids of revolution was first demonstrated by the data of Huang and Glicksman,⁷ and more recently by other researchers^{14–18} including LaCombe et al.¹⁹ By assuming the form of a fourth-order polynomial, rather than a second-order parabola, it is possible to characterize more realistically the shape of dendrite tips. Such a fourth-order equation describing a dendritic profile is $Y=X^2/2+Q(f)X^4$, where X and Y are dimensionless coordinates, normalized with the radius of curvature at the tip of the dendrite. $Q(f)$ will vary with the azimuthal direction, and is generally assumed to be proportional to $\cos(4f)$.^{14–18} However, the recent work of LaCombe et al.,^{19,20} has shown that the $\cos(4f)$ form does not adequately describe the axial asymmetry. This is seen most readily in figure 10 of reference 19 and figure 4 of reference 20 where the $\cos(4f)$ functional form is superimposed upon the experimentally observed data describing the actual shape. Furthermore, for terrestrial data, this shape is seen to be independent of supercooling (i.e., the three-dimensional shape scales with the size of the dendrite).

At the lower supercoolings ($\Delta T < 0.4$ K), variations in the growth speed beyond that due to measurement uncertainties, and a significant deviation of the heat transfer from that predicted from diffusive transport theory with boundary conditions at infinity. Recently, two models, both based on Cantor and Vogel's confocal parabola modification to Ivantsov,²¹ described in the *Journal of Crystal Growth*, have suggested mechanisms for the heat transfer of a dendrite growing into a supercooled melt. One model, by Sekerka et al.,²² describes how convection resulting from the residual microaccelerations present on orbit could enhance the heat transfer. Another, by Pines et al.,²³ describes the observed speed enhancement as a thermal boundary layer effect arising from the proximity of the growth chamber wall.

Both models, by the adjustment of one parameter, describe the trends in the IDGE microgravity data, and the Stagnant Film Model of Sekerka et al., also describes the terrestrial data. However, when examined in precise detail^{24,25} we have shown that neither model is correct. The chief reason being that both models rely on, and are thereby “handcuffed” by the Ivantsov solution, which we have already shown is incorrect. In addition, since both models are, in part, based on the same formulation, we could not discriminate between the two of them based on the IDGE data from USMP–2 alone.

Thus, in the higher supercooling range investigated, both the heat transfer and the crystal growth physics components of current dendritic growth theories are in need of modification. In the lower supercooling range, the data are inconsistent with several models of dendritic growth that attempt to modify the basic diffusion-limited theory with the boundaries at infinity to include convection or container effects.

3.5 THE IDGE ON USMP–3

The scientific objectives of the second flight of the IDGE were to: 1) Characterize the three-dimensional shape of a dendrite tip; 2) accumulate a dense data set on dendritic velocities and radii in the diffusion-limited infinite boundary regime; and, 3) to form dendritic velocity data sets to clarify current issues in the

literature about whether convection or near-field boundary conditions affect the dendritic growth measurements in microgravity in the lower supercooling range.

The second flight of the IDGE took place on USMP-3 in February and March of 1996. The growth chamber filled with succinonitrile and the temperature control system were identical to those used for USMP-2. In addition to the high-resolution film data collected after the Shuttle landed, growth velocities were measured in near real time by downlinked binary Charge Coupled Device (CCD) images. Because only a limited supply of film could be carried on the Shuttle, many growths were measured from CCD images alone. These steady-state velocity measurements were accurate to 2 percent.

3.6 RESULTS FROM THE IDGE ON USMP-3 AT LANDING PLUS ONE YEAR

The microgravity environment on the Space Shuttle varied throughout the mission. Shuttle maneuvers, changes in attitude, motions of equipment or astronauts, all changed the amplitudes and directions of the microacceleration vectors. The Tethered Satellite System deployed on the same mission as USMP-3 also had profound effects on the microgravity environment. While the tether was reeled out and the massive (1 tonne) satellite moved away from the Shuttle, the mass centroid gradually moved in the direction of the satellite. This caused the acceleration at the IDGE location to rise by a factor of about 80 in approximately 20 hours. When the tether broke in an unfortunate accident, the microgravity suddenly returned to its initial low level.

Quasi-static microgravity levels were measured by the Orbital Acceleration Research Experiment (OARE) throughout the USMP-3 mission (see reference 26 and other submissions to this report volume). These measurements were corrected for the gravity gradient from IDGE to the Shuttle's center of gravity. Although each measurement is accurate to about 5 percent, any time average of the microgravity level reveals significant variations in the quasi-static accelerations.

The telemetry data obtained during flight (fig. 3-1), indicates that we accumulated sufficient data to meet our objectives. Currently, we are conducting data reduction and analysis to further our analysis in the diffusion-limited infinite boundary regime, and to characterize and compare the three-dimensional shape of a dendrite tip at both terrestrial and microgravity conditions. However, we have already acquired enough data, and performed analysis, to make conclusions about whether convection or near-field boundary conditions affect the dendritic growth measurements in microgravity in the lower supercooling range.

Dendrite tip velocity measurements at low supercoolings showed more run-to-run variation and proved to be much larger than diffusion-controlled models would predict. We sought to correlate the variation in growth velocities with the microgravity level. Data sets taken at supercoolings of 0.18 K, 0.26 K, and 0.36 K all show these effects. At the time of this report, our most complete analysis is for data obtained at a supercooling of 0.26 K.

The variation in growth velocity among the various repeated experiments is much larger than the measurement uncertainty, ± 2 percent, of an individual run. Each growth cycle included in the data set had a tip growing with constant angle (relative to the growth chamber) and velocity for at least 15 min. We anticipated that both the magnitude of the microgravity level and the growth angle with respect to the quasi-static microgravity vector would affect the results. Figure 3-2 shows observed dendritic velocities

plotted in a space representing the growth axis angle and the magnitude of the quasi-static microgravity vector. Reading along any horizontal or vertical set of data, we could not detect any clear trend. However, the fluctuations occurring in microgravity level during each 15-min period could obscure any correlations among growth cycles. Adding uncertainty measurements to the plot (fig. 3-3) makes it apparent that these data are inconclusive.

A more detailed examination of each growth cycle should reveal any correlations occurring on a shorter time scale. Specifically, we plotted the instantaneous dendrite tip positions relative to the regressed tip position calculated from the average steady-state velocity. A typical example is shown in figure 3-4. Again, we could not detect a correlation of the growth speed with the magnitude or direction of the quasi-static microgravity level for any of the 30 cycles for which data are available. Even for the cycle during which the tether broke (fig. 3-5), and a large change occurred in the microgravity level, the dendrite that was growing still appeared to grow at the same constant velocity. Aside from a possible brief transient, the growth rate is neither faster nor slower than that observed before the break.

The variation in steady-state dendritic growth velocity does not appear to correlate with the measured changes in the quasi-static microgravity environment. This result suggests that changes in the microgravity level (10^{-7} to $10^{-5} g_0$) do not significantly affect dendritic growth rates in SCN in the supercooling range above 0.18 K in the IDGE growth chamber.

3.7 CONCLUSIONS ABOUT REMOTE TELESCIENCE FROM THE IDGE ON USMP-3

In the investigation of dendritic growth phenomena, the IDGE team members were the experimenters, manipulating parameters and conditions in near real time, making measurements, and analyzing data, and changing the subsequent experimental parameters. However, with respect to the operations of the flight hardware from a terrestrial laboratory, the IDGE was part of a larger experiment in remote teleoperations, paving the way to the microgravity science operations on the future *International Space Station (ISS)*. NASA Headquarters and the Telescience Support Center (TSC) at LeRC, with the goal of developing the experience and expertise to set up remote, non-NASA locations from which to control *ISS* experiments, used our recent IDGE Space Shuttle experiment as a proof-of-concept of remote operations. During the flight of IDGE on STS-75 in February and March of 1996, team members monitored this experiment from a remote laboratory set up at Rensselaer rather than at the Payload Operations and Control Center (POCC) at the Marshall Space Flight Center, in Huntsville, Alabama, where all such operations usually originate. During the last 4 days of the mission, we expanded the team at Rensselaer and uplinked commands to the experiment. During the entire 14-day mission, graduate and undergraduate students, whom we had trained, were present at the Rensselaer facility.

Some details of this test of remote telescience have been published elsewhere.²⁷ Our brief experience at operating a microgravity space flight experiment from a remote non-NASA location successfully identified some of the scientific advantages and many of the issues and challenges of remote teleoperations. Naturally, not all the potential issues of remote teleoperations could be identified based on one experiment's experience on one Shuttle flight. For example, several issues of facility security and room access need to be better examined. Furthermore, only one experiment, the IDGE, and one instrument, the Space Acceleration Measurement System (SAMS), were operating from remote sites. How several similar experiments would operate simultaneously from different remote sites has not been examined or tested.

We have avoided any discussion of solutions and improvements to what was done at Rensselaer during USMP-3/STS-75, although in many cases solutions and improvements are self-evident. However, in some cases solutions and improvements are not the province of a single project but that of a larger more encompassing organization. Nevertheless, the experience we gained operating the IDGE on USMP-3/STS-75 from Rensselaer, and our discussions with some of the experimenters who operated remote sites during USML-2, allows us to make some general suggestions on how to proceed to more robust remote teleoperation facilities.

First is merely to recognize the different modes of operations between how Space Shuttle microgravity experiments are conducted, and how a future Space Station microgravity experiment will most likely be conducted. For Shuttle experiments, the limited time from launch to landing dictates many of the operational elements. One must be fully prepared well before launch, and there is little or no time to change plans or recover from mistakes. This requires that both the principal investigator/development teams and the POCC cadre be fully on line for the duration of the mission. In addition, the short duration of Space Shuttle flights makes traveling and operating from the POCC eminently reasonable and practical.

The entire constraint for Space Station experiments changes because time is not the limiting variable. One does not need to operate around the clock for every minute the experiment is on orbit. In fact, for the Space Station this would be precluded by other constraints. Thus, time becomes a resource to be used liberally to think, replan, and, if necessary, set up supplemental ground-based tests, and only then take the appropriate action. Under those circumstances, traveling to the POCC is not the best use of the experimental team's time or resources with respect to the best way to operate a microgravity experiment. Thus, for Space Shuttle experiments, the POCC is the best place to be, and remote sites only need be developed and implemented in support of testing for longer duration *International Space Station* experiments where we expect most PI's would better operate from their home facilities.

In consideration of the previous observation, it is counterproductive to tax the experiment teams, the POCC, and the TSC to set up complete remote teleoperations facilities with the near 100 percent guaranteed reliability demanded for a Space Shuttle experiment. Rather, the larger decision-making bodies need to determine what are the crucial elements of the future Space Station experiment operations and what elements of the current Space Shuttle experiments are similar to them. Then, various experiment teams like IDGE can operate limited remote teleoperation sites with the express purpose of conducting their science while simultaneously testing specific elements of remote teleoperations for the further development of Space Station remote facilities.

The remote teleoperation activities during USMP-3 performed as we had hoped, and based on this experience we understand the advantages and benefits versus the costs and challenges of such endeavors for the overall enhancement of the scientific return from on orbit. Remotely operating the IDGE aboard USMP-3 greatly enhanced our in-flight analytical capabilities, and served as a technical "shakedown" of hardware and procedures that are destined to become commonplace in future microgravity research. In the course of this we learned that it is important to have reliability in the data and command path. Until the technology is thoroughly tested and fine-tuned, it is advisable that appropriate backup data sources are maintained during the flight. Our approach to this was handled by maintaining the ability for these functions to be performed at the POCC if needed. The absence of some of the telemetry was restricting, but the additional space, equipment and manpower available at the university site were significant assets.

The experience gained in operating a microgravity experiment during USMP-3 is proving to be invaluable for planning future IDGE activities as well as other Space Shuttle and Space Station experiments. Once technical and reliability issues are resolved, university-based experiment operation benefits such as operational efficiency, cost savings, public exposure, and educational opportunities, will further improve the yield from microgravity research.

The microgravity community is poised to prepare for the coming Space Station era by learning from the experiences of remote teleoperations like those performed on USMP-3, and before that on USML-2. In this way, the development of each new teleoperation facility can build toward the *ISS* having learned from the evolution of such facilities from the recent past. In this way the promise of remote teleoperations as verified by this proof-of-concept can be brought to fruition. To prepare for the *ISS* era, we plan to do additional tests of remote telescience during the IDGE's third flight on USMP-4/STS-87.

3.8 PLANS FOR THE IDGE ON USMP-4

The third flight, scheduled for launch in October 1997, will repeat the experimental protocols of the first two flights, but with a different sample material. This second test material, pivalic acid (PVA), is similar to SCN, but with a 10-times-higher surface energy anisotropy.^{28 29} The surface energy and the surface energy anisotropy are important parameters in the crystal growth physics of dendritic growth^{1 29} and may be related to the three-dimensional anisotropy observed in the dendritic tip shape. In addition, we want to develop the data and analytical tools to characterize the non steady-state dynamic parameters, which lead to side branching and, we believe, will be another key in explaining the differences between the IDGE data and predictions from current steady-state dendritic growth models.

REFERENCES

1. Glicksman, M.E.; and Marsh, S.P.: "The Dendrite," in *Handbook of Crystal Growth*, Hurle, D.J.T. , ed., Elsevier Science Publishers B.V., Amsterdam, Vol. 1B, p. 1077, 1993.
2. Glicksman, M.E.; et al. :*Met. Trans. A*, Vol. 19A, p. 1945, 1988.
3. Glicksman, M.E.; Koss, M.B.; and Winsa, E.A.: *JOM*, Vol. 47(8), p. 49, 1995.
4. Glicksman, M.E.; Koss, M.B.; Bushnell, L.T.; LaCombe, J.C.; and Winsa, E.A.: *6th International Symposium on Experimental Methods for Microgravity Science*, R.J. Schiffman, ed., The TMS, p. 51, 1995.
5. Ivantsov, Dokl. Akad. Nauk SSSR, Vol. 58, p. 56, 1947.
6. Glicksman, M.E.; Schaefer, R.J.; and Ayers, J.D.: *Met. Trans. A*, Vol. 7A, p. 1747, 1976.
7. Huang, S.C.; and Glicksman, M.E.: *Acta Metall.*, Vol. 29, p. 701, 1981.
8. Glicksman, M.E.; and Huang, S.C.: Convective Transport and Instability Phenomena, Zierep and Ortel, eds., Karlsruhe, p. 557, 1982.
9. Ananth, R.; and Gill, W.N.: *J. Crystal Growth*, Vol. 91, p. 587, 1988, and Vol. 108, p. 173, 1991.
10. Glicksman, M.E.; Koss, M.B.; and Winsa, E.A.: *Phys. Rev. Lett.*, Vol. 73, p. 573, 1994.
11. Glicksman, M.E.; Koss, M.B.; Bushnell, L.T.; LaCombe, J.C.; and Winsa, E.A.: *ISIJ International*, Vol. 35, p. 604, 1995.
12. Glicksman, M.E.; Koss, M.B.; Bushnell, L.T.; and LaCombe, J.C.: Modeling of Casting, Welding, and Advanced Solidification Processes VII, Cross, M. and Campbell, J., eds., The Minerals, Metals, and Materials Society, Warrendale, Pennsylvania, 1995.
13. Koss, M.B.; Bushnell, L.T.; LaCombe, J.C.; and Glicksman, M.E.: *Chem. Eng. Comm.*, Vol. 152–153, p. 351, 1996.
14. Maurer, J.; Perrin, B.; and Tabeling, P.: *Europhys. Lett.*, Vol. 14, p. 575, 1991.
15. Kessler, D.; and Levine, H.: *Phys. Rev. A*, Vol. 36, p. 4123, 1987.
16. Kessler, D.; and Levine, H.: *Acta Metall.*, Vol. 36, p. 2693, 1988.

17. Amar, M. Ben; and Brener, E.: *Phys. Rev. Lett.*, Vol. 71, p. 589, 1993.
18. Brener, E.: *Phys. Rev. Lett.*, Vol. 71, p. 3653, 1993.
19. LaCombe, J.C.; Koss, M.B.; Fradkov, V.E.; and Glicksman, M.E.: *Phys. Rev. E*, Vol. 52, p. 2778, 1995.
20. LaCombe, J.C.; Koss, M.B.; Glicksman, M.E.; Bushnell, L.T.; and Hamly, K.D.: "Thermodynamics and Kinetics of Phase Transformations," *Mat. Res. Soc. Symp. Proc.* 398, Im, J.S.; Park, B.; Greer, A.L.; and Stephenson, G.B., eds., Materials Research Society, Pittsburgh, Pennsylvania, 1996.
21. Cantor, B.; and Vogel, A.: *J. Crystal Growth*, Vol. 41, p. 109, 1977.
22. Sekerka, R.F.; Coriell, S.N.; McFadden, G.B.: *J. Crystal Growth*, Vol. 154, p. 370, 1995.
23. Pines, V.; Chait, A.; and Zlatkowski, M.: *J. Crystal Growth*, in press, 1996.
24. Glicksman, M.E.; Koss, M.B.; Bushnell, L.T.; LaCombe, J.C.; and Winsa, E.A.: Reprint No. AIAA 96-0251, 1996.
25. Bushnell, L.T.; Koss, M.B.; LaCombe, J.C.; and Glicksman, M.E.: *J. Crystal Growth*, in press, 1997.
26. Rogers, M.J.B.; and Delombard, R.: Summary Report of Mission Acceleration Measurements for STS-75, 1996.
27. Koss, M.B.; LaCombe, J.C.; Glicksman, M.E.; Bushnell, L.T.; Malarik, D.C.; and Winsa, E.A.: 8th International Symposium on Experimental Methods for Microgravity Science, Schiffman, R.J. ed., The TMS, in press, 1996.
28. Singh, N.B.; and Glicksman, M.E.: *J. Crystal Growth*, Vol. 98, p. 573, 1989.
29. Muschol, M.; Liu, D.; and Cummins, H.Z.: *Phys. Rev. A*, Vol. 46(2), p. 1038, 1992.

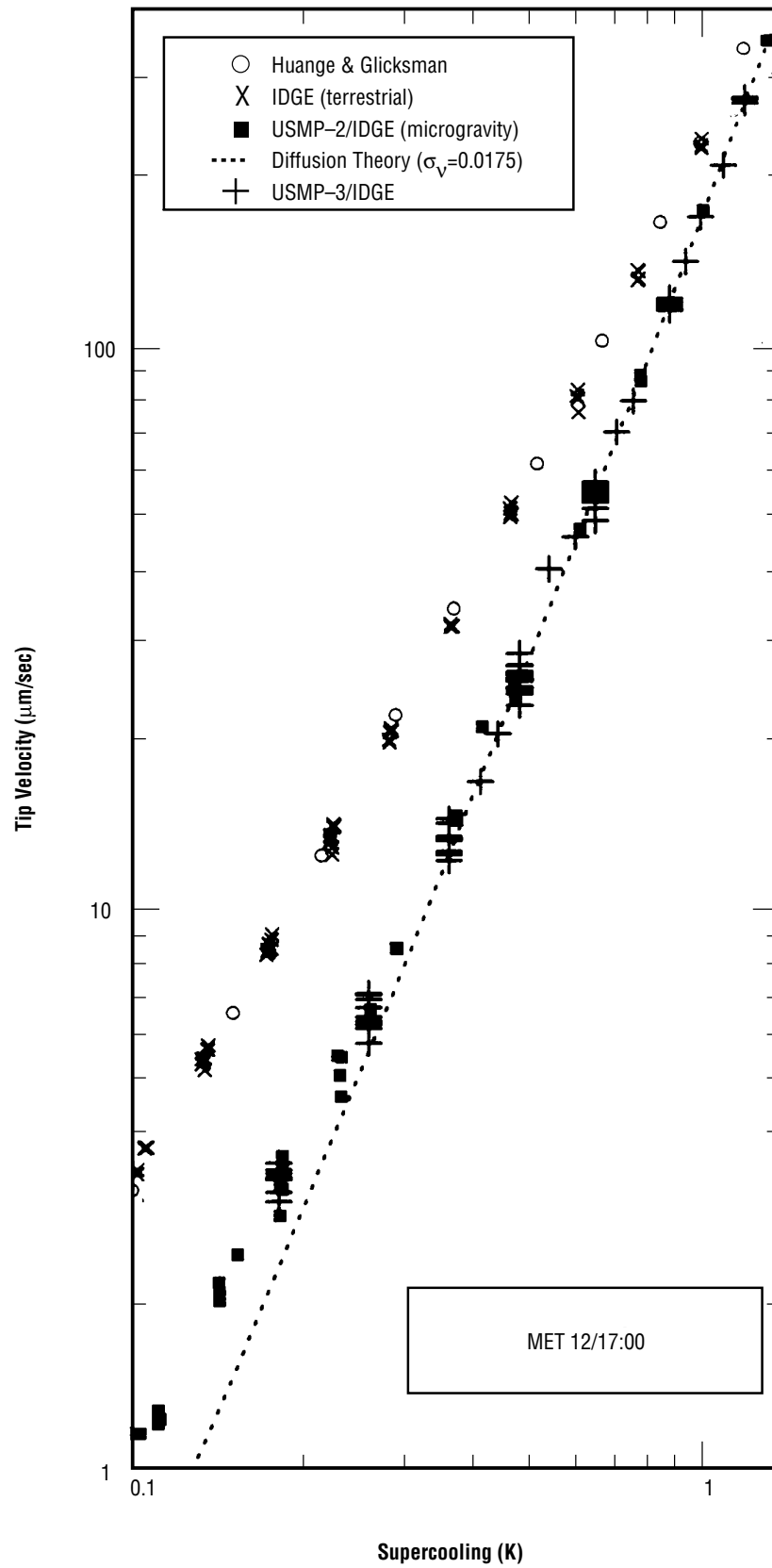


Figure 3-1. In situ dendritic growth velocity measurements from IDGE on USMP-3 during STS-75.

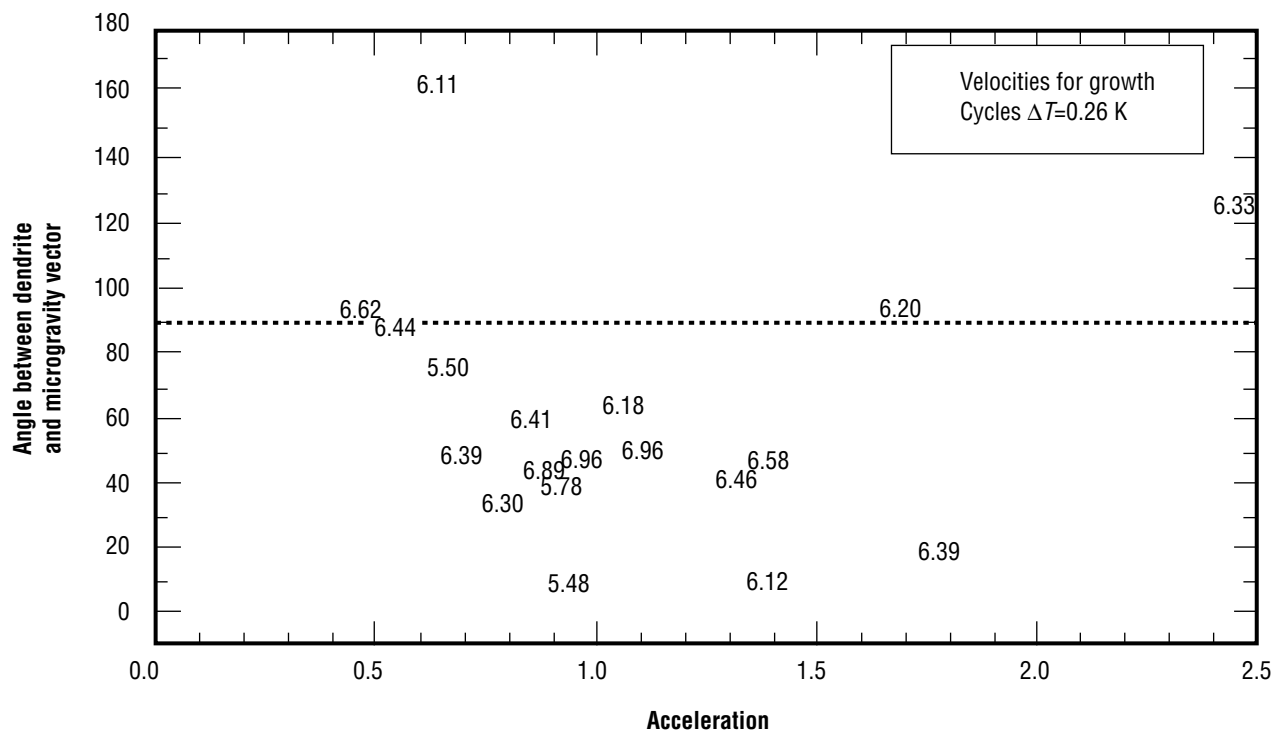


Figure 3-2. There is no clear correlation between steady-state dendrite velocity and the microgravity vector.

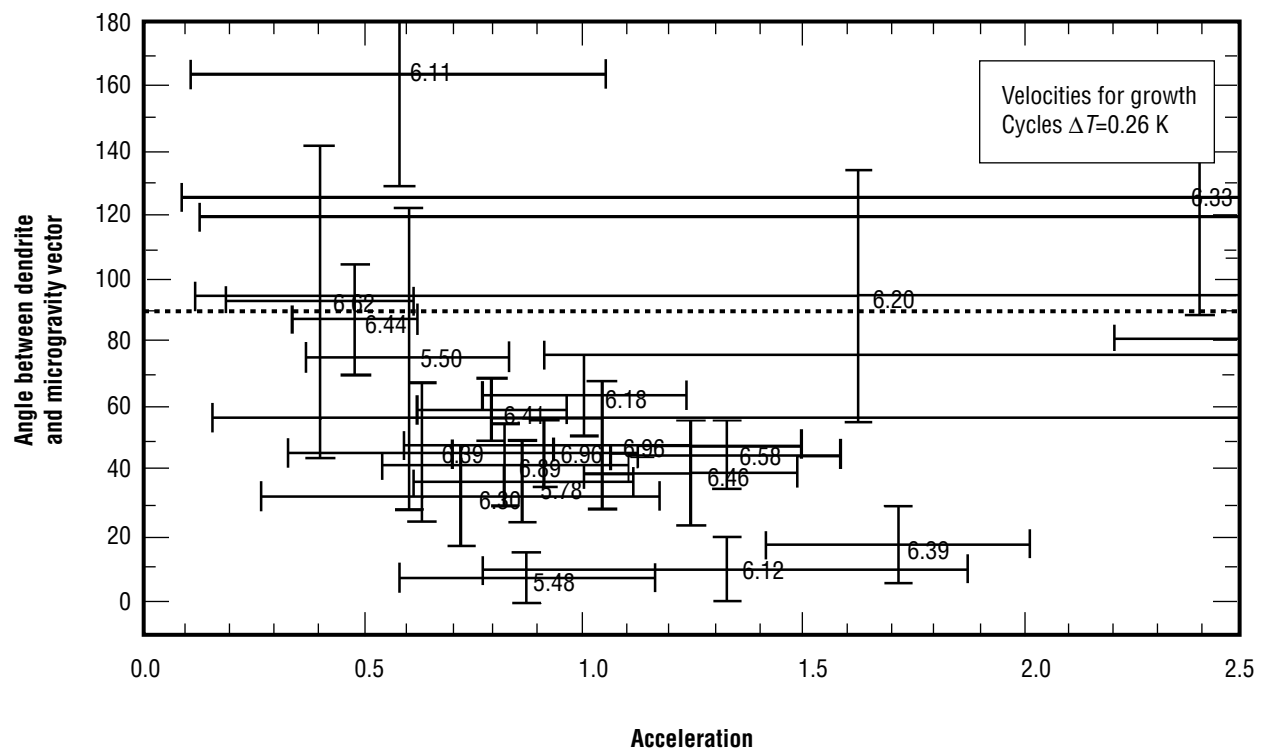


Figure 3-3. Variation in the quasi-static microgravity vector obscures any possible correlation with dendrite velocity.

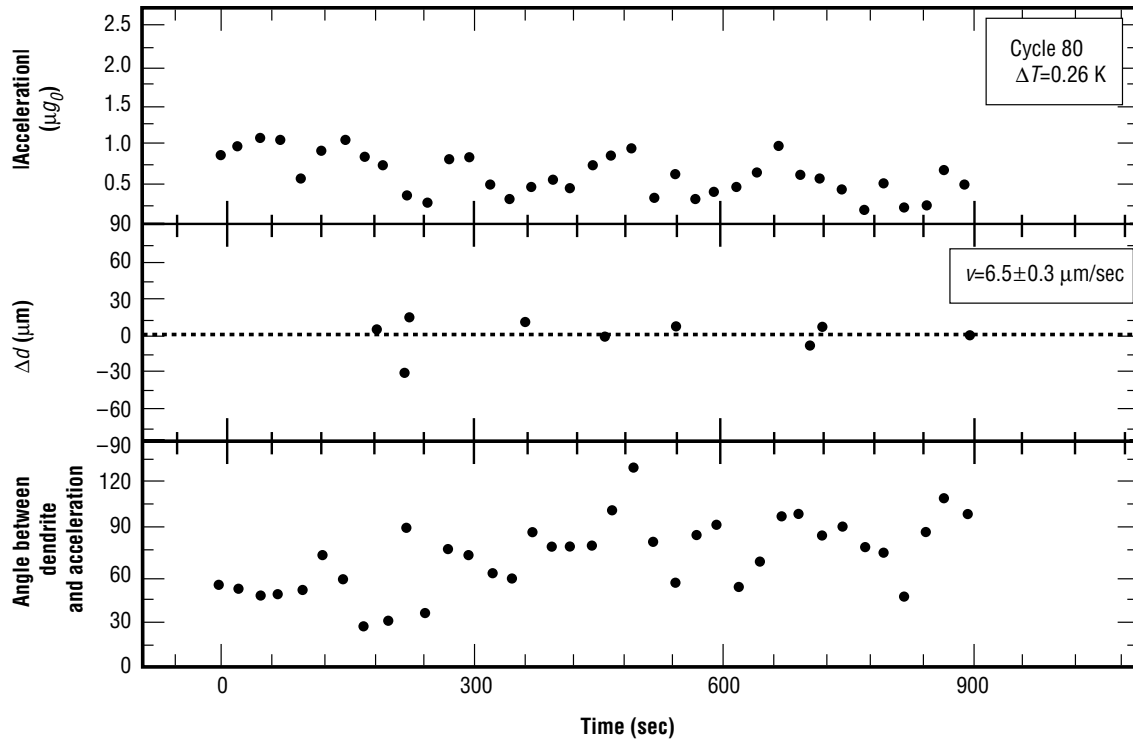


Figure 3-4. Noise in the dendritic growth does not appear to correlate with noise in the microgravity vector.

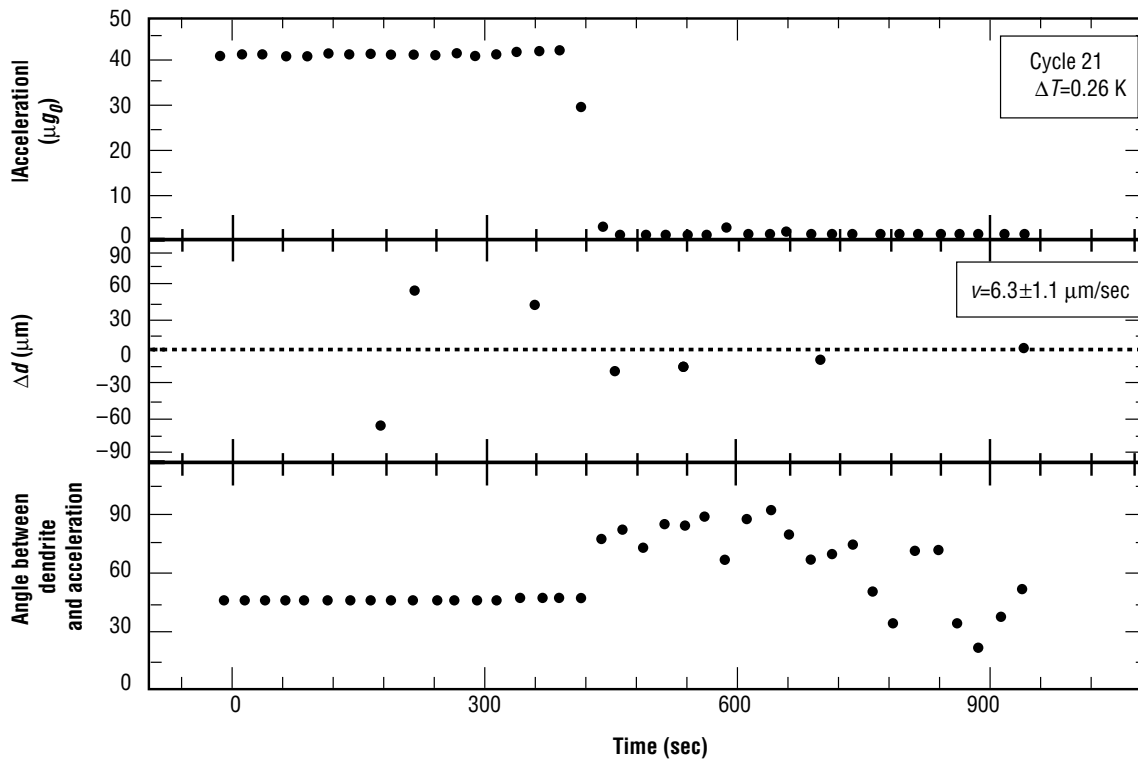


Figure 3-5. An abrupt change in the microgravity vector does not seem to affect the dendrite.

SECTION IV.

THE EFFECT OF MICROGRAVITY DIRECTION ON THE GROWTH OF PbSnTe

Acknowledgments

Many thanks to the people who made this exciting work possible. To acknowledge everyone who contributed to the years of effort that went into this work would exceed the page limit of this paper. The investigators are truly humbled by the effort, dedication, sacrifice, and brilliance offered by so many program, project, and support staff that make these esoteric space projects possible. They are the people who do all of the work while we get the glory. Thank you.

A precious few must be mentioned by name which in no way detracts from all the rest. We offer special thanks to Bob Rhome who guided the program and encouraged us to stay with it during internal reorganizations; Mike Wargo who shepherded the science and kept us on our toes; Roger Crouch, the sparkplug so vital to us in the earlier days; Fred Reeves, Jim Sledd, and Linda Jeter who kept nuts, bolts, and schedules together; Kent Pendergrass and Wayne Gandy who helped us learn what the furnace could do; Sandor (Alex) Lehoczky, Don Gillies, Peter Curreri, and Sherwood Anderson who guided us to flight; Bob Berry, Dick Simchick, Ned Baker, Glenn Woodell, and Jim Wells who have done so much for us at Langley; and Peter Engel at KSC for his expertise with the CAT unit. To one and all of them I say a very sincere and heartfelt, “Thank you.”

THE EFFECT OF MICROGRAVITY DIRECTION ON THE GROWTH OF PbSnTe

A.L. Fripp, and W.J. Debnam

NASA Langley Research Center
Hampton, VA 23681
Phone: 757-864-1503
Fax: 757-864-7891
E-mail: a.l.fripp@larc.nasa.gov

W.R. Rosch

National Research Council
NASA Langley Research Center
Hampton, VA 23681-0001
Phone: 757-864-1534
Fax: 757-864-7891
E-mail: w.r.rosch@larc.nasa.gov

R. Narayanan

Department of Chemical Engineering
University of Florida
Gainesville, FL 32611
Phone: 352-392-9103
Fax: 352-392-9513
E-mail: ranga@pine.circa.ufl.edu

4.1 INTRODUCTION

The Space Shuttle Columbia was launched as STS-75 at 2018 GMT (Greenwich Mean Time) on February 22, 1996. One of the two major experiment packages was the Third United States Microgravity Payload (USMP-3), and one of the principal instruments on the USMP was the Advanced Automated Directional Solidification Furnace (AADSf). The AADSf is a multizone directional solidification furnace, and at the time of the USMP-3 flight was capable of processing only one sample per Shuttle mission which, for that flight, was a lead tin telluride (PbSnTe) crystal growth experiment. Archibald L. Fripp of the NASA Langley Research Center was the principal investigator.

In the 1 year since the flight experiment, the sample has been retrieved from the spacecraft and analysis has begun. After presenting introductory material on why PbSnTe was chosen as a test material, why microgravity processing was expected to produce desired results, and what we expected to find in conducting these tests, this report will discuss the results to date which are far from complete.

4.1.1 Lead Tin Telluride

Lead tin telluride is an alloy of PbTe and SnTe. The technological importance of PbSnTe lies in its bandgap versus composition diagram which has a zero energy crossing at approximately 40 percent SnTe. This facilitates the construction of long-wavelength ($>6\ \mu\text{m}$) infrared detectors and lasers. The properties and utilization of PbSnTe are the subject of other papers.^{1,2}

PbSnTe is amenable to study because it is easily compounded, it has a relatively low vapor pressure, and it is miscible with the same crystal structure for all compositions. There is also existing, though limited, literature on its growth and properties. The nominal composition for this work is 20 percent SnTe and 80 percent PbTe that produces a bandgap to match the long-wavelength atmospheric window.

PbSnTe is also interesting from a purely scientific point of view. It is, potentially, both solutally and thermally unstable due to the temperature and density gradients present during growth. Density gradients, through thermal expansion, are imposed in directional solidification because temperature gradients are required to extract heat. Solutal gradients occur in directional solidification of alloys due to segregation at the interface. The gradients vary with both experiment design and inherent materials properties.

In a simplified one-dimensional analysis with the growth axis parallel to the gravity vector, only one of the two instabilities works at a time. During growth, the temperature in the liquid increases ahead of the interface. Therefore the density, due to thermal expansion, is decreasing in that direction. However, the phase diagram shows that the lighter SnTe is preferentially rejected at the interface. This causes the liquid density to increase with distance away from the interface, which is opposite from the density change due to the furnace temperature profile. Figure 4-1 is a plot of the composition versus axial position of a typical Earth-grown crystal. The data points are plotted along with the analytical solution for the totally mixed case.

Coriell, et al.³ have shown that the two opposing density gradients cannot be readily balanced to stabilize the flow. Moreover, both experiments^{4,5,6,7} and numerical analyses^{5,8} have demonstrated that radial thermal gradients will start fluid motion long before the onset of convection predicted by a one-dimensional model. Hence, there will always be convection in the liquid.

Computational fluid dynamics (CFD) was utilized to predict the extent of convection in microgravity. The CFD calculations were based on a finite volume technique.⁹ The computational code allowed the calculations of time-dependent three-dimensional flows and associated temperature and concentration profiles. The method behind the calculations involves the division of the calculation domain into a number of cells. The field equations for mass, momentum and energy conservation are then integrated over the volume of the cell. The calculation routine then involves the prediction of the field variables of temperature, concentration, velocity components and pressure at the various cell faces.

In practice the finite volume technique is used iteratively. Temperature and concentration fields are first guessed; they affect the body force through their effect on buoyancy. The corresponding velocity and pressure fields are then calculated. The computed velocity field is used to correct the earlier estimate of the temperature and solutal concentration field, and the process continues until a desired convergence is reached.

This procedure is best explained by considering figure 4-2. The ampoule liquid region is assumed to be constant as the solidification rates are normally very small. The boundary conditions indicate hot and cold zones as well as insulating zones. The far-field concentration is assumed to be constant and the interface condition respects mass conservation along with solutal segregation. The effect of the magnitude of the gravity vector is seen in figures 4-3 and 4-4, and we immediately conclude that the flow at low-frequency, low-amplitude accelerations ($10^{-5}g_e$) will be of a weak toroid. Higher amplitude forces will cause solutal convection to come into play, but such high-amplitude acceleration vectors were not present at the low frequency levels during USMP-3 and were mainly associated with high-frequency activities such as booster firings and water dumps. While we do not presently have any predictions on the effects of high-frequency g-jitter, it is clear from the order-of-magnitude of the calculated velocity vectors for the case of low frequency with $10^{-5}g_e$, that very little mixing should take place. The velocity is no greater than 10^{-5} cm/sec. Given an initial liquid region size of 5 cm, this small velocity amounts to an initial mixing time of 10^6 sec. Meanwhile the solidification is at the rate of 1 cm/hr. When the liquid region size is about 1 cm the mixing time is about 2×10^5 sec. Clearly this is insignificant because the entire growth period is about 2×10^4 sec. In other words we predict that only diffusion-controlled growth ought to prevail at $10^{-5}g_e$ and this is even more true at the lower gravitational levels experienced during the USMP-3 mission.

The effect of a 5° offset with respect to the vertical orientation was calculated, and the results are graphically shown in figure 4-3(c). What is seen from this figure is that small tilts give rise to swirling flow and this flow contains the solutal boundary layer to the depleting surface. This may be contrasted with toroidal flow in figure 4-3(a) (for the vertical orientation) that sweeps the solute out of the solutal boundary layer. The solutal boundary layer contains most of the rejected SnTe, and so swirling flow if anything should help by making diffusive growth more probable. In other words one might conclude that a constant off-axis arrangement is better than if the acceleration vector were perfectly aligned along the ampoule. Figure 4-4 is a depiction of the mixing patterns that are seen when the ampoule is subjected to a time-dependent tilt. It must be noted that the velocities are still very small and so even in the case when the tilt is a periodic function of time the growth is expected to be diffusion controlled.

In summary, we have concluded that diffusive growth was predicted under low-frequency g-jitter conditions. The high frequency was not studied, but we did conclude that the time constant for the fastest transporting mechanism (heat transfer) was much larger than the corresponding period for high-frequency (5-Hz) g-jitter.

4.1.2 Bridgman Growth

Bridgman crystal growth offers the opportunity to independently fix the temperature gradient and interface position with respect to the furnace. However, these parameters cannot be varied without bound. There are temperature limits on the furnace and ampoule as well as limits imposed by the growth process. An excellent review of recent advances in Bridgman growth has been given by Favier.¹⁰

The limits imposed by the growth process are primarily concerned with maintaining an initial solutal translation zone of reasonable length and preventing interfacial instability. Second-order problems are the maintenance of interface shape control and thermal strain in the solid.

Due to the size of the AADSF, a sufficiently high growth rate is required to achieve steady-state

composition within 20 to 30 millimeters of the start of growth. The furnace must then be controlled to produce an axial thermal gradient in the melt that is sufficient to maintain a stable interface. If the growth is diffusion controlled, the growth distance required to get within 1 percent of compositional steady state (i.e. uniform) growth is¹¹

$$z_{ss} = 5D/kR . \quad (1)$$

However, the permissible growth rate is limited by the fundamental phenomena of interface breakdown. The short form of the equation for preventing breakdown is

$$\frac{Gr}{R} > \frac{C_s}{D} \frac{(l-k)}{k} |m| . \quad (2)$$

Equation (1) shows that a short initial transition zone requires a high growth rate while equation (2) shows that a high growth rate requires a large thermal gradient to avoid interfacial breakdown. Increasing either the axial thermal gradient or the growth rate increases the density gradient and the mixing in the liquid. Consequently, it can be seen that there is a tradeoff between growth rate, temperature gradient and the degree of mixing for a given acceleration level.

The PbSnTe growth experiment on USMP-3 was launched in February 1996. During the flight, three separate crystals were grown in a single, segmented ampoule. The crystals were grown in series, each in one of the three primary orientations with respect to the residual acceleration vector. The growths were roughly analogous to hot-on-top, cold-on-top, and horizontal growth.

While the immediate objective of that experiment was to grow PbSnTe and establish its fundamental growth properties, another, more important objective was to gain a better understanding of the mechanisms involved in generalized crystal growth, particularly those affected by gravity. This information will not only help produce better quality materials on Earth, but will also help define future efforts of crystal growth in space and lead the way to more extensive materials science research.

4.1.3 Segmented Ampoule

As mentioned before, the USMP-3 AADSF experiment used a single segmented ampoule to grow three separate PbSnTe crystals in series. The ampoule, represented in figure 4-5, allows each of the three crystals to grow with different conditions without affecting the outcome of the others. For USMP-3, each crystal was grown identically except for the orientation of the ampoule with respect to the residual acceleration¹² vector.

Even though the use of a three-cell ampoule decreases the total crystal length, and the percentage of crystal grown where the growth rate nearly matches the translation rate, it allows each of the cells to be grown under nearly identical conditions. A long crystal will obtain a nearly thermal steady-state growth region sandwiched between two end effect thermal and compositional transient regions. Using the three-cell sample decreases the length of any steady-state region; however, it provides growth conditions that are nearly thermally equivalent for each of the three cells. Most important, it keeps the composition for the three different regions separated, so that each crystal will have identical starting compositions. Each cell is long enough to reach compositional steady state before the liquid diffusion tail reaches the end of the ampoule.

4.2 RESULTS

4.2.1 Flight Operations

Space Shuttle Columbia (STS-75) was launched at 2018 GMT on February 22, 1996. The launch time defined Mission Elapse Time (MET) as 00 days/00 hr:00 min. This nomenclature, MET xx/yy:zz, without units, will be used to identify the relative time of events throughout the text of this report.

With the sample withdrawn 35 mm from its fully inserted launch position, the AADSF started heating at MET 06/10:07. Ampoule positions will be given by a translation position measurement (tpm) taken as the distance the ampoule is extracted, in mm, from full insertion, hence the present position is tpm=35. The furnace was at temperature, hot zone 1150 °C and cold zone 525 °C, at MET 06/14. After a 4-hr thermal stabilization period the sample was repositioned to tpm=37 where T_c 1, in the base of cell No. 1, read 930 °C, which was the so called “start condition.” Translation, at 10 mm/hr, to nucleate a seed in cell No. 1 started at MET 06/20:50. As deep undercooling¹³ is not anticipated and the recalescence event is clearly obvious, at least on Earth, nucleation was expected within 15 cm (1 hr 30 min) after the start of translation. As of MET 06/22:55 no recalescence had been noted, and the translation was reversed to remelt, assuming nucleation had occurred, the solidified portion of the sample and re-examine the small temperature rise in T_c 1 observed at 06/21:55. The sample was taken back to tpm=37 and extraction translation resumed at MET 07/03:14, and the same perturbation in T_c 1 occurred approximately 1 hr 5 min into the translation as it had done so the first time around (fig. 4-6). This was taken as confirmation of recalescence and translation was stopped at MET 07/04:23. This remelting and renucleation procedure did not leave sufficient time for solutal diffusion before our “microgravity time” ended for day 7. An extra day for AADSF operations was requested and received.

At 08/02:14 the Shuttle was put into attitude pitch =184.5°, yaw=0°, and roll=7° which had been calculated¹² to produce a nominal hot-on-top growth with respect to the microgravity acceleration vector. Dedicated microgravity time for cell No. 1 began at MET 08/03:00, and translation to grow the crystal in cell No. 1 started 1 hr later.

At MET 08/06:11, approximately 20 mm into the crystal growth, the Shuttle was put into an unscheduled free drift to help warm up a cold thruster nozzle. During a loss of signal (LOS) period the drift extended past expectations and at 08/06:41 had reached pitch=187.6°, yaw=5.2°, and roll=27.9°. The Shuttle attitude was back to nominal settings by MET 08/06:48, but during the free drift time the acceleration vector alignment with respect to the furnace axis went from approximately 2° to approximately 45°. Figure 4-7 shows the three-axis acceleration measurements at the AADSF position during this period.

Translation was to continue until recalescence in cell No. 2. Both thermocouples in cell No. 2 were inoperable by this time so this step had to depend on knowledge of prior furnace calibration and tpm position rather than the observation of recalescence temperature changes. Translation continued to tpm=120 which is well past the anticipated recalescence position and then reversed to tpm=114.75 to remelt excess seed material. At this time all furnace translation stopped until the next dedicated microgravity time.

The Shuttle was positioned in attitude pitch =90°, yaw=-17°, and roll=0° at MET 09/02:19. Microgravity time begin at MET 09/03:00, and translation commenced 1 hr later to grow the crystal in cell No. 2. The cell No. 2 growth proceeded without any observed perturbations; however, the anticipated advent of recalescence in cell No. 3 looked as if it would occur in the midst of a forthcoming LOS period starting at approximately MET 09/11:12. As described previously, the plan had been to pause the furnace before the LOS, wait until reacquisition of signal, and then continue translation. However, the diminution of the recalescence signal received from space as compared to that observed on Earth made reading the event amongst the stopping and starting of ampoule translation unlikely. It was decided to maintain the translation during the LOS, continue looking for the recalescence after the LOS until such tpm position where translation would have been stopped if both thermocouples had failed as with cell No. 2, and then to patch in the delayed transmission temperature data onto the curve as soon as it was available.

Translation was stopped at MET 09/11:36. The playback of LOS temperature data came in at 09/11:56 and showed that the recalescence in cell No. 3 occurred at about 09/11:17, the middle of the LOS. The translation was reversed for 2.5 mm to remelt part of the seed and then was stopped at tpm=184.7 at MET 09/13:49 to await the next microgravity period to grow the crystal in cell No. 3.

The Shuttle went into the prescribed attitude pitch=123°, yaw=0°, and roll=0° at MET 10/02:03. Microgravity time started at 10/03:00, and translation started at 10/04:00. The sample processed without major incident, and translation ceased at MET 10/10:36:48 at tpm=250.28. A controlled furnace cool down started at MET 10/11:40:55. The ampoule was stored in the cold furnace at MET 10/20:02.

4.2.2 Acceleration Magnitudes and Directions

Calculation of the acceleration vectors at the insulation zone of the AADSF as a function of the Space Shuttle attitude produces a transcendental equation as the resultant transformation matrix is dependent on time and attitude varying drag, orbit shape and altitude, and the distance and direction of the AADSF from the center of gravity of the Shuttle. See references 14, 15, 16, and 17 for more information on this topic. As the attitude to produce what is essentially hot-on-top, hot-on-bottom, and horizontal growths could not be obtained from minimization of the transformation equation, a study¹⁸ was undertaken to try to zero in on the preferred attitudes. This and a subsequent, unpublished, study determined the Shuttle attitudes for the three different growth orientations with the following acceleration vectors and concomitant angles.

Note: The following values are nominal. They vary with, among other things, Shuttle drift, orbit position, and sun angle. Also, directions are given in body coordinates for the direction an object would travel in a less massive fluid. In this system an object, at the AADSF location, in attitude No. 1 would travel away from the center of the Shuttle through the cargo bay doors. This direction is from the hot zone of the AADSF toward the cold zone which is analogous to hot-on-top furnace orientation on Earth.

Attitude No. 1, Hot-on-top growth.

Pitch=185°, Yaw=0°, Roll=7°

Acceleration along the *z* axis=-0.75 micro g

Acceleration along the *x* axis=0.01 micro g

Acceleration along the *y* axis=0.02 micro g

Approximate angle of acceleration vector with respect to AADSF center bore is approximately 2° .
The desired angle is 0° .

Attitude No. 2, Hot-on-bottom.

Pitch= 90° , Yaw= -17° , Roll= 0°

Acceleration along the z axis=0.2 to 0.4 micro g acceleration along the
 x axis= -0.01 micro g

Acceleration along the y axis=0.1 micro g

Approximate angle of acceleration vector with respect AADSF center bore is 140° to 160° . The
desired angle is 180° .

Attitude No. 3, Horizontal growth.

Pitch= 123° , Yaw= 0° , Roll= 0°

Acceleration along the z axis=0.1 to 0.1 micro g acceleration along the
 x axis= -0.4 micro g

Acceleration along the y axis=0.15 micro g

Approximate angle of acceleration vector with respect to AADSF center bore is -76° to 76° . The
desired angle is 90° .

None of these attitudes are ideal. Attitude No. 1 is closest to that desired, and attitude No. 3 averages to the desired value of 90° , but the 14° variation is not desirable.

In addition to the drag and position effects of the low-frequency accelerations on the sample, the drag deceleration and the tendency for the orbiter to get into an aerodynamically stable mode necessitated the need for vernier booster firings. The forces associated with these corrective measures were of high magnitude (roughly $10^{-3}g_e$ to $10^{-4}g_e$) but were of a high frequency (5 to 10 Hz).

Comparison of these calculations to the measurements made in flight will be the subject of a subsequent paper.

4.3 RESULTS, POSTFLIGHT

4.3.1 X- and Gamma-Ray Radiography

The flight sample was retrieved from the AADSF at the Kennedy Space Center in April 1996. Microfocus x ray was used to examine the quartz ampoule for cracks before removal of the Inconel cartridge. No cracks in the fused quartz ampoule were observed, but the shadow outline of the crystals appeared much longer than expected.

The samples were further examined, still in the Inconel cartridge, with the 420 KV computer aided tomography (CAT) unit also available in the KSC nondestructive test laboratory. These high-voltage x rays are capable of penetrating the PbSnTe samples and exposing any voids, large pits, and bubbles. The results

shown by this examination were totally unexpected; the crystals are cratered with large voids and riddled with meandering channels. Figure 8 shows a selected vertical slice of each crystal. This figure was made by reconstructing the transverse slices gathered in the normal CAT fashion. The CAT slices of each crystal are shown in figures 4-9 to 4-11.

Similarities among the three crystals are that the initial formation, in the cold end of each of their respective cells, is a complete solid crystal that completely filled the base of that cell. (This solidarity of structure in the base did not hold upon microscopic examination. This topic will be discussed more fully in a later section.) After the formation of the base section, which is longer than the anomalous compositional distribution due to recalescence, each crystal then necked down almost to the point of discontinuity. The channels and cavities emanate from the upper (terms such as base and upper, of course, have their etymology in references to Earth gravity; here they are merely convenient terms to refer to positions relative to the coldest part of each experimental growth cell) ends of the voids that formed the necked down region. Finally, the last to freeze ends of the crystals become solid again.

The primary difference in x-ray appearance is the way a double set of cavities formed in cell No. 1 as opposed to the surface channels in the other two crystals.

These results were totally unexpected. Large pores or voids have been found in other space-grown crystals,^{19 20} but no large pores or other voids were found in the PbSnTe crystal grown on the 1985 STS-61A mission. Although Kinoshita²³ reported some porosity, his photographs showed monolithic crystals compared to these.

4.3.2 Sample Composition

The primary objective of this flight experiment was to examine the effect of the direction of the microgravity vector on the convective mixing of the liquid during directional solidification. The measurable physical parameter that is the most sensitive monitor of mixing in the liquid is the compositional profile in the solidified crystal. The difference in the analytical solutions for the profiles for both fully mixed and mixing via diffusion alone is shown in figure 4-12.

Figures 4-13 to 4-15 are axial compositional profiles for cell Nos. 1 to 3, respectively. Each cell shows evidence of considerable mixing. With one minor exception, the free drift period already discussed, the Space Shuttle performed the predetermined maneuvers for the growth periods as required, but the presence of voids creates the condition for surface driven (Marangoni) convection.²² The problem now becomes that of separating Marangoni convection from density driven convection.

Figure 4-13 shows the axial compositional distribution of cell No. 1. The anticipated spike of SnTe shows the recalescence area at the left side of the plot, then the data flattens for what may be growth during thermal stabilization after the release of the latent heat. At 5 mm of growth, approximately the length of the produced seed after the solutal diffusion time, the composition shows signs of trying to go to diffusion growth but failing. At approximately 25 mm of growth, the curve closely approximates the fully mixed case. The following deserves further study, but the melt-solid interface would have been 25 mm from the base of cell No. 1 at approximately MET 08/06:30, the time of the Shuttle free drift which would have essentially turned the AADSF on its side for a few minutes.

After recalescence the axial compositional profile of the crystal in cell No. 2, the nominally hot-on-bottom orientation, follows the completely mixed curve for the first 45 mm of growth and then exhibits deviations (fig. 4-14) that are, as yet, unexplained. Similar deviations occur in the axial compositional profile of the crystal grown in cell No. 3, but over a longer section (fig. 4-15). As yet no acceleration perturbations have been related to these compositional variations. These crystals will be examined to try to correlate these compositional deviations with crystalline microstructure and the defect formation.

4.3.3 Microporosity

Figures 4-16 to 4-18 are photomicrographs of the first to freeze regions of cell Nos. 1 to 3 respectively. The first to freeze regions of the crystals grown in cell Nos. 1 and 3 clearly show random patterns of submillimeter pores which were not visible on the CAT scans. A few pores were seen at the very base of the crystal from cell No. 2, but the defects are not clearly visible in the attached figure. The volume of the pores in cells No. 1 and No. 3 were estimated using a retinex²³ technique to be approximately 4 percent of total in the base region. This value is the same as the volume reduction upon the phase change from liquid to solid state.

4.4 SUMMARY

This paper is a work in progress for we are far from finishing the analysis of these fascinating and tantalizing samples. We started the flight experiment to determine the small, but predictable, differences in convective mixing due to the alignment of the acceleration vector. We are still trying to extract data on that topic, but such information is buried in the myriad observations of the large pore, void, and channel formations.

We have been able to show a few things within this time frame that are useful to the microgravity materials science community, and we believe that we will deliver a complete story when we complete the evaluation and analysis of the USMP-3 experiment, especially when we couple the results with the upcoming USMP-4 crystal growth experiments and the experiments of others in this area.

REFERENCES

1. Harman, T.C.: "Control and Imperfections in Crystals of PbSnTe, PbSnSe and PbSSe," *J. Nonmetals I*, p. 183, 1973.
2. Parker, S.G.; and Johnson, R.W.: "Preparation and Properties of PbSnTe," *Preparation and Properties of Solid State Materials*, Vol. 6, Wilcox, W.R., ed., Marcel Dekker, Inc., New York, p. 1, 1981.
3. Coriell, S.R.; Cordes, M.R.; Boettinger, W.J.; and Sekerka, R.F.: "Convective and Interfacial Instabilities During Unidirectional Solidification of a Binary Alloy," *J Crystal Growth*, Vol. 49, p. 13, 1980.
4. Hurst, J.H.: "Electrochemical Visualization of Convection in Liquid Metals," Ph.D. Dissertation, The University of Florida, Chemical Engineering, 1990.
5. Sears, B.; Narayanan, R.; Anderson, T.J.; and Fripp, A.L.: "Convection of Tin in a Bridgman System: I. Flow Characterization by Effective Diffusivity Measurements," *J. Crystal Growth*, Vol. 125, p. 404, 1992.
6. Sears, B.; Fripp, A.L.; Debnam, W.J.; Woodell, G.A.; Anderson, T.J.; and Narayanan, R.: "Convection of Tin in a Bridgman System: II. An Electrochemical Method for Detecting Flow Regimes," *J. Crystal Growth*, Vol. 125, p. 415, 1992.
7. Sears, B.; Anderson, T.J.; Narayanan, R.; and Fripp, A.L.: "The Detection of Solutal Convection During Electrochemical Measurement of the Oxygen Diffusivity in Liquid Tin," *Metallurgical Transactions B*, Vol. 24B, p. 91, 1993.
8. Carlson, F.M.; Fripp, A.L.; and Crouch, R.K.: "Thermal Convection During Bridgman Crystal Growth," *J. Crystal Growth*, Vol. 68, p. 747, 1984.
9. Patankar, S.: "Numerical Heat Transfer and Fluid Flow," Taylor and Francis, Bristol, Pennsylvania, 1980.
10. Favier, J.J.: "Recent Advances in Bridgman Growth Modeling and Fluid Flow," *J. Crystal Growth*, Vol. 9, p. 18, 1990.
11. Tiller, W.A.; Jackson, K.A.; Rutter, J.W.; and Chalmers, B.: "The Redistribution of Solute Atoms During the Solidification of Metals," *Acta Met. I*, p. 428, 1953.

12. Matisak, B.P.; Zhao, A.X.; Narayanan, R.; and Fripp, A.L.: "The Microgravity Environment: Its Prediction, Measurement, and Importance to Materials Processing," presented at The Tenth American Conference on Crystal Growth, August 4–9, 1996, Vail, Colorado, and accepted for publication in the *Journal of Crystal Growth*.
13. Fripp, A.L.; Crouch, R.K.; Debnam, W.J.; Clark, I.O.; and Wagner, J.B.: "Effects of Supercooling in the Initial Solidification of PbTe-SnTe Solid Solutions," *J. Crystal Growth*, Vol. 73, p. 304, 1985.
14. Blanchard, R.C.; Hendrix, M.K.; Fox, J.C.; Thomas, D.J.; and Nicholson, J.Y.: "Orbital Acceleration Research Experiment," *J. Spacecraft and Rockets*, Vol. 24, p. 504, 1987.
15. Alexander, J.I.D.; and Lundquist, C.A.: "Motions in Fluids Caused by Microgravitational Acceleration and Their Modification by Relative Rotation," AIAA 25th Aerospace Sciences Meeting, January 12–15, 1987, Reno, Nevada, *paper AIAA-87-0312*.
16. Matisak, B.P.; Rogers, M.J.B.; and Alexander, J.I.D.: "Analysis of the Passive Accelerometer System (PAS) Measurements During USML-1," AIAA 32nd Aerospace Sciences Meeting, January 10–13, 1994, Reno, Nevada, *paper AIAA-94-0434*.
17. DeLombard, R.: "Compendium of Information for Interpreting the Microgravity Environment of the Orbiter Spacecraft," *NASA Technical Memorandum 107032*, August 1996, NASA Lewis Research Center, Cleveland, Ohio.
18. Matisak, B.P.: "Update to USMP-3/STS-75 AADSF Attitude Design Study," No. 410RPT0736, Teledyne Brown Engineering, Huntsville, Alabama, August 31, 1995.
19. Matthiesen, D.H.; and Majewski, J.A.: "The Study of Dopant Segregation Behavior During the Growth of GaAs in Microgravity." NASA Conference Publication 3272, Vol. 1, p. 223, May 1994. Joint Launch + One Year Review of USML-1 and USMP-1 with the Microgravity Measurement Group.
20. Andrews, J.B.; Hayes, L.J.; Arikawa, Y.; and Coriell, S.R.: "Microgravity Solidification of Al-In Alloys." 35th Aerospace Sciences Meeting, AIAA, Reno, Nevada, January 6–10, 1997.
21. Kinoshita, K.; and Yamada, T.: "PbSnTe Crystal Growth in Space," *J. Crystal Growth*, Vol. 147, p. 91, 1995.
22. Naumann, R.J.: "Marangoni Convection Around Voids in Bridgman Growth," *J. Crystal Growth*, Vol. 154, p. 156, 1995.
23. Jobson, D.J.; Rahman, Z.; and Woodell, G.A.: "Properties and Performance of a Center/Surround Retinex," *IEEE Transactions on Image Processing*, Vol. 6, p. 451, 1997.

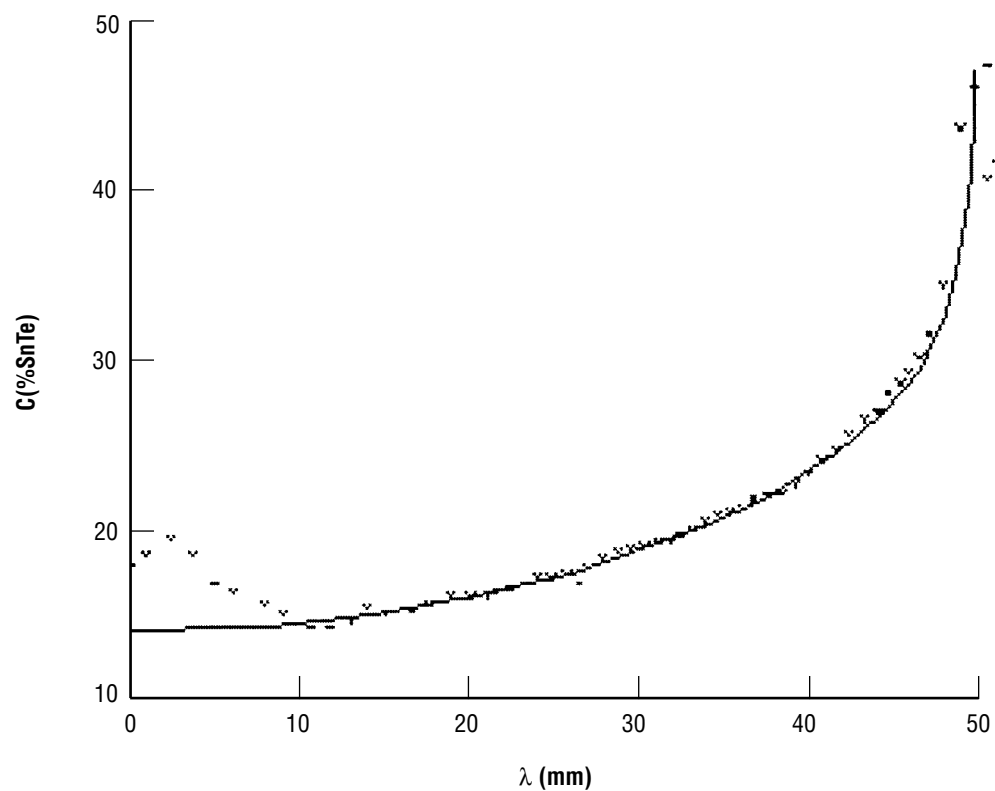


Figure 4-1. Axial composition of Earth-grown PbSnTe crystal. The solid line is from the analytical equation for totally mixed melt. This crystal was grown in a low gradient furnace, hence the first to freeze region is larger than that of crystals grown in the AADSF.

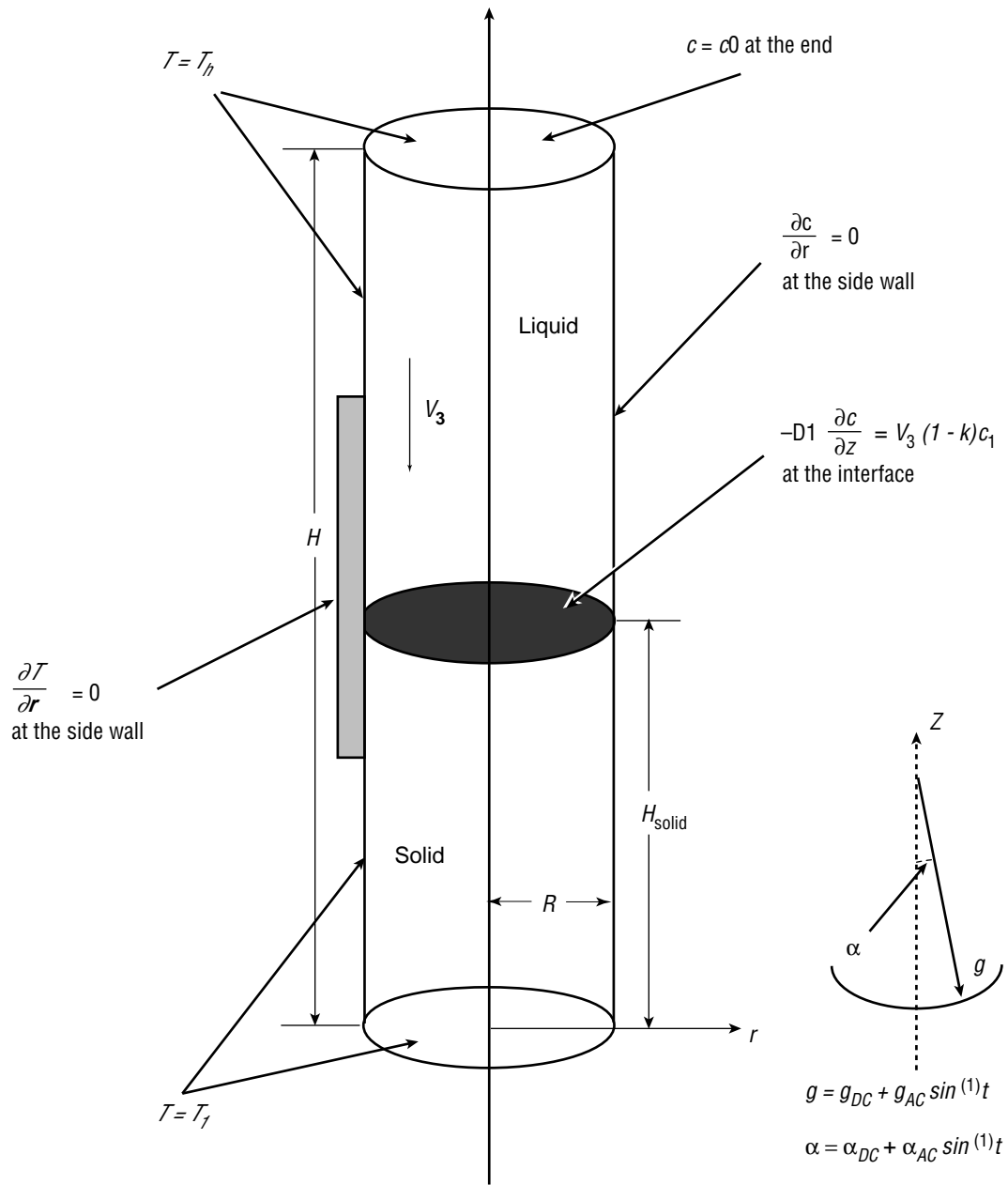


Figure 4-2. Schematic of the geometric, thermal, and concentration boundary conditions used in the computational fluid dynamical calculations in this study.

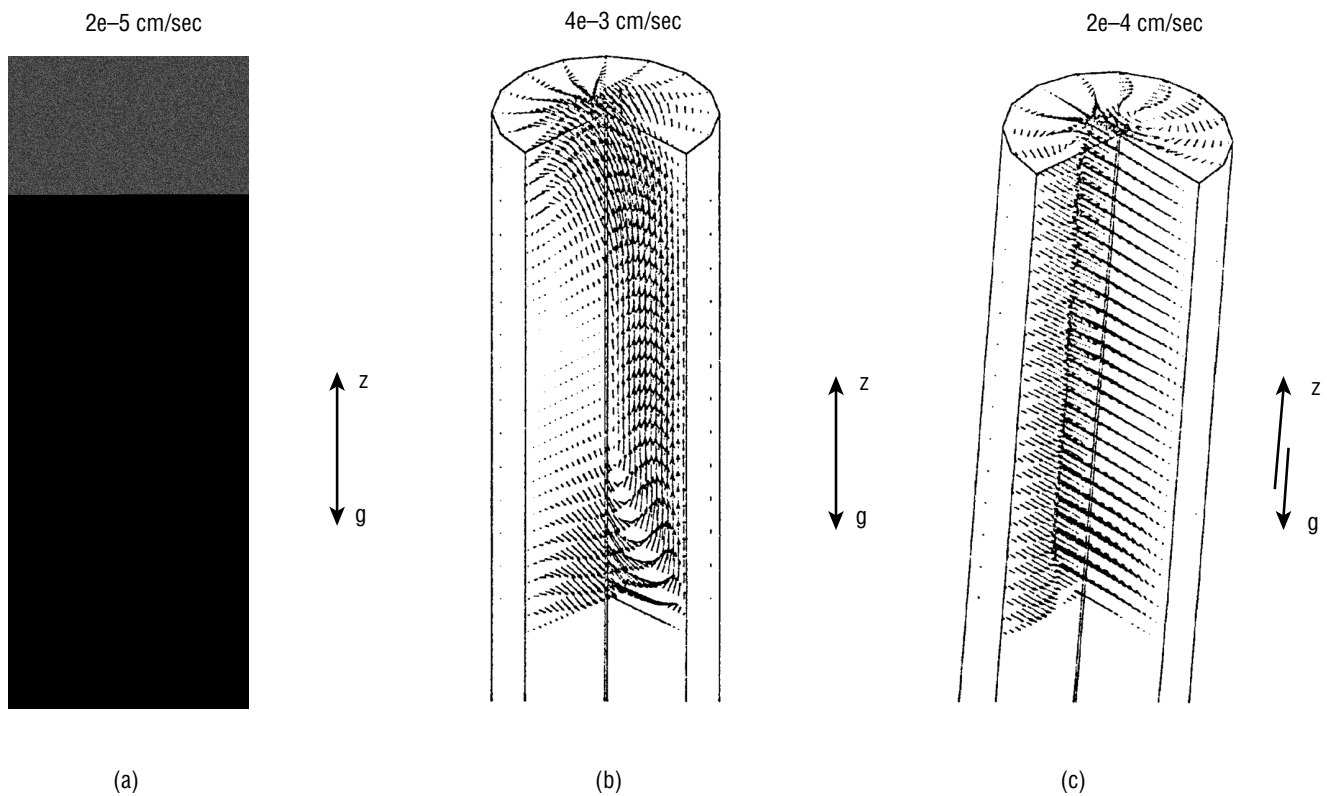


Figure 4-3. The three-dimensional flow field in the liquid region with constant acceleration magnitude and direction. (a) Acceleration is aligned with ampoule axis at 10^{-5} Earth gravity. (b) Acceleration is aligned with ampoule axis at 10^{-4} Earth gravity. (c) Acceleration is misaligned with ampoule axis by 5° with magnitude of 10^{-5} Earth gravity.

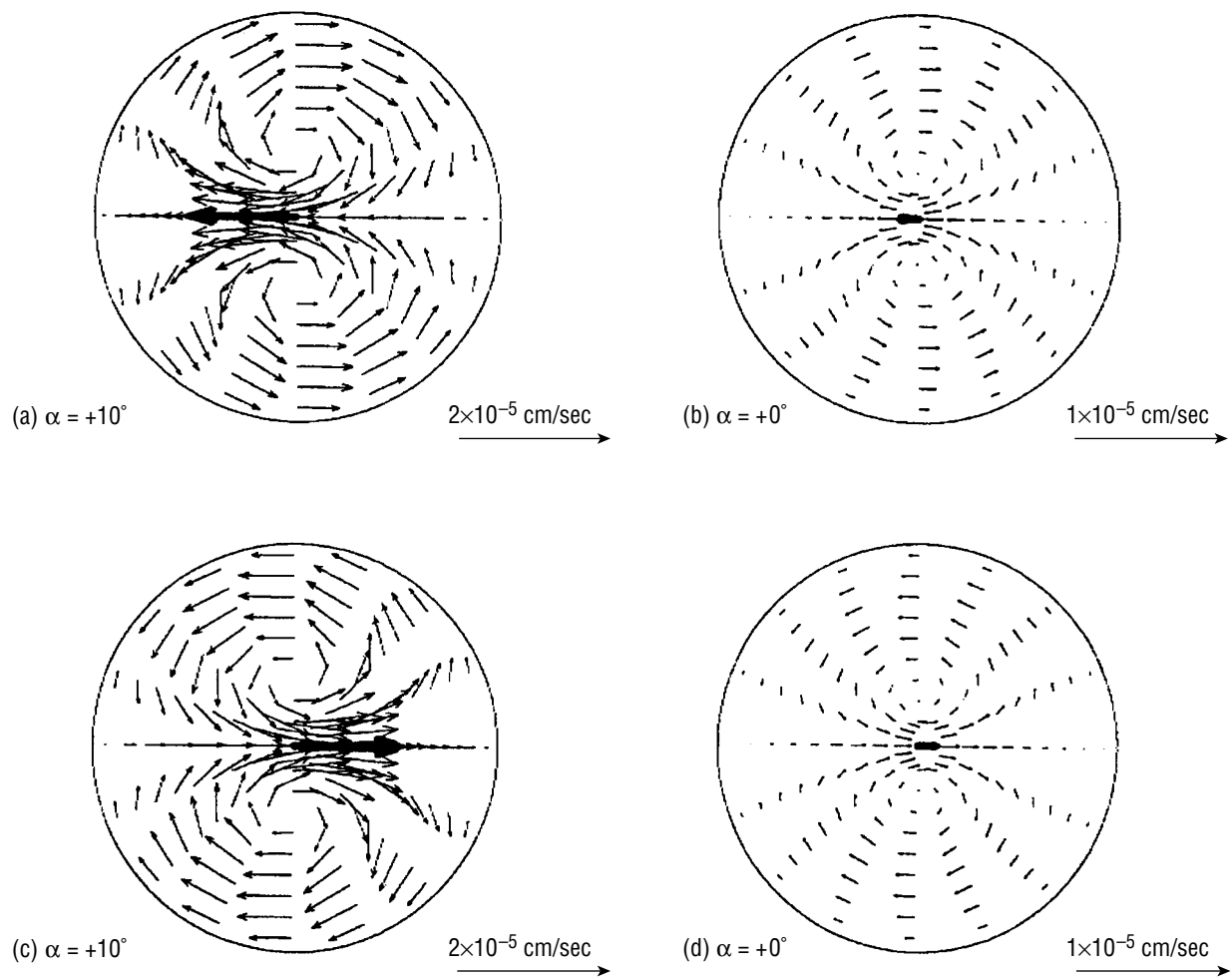


Figure 4-4. The two dimensional flow field near the melt solid interface when the acceleration vector (magnitude of 10^{-5} Earth gravity) is undergoing a 10° time dependent tilt variation at a frequency of one cycle per hour.

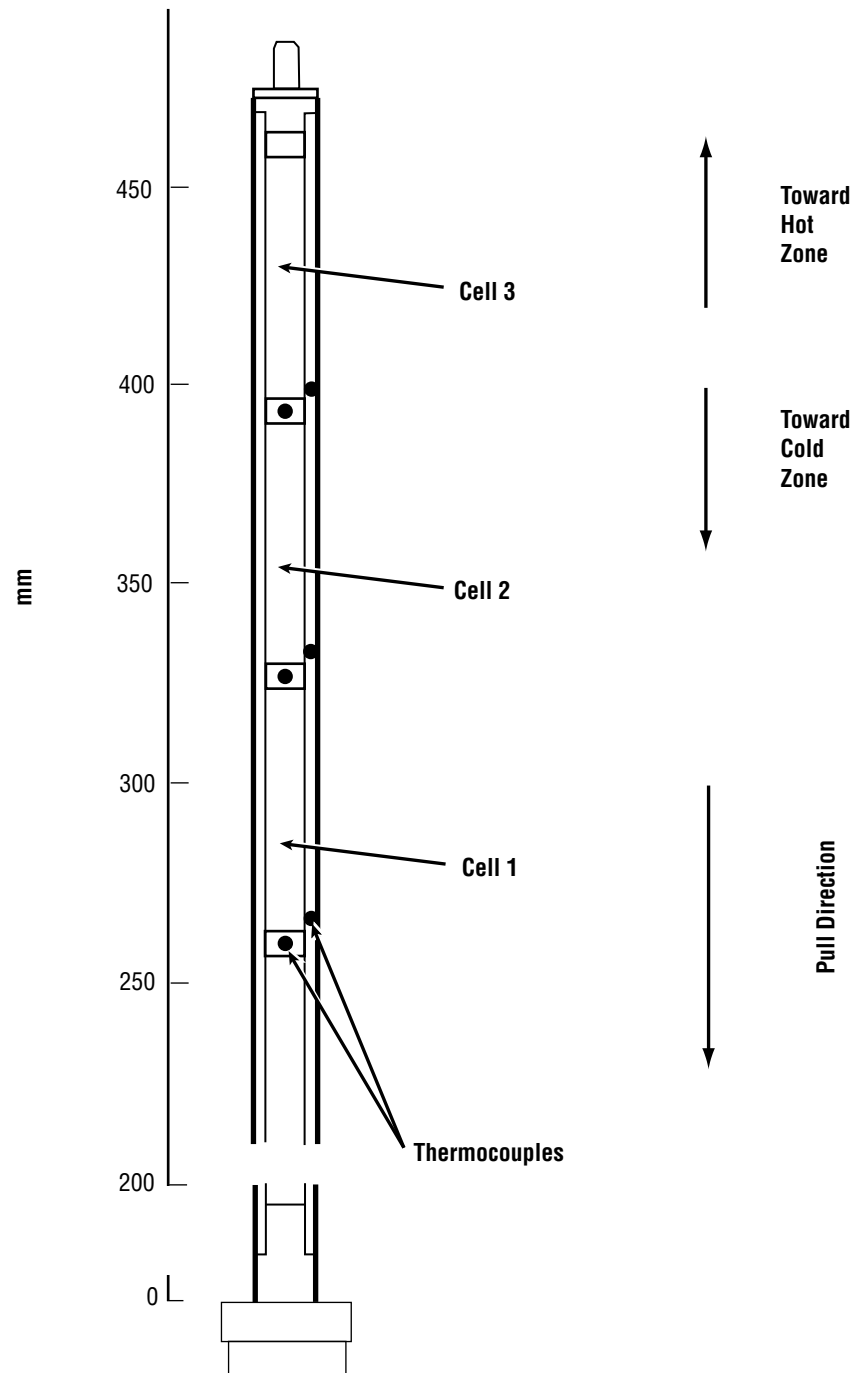


Figure 4-5. A typical segmented ampoule showing the three cells, and the location of the sample thermocouples.

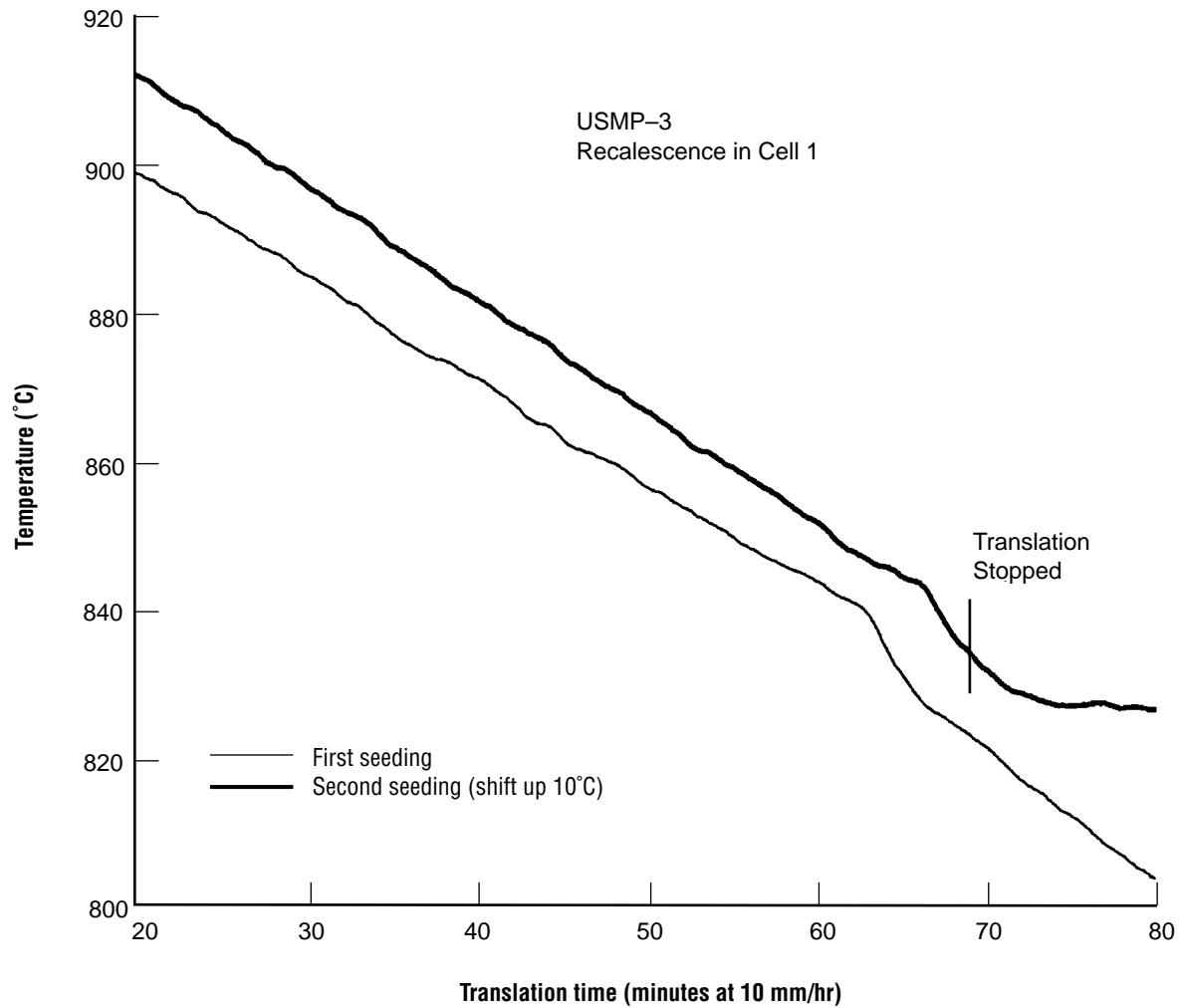


Figure 4-6. Temperature response the recalcence in cell No. 1. The response did not show a sharp peak as in Earth-grown events, but showed a rounded temperature change. The event was repeated (upper curve displaced by 10°C for clarity) to verify the observation.

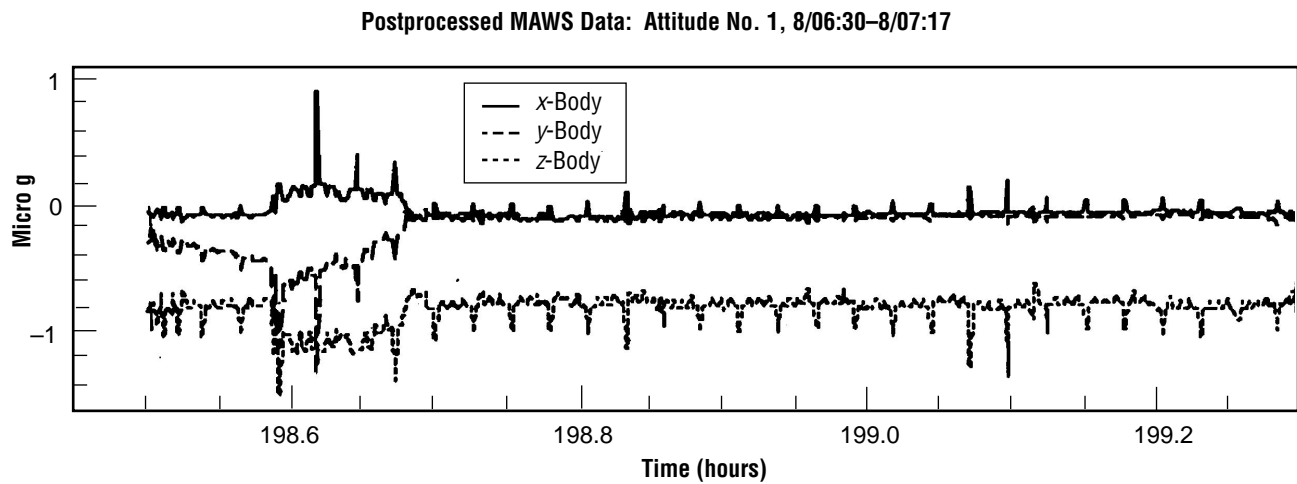


Figure 4-7. The acceleration magnitudes, at the AADSF freeze zone, for each of the three primary directions. The z acceleration is along the AADSF furnace bore and in such direction that more dense fluid would move from the hot zone toward the cold zone. This time slice shows the acceleration during the free drift period that occurred at approximately MET 8/06:30 (198.6 hours on the graph).

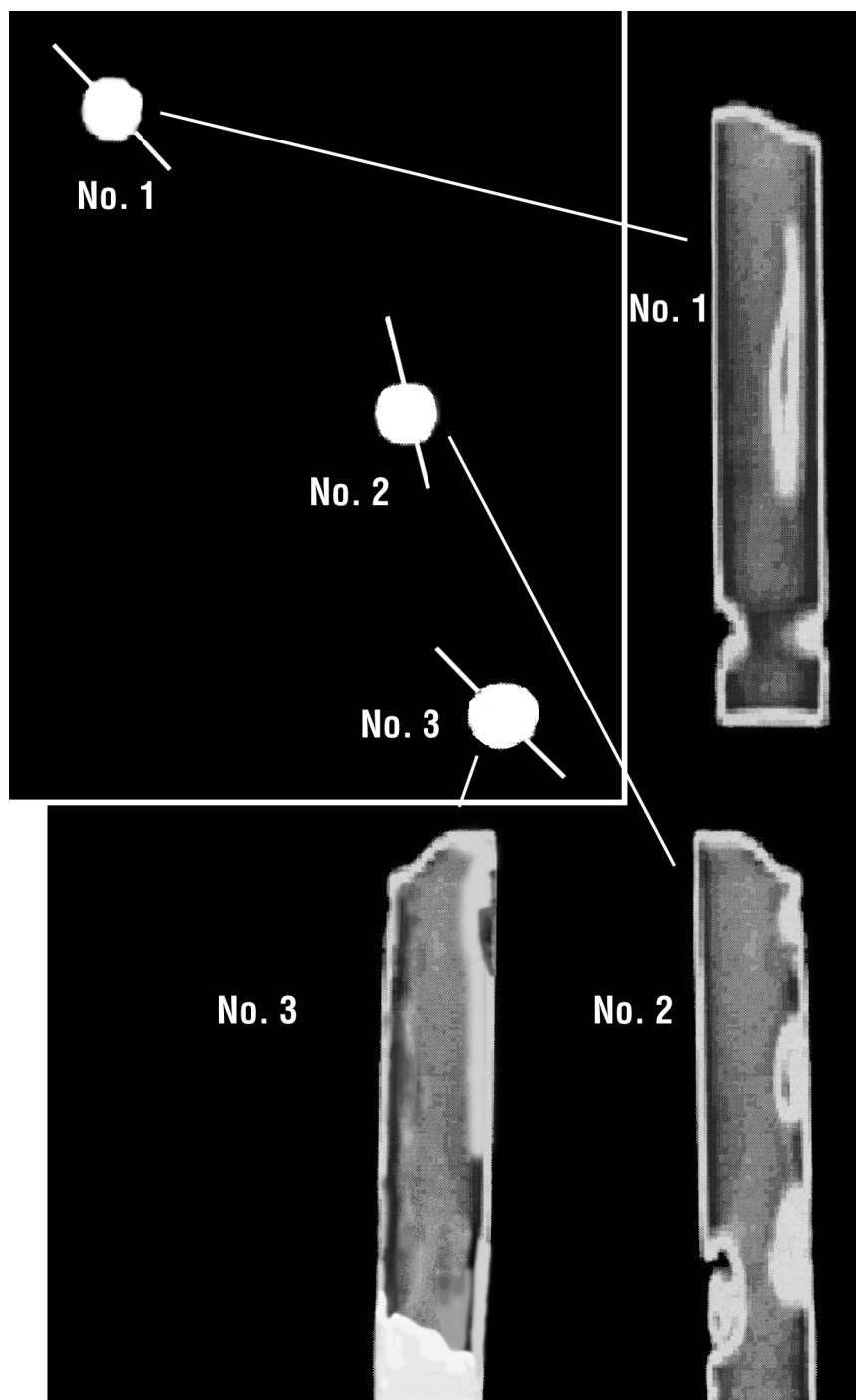


Figure 4-8. Vertical slices of the three USMP-3 PbSnTe crystals. These scans were made from the integrated results of CAT scans. Each crystal is positioned with the first to freeze end down. The insert at the upper left shows the position of the vertical slice for each crystal.

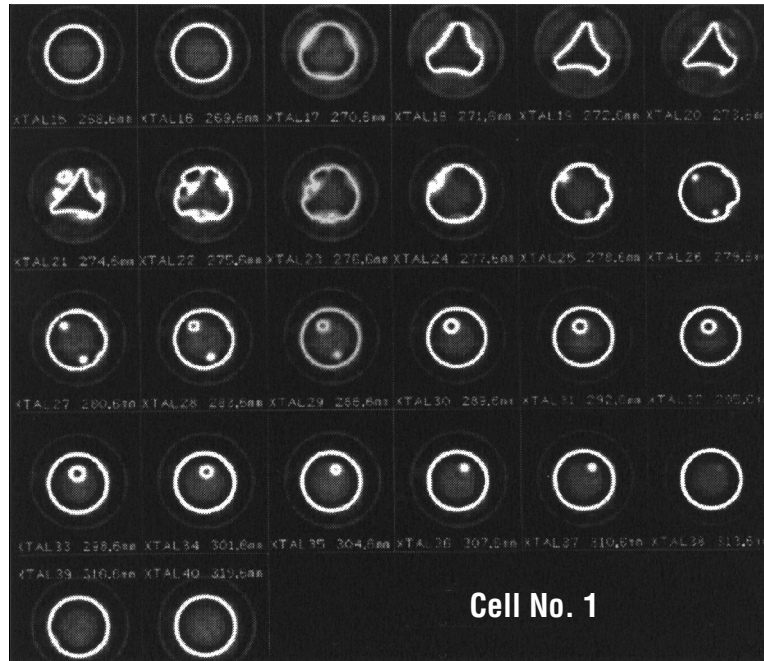


Figure 4-9. Successive CAT, horizontal, slices of cell No. 1. The first to freeze end is at upper left. The first 13 slices were taken at 1-mm steps and the remaining slices at 3-mm steps. Images were made with 420-kV x rays.

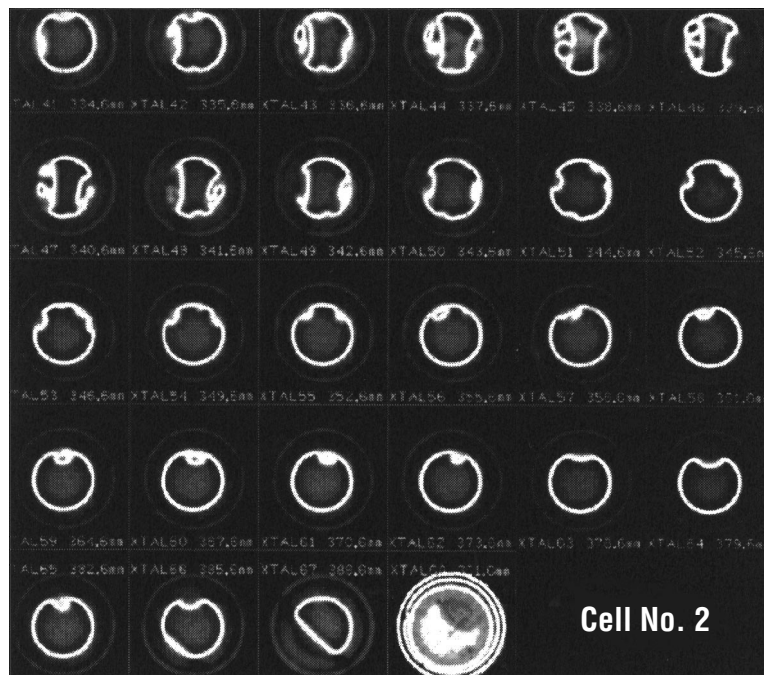


Figure 4-10. Successive CAT, horizontal, slices of cell No. 2. The first to freeze end is at upper left. The 13 slices were taken at 1 mm steps and the remaining slices at 3-mm steps. Images were made with 420-kV x rays. The first scan was taken approximately 8 mm above the base of the crystal hence it shows the beginning of the void formation.

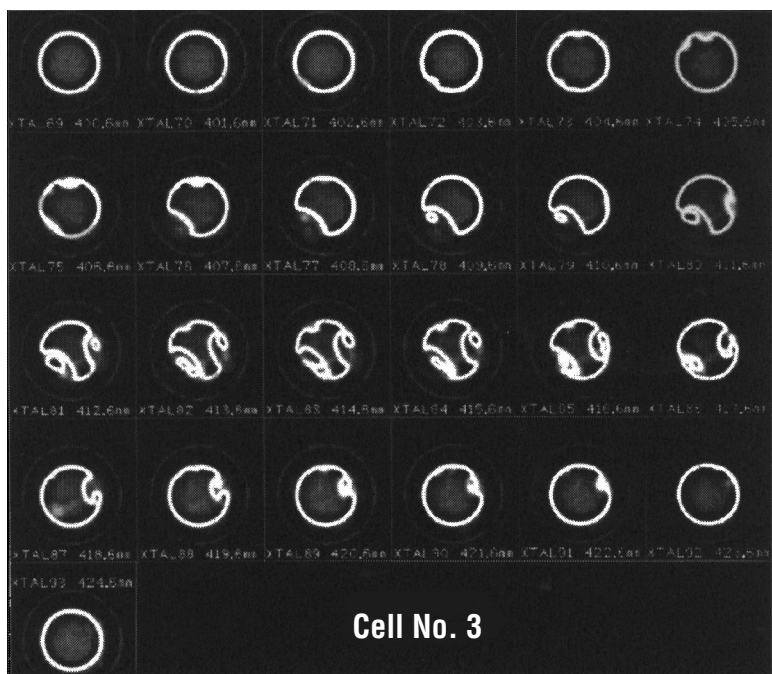


Figure 4-11. Successive CAT, horizontal, slices of cell No. 3. The first-to-freeze end is at upper left. The first 26 slices were taken at 1 mm steps and the remaining slices at 3-mm steps. Images were made with 420-kV x rays.

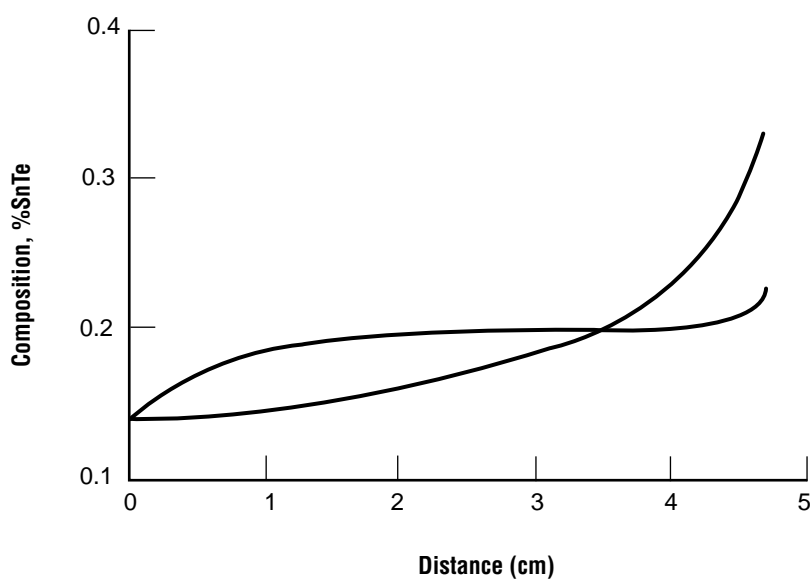


Figure 4-12. Graphs of the one dimensional analytical solutions for the profiles for both fully mixed and mixing via diffusion only during the directional solidification of PbSnTe.

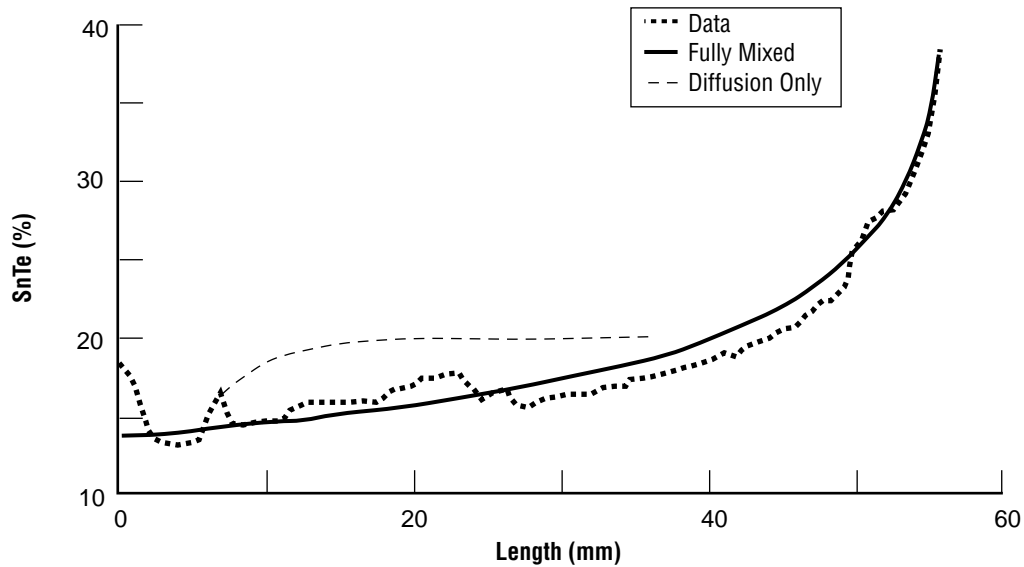


Figure 4-13. Axial composition scan of cell No. 1. The data scan was made 2 mm from the center line. Also shown are the analytical curves for a totally mixed sample and the start of one grown with diffusion mixing only. The anticipated composition spike of SnTe shows at the recalescence area at the left side of the plot, then the data flattens for what may be growth during thermal stabilization after the release of the latent heat. At 5 mm of growth the composition shows signs of trying to go to diffusion controlled growth. At approximately 25 mm of growth the curve closely approximates the fully mixed case.

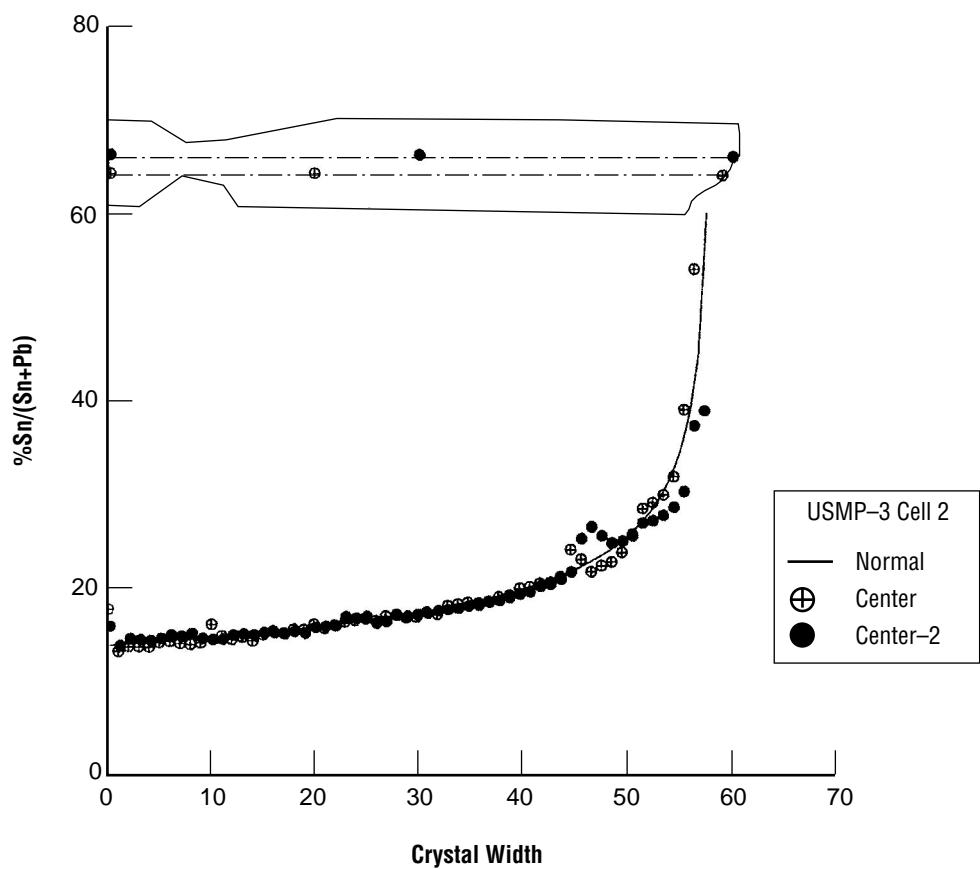


Figure 4-14. Axial compositional profile of the crystal in cell No. 2, the nominally hot on bottom orientation, follows the completely mixed curve for the first 45 mm of growth and then exhibits deviations that are, as yet, unexplained.

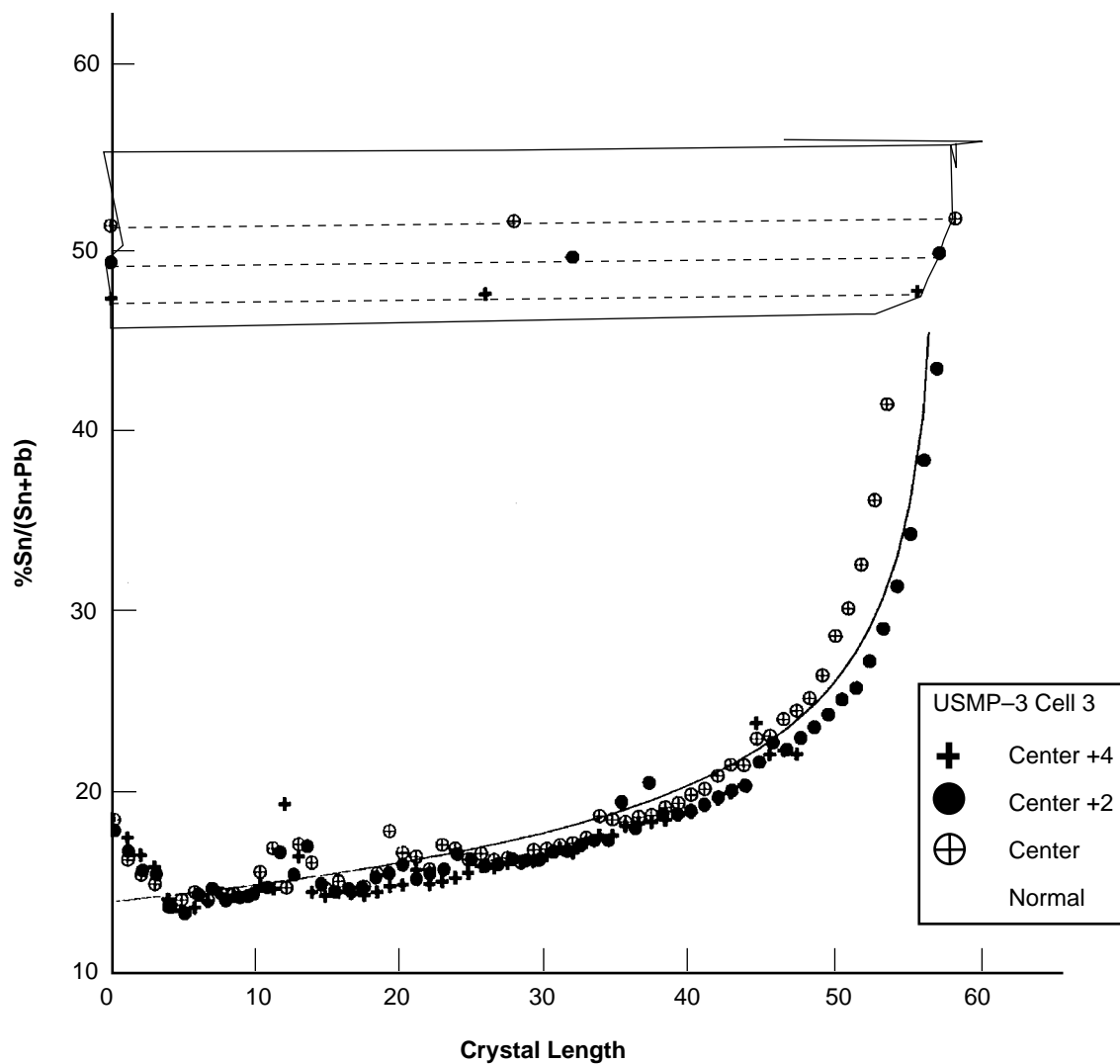


Figure 4-15. Axial compositional profile of the crystal grown in cell No. 3. This crystal shows similar deviations from totally mixed as the crystal in cell No. 2 but over a longer section.

USMP-3 Cell No. 1

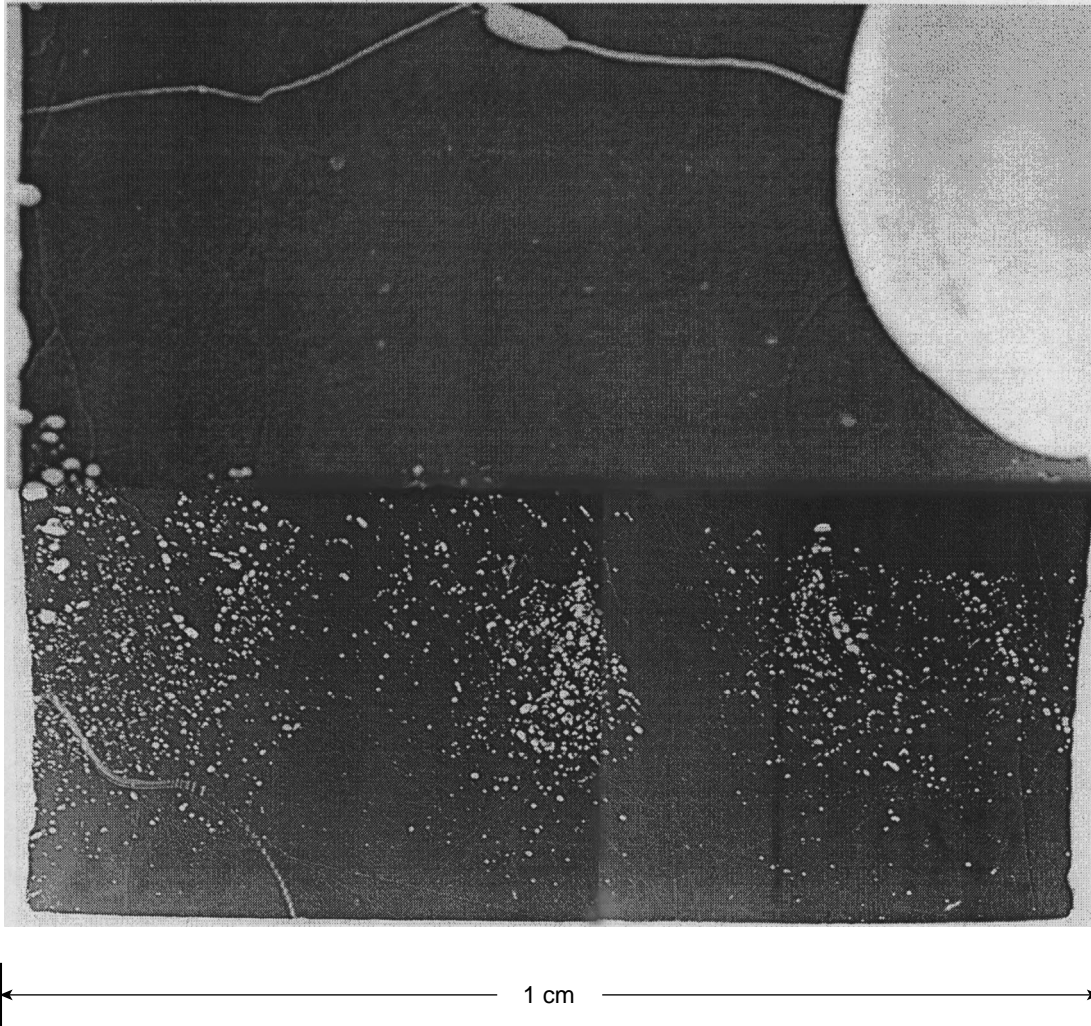


Figure 4-16. Photomicrograph of the first to freeze region of cell No. 1. The first to freeze region clearly shows random patterns of sub millimeter pores which were not visible on the CAT scans.

USMP-3 Cell No. 2

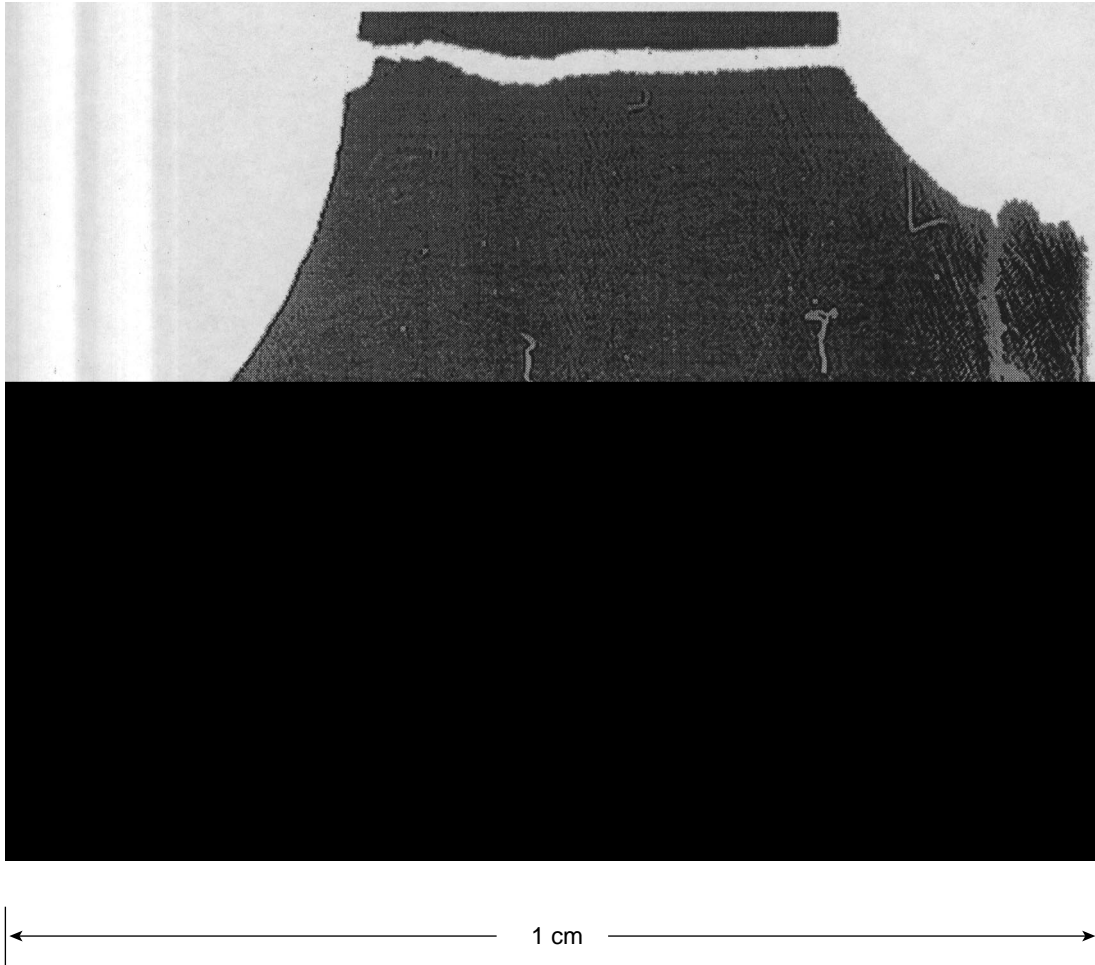


Figure 4-17. A few pores were seen at the very base of the crystal from cell No. 2, but the defects are not clearly visible in the photograph.

USMP - 3 Cell #3

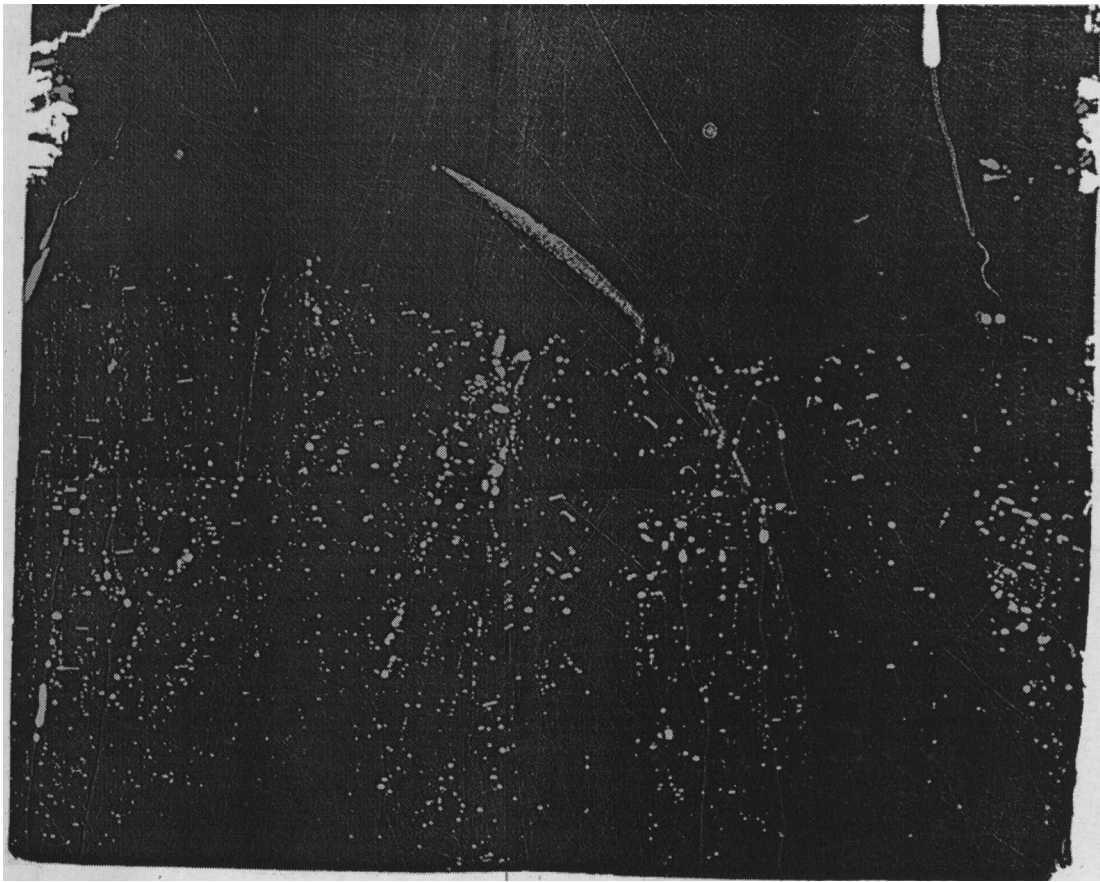


Figure 4-18. Photomicrograph of the first to freeze region of cell No. 3. The first to freeze region clearly shows random patterns of sub millimeter pores which were not visible on the CAT scans.

SECTION V.

FORCED FLOW FLAME SPREADING TEST: PRELIMINARY FINDINGS FROM THE USMP-3 SHUTTLE MISSION

Acknowledgments

The authors would like to acknowledge the herculean efforts put forth on our behalf by many people associated with the USMP-3 mission and the building of our experiment. In particular, we would like to thank Brian Quigley and Terry Rodgers, and the many technicians and fabrication specialists at the NASA Lewis Research Center for yet another excellent job. We would also like to express our gratitude to the members of the Teledyne Brown and NASA Marshall Space Flight Center Glovebox Team, who always found a way.

**FORCED FLOW FLAME SPREADING TEST:
PRELIMINARY FINDINGS FROM THE USMP-3 SHUTTLE MISSION**

Kurt R. Sacksteder

Microgravity Combustion Science Branch
MS 500-115, NASA Lewis Research Center
Cleveland, Ohio, 44135
Phone: 216-433-2857
E-mail: Kurt.Sacksteder@lerc.nasa.gov

James S. T'ien

Mechanical and Aerospace Engineering
Case Western Reserve University,
Cleveland, Ohio, 44106
Phone: 216-368-4581
E-mail: jst2@po.cwru.edu

Paul S. Greenberg

Microgravity Combustion Science Branch
MS 110-3, NASA Lewis Research Center
Cleveland, Ohio, 44135
Phone: 216-433-3621
E-mail: Paul.Greenberg@lerc.nasa.gov

Paul V. Ferkul

Analex Corporation
MS 500-115, NASA Lewis Research Center,
Cleveland, Ohio, 44135
216-433-8107
E-mail: Paul.Ferkul@lerc.nasa.gov

Richard D. Pettegrew

Case Western Reserve University
MS 500-115, NASA Lewis Research Center
Cleveland, Ohio, 44135
Phone: 216-433-8321
E-mail: Richard.Pettegrew@lerc.nasa.gov

Hsin-Yi Shih

Mechanical and Aerospace Engineering
Case Western Reserve University
Cleveland, Ohio, 44106

5.1 ABSTRACT

The Forced Flow Flame Spreading Test (FFFT) is a study of flame spreading over solid fuels in very low-speed air flows. The FFFT experiment is part of a peer-reviewed, NASA Research Announcement Award for a space-based experiment entitled, "Solid Inflammability Boundary at Low Speeds," (SIBAL) intended for operations on the Space Station. In the FFFT experiment, a series of 15 experiments conducted aboard the Space Shuttle during the USMP-3 mission provided information about the structure and spreading characteristics of flames in low-speed, concurrent flows. The test samples included flat sheets of cellulose and cast cylinders of cellulose, burned in air at velocities of approximately 1 to 8 cm/sec. The test results have been successfully compared to theoretical predictions of the SIBAL program, a fundamentally based numerical simulation of concurrent flow flame spread. Additionally, some guidance for the design characteristics of the SIBAL flight experiment has been obtained including some verification of the theoretical predictions of flame size versus the required size of the SIBAL flow duct, and the effect of the presence of thermocouples in the vicinity of near-limit flames in microgravity.

5.2 INTRODUCTION

Flame spreading over solid fuels is a classic problem in combustion science. Over the past few decades, many workers have attempted to unravel the complex interaction of chemical and physical processes that control spread rates and flammability. Considerable progress has been made in understanding the mechanisms of spreading flames under certain conditions; nearly all under the influence of normal gravity. A more complete understanding of the spreading and flammability limit mechanisms can be obtained if the domain of experimental and modeling efforts is extended into subnormal levels of gravitational acceleration, because only in reduced gravity are low, controllable, oxidizer flow velocities in the flame zone obtainable.

In the study of flame spreading mechanisms, two broad classes are distinguished: Flame spread in opposed flow, in which the direction of the oxygen flow is opposite to the direction of flame spread; and concurrent flow, in which the flame advances in the same direction as the oxygen flow.¹ In general, the magnitude of the relative velocity between the flame and the oxidizer affects flame spread and extinction because of the convection of heat, oxygen and products. In a natural convective environment in normal gravity, the gas phase is accelerated by body forces acting on density (temperature) gradients in and near the flame; thus velocities vary along the length of the flame. The minimum characteristic velocity near the bottom of the flame are estimated, for air at normal pressure, to be 20 to 90 cm/sec, depending upon the flame temperature associated with a particular fuel. This buoyant velocity is the minimum observable air velocity regardless of how the solid is oriented, or whether or not an imposed flow (e.g., wind) is added in any direction. Thus, in the normal gravity environment, flame behavior and extinction mechanisms cannot be studied in relative flow velocities below approximately 20 cm/sec.

Flame spreading and flammability studies in flow velocities that are smaller than this, i.e., the same order as the diffusional velocities, provide additional insight into the mechanisms that control flame spread rates and the mechanisms that cause flame extinction. Already, the small amount of existing data on flow effects on flame spreading obtained in microgravity experiments and modeling has revealed the existence of an extinction mechanism that could not be anticipated by extrapolations from normal-gravity data. In low-speed flows, radiative emissions from the fuel surface and from the flame become sufficiently large compared to the rate of heat release from the flame that, 1) can achieve a steady length and spread rate in concurrent flows, rather than the acceleratory growth normally observed in normal gravity upward burning, and, 2) can be extinguished because of the radiative losses, rather than through diminished reactant residence time in the flame to which normal-gravity upward burning flammability limits are attributed.

We are developing a space experiment (references 1–12) for flight aboard the *International Space Station* attempting to validate the theoretical prediction of the flammability boundary for a thin combustive solid in low-speed, forced-concurrent flow. In the Solid Fuel Inflammability Boundary at Low Speed experiment, or SIBALS, a sequence of variations in atmospheric oxygen percentage and flow velocity will be used to determine the flammability boundary. In addition, diagnostic measurements of flow parameters,

¹Thus in normal gravity burning of vertical surfaces, buoyancy induces opposed flow in downward burning and concurrent flow in upward burning.

temperatures, gas-phase chemical species and radiant emissions will be used to determine the structure of the spreading flame as it approaches the flammability boundary.

The typical way of determining the flammability boundary for a material is a tedious process involving a number of tests to map the go/no-go conditions. In light of the volume and stowage limitations of spacecraft, we have developed a novel flammability test device which facilitates the proposed experiment. A schematic of the SIBALS experiment is shown in figure 5-1 in which illustrates that by dispensing the thin solid fuel from a spooled source at a rate equal to the rate of fuel consumption in the flame, the flame can be rendered stationary with respect to the experiment apparatus and the array of diagnostic devices needed to record the flame structure. The fuel is guided through the length of a flow duct complete with appropriate flow conditioning devices. In a single run, several combinations of atmospheric oxygen content and flow velocity can be imposed upon an existing flame until one of these parameters falls outside the locus of flammable conditions.

Some important aspects in the design of such an experiment include the length of the flow duct needed to express the entire flame length without interference from artificial heat losses either to the upstream flow conditioning devices or the downstream duct exit, where the incoming fuel begins heating. Additionally, establishing the existence of test conditions under which a steady flame length and propagation speed can be reached could provide added confidence that the required diagnostic devices can function sequentially yet observe an unchanging flame.

The Forced Flow Flame spreading Test (FFFT) was conceived as part of the SIBALS experiment for the purpose of providing preliminary observations of steady flame propagation in low speed flows, then, provided that quasi-steady flames could be achieved, providing some estimate of the flame size, luminosity and temperatures for use in the design of the SIBALS experiment. The FFFT was built to operate inside the Middeck Glovebox Facility, (MGBX) which was designed to provide electrical power, circulating air that is filtered and cooled, photographic capabilities, and a degree of isolation between the operating experiment and the crew member.

The FFFT glovebox experiment hardware, shown in figure 5-2, consists primarily of 16 fuel-sample assemblies (2 examples shown) and 2 low-speed wind tunnel modules. The modules have a flow cross-section of 7 cm by 10 cm and a 17 cm test section length, with the flow drawn (pulled) by a small fan through the test section at speeds of between approximately 1 and 8 cm/sec. Because the air flow velocity was considered such a crucial parameter in the data return from the FFFT, a special low-speed flow anemometer device was fashioned and installed upstream of the test section to measure the air flow directly and avoid relying upon a secondary measurement. The test section was isolated from the surroundings by metal walls with polycarbonate windows and small-mesh metallic screens at the inlet and outlet cross sections for flow conditioning, heat absorption and particulate capture. The windows were arranged for imaging flames in each of two orthogonal directions; the front window also contained displays of thermocouple temperatures and an image of the low-speed flow anemometer.

The fuel sample assemblies consisted of steel cards to which the fuel was mounted, electrical wiring for the fuel ignitor, thermocouple wire pairs and, in some cases, a fuel heater element. A total of 16 fuel samples were flown. Of the 16 samples, 11 were flat samples of an ashless filter paper. The flat samples (an example is shown in fig. 5-3) were taped to the steel cards using a kapton tape. Ignition was planned using

an electrically heated wire. To explore the influence of thermocouples on flames in low-speed flows near the predicted flammability limit, thermocouples were arrayed in two different configurations in the flat samples and, as a reference, in some cases omitted entirely. The thermocouples were intentionally configured asymmetrically to avoid missing an influence of their presence due to a symmetrical interference.

The remaining five samples were cylinders of cast cellulose prepared from a slurry of ground paper. The cylinders were cast around small electrical heater rods (an example is shown in fig. 5-4) used to raise the initial fuel temperature in a controlled way just before ignition. Because thermocouples are less likely to influence the slowly spreading flames over thicker fuels, the cylindrical samples were each instrumented with nearly identical thermocouple arrays.

The test matrix for the samples was arranged to obtain redundant observations for a limited number of test conditions. The flat samples were all essentially the same except for the individual thermocouple array configurations and were grouped to obtain observations at each of three air flow velocities. At each flow velocity, the effect of the different thermocouple arrays would be observed. The cylindrical samples were to be burned at the same three flow velocities, and a single velocity to be chosen during the flight for varying the initial fuel temperature.

The cylindrical samples were conceived as a method for controlling the temperature of a relatively thick fuel while keeping the amount of fuel to a minimum. From the standpoint of theory, the cylindrical samples also provide modelers a simplified fuel-surface and gas-phase radiation boundary condition, reducing their problem from three dimensions to two.

The flow anemometers in the two FFFT modules were each carefully calibrated. Mass flow controllers were used to measure total mass flow through the duct inlet and the indicated flow speed in the modules was set to the plug-flow velocity (i.e., uniform profile) corresponding to the reference mass-flow measurements and occurring at the entrance screen. Limited hot wire anemometry measurements were made at the test section centerline whose measurements corresponded to the peak velocity calculated using a viscous flow code model of the flow duct. Considerable effort, including DC-9 reduced gravity tests, were made to ensure that the flow calibrations were isolated from gravitational influences such as possible effects of the mass of the anemometer element.

The intent of this document is to provide a summary of the most important results of the FFFT experiment conducted during the USMP-3 mission and to discuss how these results can be used to better understand the flame spreading process and to improve the design concepts of the SIBALS project.

5.3 A SUMMARY OF THE USMP-3 MISSION ACTIVITY

During the USMP-3 mission, 10 flat samples of ashless filter paper and 5 cylindrical samples of cast cellulose were burned using concurrent flow speeds of 2 to 8 cm/sec. One of the flat samples did not ignite even with several attempts by the crew to do so. The ignitor of the failed sample was seen to clearly function in the video recording, but the sample was handled so much that a determination of the cause of the ignition failure could not be made. We note that this sample was stowed next to the flight sample that was inadvertently given to and burned by the crew during ground training at the Johnson Space Center (JSC) shortly before launch. The repaired sample and its neighbor were inspected before they were turned

over for the second time for flight, but no faults were detected. The refurbished fuel sample assembly burned normally in flight, and the refurbished FFFT module, damaged in the training incident, worked without flaw.

The 16 samples were grouped together in sets of 4, in most cases 3 flat samples and 1 cylindrical sample. The last group of four was reserved for test conditions to be determined during the flight. Each group of samples was to be burned in the same velocity air flow. Each group of three flat samples included one sample with no thermocouples, one with the six thermocouples each at a different distance from the fuel surface, and one with thermocouples arranged in a repeated pattern. After the first burns, the thermocouples were found to disrupt the progress of the flame and fuel-surface pyrolysis. With this clear demonstration made early, the astronaut crew was asked to bend most of the installed thermocouples away from the remaining flat samples, leaving one downstream near the end of each sample.

Before any samples were ignited the crew reported that the flow velocities indicated by the calibrated anemometers of both modules were quite high and independent of the FFFT fan control setting. The crew was asked to check, and reported that the glovebox air circulation was set to the lowest speed (or off) as specified in the procedures (since we were aware of the interaction between the air circulation system set at a high speed and the FFFT module anemometer). To compensate for the apparently high flow, the crew attached multiple sheets of first-aid gauze as a flow impedance over both module inlets where the anemometers are located, returning the anemometers to approximately nominal behavior. With testing after the mission both in the MGBX and with mass flow controllers used both in normal gravity and aboard the DC-9 aircraft, we determined that the high velocity indications were caused by flow from the glovebox air circulation fan impinging upon the FFFT inlet, and that the MGBX air circulation fan was working normally. Additional postflight calibrations (in normal gravity and in reduced-gravity aircraft tests, with and without the gauze the crew added to the module inlets) have also shown that the calibrations of the flow anemometers were not changed during the mission. Hence, the flow speed indications recorded in flight are still acceptable. The uncertainty introduced into the flight data interpretation because of the gauze is a slight reduction in the absolute pressure in the vicinity of the sample burning and some unquantifiable disturbance to the velocity distribution apparent in the latter portions of some of the flame-image sequences.

5.4 RESULTS

5.4.1 Flat Samples

Ten flat samples were burned successfully in concurrent flow air velocities of about 1 cm/sec to about 8 cm/sec. The detailed results of sample six are presented here as an example of the broader data set.

Figure 5-5 shows the data extracted from the video and film images of sample six in which the flame spread in the presence of approximately 1 cm/sec indicated air flow. The dark symbols are measurements taken from the video record of the fuel surface along a line parallel to the direction of flow and flame spreading, and show the behavior of the charring pyrolysis region of the fuel. These data provide some visualization of any transient response of the fuel to the flame and any thermal disturbances such as the thermocouples. These data began about 13 sec after the sample was ignited when the video image showed a distinct flame unaffected by the bright glare of the ignitor wire. By the time the pyrolysis region could be

tracked, its length had reached about 1.5 cm from which it varied by ± 0.1 cm until about 30 sec after ignition.

The clear symbols in figure 5-5 indicate the progress of the visible flame measured from a series of still photographs made from the perspective of the edge view of the flat paper sample. The first of these photographs was taken shortly after ignition when the flame, enhanced by the energy of the ignitor, had a length of about 2.2 cm. When the ignitor was switched off, the flame decreased in size until reaching approximately the same length as the pyrolysis region of the fuel surface, at about 13 sec. The change in flame length is associated with the energy deposition rate of the ignitor which is larger than the energy release from the flame. While the ignitor is energized, the fuel pyrolyzes at a greater rate than achievable by the flame alone. Hence, more vaporized fuel is available to the air stream and the resulting flame is longer.

Between about 13 and 30 sec after ignition, the flame and pyrolysis lengths are approximately the same. At 30 sec, the flame appears to accelerate. The video view of the fuel surface reveals that at that time, the fuel begins to burn asymmetrically. We have interpreted this asymmetry as being caused by a small flow disturbance caused, in turn, by the application of the medical gauze at the FFFT duct inlet. The apparent abrupt shortening of the flame and pyrolysis length, indicated at about 37 sec, is an artifact of the asymmetry effect on the flame tracking algorithm and is not physical.

Figure 5-6 shows a comparison between an image of the flame in FFFT test six and the results of the numerical simulation of concurrent flow flame spreading developed as part of the SIBALS project. The numerical model includes full Navier Stokes equations for low-speed flows and detailed estimations of gas-phase radiation for a gray absorbing, emitting and nonscattering medium. The simulation was specially modified to model the conditions expected in the FFFT experiment in particular by altering the boundary conditions to simulate the duct dimensions of the FFFT modules. Figure 5-6 shows the results of the simulation with the free-stream velocity of 1 cm/sec. Contours of the logarithm of the reaction rate, i.e., the disappearance rate of fuel mass, overlay the image from the FFFT test six. The curvature of the flame's blue region (the darker region in the monochrome image) matches that of the contour of 10^{-4} gm/cm³/sec, particularly near the flame's stagnation point or plane of symmetry. Reaction rate contours are sometimes used instead of temperatures for comparison with the visible flame, because the blue emissions from the flame are related to the population of excited intermediate species in the flame, which only exists in regions of higher chemical reactivity.

Figure 5-7 shows the temperature history of the single thermocouple that was in contact with the fuel surface near the downstream end of the fuel sample in test six. Between the time of ignition and approximately 53 sec thereafter, the fuel is slowly heated. At approximately 53 sec after ignition, the flame reaches the vicinity of the thermocouple raising the temperature in 3 to 4 sec to the pyrolysis temperature of about 720 K. While the fuel pyrolyzes and vaporizes, the temperature is approximately constant. Upon the completion of the fuel vaporization (fuel burnout) the thermocouple experiences gas phase temperatures. As the fuel burnout point and flame continue to propagate downstream, the thermocouple passes through the flame, experiencing the peak flame temperature that occurs in the plane of symmetry previously occupied by the fuel.

The pyrolysis and flame temperature shown in figure 5-7 are quite similar to earlier measurements obtained in drop tower tests and to the results of the numerical modeling. However, since the flame spread

was clearly affected by the thermocouple, the temporal distribution shown in figure 5-7 may not represent what would be predicted for unaffected spreading.

The flat samples burned in higher air velocities all seemed to grow throughout the test time or exhibited flame lengths that were as high as 8 cm. Because of the limitations in size imposed upon experiments in the glovebox facility, we cannot be certain that the growing flames were approaching what might eventually have been a steady length as the theory predicts. The flames in the lower air velocities, ie., about 1 to 3 cm/sec, appear to have achieved a steady length in about 13 to 15 sec. It is difficult to claim, however, that the entire flame/fuel system had reached a steady configuration because residual, and much slower, transients could still be possible in the fuel induced by the energetic ignition phenomena. We would require that the flame traverse at least two times the pyrolysis length after achieving a steady flame length in order to be confident that the solid fuel transients had been dissipated. However, we interpret the observed flame length, and its successful comparison to the theory, to be supportive of the theoretical results.

5.4.2 Cylindrical Samples

Five cylindrical samples were burned successfully in concurrent flow air velocities of about 2 cm/sec to about 8 cm/sec. Figure 5-8 shows a summary of the lengths of the flames spreading over the samples in varying flow velocities at a fixed initial fuel temperature and varying initial fuel temperature with a single fixed-flow velocity. These data were obtained from the results of the 35-mm film camera, the framing rate of which was adjusted to attempt to capture the flame over the duration of the experiment. The experiment conducted at 5 cm/sec and 100 °C was the first FFFT cylinder burned, and the framing rate was too high (based upon our premission guess of the spread rate) to capture the entire experiment. After the first experiment with cylindrical samples, the framing rates were adjusted, hence the data from other samples are more complete.

The solid plotting symbols show flame length variations with time for samples burned with an initial fuel temperature of 100 °C, but with varying flow velocity. During the observation time available, the flame grew for samples burning in air flow velocities of 5 and 8 cm/sec. However, in a flow velocity of 2 cm/sec, the flame reached an approximately steady length after about 45 to 50 sec, and maintained this length for the remainder of the observable test time.

The hollow plotting symbols show flame length variations with time for samples burned at a fixed air flow velocity of 2 cm/sec, but with variations in initial fuel temperature. For the sample preheated to an initial temperature of 125 °C, the flame grew for the entire observable test time. The sample heated to only 75 °C, rendered a flame that reached a peak length at about 40 sec, then began to shrink. The sample at 100 °C, as we have already observed, exhibited an apparently steady flame length.

These results are to be quite useful for the future development of theoretical simulations of cylindrical fuel sample burning. They include a possible spreading regime transition, based on flow velocity, between large and growing flames at higher flow velocities and steady spreading at lower flow velocities. Similarly, a possible regime transition, based on the initial fuel temperature, may have been observed between growing, steady and shrinking flames. This interpretation of the data is subject to the limitation discussed earlier that steadiness is not assured until the flame has spread far from the ignition region because of transitory effects on the solid fuel.

In the final burning of cylindrical samples, the crew accepted our request to shut off the air flow in the FFFT module just before the flame reached the end of the fuel sample. Upon stopping the air flow, the flame very quickly shrank and quenched, providing a dramatic demonstration of the flow effects on fuel flammability in microgravity.

5.5 CONCLUSIONS

The FFFT experiment conducted aboard the USMP-3 mission was considered quite successful, providing some data that can be compared directly to the results of theoretical predictions. Perhaps more importantly, the results are quite useful for the preparations of the more complete experimental effort planned for the Space Station era.

For the flat fuel samples, the results indicate that the theoretical predictions of the flame structure, as evidenced by the observed flame length, are quite reasonable for the low-velocity portion of the test matrix. The flames at higher flow velocities grew too large for a reasonable comparison because of the size limitations of the glovebox. Flame length is not nearly complete, however, in terms of the requirements for verifying the numerical simulation. More detailed diagnostics, such as gas-phase species measurements, are needed and are planned for the SIBALS experiment.

The FFFT module duct is too short to capture the behavior of flames spreading in air flow velocities above about 2 to 3 cm/sec. Together with the confidence obtained in the numerical simulation, this information will refine the design of the flow duct for the SIBALS experiment.

The obvious effect of the thermocouples on the progress of the flames spreading over the thin fuel samples provides a cautionary note to the design of thin fuel experiments. We believe that these effects are the most prominent for test conditions where the flame spreads quickly. Where the flame spreads more slowly, the transient influence of the thermocouples may not be so pronounced.

The cylindrical fuel sample data have provided benchmark data for the development of numerical simulations. This configuration might be a more fundamental configuration than the flat sample case because of the simplification in the radiation modeling that is obtained from the inherently two-dimensional axisymmetric geometry. The apparent transition between growing, steady and shrinking flames that have been observed provide a challenge to the theory to reproduce.

REFERENCES

1. Frey, A.E.; and T'ien, J.S.: "Near-Limit Flame Spread Over Paper Samples, *Combustion and Flame*," Vol. 26, p.257–267, 1976.
2. Frey, A.E.; and T'ien, J.S.: "AA Theory of Flame Spread over a Solid Fuel Including Finite-Rate Chemical Kinetics, *Combustion and Flame*," Vol., 36, p. 263–289, 1979.
3. Altenkirch, R.A.; Eichhorn, R.; and Shang, P.C.: "Buoyancy Effects on Flames Spreading Down Thermally-Thin Fuels," *Combustion and Flame*, Vol. 37, p.71, 1980.
4. T'ien, J.S.: "Diffusion Flame Extinction at Small Stretch Rates: The Mechanism of Radiative Loss," *Combustion and Flame*, Vol. 65, pp. 31–34, 1986.
5. Olson, S.L.; Ferkul, P.V.; and T'ien, J.S.: "Near-Limit Flame Spread Over a Thin Solid Fuel in Microgravity," Twenty-Second Symposium (International) on Combustion, pp. 1213–1222, The Combustion Institute, 1988.
6. Vedha-Nayagam, M.; and Altenkirch, R.A.: "Gravitational Effects on Flames Spreading over Thick Solid Surfaces, *Acta Astronautica*, Vol. 12, No. 7/8, pp. 565–572, 1985.
7. Bhattacharjee, S.; Altenkirch, R.A.; and Sacksteder, K.R.: "Implications of Spread Rate and Temperature Measurements in Flame Spread Over a Thin Fuel in a Quiescent, Microgravity, Space-Based Environment," *Combustion Science and Technology*, Vol. 91, Nos. 4 to 6, pp. 225, 1993.
8. Bhattacharjee, S.; Altenkirch, R.A.; and Sacksteder, K.R.: "The Effect of Ambient Pressure on Flame Spread Over Thin Cellulosic Fuel in a Quiescent, Microgravity Environment," *Journal of Heat Transfer*, Vol. 118, pp. 181–190, 1994.
9. Ramachandra, P.A.; Altenkirch, R.A.; Bhattacharjee, S.; Tang, L.; Sacksteder, K.R.; and Wolverton, M.K.: "The Behavior of Flames Spreading Over Thin Solids in Microgravity," Twenty-Fifth Symposium (International) on Combustion, *Combustion and Flame*, Vol. 100, pp. 71–84, 1995.
10. West, J.; Tang, L.; Altenkirch, R.A.; Bhattacharjee, S.; Sacksteder, K.R.; and Delichatsios, M.: "Quiescent Flame Spread Over Thick Fuels in Microgravity," Twenty-Sixth Symposium (International) on Combustion, The Combustion Institute, 1996.

11. Sacksteder, K.R.; and T'ien, J.S.: "Buoyant Downward Diffusion Flame Spread and Extinction in Partial-Gravity Accelerations," Twenty-Fifth Symposium (International) on Combustion, pp. 1685–1692, The Combustion Institute, 1994.
12. Sacksteder, K.R.: "The Implications of Experimentally Controlled Gravitational Accelerations for Combustion Science," Twenty-Third Symposium (International) on Combustion, the Combustion Institute, pp. 1589–1596, 1990.

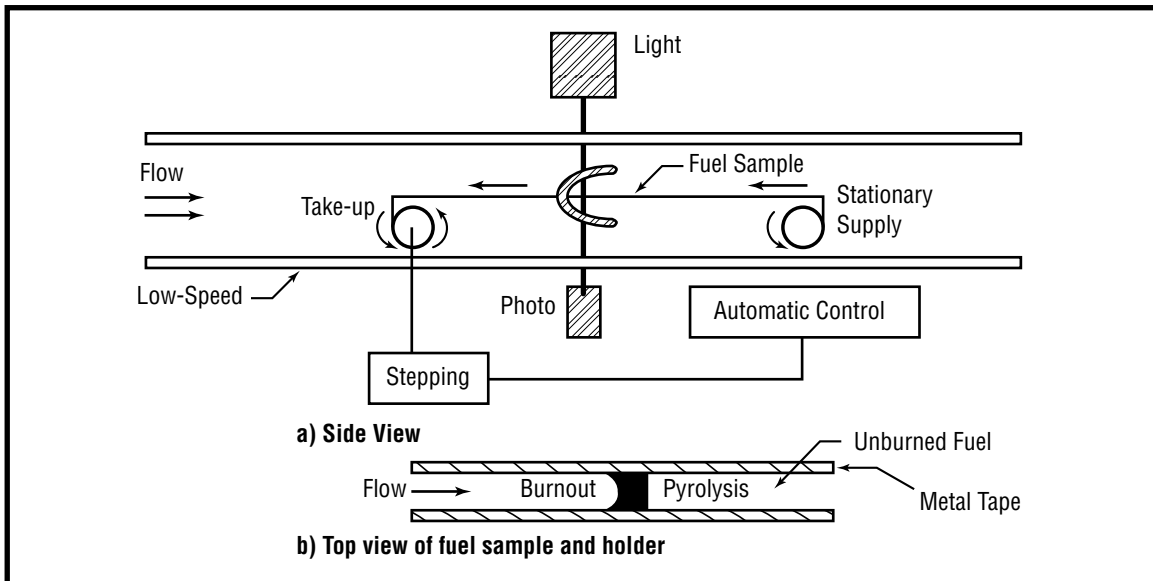


Figure 5-1. Schematic concept of the SIBALS experiment concept.

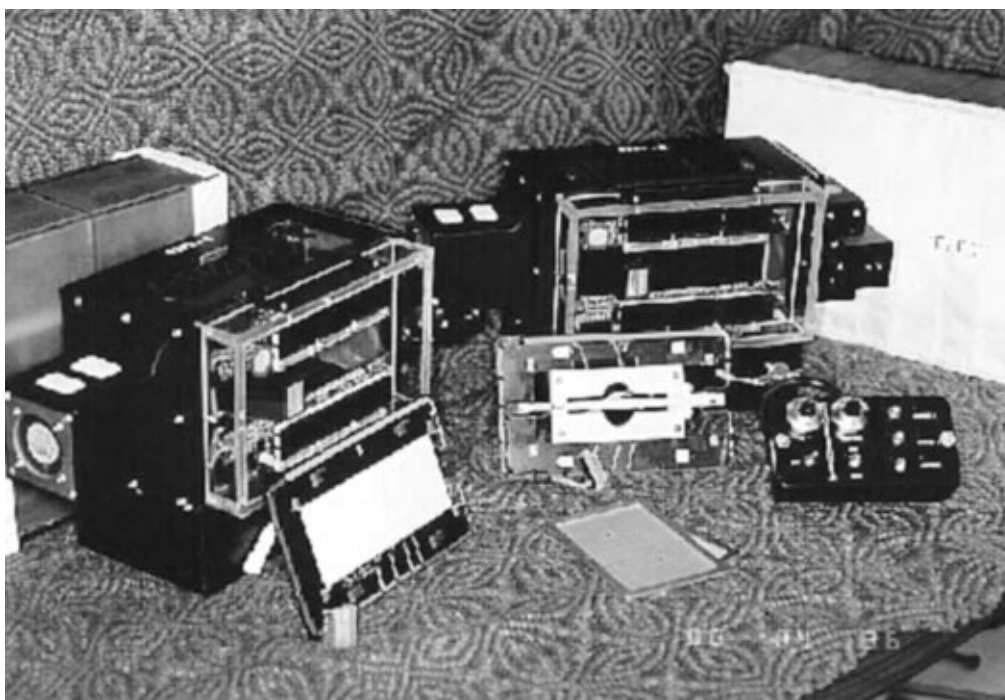


Figure 5-2. Forced Flow Flame Spread Test (FFFT) Flight hardware including the 2 FFFT wind-tunnel modules, 1 of 11 flat samples, 1 of 5 cylindrical samples, 2 of the 16 exit screens and the FFFT control box.

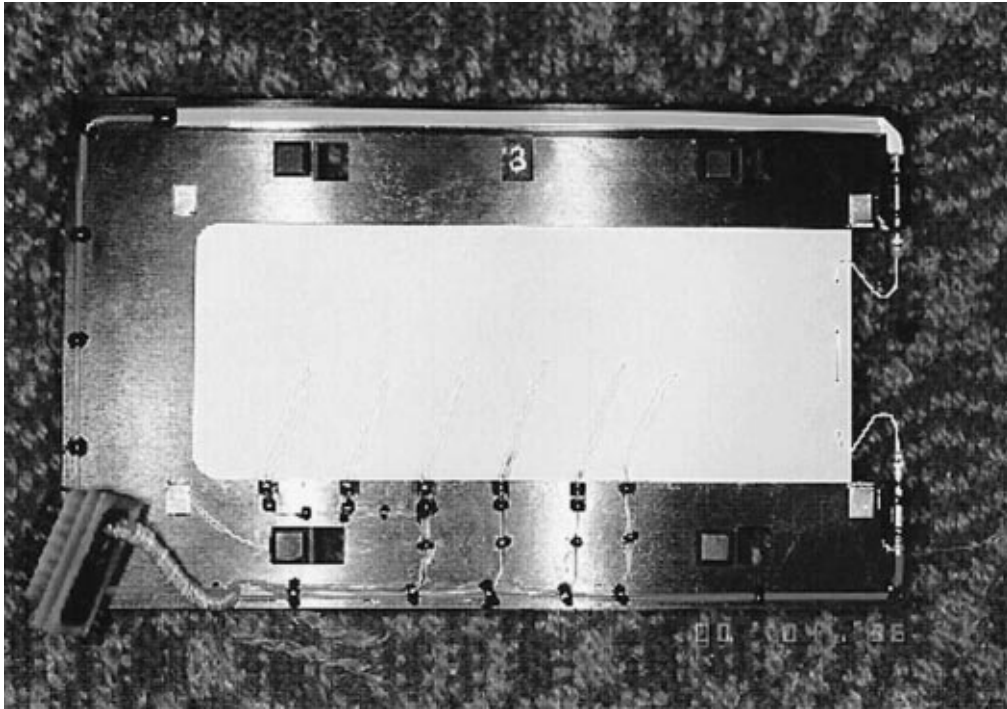


Figure 5-3. FFFT Flat cellulose sample. Ignitor wire is shown on the right end of the sample and the thermocouple array is positioned along the sample centerline. During combustion the air flows from right to left to obtain concurrent flow flame spreading.

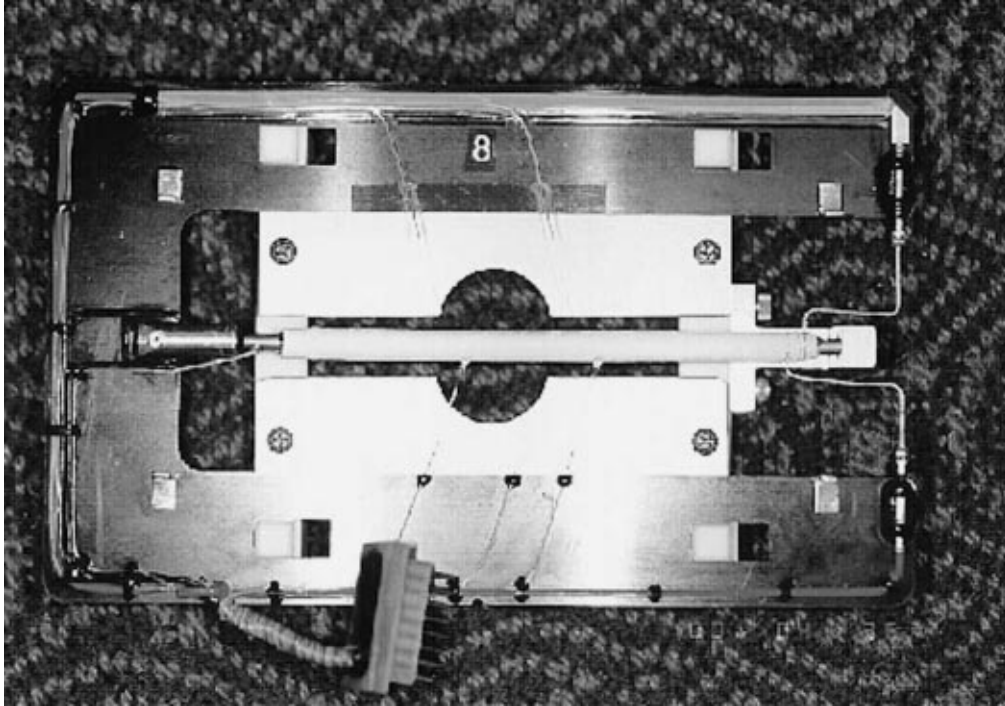


Figure 5-4. FFFT cylindrical cellulose sample. Fuel materials is cast over a cylindrical heater rod. Ignitor wire is located on right hand end of fuel sample and thermocouple array positioned in the plane of the sample mounting card. During combustion the airflow is from right to left to obtain concurrent flow flame spreading.

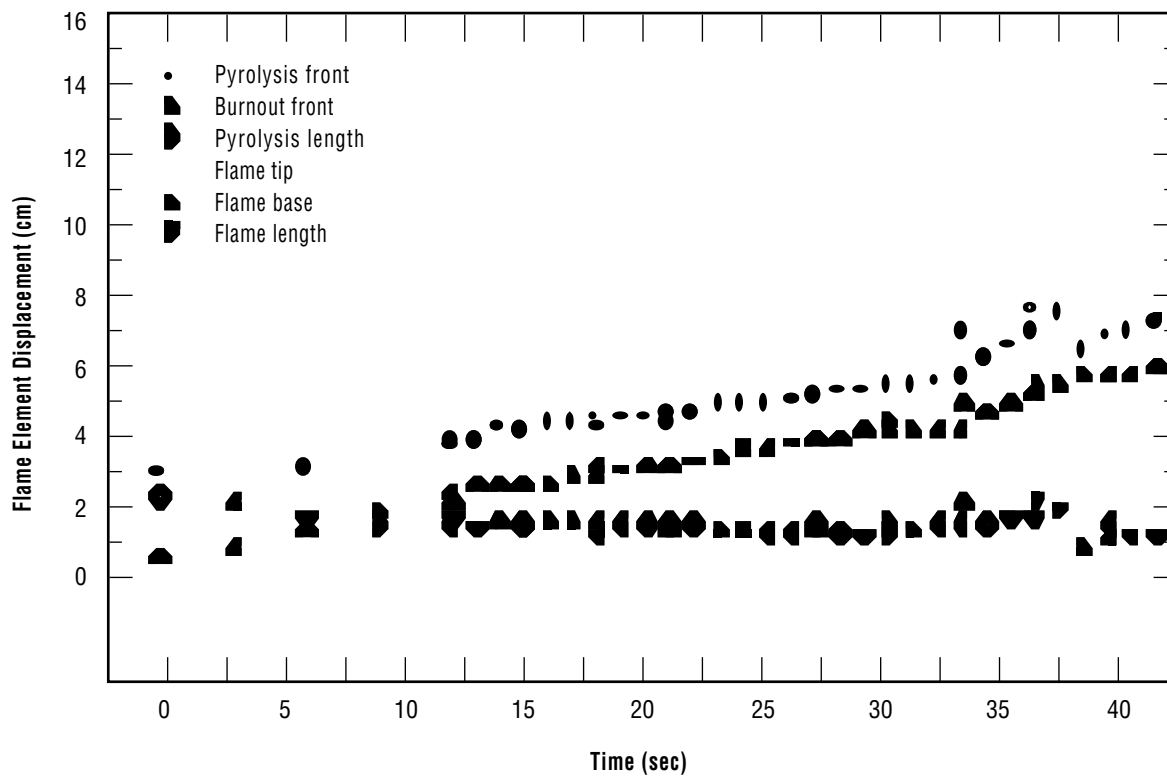


Figure 5-5. Position of flame features versus time during the burn of FFFT sample six, ashless filter paper, burning in air at normal pressure at approximately 1 cm/sec.

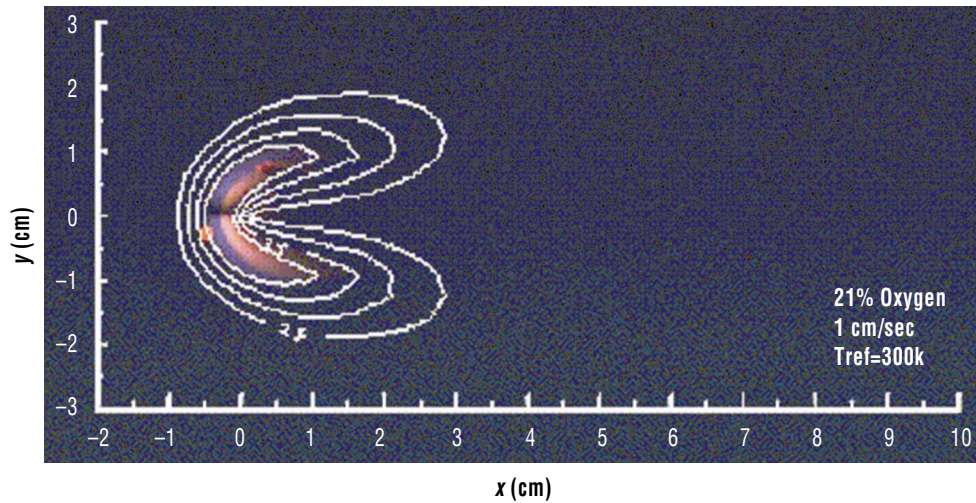


Figure 5-6. Comparison of a flame image from FFTT test six with reaction rate contours from the numerical simulation of concurrent-flow flame spreading.

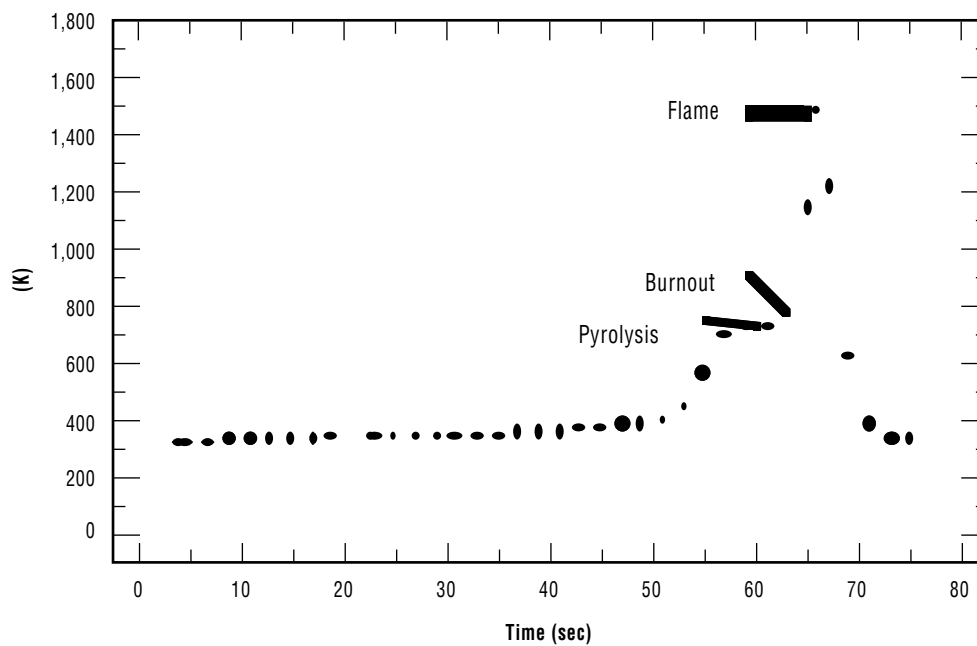


Figure 5-7. Time history of temperature at a point on the fuel surface for a flame spreading over ashless filter paper in a purely forced concurrent flow of 21 percent oxygen/79 percent nitrogen in an indicated free stream velocity of approximately 1 cm/sec.

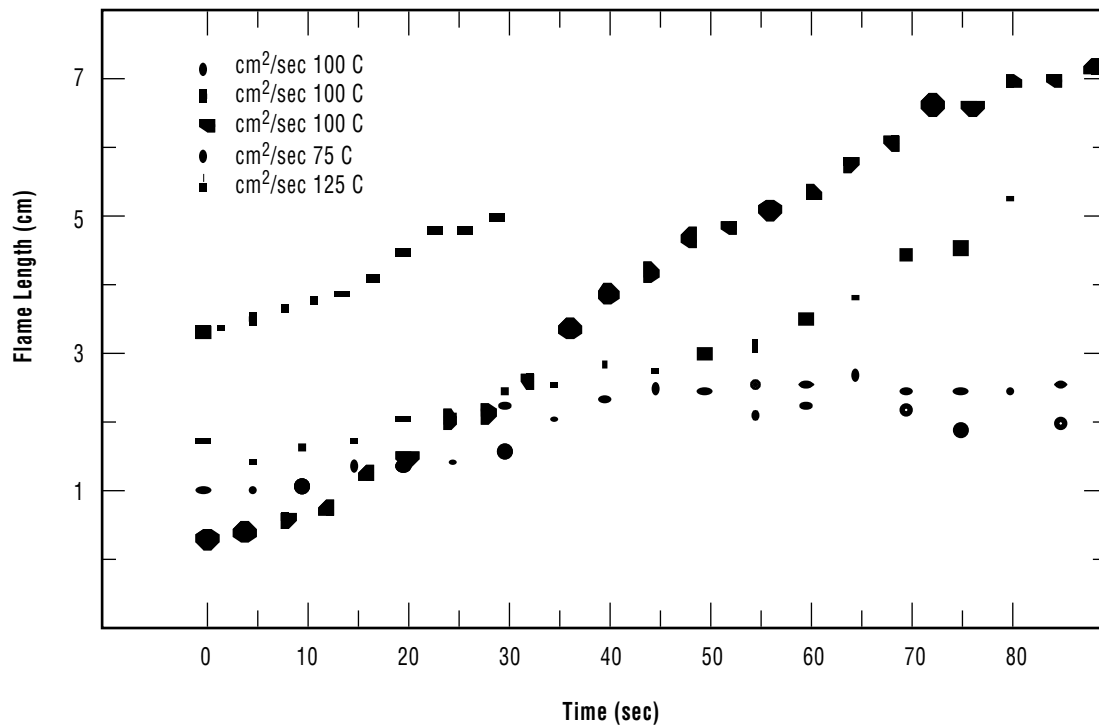


Figure 5-8. Comparison of a flame lengths for FFFT cylindrical samples in various air flow velocities and initial fuel temperatures.

SECTION VI.

RADIATIVE IGNITION AND TRANSITION TO SPREAD INVESTIGATION (RITSI)

Acknowledgment

This work is funded by the NASA Microgravity Science Program under the Interagency Agreement No. C-32001-R.

RADIATIVE IGNITION AND TRANSITION TO SPREAD INVESTIGATION (RITSI)

Takashi Kashiwagi

Building & Fire Research Laboratory
NIST

Gaithersburg, MD 20899

Phone: 301-975-6699

Fax: 301-975-4052

E-mail: takashi.kashiwagi@nist.gov

Sandra L. Olson

Lewis Research Center

NASA

Cleveland, OH 44135

Phone: 216-433-2859

Fax: 216-433-8660

E-mail: sandra.olson@lerc.nasa.gov

6.1 ABSTRACT

Twenty-five experiments were conducted in the glovebox facility on the USMP-3 mission to study the behavior of both flaming and smoldering ignition events, the transition from ignition to flame/smoldering spread, and the flame/smoldering growth patterns in air. Twenty-one of the 25 experiments were flaming and the remainder were smoldering. Ignition was initiated by a heated wire across a thermally thin filter paper in the middle of the sample for the two-dimensional configuration and by a focused beam from a halogen/tungsten lamp at the center of the sample for the three-dimensional configuration. The external air flow velocity was varied from 0 cm/sec to 6.5 cm/sec. The ignition and subsequent flame spread events were recorded by a video camera, a 35-mm camera, and six thermocouples (two in the gas phase and four in the sample). The results indicate that nonpiloted radiative ignition of the paper by external thermal radiation tends to occur more easily than in normal gravity. In the two-dimensional configuration, the transition from ignition to downstream flame spread never occurred; only the transition to upstream spread took place. In the three-dimensional configuration, a char growth pattern emerged in the shape of a fan, with the ignited area as the center of the fan and the fan spreading in the upstream direction. The internal angle of the fan increased with an increase in external flow velocity (higher flow velocity gave a more opened fan pattern). At an external flow velocity of 5 cm/sec, the flame was horseshoe-shaped and the char pattern became an elongated semicircle toward upstream. It appears that the peak upstream flame spread rate was reached at a higher external velocity than for the two-dimensional flame front. Flame spread occurred much faster along open edges of the sample paper than along the sample face, presumably due to there being a larger supply of oxygen and energy feedback at the open edges than at the surface. These results indicate the possible importance of the effect of the flame front shape such as the curvature of the flame front on spread rate and flame strength. A complex, unexpected finger-shaped char growth pattern was observed during the smoldering experiment. Higher external flow velocity increased the number of localized smoldering fronts, of the char fingers they left behind, and frequency of bifurcations from the fingers. At present, it is not clear what caused such a complex char growth pattern.

6.2 INTRODUCTION

Ignition of solid fuels by external thermal radiation and subsequent transition to flame spread are processes that not only are of considerable scientific interest but which also have fire safety applications. The fire safety strategy in a spacecraft is, 1) to detect any fire as early as possible, 2) to keep any fire as small as possible, and 3) to extinguish any fire as quickly as possible.^{1,2} This suggests that a material which undergoes a momentary ignition might be tolerable, but a material which permits a transition to subsequent flame spread would significantly increase the fire hazard in a spacecraft. If the transition does not take place, then by definition flame spread does not occur. Therefore, the limiting condition under which flame cannot spread should be calculated from a model of the transition from ignition instead of by the traditional approach based on limits to a steady flame spread model. However, although the fundamental processes involved in ignition have been suggested,^{3,4,5,6} there have been no definitive experimental or modeling studies due to the flow motion generated by buoyancy near the heated sample surface. One must solve the time-dependent Navier-Stokes equations over an extended region to represent the highly unstable buoyant plume accurately. It is especially important to provide correct far-field boundary conditions, particularly velocities. This is also important during the transition period from ignition to flame spread but there has been little previous work on this transition.

Almost all previous works have studied ignition and flame spreading separately,^{7,8} In order to avoid the specification of the boundary conditions, previous detailed radiative ignition models were assumed to be one-dimensional^{9,10,11} or were applied at a stagnation point.¹² The mismatch between experimental and calculated geometries in normal gravity means that theories cannot be compared directly with experimental results except for specific configurations under which the plume is not formed. In previous flame spread studies, time-dependent flame spread models are limited to upward flame spread over a vertically oriented material surface in normal gravity and is generally assumed to be two-dimensional. Almost all detailed flame spread models^{7,8,13} were based on the steady-state flame spread rate and, as far as we are aware, there are no previous studies of three-dimensional time-dependent flame spread which is initiated from a small, localized ignited area. This scenario is most common in real fires. The mechanism of the transition from ignition to flame spread also controls the extinction limit of flame spread, which is affected by the flame history, starting at ignition. Since this is an inherently transient process, conventional approaches analyzing the steady-state flame spread near its extinction limit cannot truly reveal the dynamic aspects of the transition. Modeling of the transition from ignition to flame spread is extremely difficult in a normal gravity environment. Thus, the study of localized ignition and the subsequent transition to flame spread in a three-dimensional configuration in a microgravity environment is needed to obtain new information for understanding transition mechanisms.

Smoldering (nonflaming glowing combustion) is one of the common modes of initiation of fires; it might provide potentially hazardous conditions due to its high CO yield, but there are only a limited number of studies available. Therefore, its detailed mechanism is not fully understood. Although the heat release rate from smoldering is smaller than that from flaming, the temperature of the smoldering front is as high as 800 °C or more and the induced buoyant flow from the high temperature smoldering front cannot be neglected in normal gravity. The induced buoyant flow makes it extremely difficult to quantify

and control the supply rate of oxygen to the smoldering front in normal gravity. Since the supply of oxygen to the smoldering front is one of the critical parameters which controls smoldering spread rate, it is extremely difficult to predict the effects of slow external flow on smoldering behavior and its spread rate over a cellulosic surface.

6.2.1 Experimental Objectives

The RITSI experiment was designed to obtain test data on the following phenomena:

1. Observe and measure the effects of low external flow velocity similar to ventilation velocities in a spacecraft on flaming ignition, transition, and flame growth pattern over a thin cellulosic paper surface in the two-dimensional configuration and also in the three-dimensional configuration.
2. Observe and measure flame spread along open edges and corner of thin paper at different external low flow velocities.
3. Observe and measure the effects of low external flow velocity on the growth pattern of smoldering from localized smoldering ignition.

To make these observations, 15 experiments were planned with an additional 10 samples if added experimental time became available. Fortunately, all 25 tests could be conducted over 3 days; the test conditions are listed in table 6-1. Fifteen tests were conducted for item No. 1, six tests were for item No. 2 and four tests were for item No. 3.

6.2.2 Experimental Hardware and Operations

RITSI USMP-3 glovebox experiment hardware, shown in figure 6-1, consists of 2 experimental modules, a control box, a display box, and 2 parts boxes, which house the 15 individual sample boxes and other miscellaneous supplies, including 10 additional fuel samples. One sample box is shown opened to reveal the sample card, product filter, and cleaning supplies (not visible) stowed inside. The small external control box (which attaches to the outside of the glovebox front door) include fan on/off and variable speed control, ignitor wire activation radiant heater activation and variable power adjustment, and chamber light on/off switch.

Each experimental module, shown schematically in figure 6-2, uses a small fan to generate a low flow velocity of up to 6.5 cm/sec through the test section. The test section was 85-mm wide by 95-mm high by 171-mm long. The transparent lid of the duct opens for access to change sample cards. A filter downstream of the combustion event collects particulates and other combustion products.

A near-infrared tungsten/halogen radiant heater is used to ignite most samples, and is recessed into the back wall of the duct to minimize disturbances to the flow, also shown schematically in figure 6-2. The power to the lamp was measured during each test. The lamp automatically deactivated at a preset time. The emission spectrum of the lamp was measured from 2 to 20 μm using an FTIR.

A sample card is shown in figure 6-3. A 10 cm by 8.7 cm sheet of Whatman 44¹ ashless filter paper was used as the sample. The center part of the sheet over the irradiated area was blackened to increase absorption of the incident beam from the lamp. The absorptivity of the blackened paper was measured by the NIST radiometric group between 1 and 20 μm . The samples were ignited at a central location either by the focused beam from the lamp (three-dimensional configuration) or along a line by a heated wire to observe planar flame growth (two-dimensional configuration). A few samples were doped with a smolder promoting agent, potassium acetate, to study smolder propagation from a central ignition point. Six 0.05-mm-diameter type K thermocouples and an ignitor wire (30-gauge Kanthal wire) were preinstalled across the sample on each sample holder. Four thermocouples were installed in the sample at the center, 2 cm and 4 cm downstream from the center and at 2 cm upstream. Two thermocouples were installed at 2 mm above the sample surface at 2 cm upstream and also downstream locations from the center. The thermocouple data were recorded along with radiant heater power, ignitor power, and flow velocity.

Color video pictures were taken in the direction normal to the sample surface to view changes in the flame shape and char pattern. Red diodes were used to illuminate the sample surface. Still color photographs were taken at an oblique angle to the sample by a motor-driven 35 mm camera. The flaming tests require the use of a blue transmitting/red blocking top window to observe the dim flame through the near-infrared lamp light being scattered by the smoke, in addition to the red LED light being scattered. A window transmissive throughout the visible was used to image the smoke patterns for the smoldering tests.

The test matrix is given in table 6-1. The first 15 tests were instrumented with thermocouples; the last 10 were assembled in orbit without thermocouples using the spare sample materials flown.

¹Certain company products are mentioned in the text in order to specify adequately the experimental procedure and equipment used. In no case does such identification imply recommendation or endorsement by the National Institute of Standards and Technology and NASA, nor does it imply that the products are necessarily the best available for the purpose.

6.3 TEST RESULTS AND DISCUSSION

6.3.1 Ignition

Ignition was achieved in almost all tests using either a heated wire or a lamp. Since radiative ignition was not achieved with the same system in normal gravity, it was initially planned that a heated wire above the irradiated sample surface would be used as a pilot during the lamp irradiation if ignition was not achieved in the first radiative ignition test without the heated wire. Surprisingly, however, ignition was achieved without using a heated wire in the first test, and all tests in the three-dimensional configuration were ignited by the lamp alone. It appears that in normal gravity, hot combustible degradation products were cooled and swept away from the hot irradiated surface due to buoyancy induced flow and nonpiloted ignition was thus difficult to achieve in normal gravity. In microgravity, however, the hot combustible degradation products tended to stay near the irradiated surface (expansion and diffusion are the only mechanisms which cool and slowly move the products away from the irradiated area) and nonpiloted ignition (self-induced pilot from the hot irradiated surface) tended to occur compared to the case in normal gravity. Radiative ignition by the lamp was quite reproducible and preliminary results show that the ignition delay time (a little over 4 sec after the ignition switch was turned on) was nearly constant in the range of flow velocities used in this study. This ignition delay time included about 2.2 sec from power-on to a point where the output of the lamp reached the designated flux. Ignition by a heated wire was less reproducible than that by the lamp due to changes in wire contact with the sample caused by the expansion of the wire after it heated. Ignition tended to occur at one face of the sample surface at first followed by the second ignition on the other face of the sample surface.

6.3.2 Transition and Growth of Flame and Char Pattern

6.3.2.1 Two-dimensional Configuration

Four tests were conducted at the external flow velocities of 0, 2, and 5 cm/sec. The behavior of the flame from the side view parallel to the paper sample is shown in figure 6-4 for the three different flow velocities at three different stages: ignition, transition to flame spread, and fully developed flame spread. At ignition, figures 6-4a, 6-4d, and 6-4g, a blue flame appeared only over one face of the sample surface due to the contact condition of the expanded heated wire with the sample as discussed above. In the quiescent condition, figure 4a, an orange glow appeared over the other face of the sample surface. This glow was caused by the scattered light from the glowing heated wire by degradation products from the paper sample; it was not flame. This glow died and only the bottom side of the flame persisted, as shown in figure 6-4b. Nevertheless, a much fainter scattered vapor cloud can still be seen in this figure. At the later stage, figure 6-4c, the bottom flame disappeared leaving a faint vapor cloud similar to that over the other face of the sample surface; the transition from ignition to flame spread did not occur. These clouds indicate that there might be enough combustible degradation products in the gas phase close to the heated wire to ignite, but it appears that oxygen supply was not sufficient to yield ignition. At 2 cm/sec and 5 cm/sec, flames appeared on both sides of the sample surface and the flames continued to spread upstream to the end of the sample. This observation suggests that flames over both sides of the sample surfaces might be needed for the

transition to flame spread and the supply of oxygen appears to be the rate-controlling process to transition to flame spread. The observed upstream flame spread has been predicted in our theoretical calculation¹⁴ and the overall shape of the spreading flame calculated in this reference is very similar to that seen in these figures. The flame became longer with an increase in the external flow velocity, and the color of the flames remained blue in the range of the flow velocities used in this study.

Selected video pictures normal to the sample surface in the two-dimensional configuration are shown in figure 6-5. Since the blue color of the flames was faint, only the growth pattern of the char layers (faint dark color) can be seen in these figures. Careful observation reveals that a spreading blue flame front was several millimeters ahead of the char front. This is also confirmed by an earlier temperature increase (2 mm above the sample surface) above that of the temperature increase in the sample at a location 2 cm upstream from the center of the irradiated area, as shown in figure 6-6. The figure shows a rapid sample temperature increase at the center of the irradiated area up to about 450 °C; it stayed at this temperature even when the lamp was turned off at about 6 sec. After about 8 sec, this temperature started to increase gradually up to almost 700 °C, presumably due to glowing (smoldering) of the char. The increase in sample temperature at two downstream locations (2 cm and 4 cm from the irradiated center) occurred at an earlier time than that at 2 cm in the upstream, but its rate of increase in the downstream location was much less than that in the upstream location. This indicates that hot combustion products were swept downstream shortly after the onset of ignition, but the sample temperature at the 2-cm downstream location was not high enough (only up to about 200 °C until 10 sec and later up to about 250 °C) to generate char. Even the gas phase temperature at 2 mm from the surface at the 2-cm downstream location went up to only about 400 °C compared to above 800 °C at the 2-cm upstream location. At the 4-cm downstream location, the sample temperature increases up to only about 150 °C. It is expected that at least 300 °C is needed to form char for this sample.¹⁵ Therefore, the char layer growth was observed only in the upstream side at 2 and 5 cm/sec flow velocities. With the measured sample temperature history during the approaching flame front (fitting with a linear temperature increase with time), the net energy feedback rate (total feedback rate minus radiative/convective losses from the sample surface) from the upstream spreading flame front to the sample at the 2-cm upstream position and also those from hot combustion products flow at 2-cm and 4-cm downstream locations were calculated. In the calculation it was assumed that the sample was thermally thin and the flame and the flow were symmetric about the sample; the net energy feedback rate from the upstream flame is $3.3 \text{ W/cm}^2 \pm 10 \text{ percent}$ for each surface (top and bottom), from the hot products flow at the 2-cm downstream location is $0.6 \text{ W/cm}^2 \pm 10 \text{ percent}$ for each surface and that at the 4-cm downstream location is $0.2 \text{ W/cm}^2 \pm 10 \text{ percent}$ for each surface.

Since the flame was faint and hard to see clearly in the recorded videos, the growth of the char patterns shown in figure 6-5 was used to calculate char spread rate. As the distance between the spreading char front and traveling flame front appeared to be nearly constant, it was assumed that the char spread rate was the same as flame spread rate. The position of the char front spreading toward upstream was measured at different times for the external flow velocities of 2 cm/sec and 5 cm/sec; the results are plotted in figure 6-7. As shown in this figure and discussed above, the flame hardly spread when only one side of the sample was ignited. After the second ignition at the side opposite from the first ignition, the flames started to spread. At 2 cm/sec, it appears that char spread at an apparently steady rate shortly after the second ignition but at 5 cm/sec, initially char spread slowly and then reached the apparently steady rate. Both apparently steady char spread rates are about the same; they were $0.11 \pm 0.01 \text{ cm/sec}$. Since the char spread rate for the case of 5 cm/sec appears to increase with an increase in distance from the ignited area, as shown in figure 6-7, some caution is needed for the spread value at an external flow velocity of 5 cm/sec.

6.3.2.2 Three-dimensional Configuration

Although flaming ignition was observed in the quiescent condition, transition to flame spread did not occur. However, that transition did occur at external flow velocities of 0.5 cm/sec, 1 cm/sec, 2 cm/sec, 3.5 cm/sec, 5 cm/sec and 6.5 cm/sec. The growth patterns of flame for the 0.5 cm/sec, 2 cm/sec, and 6.5 cm/sec cases are shown in figure 6-8. These pictures were taken by a 35-mm camera looking downward at an oblique angle. The color of the flames was blue during the experiments, similar to the above cases for the two-dimensional configuration. At 0.5 cm/sec, a small flame spread only upstream maintaining the initial flame shape from shortly after ignition. The flame never grew laterally from the initial width and this is also clearly seen in the growth pattern of char in figures 6-9a to 6-9c. However, the flame and char growth patterns did grow laterally outward with an increase in the external velocity, as shown in figures 6-8 and 6-9. At 2 cm/sec, the flame had a crescent shape and the char growth pattern was initially an elongated circle pointing upstream; at later times, it became fan-shaped. At 6.5 cm/sec, the shape of the flame became like a horseshoe with the tails of the horseshoe flame extending downstream. The char pattern became an elongated circle in the upstream direction with a relatively flat downstream side. A similar shape was also observed in 35 percent and 50 percent oxygen concentrations at 5 cm/sec external flow velocity,¹⁶ although the color of these flames was orange. Our theoretical calculations predicted a similar shape of flame at 5 cm/sec.¹⁶ A major difference in flame shape between air in this study and 50 percent oxygen concentration is that a spreading spherical flame was observed in a quiescent condition in 50 percent oxygen concentration compared with no transition to flame spread in the air case. Therefore, at low external velocities, the char patterns were more or less spherical in 50 percent oxygen concentration instead of the narrow strip char pattern observed in the air case. The observed trend of opening the angle of the char pattern in the upstream direction with an increase in external flow velocity of air in microgravity is quite different from the narrowing angle trend of the downstream flame with an increase in external flow velocity in normal gravity. However, it is expected that a further increase in external velocity in microgravity would eventually reduce the upstream flame spread rate and be sufficient to promote downstream flame spread. Thus, this observed trend of the char pattern is unique and should occur only at low external flow velocities and low oxygen concentrations, such as in air, in microgravity.

The sample temperatures were measured along the center line at four locations— one at the center of the irradiated area, one at the 2-cm upstream location, and two at 2-cm and 4-cm downstream locations. The gas phase temperatures were measured 2 mm above the sample surface at the 2-cm downstream location and at the 2-cm upstream location. The results for an external flow velocity of 5 cm/sec are shown in figure 10. Time zero was defined as the moment when the power to the lamp was turned on. The delay of temperature increase at the center of the irradiated area was due to the lamp's heat-up time, as discussed above. Unfortunately, the LED display for the center thermocouple was obscured by the reflection of the lamp light, and its output could not be read shortly after ignition until the lamp was turned off. A high center temperature indicates that there might be some additional increase in the thermocouple temperature due to the absorption of external radiation from the lamp by the thermocouple bead. Ignition can be recognized as the sudden jumps in the two gas phase temperatures at the locations 2 cm from the center of the irradiated area. The downstream gas phase temperature continued to increase after the ignition due to the flow of hot combustion products but the upstream gas phase temperature dropped rapidly. However, the downstream gas phase temperature went up only to about 500 °C which is much lower than a realistic flame temperature. The behavior of the upstream gas phase temperature indicates that a sudden expansion of flame at ignition momentarily reached this location, but the gas there contracted and the external flow quickly cooled down

the local gas temperature. The downstream sample temperatures at the 2-cm and 4-cm locations increased earlier than that at the 2-cm upstream location due to the convecting heating from the hot combustion products flow. However, the downstream sample temperature increased up to only about 350 °C at 2 cm and to about 220 °C at 4 cm. The upstream temperature at 2 cm increased rapidly to about 430 °C and a further increase appears to be caused by movement of the thermocouple bead into the gas phase. The first peak of the downstream gas phase temperature 2 mm above the sample surface at 2 cm was due to the traveling flame front and the second peak was due to the approach of the tail end of the flame. The net energy feedback rate from the traveling downstream flame to the sample surface was calculated with the temperature plot at 2 cm upstream location using the same assumptions described in the two-dimensional configuration. The value is $4.1 \text{ W/cm}^2 \pm 10 \text{ percent}$ for each face of the sample surface (two flames along the two faces of the sample); this is about 25 percent higher than that in the two-dimensional configuration discussed above. The net energy feedback rates at the two downstream locations are $1.6 \text{ W/cm}^2 \pm 10 \text{ percent}$ and $0.5 \text{ W/cm}^2 \pm 10 \text{ percent}$. These values are also significantly larger than those in the two-dimensional configuration: about 30 percent and 100 percent, respectively.

The histories of the char front spreading upstream along the center line are plotted in figure 6-11 using the results shown in figure 6-9 to determine the relationship between the location of the char front and time after the initial glow of the ignitor wire. Although the shape of the flame and the curvature of the flame front changed with time, the relationships can be reasonably well fitted by linear equations except when the char front comes close to the sample edge. Thus, apparent steady-state-like char front spread rates along the center line are obtained for each external flow velocity. These apparent steady-state char spread rates are plotted against the external flow velocity in the two- and three-dimensional configurations. The results are shown in figure 6-12. Some caution is needed in comparing the results between the two-dimensional configuration and the three-dimensional configuration due to the transient nature of the three-dimensional flame and the fact that there is only one data point at 5 cm/sec in the two-dimensional configuration. However, it is interesting to note that in the three-dimensional configuration, the char spread rate continues to increase with an increase in external velocity, and it appears that the maximum spread rate might not have been reached. On the other hand, it appears that the maximum flame might already be reached in the two-dimensional configuration. (The existence of a maximum flame spread with respect to external flow velocity was first demonstrated by Olson.¹⁷) Since only four experiments were conducted in the two-dimensional configuration (and also since there is some unsteady nature of the char spread rate for the case of 5 cm/sec), further experiments are needed to determine the relationship between the spread rate and external flow velocity. If this trend is true, the above discussed higher net energy feedback rate from the flame to the sample surface in the three-dimensional configuration indicates that the three-dimensional flame front might be more intense, due possibly to a larger oxygen supply at the curved flame front. In the regime where oxygen supply is a critical rate-controlling process, a curved flame front has a larger area for incoming oxygen to reach. A similar trend of a higher maximum flame spread rate in the three-dimensional configuration versus that in the two-dimensional configuration was also observed in 35 percent and 50 percent oxygen concentrations in our drop tower experiments. However, if our explanation is correct, the flame spread rate in the three-dimensional configuration should decrease as the curvature of the flame decreases with an increase in the distance from the ignition area. Although a slowdown of spread rate beyond 4 cm from the center is observed, as shown in figure 6-11, it is not clear that this was caused by a more planar flame front or by the flame front moving at a higher flow velocity when the flame got close to the leading edge of the boundary layer. In order to confirm this trend further, we need to conduct more tests in the two-dimensional configuration, with larger size samples in the three-dimensional configuration, and also at higher external flows.

6.3.2.3 Flame Spread Along the Open Edges of Samples

The flame spread behavior along the open edges of the paper sample was studied using a narrow sample, 4 cm in width, in the same sample holder. Ignition was achieved by the lamp illuminating the center of the sample; initially, the flame spread radially upstream. This behavior is shown in figure 6-13. Once the flame reached the open edges of the sample, the flames at each edge spread much more rapidly than the flame along the center line, as shown in figures 6-13b, 6-13c, 6-13e, and 6-13f. At the open edges of the sample, oxygen supply to the flame (almost 360°) and energy feedback from the flame to the sample (from three sides) are much larger than that for the flame along the center of the sample (about 180° for oxygen supply and only two sides for energy feedback). However, under an external flow velocity of 2 cm/sec, it appears that oxygen concentration along the downstream edges was not sufficient due to dilution from the combustion products of upstream flame; flame spread occurred only along the upstream edges. Above an external flow velocity of 3.5 cm/sec, oxygen supply to the downstream edges was sufficient and flames spread downstream as well as upstream along the open edges of the sample as shown in figures 6-13e and 6-13f.

6.4 Smoldering

In RITSI, four smoldering experiments were conducted with ignition initiated at the center of the sample by the lamp. The sample was doped with potassium ions to enhance char formation and char oxidation (4.2 weight percent ± 5 percent in spatial nonuniformity). Although a ring-shaped smoldering front was initially observed in normal gravity (the ring-shaped front gradually deformed due to induced buoyant flow from the hot smoldering surface), unexpected, very complex finger-shaped char patterns with localized smoldering fronts at the finger tips were observed in microgravity; such patterns are seen in figure 14. In these pictures, the white spots are the localized smoldering fronts. The direction of growth of the char pattern was mainly upstream; higher external flow velocity tends to increase the number of localized smoldering fronts, the number of fingers, and also the frequency of bifurcations from each finger. At present it is not clear what caused this complex pattern. One possible explanation is that there is some nonuniformity in sample thickness and the concentration of potassium ions (doped to the sample to enhance smoldering) in the filter paper. Since potassium ions were heavily doped into the samples (more than needed to make sure that smoldering rate does not depend on the ion concentration), we believe that this phenomenon was not caused by a nonuniformity (± 5 percent) in ion concentration in the sample. Since smoldering induces roughly 20 cm/sec buoyancy induced flow in normal gravity, it might be that any nonuniformity of the sample tends to be suppressed in normal gravity. In microgravity, however, it appears that a flow velocity up to 6.5 cm/sec does not suppress it. Another possible explanation is that this is a unique instability phenomenon which could occur only at low flow velocities below the buoyancy induced flow velocity such as is the case under microgravity conditions.

6.5 SUMMARY

Nonpiloted ignition by external thermal radiation of a cellulosic paper tends to occur more easily in microgravity than in normal gravity. Downstream flame spread was never observed in the two-dimensional configuration exposed to external flow velocity of up to 5 cm/sec, when ignition was initiated locally in the middle part of a thin paper. This was presumably due to lack of oxygen due to the dilution of combustion products from the upstream flame (oxygen shadow effect). In the three-dimensional configuration, when ignition was initiated locally in a small circle in the center of the sample, flame spread was again mainly upstream. At the lowest flow (0.5 cm/sec) for sustained spread, the flame remained a very small hemisphere that propagated directly upstream without any lateral spread. At 1 cm/sec, the flame fanned out slightly as it propagated upstream. The fan angle increased with flow velocity. At 6.5 cm/sec, the flame became horseshoe-shaped. It appears that the three-dimensional flame front (i.e., curved flame front) might be more intense than that in the two-dimensional flame front (planar flame) due to larger oxygen supply to the curved flame front. The peak upstream flame spread rate in the two-dimensional configuration tends to occur at lower external flow velocity than that in the three-dimensional configuration. The shape of the upstream flame front might have important effects on the strength of the flame front and upstream flame spread rate.

Flame spreads much faster along open edges of a thin paper sample than along the sample surface. At the external flow velocity of 2 cm/sec, flame spread along open edges only upstream while, above 3.5 cm/sec, flame spread along open edges downstream as well as upstream.

An unexpected, complex surface smoldering char growth pattern was observed when localized smoldering was initiated at the center of the sample by a lamp. Instead of a ring-like smoldering front as is observed in normal gravity, a finger-shaped char growth pattern with several localized smoldering fronts was observed. Generally, the char growth pattern was mainly upstream. The number of localized smoldering fronts, the number of fingers, and the frequency of bifurcations of the finger increased with an increase in external flow velocity. At present, it is not clear what causes this complex char growth pattern.

REFERENCES

1. Friedman, R.; and Sacksteder, K.R.: "Fire Behavior and Risk Analysis in Spacecraft," *NASA TM100944*, December 1988.
2. Smith, R.; and Kashiwagi, T.: *J. Applied Fire Sci.* 1–2, pp. 103–113, 1990–91.
3. Kashiwagi, T.: *Fire Safety J.* 3, pp. 185–200, 1981.
4. Kashiwagi, T.: *Combust. Flame* , 34, pp. 231–244, 1979.
5. Muto, N.; Hirano, T.; and Akita, K.: Seventeenth Symposium (International) on Combustion. The Combustion Institute, Pittsburgh, pp. 1183–1190, 1978.
6. Akita, K. in "Aspects of Degradation and Stabilization of Polymers," Jellinek, H.H.G., ed., *Elsevier Scientific*, Ch. 10, 1978.
7. Bhattacharjee, S.; and Altenkirch, R.A.: Twenty-Third Symposium (International) on Combustion. The Combustion Institute, Pittsburgh, pp. 1627–1633, 1990.
8. Frey, A.E.; and Tien, J.S.: *Combust. Flame*, 36, pp. 263–289, 1979.
9. Kashiwagi, T.: *Combust. Sci. Tech.* , 8, pp. 225–236, 1974.
10. Kindelan, M.; and Williams, F.: *Combust. Sci. Tech.* , 16, pp. 47–58, 1977.
11. Krishnamurthy, L.: *Acta Astronaut.*, 3, p. 935, 1976.
12. Amos, B.; and Fernandez-Pello, A.C.: *Combust. Sci. Tech.*, 62, pp. 331–343, 1988.
13. Di Blasi, C.; Crescitelli, S.; and Russo, G.: *Fire Safety Science —Proceedings of the Second International Symposium*, pp. 119–128, 1989.
14. McGrattan, K.B.; Kashiwagi, T.; Baum, H.R.; and Olson, S.L.: *Combust. Flame*, 106, pp. 377–391, 1996.
15. Kashiwagi, T.; and Nambu, H.: *Combust. Flame*, 88, pp. 345–368, 1992.
16. Kashiwagi, T.; McGrattan, K.B.; Olson, S.L.; Fujita, O.; Kikuchi, M.; and Ito, K.: "Effects of Slow Wind on Localized Radiative Ignition and Transition to Flame Spread in Microgravity," to appear in Twenty-Sixth Symposium (International) on Combustion. The Combustion Institute.
17. Olson, S.L.: *Combust. Sci. Technol.* , 76, pp. 233–249, 1991.

Table 6-1. Test Matrix

Test No.	Configuration	Flow cm/sec	Ignitor	Notes
1	Flaming 2D	5.0	Wire	No transition
2	Flaming 3D	5.0	Lamp	
3	Flaming 3D	5.0	Lamp	
4	Flaming 2D	2.0	Wire	
5	Flaming 2D	0.0	Wire	
6	Flaming 3D	2.0	Lamp	
7	Flaming 3D	0.5	Lamp	Spread along open edges
8	Flaming 3D	2.0	Lamp	
9	Smolder 3D	0.5	Lamp	
10	Smolder 3D	5.0	Lamp	Smoldering
11	Flaming 3D	3.5	Lamp	Smoldering
12	Flaming 2D	2.0	Wire	
13	Flaming 3D	1.0	Lamp	
14	Smolder 3D	2.0	Lamp	Smoldering
15	Smolder 3D	6.5	Lamp	Smoldering
16	Flaming 3D	2.0	Lamp	Spread along open edges
17	Flaming 3D	5.0	Lamp	
18	Flaming 3D	0.0	Lamp	
19	Flaming 3D	2.0	Lamp	No transition
20	Flaming 3D	1.0	Lamp	Spread along open edges
21	Flaming 3D	0.5	Lamp	No 35 mm camera
22	Flaming 3D	6.5	Lamp	No 35 mm camera
23	Flaming 3D	5.0	Lamp	Spread along corner
24	Flaming 3D	3.5	Lamp	Spread along open edges
25	Flaming 3D	5.0	Lamp	Spread along corner



Figure 6-1. RITSI hardware picture (two modules, two sample/holder storage containers, one sample/holder, electronic control, and outputs display)

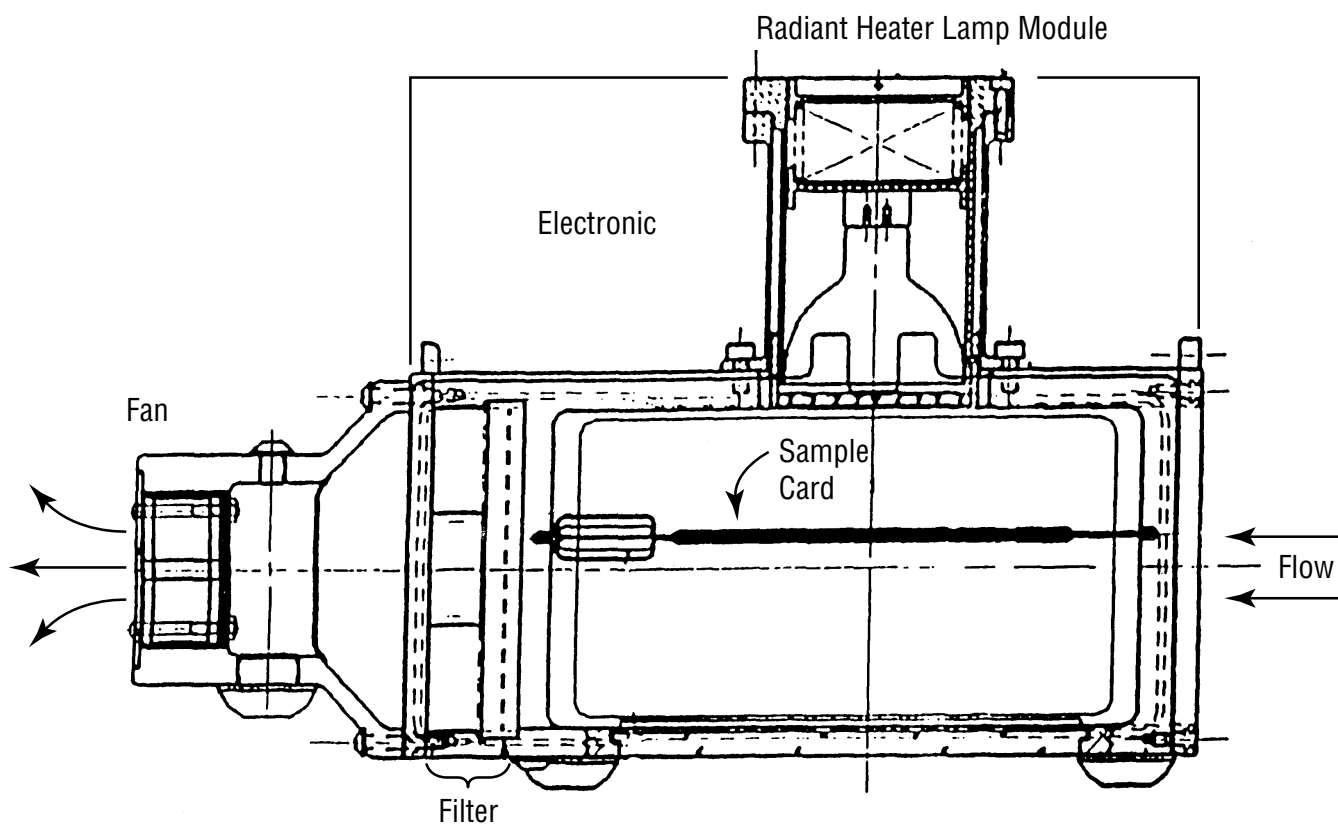


Figure 6-2. Schematic cross section view of hardware.

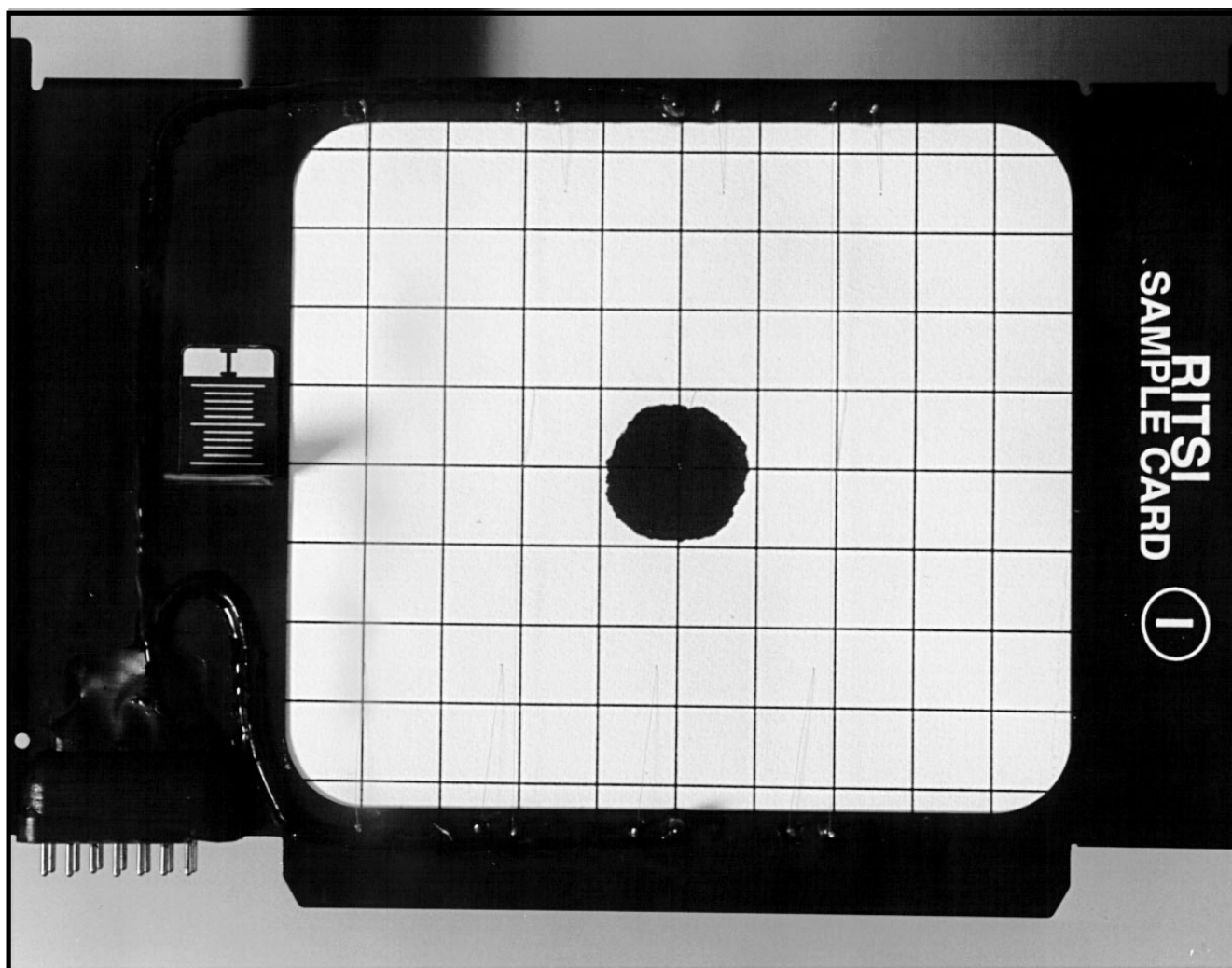


Figure 6-3. Sample card with 1 cm by 1 cm grid.

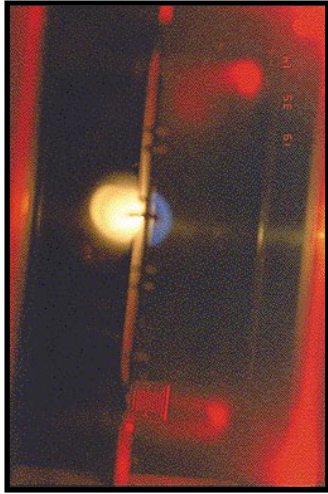


Figure 6-4a: Quiescent ignition



Figure 6-4b: Quiescent transition



Figure 6-4c: Quiescent extinction



Figure6- 4d: 2 cm/sec ignition

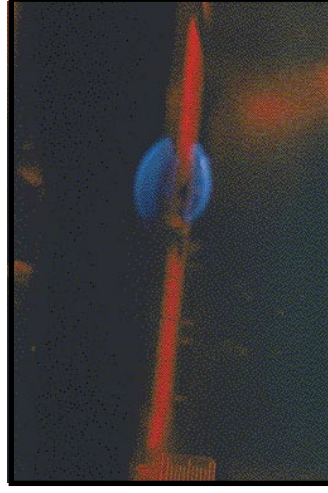


Figure6- 4e: 2 cm/sec transition



Figure6- 4f: 2 cm/sec flame spread



Figure6- 4g: 5 cm/sec ignition



Figure 6-4h: 5 cm/sec transition



Figure6- 4i: 5 cm/sec flame spread

Figure 6-4. Flame spread at three different flow velocities in two-dimensional configuration (flow from right).

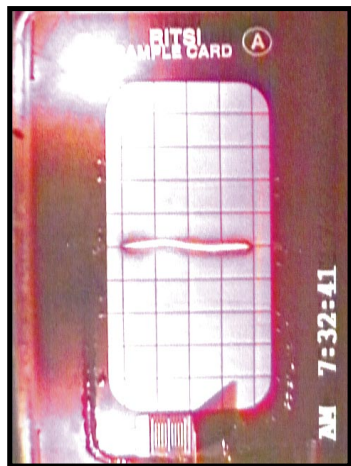


Figure 6-5a: Quiescent ignition



Figure 6-5b: Quiescent transition



Figure 6-5c: Quiescent extinction

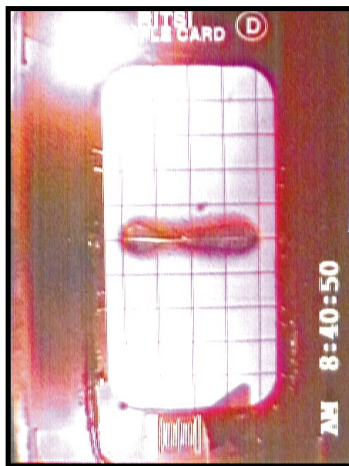


Figure 6-5d: 2 cm/sec after ignition



Figure 6-5e: 2 cm/sec spread



Figure 6-5f: 2 cm/sec fully spread



Figure 6-5g: 5 cm/sec after ignition



Figure 6-5h: 5 cm/sec spread



Figure 6-5i: 5 cm/sec nearly fully spread

Figure 6-5. Char growth patterns at three different flow velocities in two-dimensional configuration (flow from right).

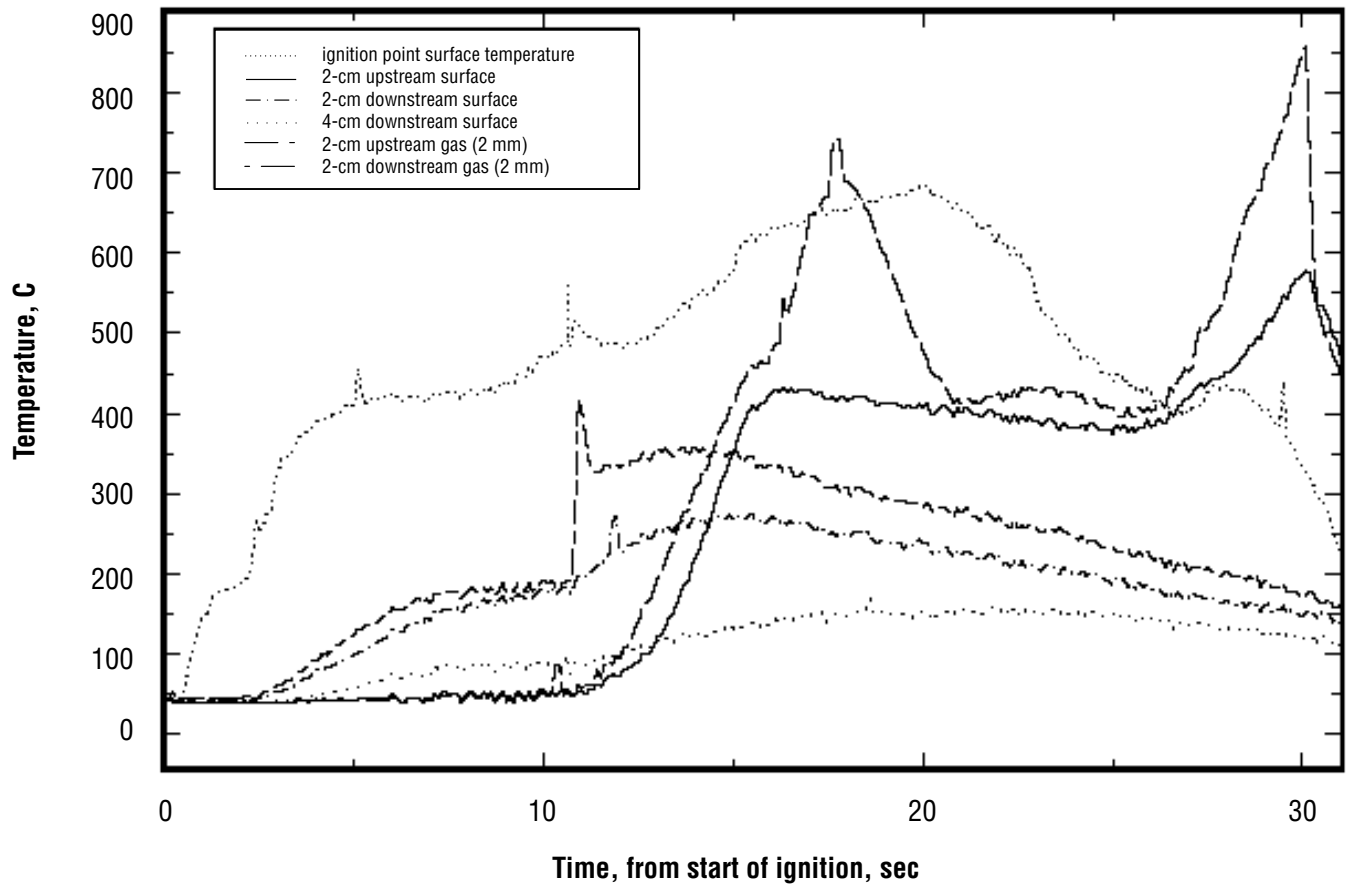


Figure 6-6. Temperature histories in two-dimensional configuration, 5 cm/sec.

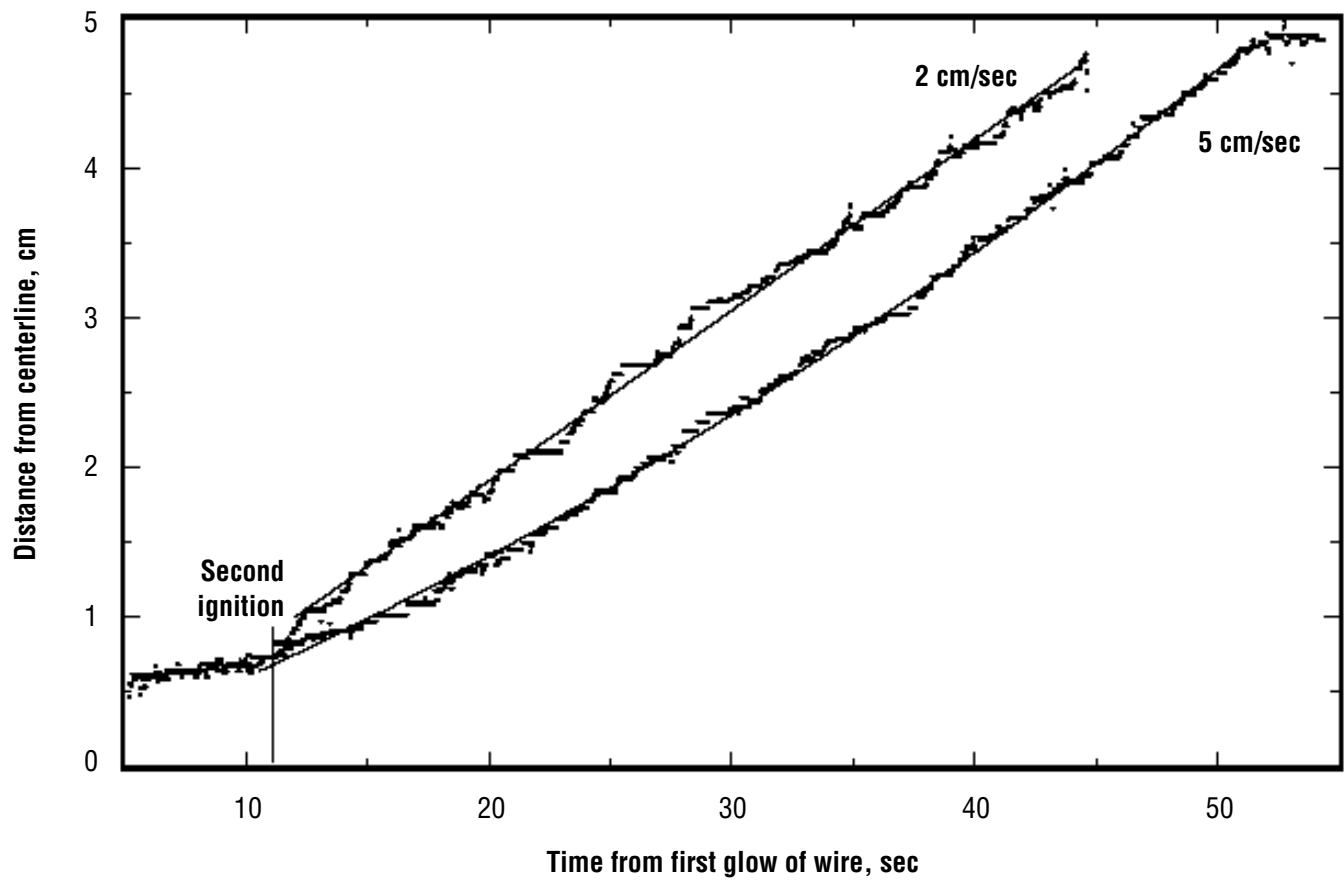


Figure 6-7. Upstream char front location histories in two-dimensional configuration.

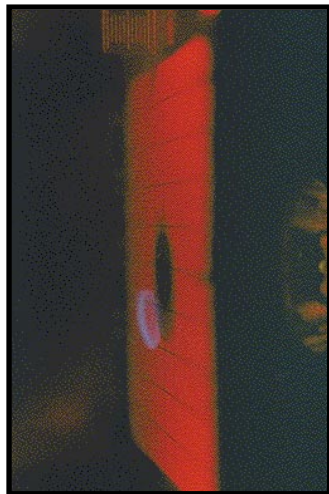


Figure 6-8a: 0.5 cm/sec after ignition

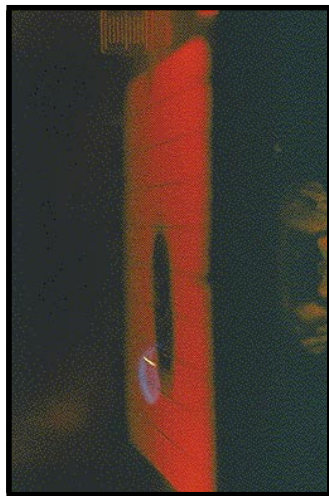


Figure 6-8b: 0.5 cm/sec spread



Figure 6-8c: 0.5 cm/sec full spread



Figure 6-8d: 2 cm/sec after ignition



Figure 6-8e: 2 cm/sec spread



Figure 6-8f: 2 cm/sec fully spread

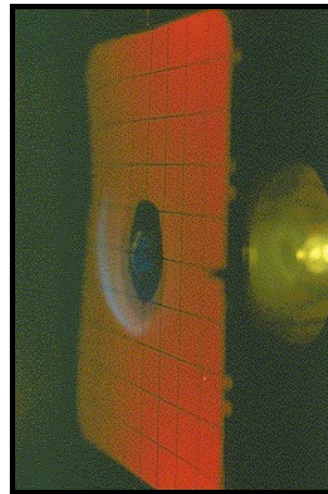


Figure 6-8g: 6.5 cm/sec after ignition



Figure 6-8h: 6.5 cm/sec spread



Figure 6-8i: 6.5 cm/sec nearly full spread

Figure 6-8. Flame spread patterns at three different flow velocities in three-dimensional configuration (flow from right).

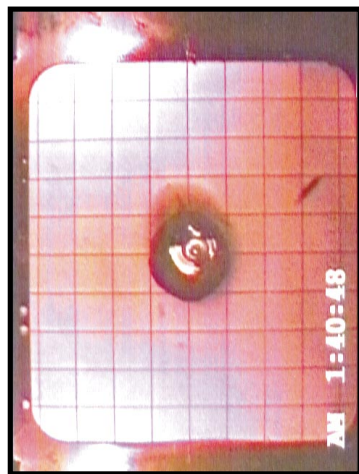


Figure 6-9a: 0.5 cm/sec after ignition

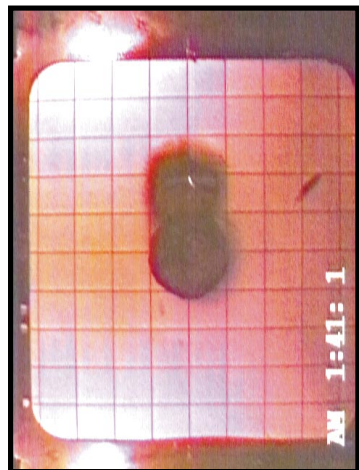


Figure 6-9b: 0.5 cm/sec spread

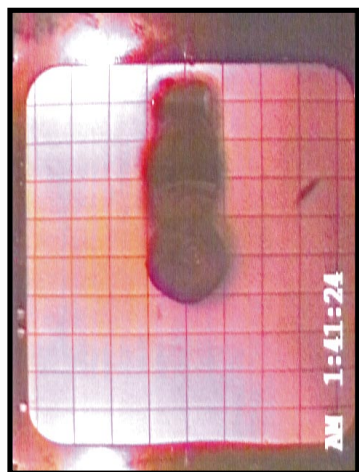


Figure 6-9c: 0.5 cm/sec fully spread upstream

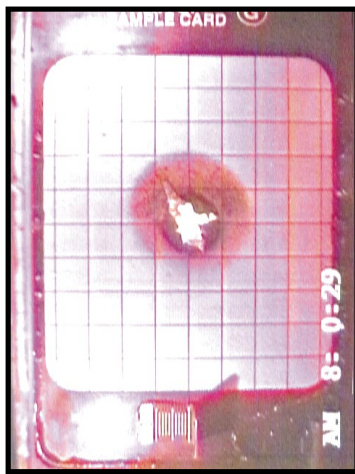


Figure 6-9d: 2 cm/sec after ignition

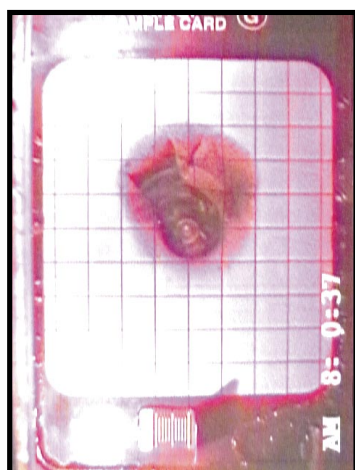


Figure 6-9e: 2 cm/sec spread

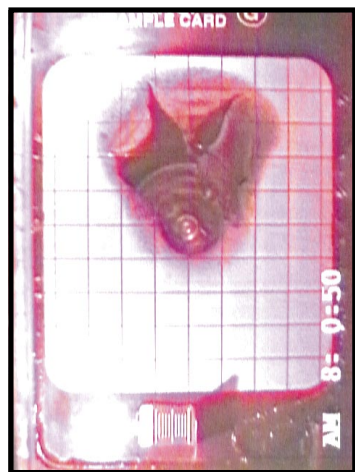


Figure 6-9f: 2 cm/sec fully spread upstream

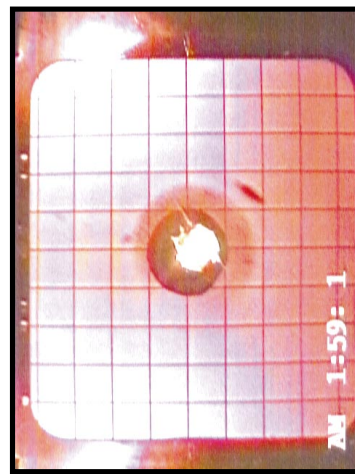


Figure 6-9g: 6.5 cm/sec after ignition

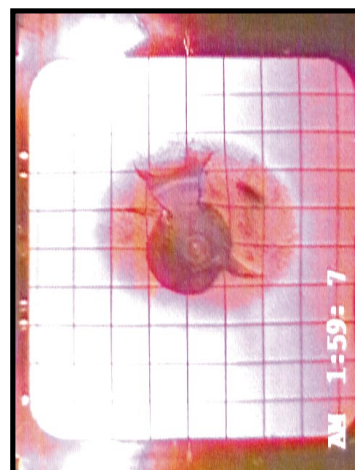


Figure 6-9h: 6.5 cm/sec spread

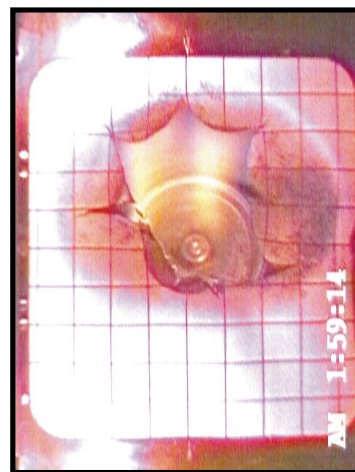


Figure 6-9i: 6.5 cm/sec fully spread upstream

Figure 6-9. Char growth patterns in the three-dimensional configuration (flow from right).

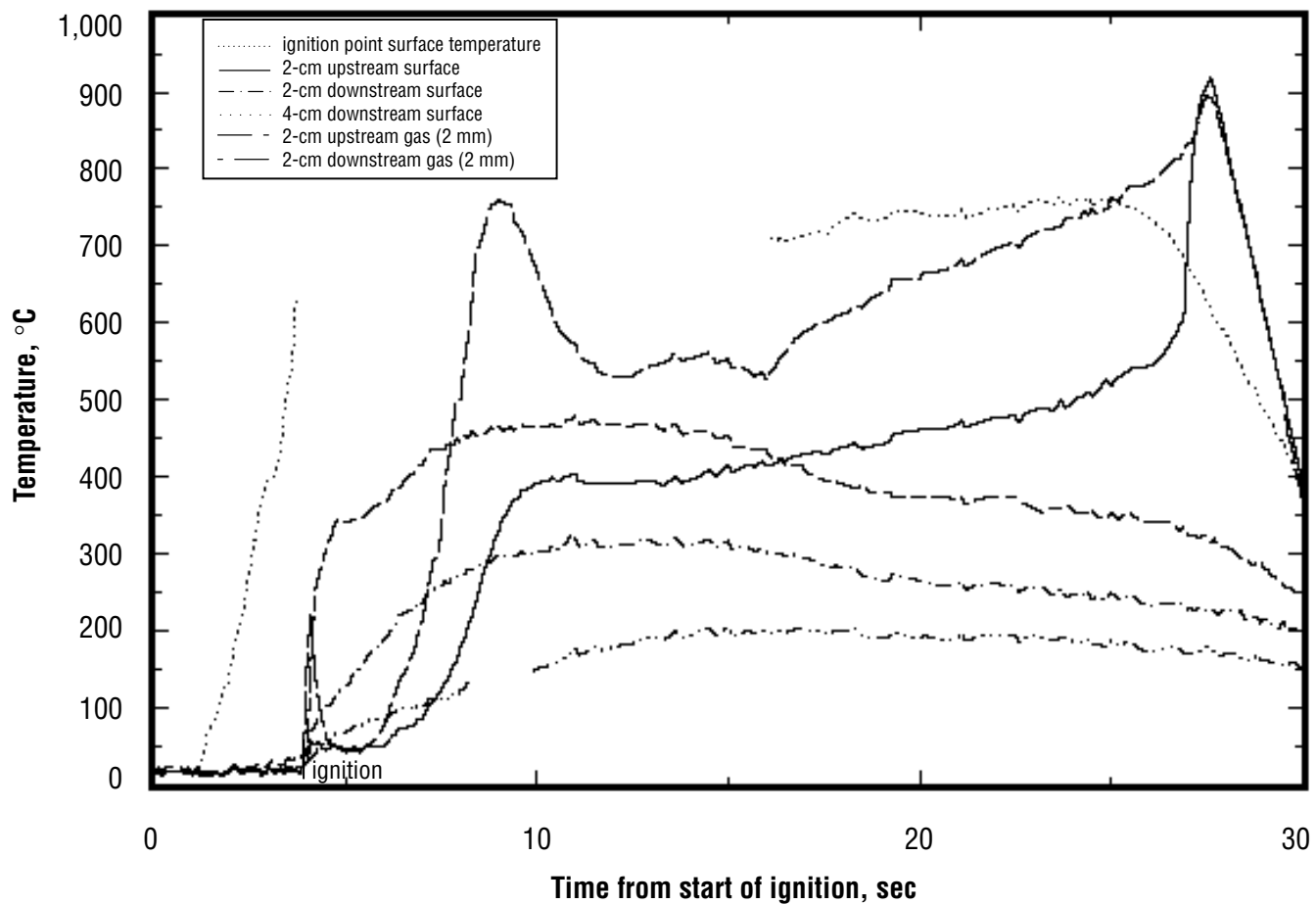


Figure 6-10. Temperature histories in three-dimensional configuration, 5 cm/sec.

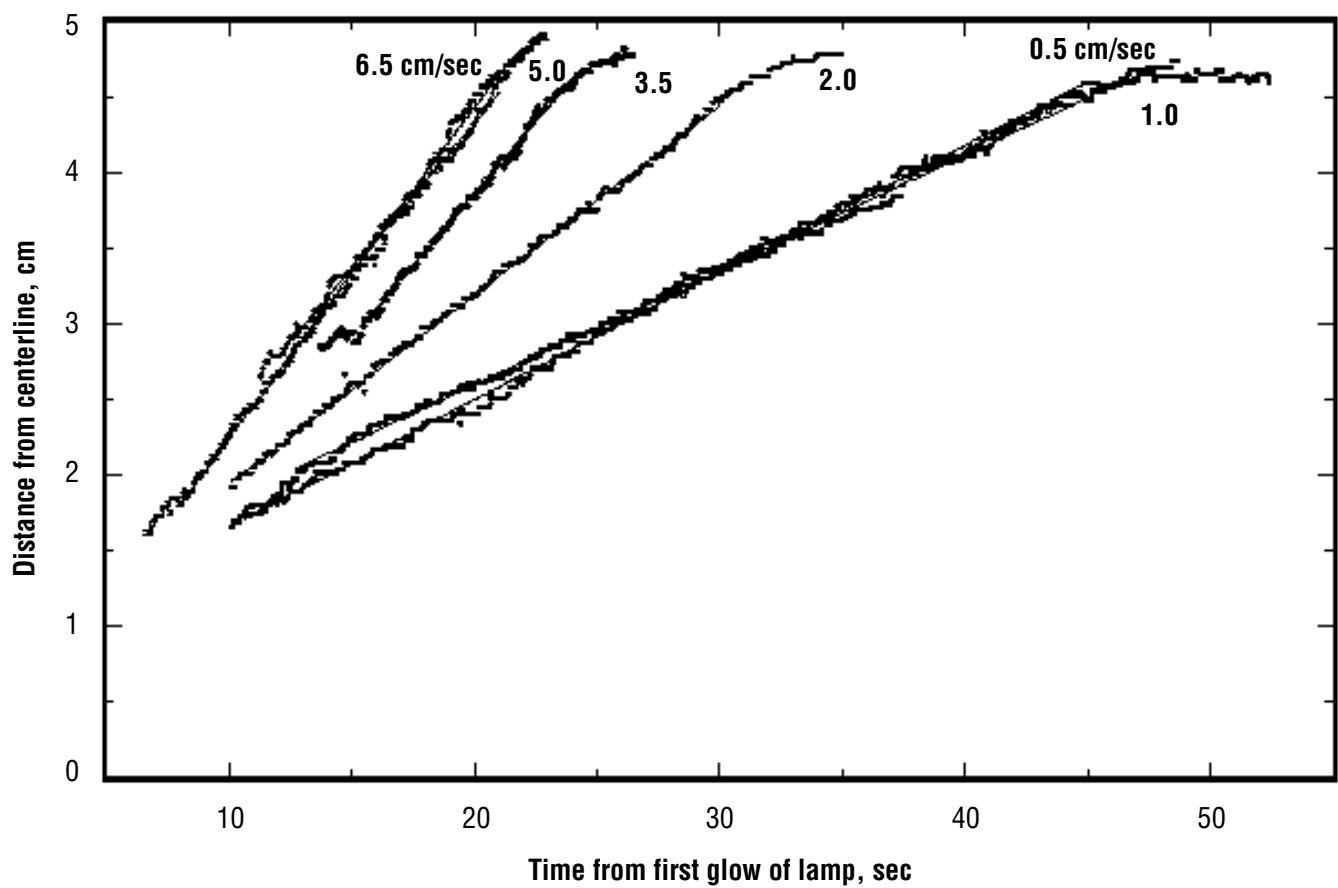


Figure 6-11. Upstream char front location histories in three-dimensional configuration.

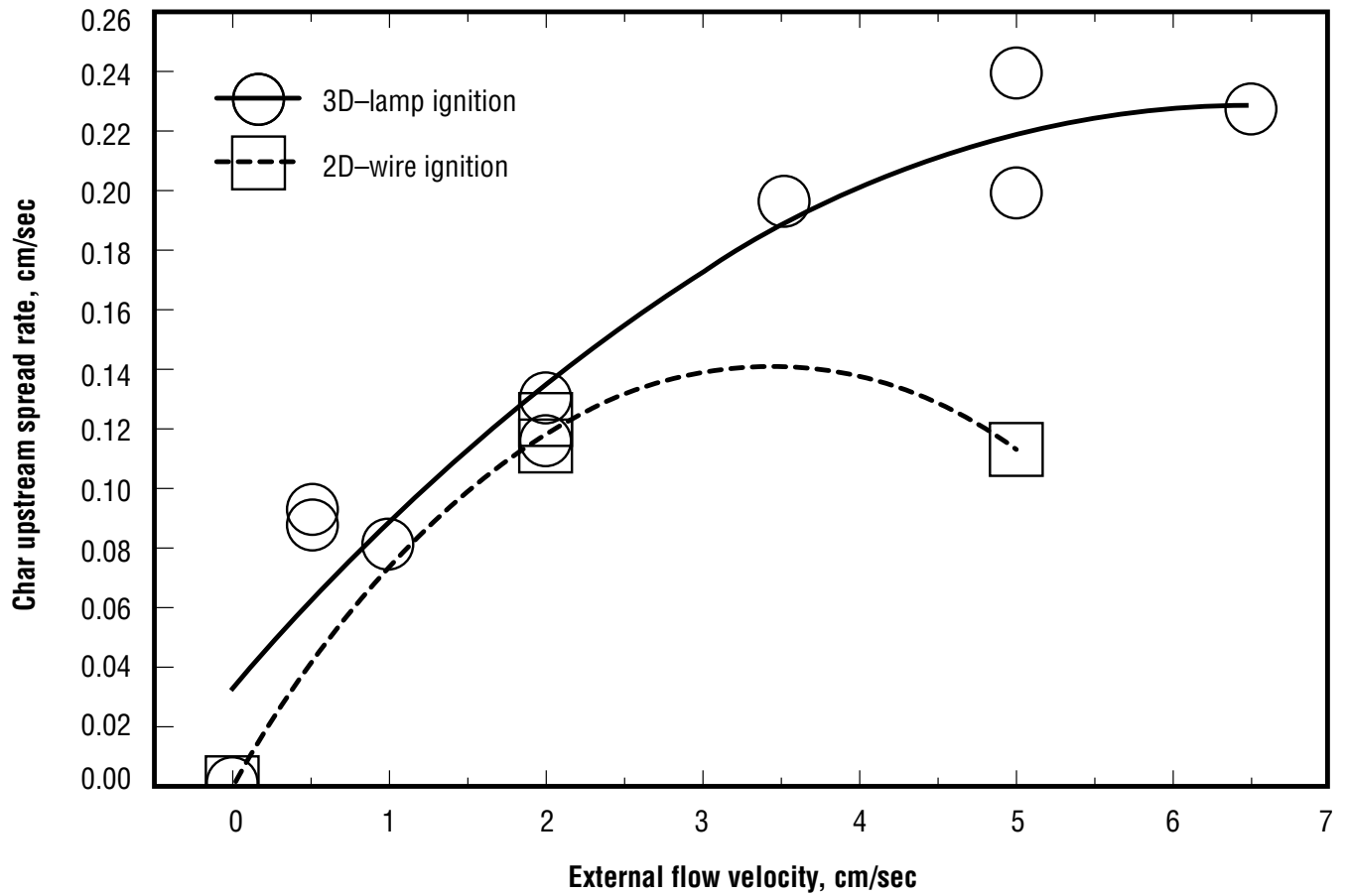


Figure 6-12. Char upstream spread rate versus external flow velocity.

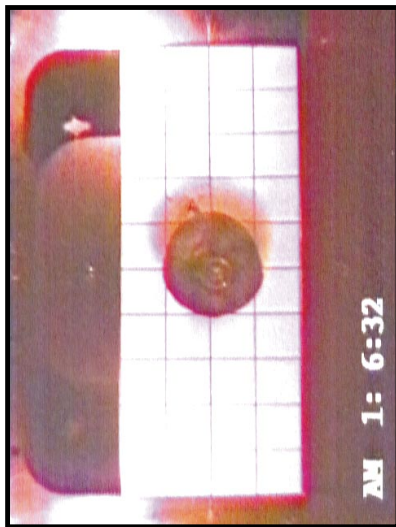


Figure 6-13a: 2 cm/sec post ignition

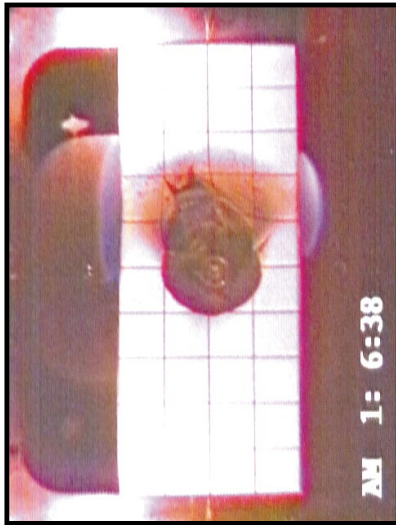


Figure 6-13b: 2 cm/sec enhanced edge spreading

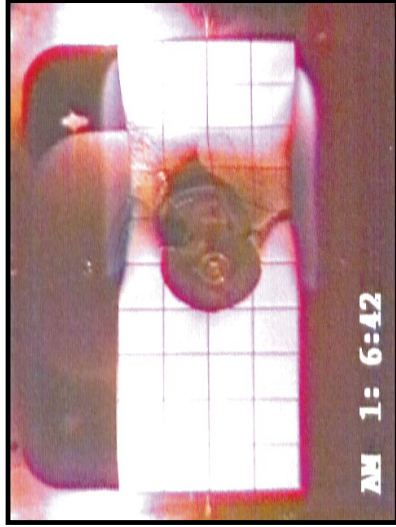


Figure 6-13c: 2 cm/sec upstream spread only



Figure 6-13d: 5 cm/sec post ignition

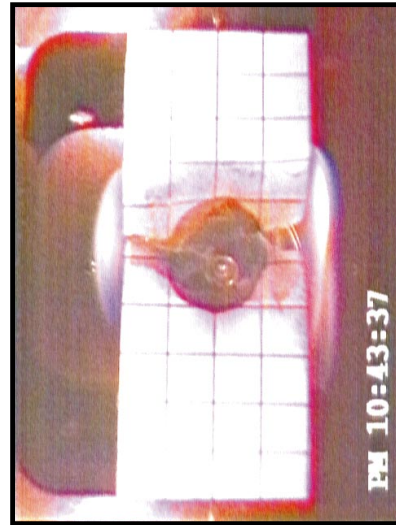


Figure 6-13e: 5 cm/sec enhanced edge spreading

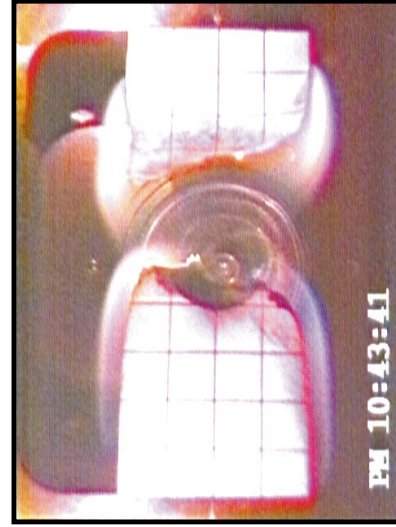


Figure 6-13f: 5 cm/sec bidirectional edge spread

Figure 6-13. Flame spread patterns along open edges (ignition was initiated at the center, flow from right).

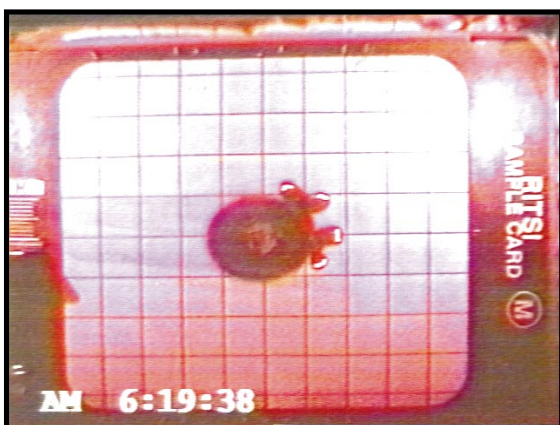


Figure 6-14a: 0.5 cm/sec flow test, just after ignition

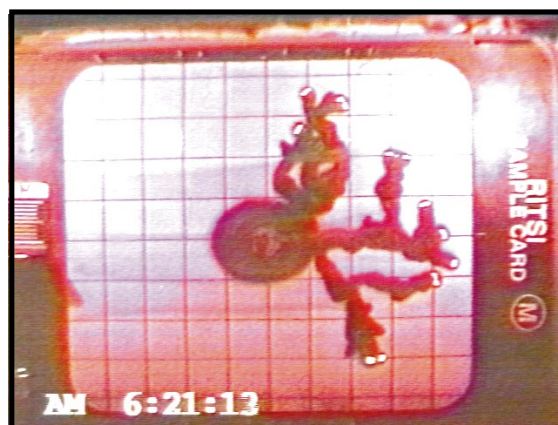


Figure 6-14b: 0.5 cm/sec flow test, later in the burn

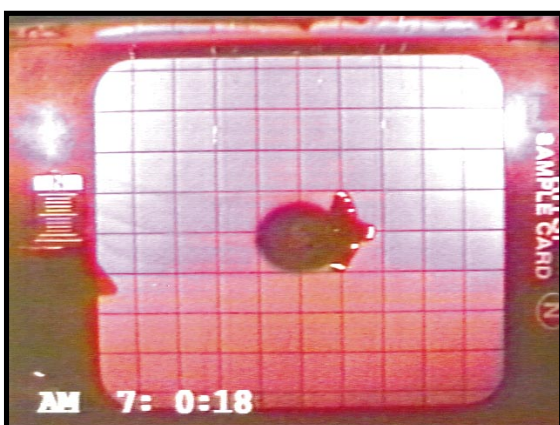


Figure 6-14c: 2 cm/sec flow test, just after ignition



Figure 6-14d: 2 cm/sec flow test, later in the burn

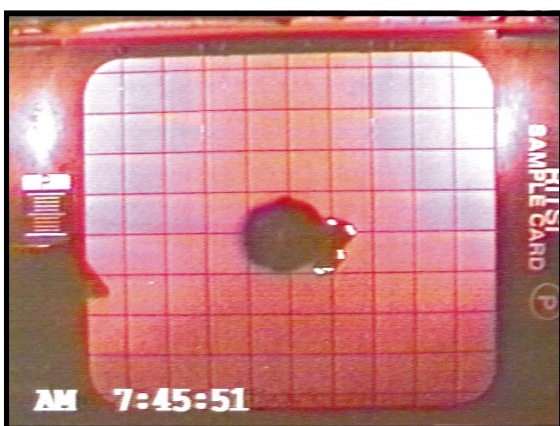


Figure 6-14e: 6.5 cm/sec flow test, just after ignition



Figure 6-14f: 6.5 cm/sec flow test, later in the burn

Figure 6-14. Smoldering char growth patterns at different flow velocities (flow from right).

SECTION VII.

COMPARATIVE SOOT DIAGNOSTICS: 1 YEAR REPORT

Acknowledgments

The assistance of D. Michael Hoy of NASA JSC in providing samples and in obtaining an orbiter smoke detector is much appreciated. This program received financial support from NASA Codes UG and Q. The in-kind assistance provided by Boeing, Allied Signal and Brunswick Defense was necessary to allow testing of flight smoke detectors. Several students (D. Crouch, L.J. Dallaire and C. Lundquist) were instrumental in performing the tests needed to develop the flight apparatus and in postflight data analysis. The careful execution of these experiments, while on orbit, by A. Allen and F. Chang-Diaz was critical to CSD's success and is much appreciated. Finally, J. Romanin and P. Howard were responsible for the bulk of the design, and the assistance of the MGBX team and the POCC cadre were all critical to the success of this experiment.

COMPARATIVE SOOT DIAGNOSTICS: ONE YEAR REPORT

David L. Urban

DeVon W. Griffin

Microgravity Science Division
NASA Lewis Research Center

Melissa Y. Gard

NASA Marshall Space Flight Center

7.1 INTRODUCTION

Even though combustion is commonly thought of as a process that consumes solid and liquid fuels via a gas phase flame, combustion of most materials produces a variety of condensed phase (solid and liquid) products. The structure and composition of these products are functions of the materials being burned and the details (environment, size, intensity) of the combustion process itself. These condensed products comprise “smoke” and can be divided into a few general groups: 1) Droplets or particles of the original polymer or its monomer, 2) incompletely oxidized pyrolysis (thermal decomposition) products of the fuel, 3) inorganic compounds (e.g., metal oxides and ash from fossil fuels), and 4) hydrocarbon soot (the major constituent of soot is carbon). Particulate from the first two groups can be either liquid or solid at room temperature, depending upon the composition.

The motivation for the Comparative Soot Diagnostics (CSD) experiment lies in the broad practical importance of understanding combustion-generated particulate. Depending on the circumstances, particulate matter can affect the durability and performance of combustion equipment, can be a pollutant, can be used to detect fires and, in the form of soot, can be the dominant source of radiant energy from flames. Bright sooty fires are desirable for efficient energy extraction in furnaces and power equipment. In contrast, soot-enhanced radiation is undesirable in many propulsion systems (e.g., jet engines). The nonbuoyant structure of most flames of practical interest (turbulent) makes understanding soot processes in low gravity flames important to our ability to predict fire behavior on Earth. These studies also have direct applications to fire safety in human-crew spacecraft, since smoke is the indicator used for automated detection in current spacecraft.^{3 4}

In addition, recent tests conducted on Mir¹ showed that a candle in a truly quiescent spacecraft environment can burn for tens of minutes. Consequently, this test and many earlier tests have demonstrated that fires in spacecraft can be considered a credible risk.^{2 3 4} In anticipation of this risk, NASA has included fire detectors on Skylab, smoke detectors on the Space Shuttle (Space Transportation System (STS)), and smoke detectors in the design for the *International Space Station (ISS)*. In the CSD experiment, these smoke detectors were tested using quasi-steady, low gravity, particulate-generating materials. Samples of the particulate were also obtained from these low gravity sources. This experiment provides the first such

measurements aimed toward understanding soot processes here on Earth and for the testing and design of advanced spacecraft smoke detection systems.

This paper describes the operation and preliminary results of the CSD, a project conceived and developed at NASA Lewis Research Center. The CSD flight experiment was conducted in the Middeck Glovebox Facility (MGBX) on USMP-3. The project is supported by NASA Headquarters Microgravity Science and Applications Division and Code Q.

In the earliest missions (Mercury, Gemini and Apollo), the crew quarters were so cramped that it was considered reasonable that the astronauts would rapidly detect any fire. The Skylab module, however, included approximately 20 UV-sensing fire detectors. The Space Shuttle has nine particle-ionization smoke detectors in the middeck and flight deck, and Spacelab has six additional particle-ionization smoke detectors. The designated detectors for the *ISS* are laser-diode, forward-scattering, smoke or particulate detectors. Current plans for the *ISS* call for two detectors in the open area of the module, and detectors in racks that have both cooling air flow and electrical power. Due to the complete absence of data concerning the nature of particulates and radiant emission from incipient and fully developed low g fires, all three of these detector systems were designed based on 1 g test data and experience. As planned mission durations and complexity increase and the volume of spacecraft increases, the need for and importance of effective, crew-independent, fire detection grows significantly. To provide this level of protection, more knowledge is needed concerning low gravity fire phenomena and, in particular, how they might be detected and suppressed.

The objectives of CSD are to examine the particulate emission from a variety of pyrolyzing and combusting sources and to quantify the performance of several particulate-sensing diagnostic techniques. Prior to CSD, no combustion-generated particulate samples had been collected near the flame zone for well-developed microgravity flames. All of the extant data either came from drop tower tests, and therefore only corresponded to the early stages of a fire, or from the exit plenum in a glovebox test in which case the sample was a time integral of the entire burn period. The fuel sources in the drop tower tests were restricted to laminar gas jet diffusion flames and very rapidly overheated wire insulation.^{5,6} The gas jet tests indicated, through thermophoretic sampling,⁵ that soot primaries and aggregates (groups of primary particles) in low gravity may be significantly larger than those in normal gravity (1 g). This raises new scientific questions about soot processes as well as practical issues for particulate size sensitivity and detection/alarm threshold levels used in on-orbit smoke detectors. Furthermore, it has been suggested, but not shown, that the aggregates of individual particles may grow to very large sizes in a microgravity fire of longer duration than available on the ground. Preliminary tests in the 2.2-sec drop tower suggest that particulate generated by overheated wire insulation may be larger in low g than in 1 g.⁶ Transmission electron microscope (TEM) grids downstream of the fire region in the Wire Insulation Flammability experiment,⁷ as well as visual observation of long string-like aggregates, further confirm this suggestion. The combined impact of these limited results and theoretical predictions is that, as opposed to extrapolation from 1 g data, direct knowledge of low g combustion particulate is needed for more confident design of smoke detectors for spacecraft.

This paper presents the results of the microgravity portion of the CSD experiment. The results include the temporal response of the detectors and average sizes of the primary and aggregate particles captured on the thermophoretic probes. Complete assessment of the microgravity data and its combination with the normal-gravity data are still in process and will be reported later.

7.2 BACKGROUND/PREVIOUS WORK

Although optical detectors (responding to a fire's radiant emission rather than the presence of particulate) were used in the Skylab module and were considered for use on *ISS*, their implementation has been hampered by the facts that they require a line-of-sight to the area to be monitored and the lack of knowledge of radiant signatures for low g fires. Consequently, smoke detection has been favored for newer spacecraft applications. As noted above, low g smoke detection has several challenges that make direct application of 1 g technology inappropriate. These issues include: Dust discrimination, sampling in the absence of buoyant flows, lack of a knowledge base of low g particulate size distributions, and lack of knowledge of appropriate alarm levels. Different portions of spacecraft raise unique design problems. Inside equipment racks (a more probable location for fires given the presence of power and heat-producing devices) free volume is limited and air flow paths may be tortuous; however, avionics air flow is often present (serving both as an oxidant source and smoke gathering mechanism). Outside the racks, in the crew space, free volume is much less limited and potential ignition sources are less common, but potential fuel is more abundant (e.g., paper, clothing, and trash materials). In addition, air residence times (and therefore detection times) in the inhabited space are long (tens of minutes in some portions of the Shuttle). Future operation plans for the *ISS* suggest that modules will have electrical systems turned on but no human occupants present. In situations such as this, adequate fire/smoke detection systems for both the racks and the crew space are needed.

Well-established normal-gravity fires emit small particulate of the size range to which ionization detectors are more sensitive than optical detectors.⁸ Less well-established or smoldering fires will produce larger particulate, owing to the large amount of condensed, unoxidized fuel pyrolysis products and the incomplete soot oxidation. For this type of fire, light scattering/obscuration detectors are more appropriate. However, for materials heated slowly as in the very early stages of some fires, the particulate can be very small, and therefore more easily sensed by ionization detectors.⁹ This analysis was used by Brunswick Defense in their decision to pursue an ionization detector (fig. 7-1) for the STS. The design consists of a dual-chamber ionization detector that is in the flow path created by a vane pump. This vane pump provides some active sampling capability and also the flow for an inertial separation system which is designed to make the detector insensitive to particulate larger than 1 to 2 μm , depending upon the particle mass. These advantages are offset by a fairly large power consumption (9 W), fan noise, and limited life due to the moving parts. The detector produces a discrete alarm signal and two analog signals related to the detected smoke density. For the tests reported here, the analog voltage was measured. This voltage has a baseline of 11.4 for the detector used here and decreases in the presence of smoke. The alarm value is set at the factory using a fixed offset from the internal detector baseline and consequently the analog output voltage at alarm is different for each detector. The analog voltage at alarm for the detector used in this work was 10.6 V.

The design developed for the *ISS* by Allied Signal (fig. 7-2) consists of a two-pass laser-diode obscuration system that also has a photodiode positioned to sense forward scattered light (30°) on the return path. The system is designed to alarm based on the magnitude of the scattered light signal. Dust discrimination is based on frequency analysis of the scattered light signal. The system is less sensitive to particles smaller than the wavelength of the laser (near IR) than it is to larger particles. The minimum reported sensitivity is 0.3 μm .¹⁰ It draws relatively little power (1.5 W) and it has a long operational life. The current planned alarm value is 2 V or 1 percent obscuration per foot.

The performance of these two detectors has been compared in normal gravity.^{10 11} Consistent with expectations, for cases where large particles were expected (punk smoke), the initial response of both detectors was about the same but the *ISS* detector reached the alarm threshold more rapidly. For sources of smaller particle-sized smoke (over heated wire) the *STS* detector was quicker both in initial response and in time to alarm. The implementation (alarm threshold selection) of both of these systems in microgravity is hampered by the lack of knowledge of their performance against low gravity combustion-generated particulate.

7.3 OBJECTIVES

The objectives of CSD are to examine the particulate formation from a variety of particulate-generating sources and to quantify the performance of several particulate-sensing diagnostic techniques. The sources include a candle tested at three coflow air velocities and four overheated materials (paper, silicone rubber, and TeflonTM- and KaptonTM-coated wires) — each tested at three heating rates. The paper, silicone rubber and wire insulations are materials found in spacecraft crew cabins, and candles produce hydrocarbon soot typical of many practical 1 g flames.

Four diagnostic techniques were employed: Thermophoretic sampling to provide samples of the particulate for size analysis, laser-light extinction measurements near the source to provide total smoke production data, and laser light scattering and ionization detector measurements to provide data concerning the performance of the detectors for these particulate sources.

7.4 HARDWARE DESCRIPTION

The CSD experimental hardware consists of two modules named the near-field module and far-field box as shown in the figure 7-3. The near-field module is installed inside the glovebox and contains the sample and the near-field diagnostics. The far-field box is external to the glovebox and contains two spacecraft smoke detectors. Products from the near-field tests are transported to the far-field box and subsequently back into the glovebox via TeflonTM hoses which enter the glovebox through ports in the airlock door. All of the combustion products are contained in either the glovebox or the far-field box; by the time the experiment is completed, all of the products are returned to the glovebox .

A photograph of the near-field module is shown in figure 7-4. It consists of a small test chamber fitted with a sample carrier that holds the sample being tested. A small fan blows air from the glovebox into the right side of the chamber past the sample and out the left side where it enters the hose to the far-field module. The sample is ignited or overheated by a resistively heated KanthalTM wire. The smoke particulate is sampled by a rake of thermophoretic probes and smoke production is detected by a laser light extinction system.

The far-field box (fig. 7-5) contains a duct and a fan to transport the smoke from the near-field module to two spacecraft smoke detectors, one matching the *STS* detector (fig. 7-1) and the other (fig. 7-2) is identical to the *ISS* detector with the exception of its signal which is amplified by a factor of 6.6 over the *ISS* standard. This amplification was added because the engineering model of the *ISS* detector that was used for developing the test matrix displayed very low signal levels. Since the tests were intended more as a test of each technology rather than specific designs or alarm levels, the signal was amplified in the model

used in the flight tests. Postflight calibration of both units by Allied Signal revealed that the engineering model was operating below specification by a factor of 5, voiding the reason for the amplification. However, despite the amplification, sufficient dynamic range exists on the measurement that it is possible to predict when an unamplified unit would show significant detection. The analog signals from the various instruments are displayed by digital readouts on the far-field box where they are recorded by a video camera for later transcription.

7.5 PROCEDURE AND OPERATIONAL SEQUENCE

The crew installed the near-field hardware in the glovebox, attached the far-field box to the glovebox, and positioned the video cameras. The operator then ran the self-diagnostic procedures on the two smoke detectors and activated the video cameras, turned on the ignitor for a predefined period of time (15 to 60 sec), and initiated the thermophoretic soot samplers to sample the smoke. The actual duration of each combustion event was typically 2 min. After the experiment, the operator stowed and reloaded the soot samplers, the test sample, and the filters at the end of the return line from the far-field box. At this point the operator either stowed the modules or initiated another run. The tests ran very efficiently and after the first two sessions, typically ran ahead of schedule. The sessions consisted of two to seven runs each. The majority of the tests were run with predefined igniter power levels; however, to examine the response threshold, some of the tests in the final session were conducted repeatedly on the same samples at small increases of power level for each retest.

7.6 DATA REDUCTION

After flight, the particulates collected on the thermophoretic probes were analyzed using a transmission electron microscope (TEM) to determine primary and aggregate particle dimensions. The remains of the samples were weighed to determine their mass loss. The digital data were transcribed from the video record and analyzed to determine the response of the detectors. Once the flight mass loss rates were determined, 1 g operation conditions to produce the same loss were determined. These conditions are being used to produce a 1 g comparison data set.

7.7 RESULTS

In all, 25 tests were performed and the data from the runs are summarized in table 7-1, which lists the mass loss rate of the sample, the time it took for the signal to reach a value of 20 percent of the operating range of the detector, and the time and value of the peak signal for both detectors. Since these tests were designed to function as a test of the detection technologies rather than the detectors themselves (or their alarm set points), 20 percent of the dynamic range was selected to tabulate as a consistent detection point for both detection technologies. The selection of the actual alarm level for each detector is more complex than mere detection as false alarm rejection and other issues must be considered. The bulk of the tests were overheated material tests in which the heating level was established to produce a target weight loss rate without causing the sample to develop a sustaining combustion reaction. The intent of these tests was to produce smoke typical of an incipient fire where much of the material is being heated but has not yet ignited. The candle tests and one of the paper tests were combustion tests where the samples were ignited so the combustion products could be observed. Figures 7-6 to 7-9 contain the signal data from two typical candle tests, one Kapton™ and one silicone rubber, respectively. The response of the smoke detectors, the

ignitor voltage and the signal for the lasers in the near-field module are plotted with respect to time. As plotted, the data for the *ISS* detector overstates the sensitivity of the flight unit since the unit used here is 6.6 times more sensitive than the flight model. These tests were neither designed nor expected to reach specific alarm levels. Instead the tests were planned to provide a measure of the relative sensitivity of the two detector types to low gravity smoke particulate by providing sufficient particulate to achieve adequate signal levels on the detectors. To explore the effect of heating rate on particle size, the different tests with each material were conducted at different ignitor power levels. The results of the tests are discussed below by sample type.

7.7.1 Candle Tests

In all tests the detector's signals showed an immediate peak that is attributed to the wax vapor released by the ignition process. This peak was detected more quickly by the *ISS* detector. Once the candle was ignited, the *STS* detector showed strong signals for all tests while the *ISS* detector showed strong signals for tests 1 and 16 (e.g., fig. 7-6) and very weak signals (if unamplified) for tests 6 and 11 (fig. 7-7). The cause of this is still under investigation.

7.7.2 Paper Tests

Runs 5g, 10 and 25e were pyrolysis runs, i.e., they did not produce a flame but instead allowed the paper to degrade into precombustion or pyrolysis products. Of these, run 10 showed appreciable mass loss and was readily detected by the *ISS* detector while the *STS* detector produced marginal signal. In contrast, 1 g comparison tests show strong signals on both detectors. Runs 5g and 25e were the last runs in a series of tests aimed at finding the threshold detection level for the sample. These tests showed slightly higher signals for the *ISS* detector; however, if scaled to real detector performance (i.e., unamplified) neither detector showed distinct signal. Test 20 was a flaming test of a small paper sample and showed a marginal advantage for the *STS* detector. Test 15 was intended to be a pyrolysis test but self-heating caused the sample to develop a self-sustaining smolder reaction late in the test. The *ISS* detector detected both the pyrolysis and flaming intervals while the *STS* detector only detected the smoldering interval.

7.7.3 Teflon™ Wire Tests

Both detectors showed strong signals for tests 3, 13, and 18. On test 8, however, the *STS* detector showed minimal signal and the *ISS* had a weak signal (unamplified). For test 21 the *STS* detector showed a weak signal compared to no signal (even amplified) for the *ISS* detector. Test 23b showed no signal for either detector.

7.7.4 Silicone Rubber Tests

For all of the tests with silicone rubber, the *ISS* detector showed very strong signals while the *STS* detector showed at most a weak signal (fig. 7-8). This is contrary to 1 g comparison test results where this material also shows a strong signal on the *STS* detector.

7.7.5 Kapton™ Wire Tests

Both detectors showed strong signals for 4, 9, 14 and 19 with both producing low signals (*STS* slightly higher) for test 24 which was a low-mass-loss test.

7.8 TEM RESULTS

Thermophoretic sampling has been used previously in the drop tower for gas jet diffusion flames and for overheated wires.^{5,6} The technique takes advantage of the tendency of small particulates to move toward and attach to cool objects. For the overheated but not burning materials, a weak thermal gradient was expected and consequently the probe was left in place for 45 sec while in the case of the much hotter candle flame the probe was left in for less than a second. When the probes were returned to Earth, the grids were removed and analyzed in a TEM to determine the primary particle and aggregate size distribution. Timing of the deployment of the soot sampler required rapid subjective decisions by the crew member. Based upon our video record, they did an excellent job. We encountered less stable flow of the smoke plume than we anticipated and had a high rate of loss of TEM grids due to failure of the adhesive. Consequently particulate samples were not obtained on all tests.

Figures 7-10a to 7-10c contain TEM images of typical particulate from Teflon™, Kapton™, and candle tests. The three images are at the same magnification and show the significant variation in the particulate morphology for the three materials.

Table 7-2 summarizes the results for the tests for which good sampling was achieved. Significantly, despite strong smoke levels visible in the video record, no particulate material was found on the TEM grids for overheated paper and silicone rubber tests. The suspected cause of this is that the particulate for these materials is actually liquid droplets which later evaporate or spread out on the grids' surface, rendering them undetectable by the TEM. The primary particle dimensions range from 30 to 40 nm for soot to 60 to 100 nm for Kapton™ and 130 to 200 nm for Teflon™. The aggregate soot dimensions grow with distance from the candle from 400 nm at 15 mm from the wick to 1,200 nm at 35 mm from the wick. The Kapton™ aggregates range from 220 to 250 nm and the Teflon™ aggregates range from 600 to 1,100 nm. The dimensions reported in table 7-2 are geometric averages (averages based on a log-normal size distribution). The probe center lines were 10 mm apart along the flow axis and are numbered sequentially beginning with the probe nearest to the sample. Each probe assembly inserted the four probes simultaneously. The size of the candle aggregates grew with distance from the candle, reaching 1.2 μm . The rejection criteria for the inertial separation in the STS detector is based on a 1-to 2- μm particle mass. Since the soot from these tests was still very successfully detected, apparently soot particles of 1.2 μm have not reached the rejection mass level. The Teflon™ and Kapton™ samples produced large primaries with the largest occurring in Teflon™ test 13 (195 nm); the resultant aggregates were 1.1 μm .

7.9 DISCUSSION

Data analysis and interpretation are well underway but have not yet been completed. The companion 1 g test program is also underway but incomplete. However, the smoke produced in the low g silicone rubber and paper tests was thick and clearly visible while in comparable 1 g tests, it was only marginally visible for the same mass loss rate. This can be explained by the absence of buoyant flows which (in 1 g) dramatically accelerate the gas velocities in the vicinity of the source, reducing the residence time of the particulate in regions of high concentration. Since particulate sizes for the smoke from these two materials

could not be obtained with TEM analysis, the reasons for the lower signal levels from the STS detector can only be inferred. It is likely that these droplets had more opportunities to coalesce into droplets whose size exceeded the maximum size for which the STS detector is sensitive (1 to 2 μm). For very low mass loss tests for wire insulation materials, the STS detector showed more signal than the *ISS* model. Once the 1 g comparison tests are complete, further analysis of the results will be possible.

7.10 CONCLUSIONS

The CSD experiment successfully produced controlled quantities of smoke particulate from a variety of sources. The response of the STS and *ISS* detectors to these smoke sources was measured and samples of the smoke particulate were successfully obtained from many of the tests. The assembled data provide the first examination of the response of spacecraft smoke detectors to microgravity smoke particulate.

The most significant conclusion to be drawn so far from this work is that sensitivity to the smoke from an individual material in 1 g does not indicate strong sensitivity to the smoke from the same material in low g. Despite the presence of a forced flow (provided by a fan) in the low g tests, the absence of buoyant flows apparently changed the particle size distribution. We have not yet determined if the change is sufficiently systematic to obtain correlations. Both detectors showed responsiveness for the majority of materials; the STS detector showed limited sensitivity to pyrolyzing materials that produce liquid particulate. The particle dimensions covered a wide range from 30 to 200 nm for primary particles and from 220 to 1,200 nm for aggregates.

REFERENCES

1. Dietrich, D.: personal communication, 1997.
2. Friedman, R.: "Fire Safety Practices and Needs in Human-Crew Spacecraft," *Journal of Applied Fire Science*, Vol. 2, pp. 243–259, 1992.
3. Friedman, R.; Sacksteder, K.; and Urban, D.: "Risks, Designs and Research for Fire Safety in Spacecraft," *NASA TM 105317*, 1991.
4. Friedman, R.; and Dietrich, D. : "Fire Suppression in Human-Crew Spacecraft," *NASA TM 104334*, 1991.
5. Ku, J.C.; Griffin, D.W.; Greenberg, P.S.; and Roma, J.: "Buoyancy-Induced Differences in Soot Morphology," *Combustion and Flame*, Vol. 102, pp. 216–218, 1995.
6. Paul, M.; Issacci, F.; Apostalakis, G.E.; and Catton, I.: "The Morphological Description of Particles Generated from Overheated Wire Insulations in Microgravity and Terrestrial Environments," *Heat Transfer in Microgravity System*, 1993, S. S. Sadhal and A. Hashemi eds, ASME-HTD, Vol. 235, pp. 59–66, 1993.
7. Greenberg, P.S.; Sacksteder, K.R.; and Kashiwagi, T.: "Wire Insulation Flammability Experiment: USML–1 1 Year Post Mission Summary," Joint Launch + 1-Year Science Review of USML–1 and USMP–1 with the Microgravity Measurement Group. *NASA CP 3272 V II*, 1995.
8. Bukowski, R.W.; and Mulholland, G.W.: "Smoke Detector Design and Smoke Properties," NBS Technical Note 973, 1978.
9. Chuan, R. L.; and Chen. H. D. : "Aerosol Characterization in an Incipient Fire," Second International Aerosol Conference, Berlin, Sept., 1986.
10. Steisslinger, H. R.; Hoy, D.M.; McLin, J.A.; and Thomas, E. C.: "Comparison Testing of the Space Shuttle Orbiter and *Space Station Freedom* Smoke Detectors," *SAE Paper 932291*, Warrendale, PA, 23rd International Conference on Environmental Systems, Colorado Springs, Colorado, July, 1993.
11. McLin, J.: "Smoke Comparison Test Report Doc. No. 93–05902," Allied Signal Aerospace, 1993.

Table 7-1. Detector signals from CSD flight tests (*ISS* values are scaled to flight detector sensitivity)

ISS Detector					STS Detector				
Test Point	Time to 20% (sec)	Time to Max (sec)	Vol. Max.	% Max.	Time to 20% (sec)	Time to Max. (sec)	Vol. Max.	% FS at Max.	Mass loss Rate
10 (Paper)	31	33	7.22	29.6	—	—	—	—	43.4
15 (Paper)	20	21	7.21	29.5	54	61	9.2	91.7	consumed
20 (Paper)	—	24	1.56	6.1	—	18	11.27	5.8	consumed
25e (Paper)	—	73	0.75	0.2	—	89	11.34	4.1	multiple tests
5g (Paper)	—	71	0.74	2.1	—	70	11.37	1.3	multiple tests
1 (Candle)	61	62	7.2	29.6	—	82	9.65	73.4	consumed
6 (Candle)	—	70	2.3	9.2	—	67	10.55	36.0	consumed
11 (Candle)	69	69	6.88	28.3	35	75	9.9	9.9	consumed
16 (Candle)	45	49	7.21	29.2	47	108	9.53	9.5	consumed
2 (Silicone Rubber)	20	20	7.22	30.1	—	82	11.14	11.6	107
7 (Silicone Rubber)	18	19	7.22	30.1	—	44	11.24	7.4	58.7
12 (Silicone Rubber)	21	23	7.23	30.1	—	31	11.39	1.2	130
17 (Silicone Rubber)	16	17	7.22	30.1	—	39	11.21	8.7	128
22 (Silicone Rubber)	32	34	7.24	30.2	—	52	11.28	6.9	15.2
3 (Teflon™)	55	62	7.23	34.5	72	76	10.88	22.6	86.2
8 (Teflon™)	—	61	4.18	16.9	—	67	11.27	6.6	141
13 (Teflon™)	27	27	7.21	29.6	—	35	11.17	10.0	155
18 (Teflon™)	31	32	7.22	29.6	39	42	10.92	20.3	143
21 (Teflon™)	—	78	0.29	0.8	—	81	11.29	6.5	47.9
23a (Teflon™)	—	46	0.51	1.7	—	59	11.36	2.5	multiple tests
4 (Kapton™)	14	15	7.21	29.6	25	37	10.1	54.4	37.5
9 (Kapton™)	14	23	7.23	29.7	28	37	10.64	32.5	56.5
14 (Kapton™)	13	14	7.21	29.6	24	33	10.19	50.8	106
19 (Kapton™)	10	10	7.21	29.6	25	30	10.36	43.6	99.4
24 (Kapton™)	—	28	0.88	3.3	—	74	11.09	14.3	4.29

Table 7-2. TEM results

Test Point	Probe Number	Primary Diameter (nm)	Aggregate Diameter (nm)
1 (Candle)	1	44	417
	2	33	742
	3	39	1185
16 (Candle)	2	38	710
	4	32	1252
8 (Teflon™)	1	136	608
	4	134	—
13 (Teflon™)	1	195	1084
	2	154	669
9 (Kapton™)	1	79	234
	4	95	253
19 (Kapton™)	3	74	119
	4	85	184
20 (Flaming Paper)	1	29	406
	2	26	425
	3	24	301

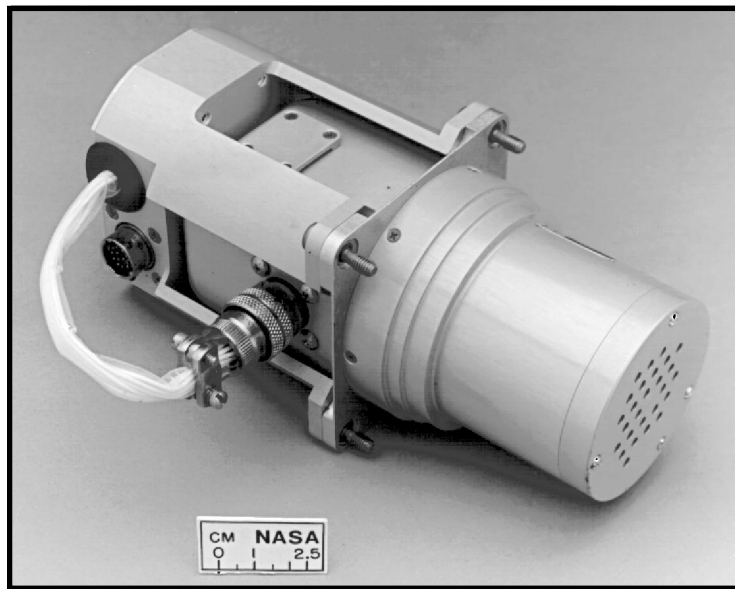


Figure 7-1. Photograph of the detector used in the orbiter (STS) fleet and on Spacelab. The air enters from the right and is exhausted out the port under the small plate on the top left.

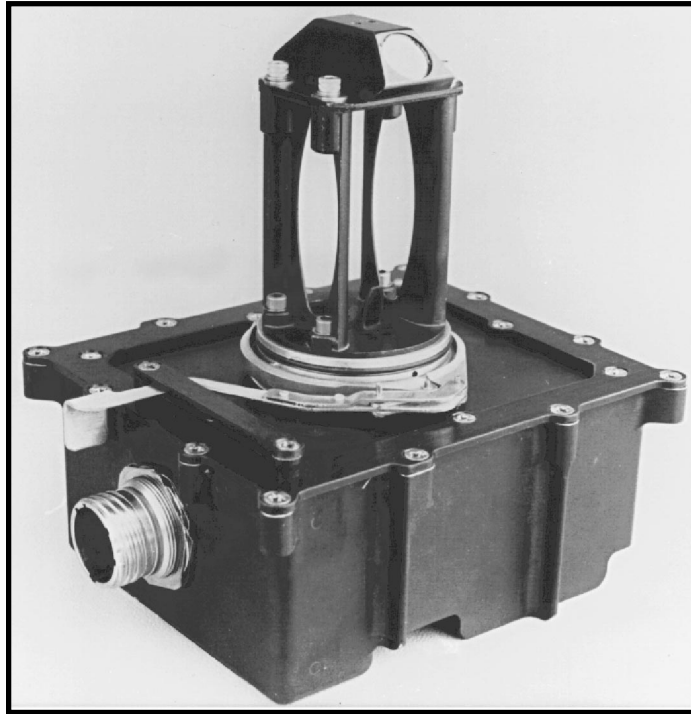


Figure 7-2. Photograph of an engineering model of the *ISS* smoke detector. The lasers and other electronics are in the black enclosure below and the laser beam passes through the space enclosed by the framework on the top, reflecting off of turning mirrors at the top.

CSD System Schematic

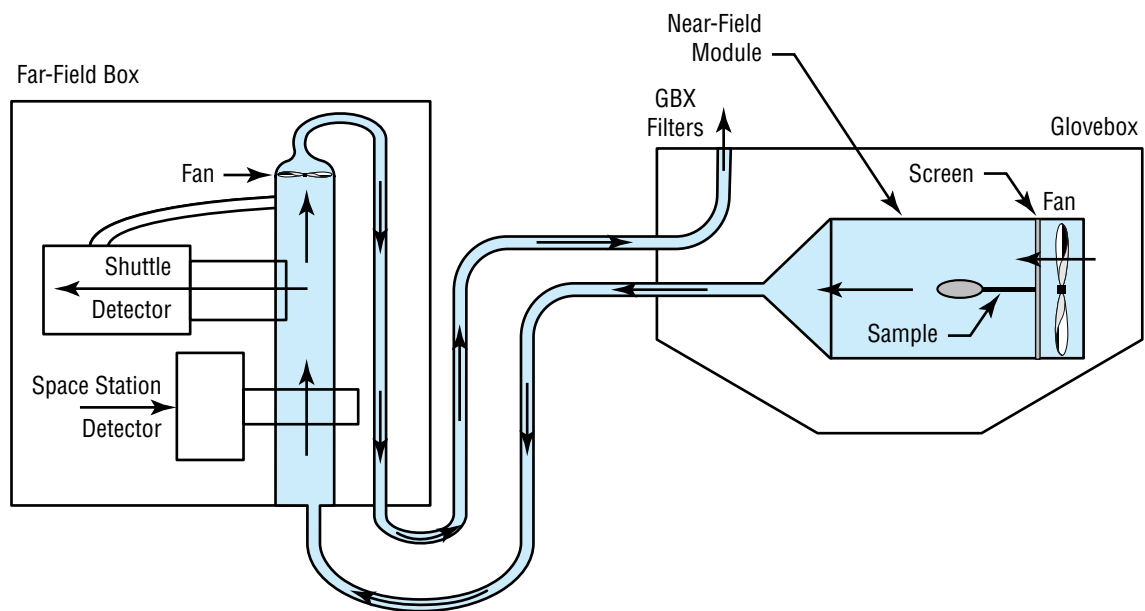


Figure 7-3. Schematic showing installation of the CSD near-field module inside the glovebox and far-field module outside of the glovebox.

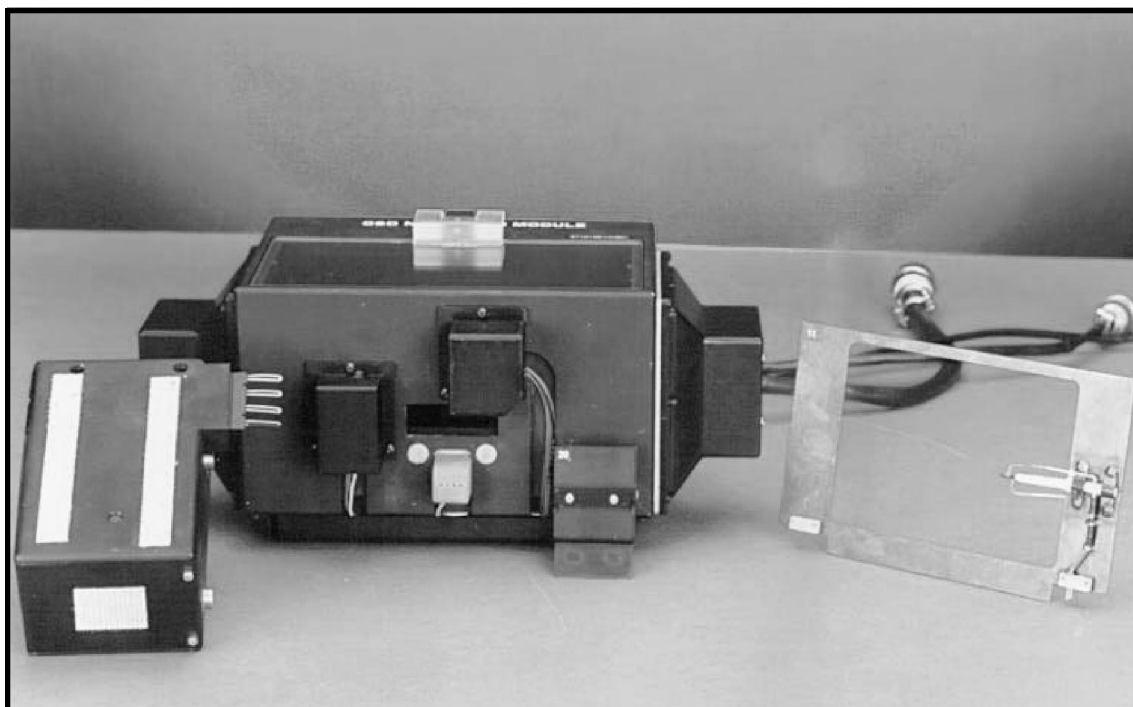


Figure 7-4. Photograph of the near-field module. The soot sampler assembly (probes extended) is on the left, and is installed in a hole in the center of the near-field module. A sample card with a candle installed is on the right.

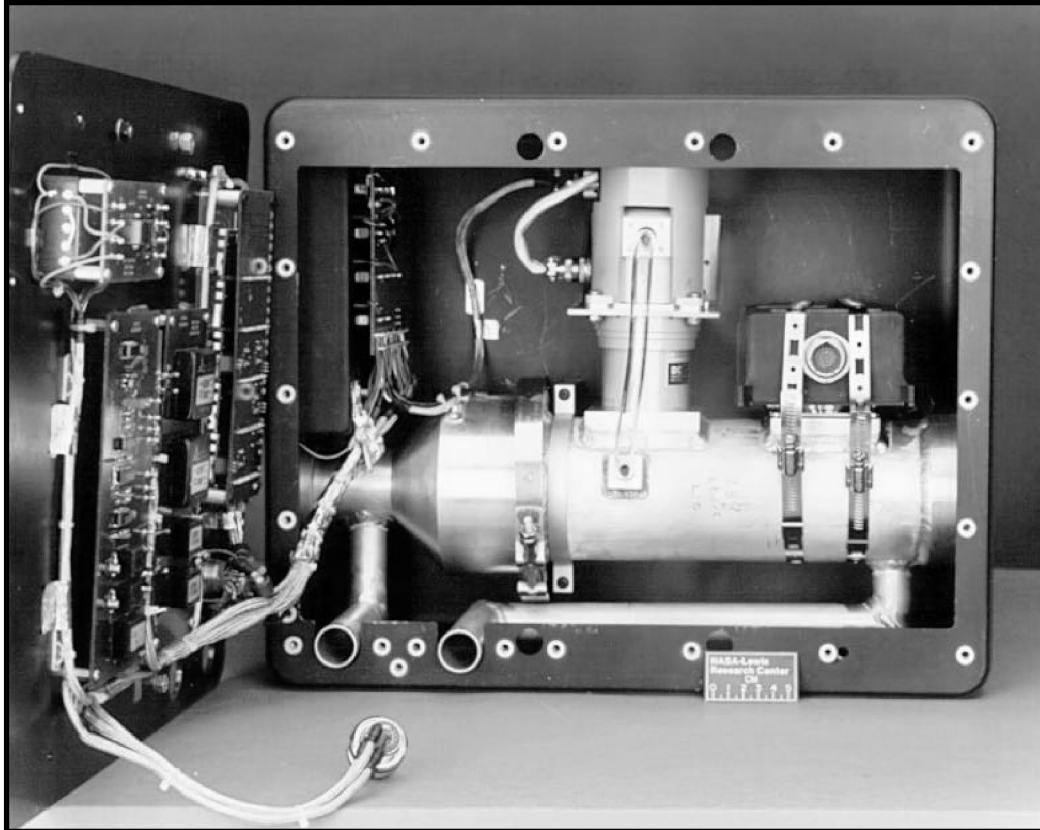


Figure 7-5. Photograph of the inside of the far-field box. The STS detector is the aluminum module in the center of the duct and the *ISS* detector is the black module on the right.

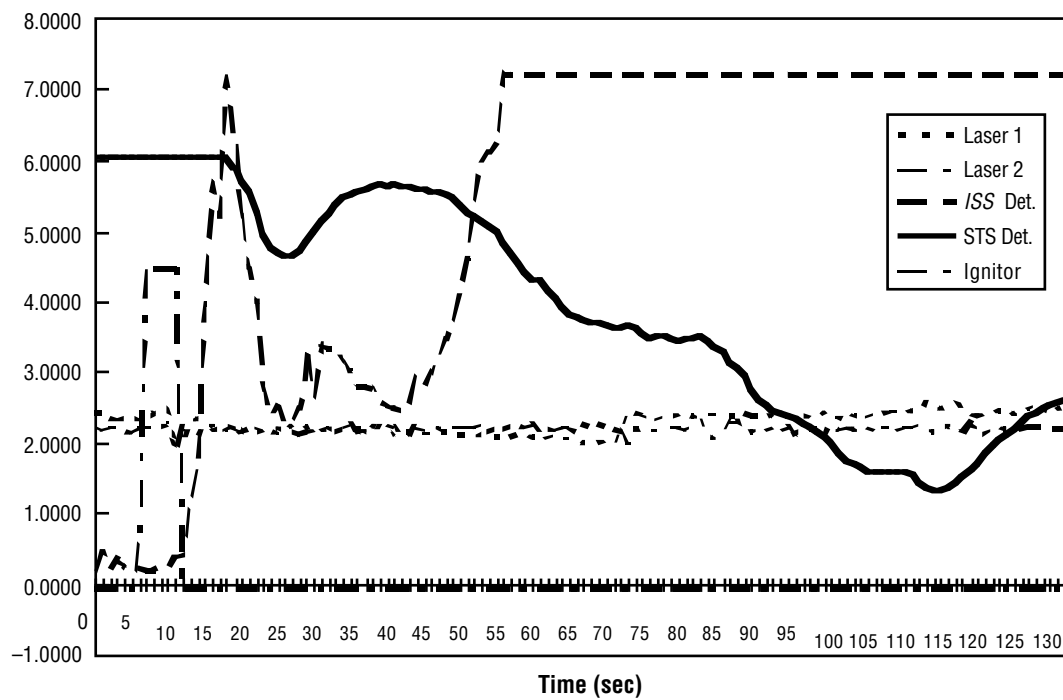


Figure 7-6. Traces of smoke detector signals as a function of time for a candle test No. 6. Initial peak on both detectors is wax vapor released by the ignition process. The units on the vertical axis are arbitrary; the smoke detector data have been scaled so their dynamic ranges have similar vertical extent.

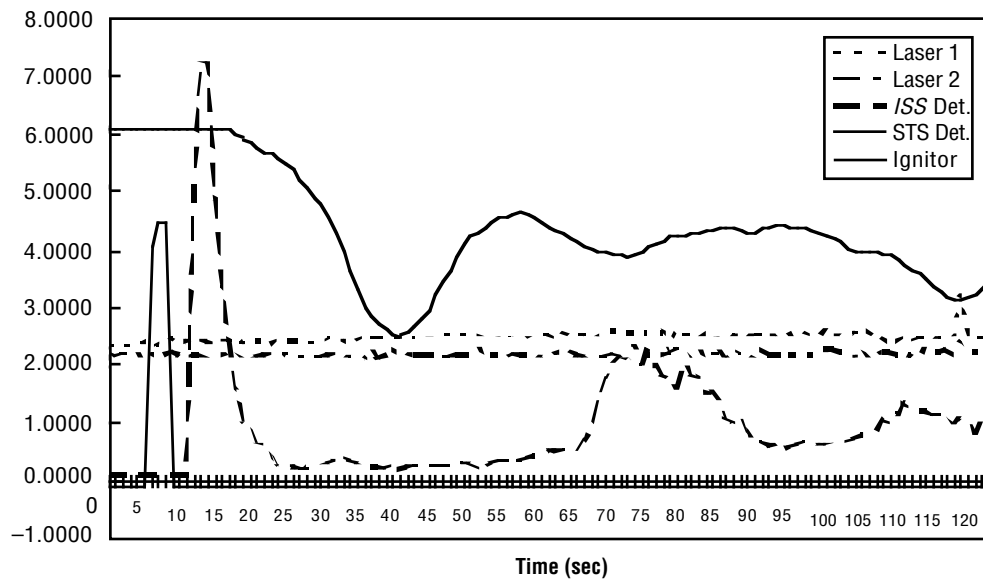


Figure 7-7. Traces of smoke detector signals as a function of time for a candle test No. 6. Initial peak on both detectors is wax vapor released by the ignition process. The units on the vertical axis are arbitrary; the smoke detector data have been scaled so their dynamic ranges have similar vertical extent.

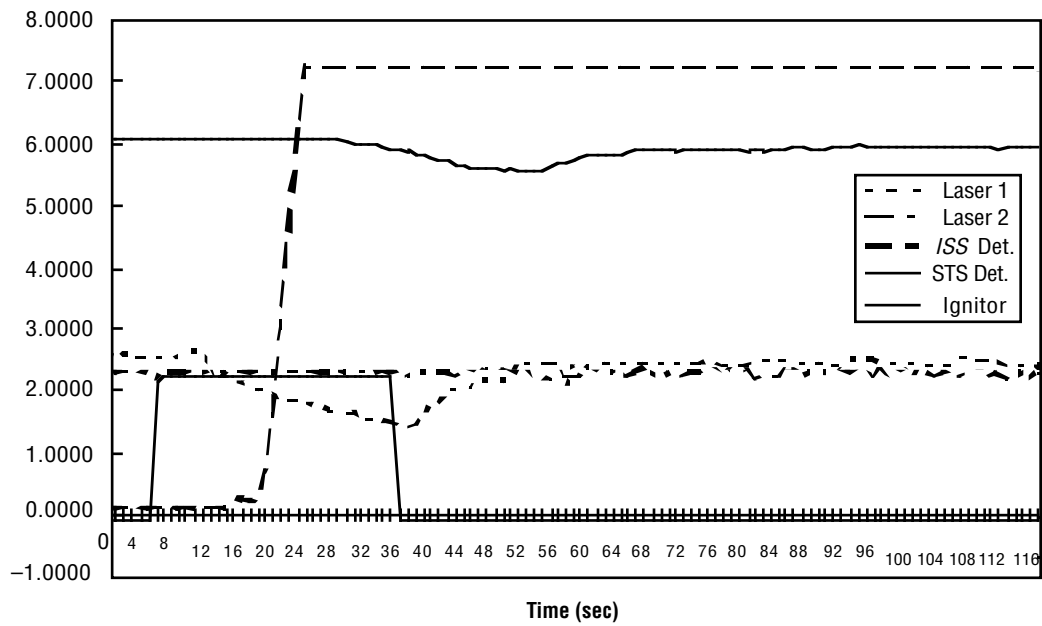


Figure 7-8. Traces of smoke detector signals as a function of time for a silicone rubber test No. 7. The units on the vertical axis are arbitrary; the smoke detector data have been scaled so their dynamic ranges have similar vertical extent.

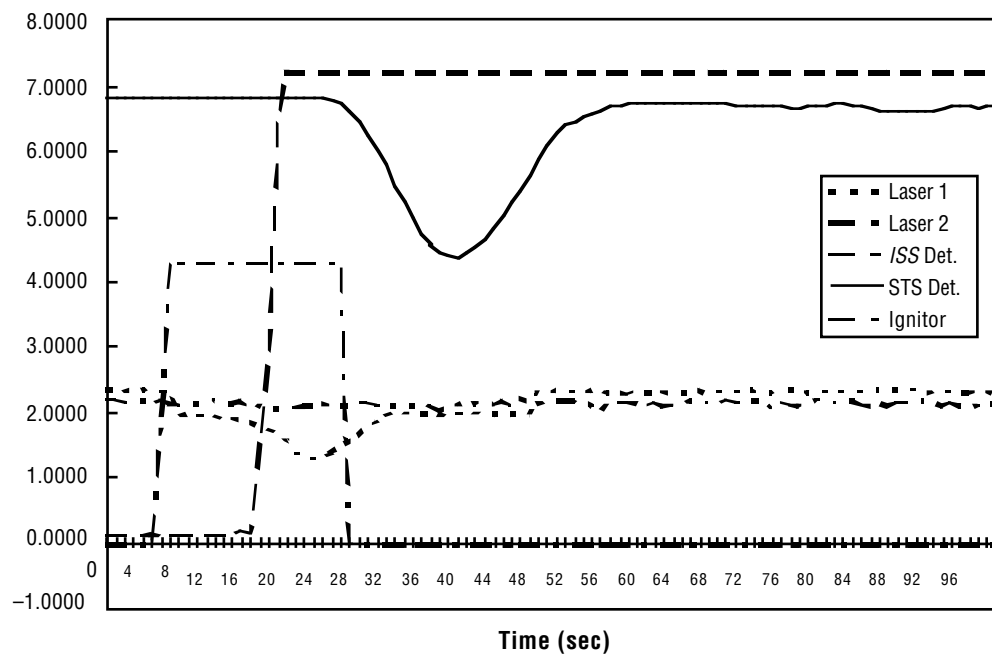


Figure 7-9. Traces of smoke detector signals as a function of time for a Kapton test No. 4. The units on the vertical axis are arbitrary; the smoke detector data have been scaled so their dynamic ranges have similar vertical extent.

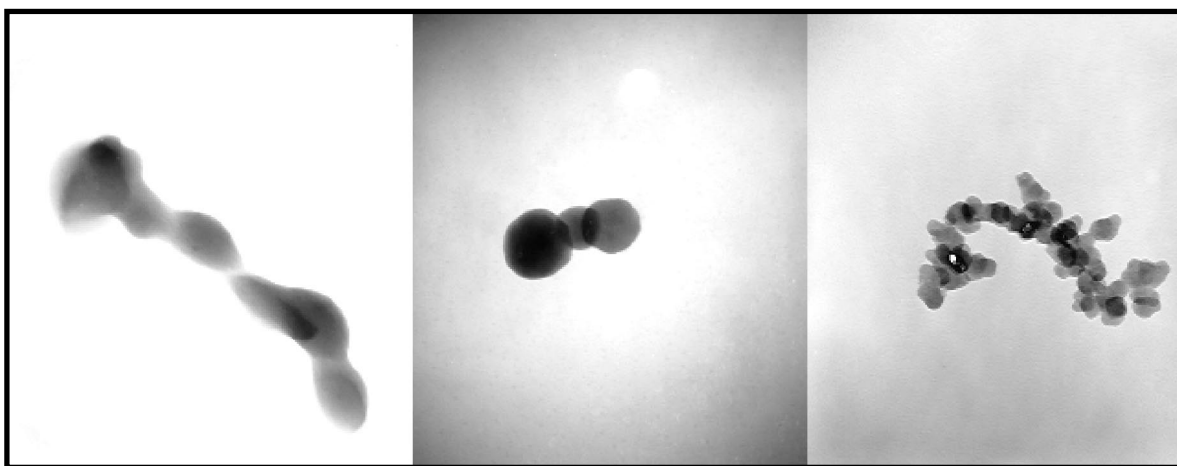


Figure 7-10. From left to right images of microgravity particulate from overheated Teflon™ and Kapton™ and Candle soot.

SECTION VIII.

PRINCIPAL INVESTIGATOR MICROGRAVITY SERVICES—USMP-3

Acknowledgments

Alan Bachik, Code DF at NASA Johnson Space Center (JSC), provided information about the Flight Control System Checkout procedure. Quinn Carelock, Code DF82 at JSC, provided information about the waste collection system and timing for compaction operations during STS–75. Kenneth J. Welzyn and Edward Litkenhaus of NASA Marshall Space Flight Center, Jeffrey Zelicksen of CAS Inc., and Nestor Voronka of the University of Michigan provided information and data pertinent to operations of the Tethered Satellite System. Michael Moses, Code DFG with Rockwell Space Operations Co. at JSC, provided thruster firing information. Ku band antenna information was provided by Richard La Brode, Code DF, Rockwell International at JSC. Brenda Eliason, with Rockwell International at JSC, provided the STS–75 Green Book which summarized the as-run mission activities.

PRINCIPAL INVESTIGATOR MICROGRAVITY SERVICES—USMP-3

Melissa J. B. Rogers, Kenneth Hrovat, Milton E. Moskowitz, Timothy Reckart

Tal-Cut Company

North Olmsted, Ohio

Kevin M. McPherson and Richard DeLombard

NASA Lewis Research Center

Cleveland, Ohio

8.1 ABSTRACT

Two accelerometers provided acceleration data during the STS-75 mission in support of the third United States Microgravity Payload (USMP-3) experiments. The Orbital Acceleration Research Experiment (OARE) and the Space Acceleration Measurement System (SAMS) provided a measure of the microgravity environment of the Space Shuttle Columbia. The OARE provided investigators with quasi-steady acceleration measurements after about a 6-hour time lag dictated by downlink constraints. SAMS data were downlinked in near real time and recorded onboard for postmission analysis. These two accelerometer systems are briefly described.

Using a combination of data analysis techniques, the microgravity environment related to several different orbiter, crew, and experiment operations is presented and interpreted. The microgravity environment represented by SAMS and OARE data is comparable to the environments measured by these instruments on earlier microgravity science missions. Thruster activity on this mission seen in the SAMS data appears to be more frequent than on other microgravity missions with the combined firings of the F5L and F5R jets producing significant acceleration transients. Of the events studied, the crew activities performed in the middeck and flight deck, Shuttle Potential and Return Electron Experiment (SPREE) table rotations, a waste collection system compaction, and a fuel cell purge, had negligible effects on the microgravity environment of the USMP-3 carriers. The Ku band antenna repositioning activity resulted in a brief interruption of the ubiquitous 17-Hz signal in the SAMS data. In addition, the auxiliary power unit operations during the flight control system checkout appeared to have a significant impact on the microgravity environment.

8.2 INTRODUCTION

Microgravity science experiments are conducted on the NASA Space Shuttle orbiters to take advantage of the reduced gravity environment available in low-Earth orbit. Accelerometer systems are flown in conjunction with these experiments to record the microgravity environment to which they are subjected. The USMP-3 and the Tethered Satellite System (TSS-1R) flew on the orbiter Columbia on mission STS-75 from February 22 to March 9, 1996. OARE and SAMS (managed by the NASA Lewis Research Center (LeRC)) flew to support the USMP-3 experiments:

The Principal Investigator Microgravity Services (PIMS) project at NASA LeRC supports principal investigators of microgravity experiments as they evaluate the effects of varying acceleration levels on their experiments. During the STS-75 mission, PIMS provided real-time displays of the SAMS data to the investigator teams, enabling them to make appropriate parameter adjustment decisions pertaining to their experiments. PIMS also provided OARE data plots to users as the data became available. The data were delayed due to downlink constraints. PIMS performed specific processing of archived SAMS and OARE data for USMP-3 and TSS-1R investigators so they could perform indepth analyses of their experiment results during the mission.

This report summarizes the microgravity environment of Columbia during the STS-75 mission. The following sections give some detail about the accelerometer systems, including the real-time data acquisition, processing, and display operations PIMS performed during the mission. Finally, the effects of specific mission and payload activities on the microgravity environment are detailed.

8.3 ORBITAL ACCELERATION RESEARCH EXPERIMENT

The OARE measures quasi-steady accelerations from below $1 \times 10^{-8} \text{ g}$ up to $2.5 \times 10^{-3} \text{ g}$, where $1 \text{ g} = 9.81 \text{ m/s}^2$. The OARE consists of an electrostatically suspended proof mass sensor, an in-flight calibration subsystem, and a microprocessor which is used for in-flight experiment control, processing, and storage of flight data.¹⁻⁴ The acceleration sensor's output signal is filtered using a Bessel filter with a cut-off frequency of 1 Hz. The output signal is digitized at 10 samples per sec and is then processed and digitally filtered with an adaptive trimmean filter prior to electronic storage onboard. During STS-75, a system write fault resulted in the corruption of the data stored electronically within OARE. The unprocessed data were recorded on the orbiter payload tape recorder. At regular intervals during the STS-75 mission, the unprocessed OARE data were downlinked from the orbiter to the MSFC Payload Operations Control Center (POCC). The POCC data reduction team transferred files of downlinked data to PIMS computers in the POCC. The PIMS computers processed the OARE data and displayed data for the PI's using the World Wide Web and the POCC video matrix.

The OARE was mounted to the floor of Columbia's cargo bay on a keel bridge, close to the orbiter center of gravity. The approximate location and orientation of the sensors are given in table 8-1 and figure 8-1. In this report, the OARE data are presented in terms of the orbiter body coordinate system. Figure 8-2 indicates the difference between the orbiter body and structural coordinate systems. The subscript *b* represents the orbiter body coordinate system. The subscript *o* is used to indicate the orbiter structural

coordinate system. The OARE data sign convention used here is such that when there is a forward thrust of the orbiter, it is reported as a negative x_b acceleration. We refer to this convention as being consistent with a frame of reference fixed to the orbiter. OARE data are available from MET 000/00:10 to 015/21:03.

8.4 SPACE ACCELERATION MEASUREMENT SYSTEM (SAMS)

The SAMS is used to measure the low-gravity environment of orbiters in support of microgravity science payloads.⁵⁻¹⁰ STS-75 was the 14th SAMS flight on an orbiter. Two SAMS units flew on STS-75. One SAMS unit was located on each MPRESS carrier in support of USMP-3 experiments. The unit designated SAMS-1 (also called Unit F) was located on the forward carrier and used two triaxial sensor heads to support the AADSF and MEPHISTO experiments. The signals from these two triaxial sensor heads were filtered by low pass filters with cut-off frequencies of 10 Hz (TSH 1A) and 25 Hz (TSH 1B). These signals were then sampled at 50 and 125 samples per sec, respectively. TSH 1A data were downlinked in near real time during the mission, and data from TSH 1B were recorded onboard using SAMS optical disks.

The unit designated SAMS-2 (also called Unit G) was located on the aft carrier and used three triaxial sensor heads to support the IDGE and Zeno experiments. The signals from these three triaxial sensor heads were filtered by low pass filters with cutoff frequencies of 5 Hz (TSH 2A), 10 Hz (TSH 2B), and 25 Hz (TSH 2C). These signals were then sampled at 50, 50, and 125 samples per sec, respectively. Data from TSH 2A and TSH 2C were alternately downlinked or recorded on optical disks on board. Data from TSH 2B were recorded on optical disks. In general, TSH 2C data were downlinked early in the mission, while TSH 2A data were downlinked later in the mission. In this report, the SAMS data are presented in terms of the orbiter structural coordinate system. The SAMS data sign convention used here is such that when there is a forward thrust of the orbiter it is recorded as a negative x_o acceleration. We refer to this convention as an inertial frame of reference fixed to a point in space. The orientations and locations of the SAMS heads, with respect to the orbiter structural coordinate system, are given in table 8-2 and figure 8-3. For STS-75, a total of approximately 3.5 gigabytes of SAMS data are available between MET 000/02:57 and 014/11:13.

The SAMS data that were downlinked were routed to PIMS computers in the POCC. The PIMS computers processed the SAMS data from both units and displayed data for investigators using the World Wide Web and the POCC video matrix. Additionally, Teledyne Brown Engineering personnel modified SAMS data display software so that the crew could capture the SAMS data stream and display it on a laptop computer. The display was a scrolling plot of 10 sec of the three axes of one unit of SAMS data, with a delay of about 20 sec. This was the first time an orbiter crew was able to use SAMS data to get real-time feedback on the effects of their activities and orbiter operations on the microgravity environment.

8.5 SAMS AND OARE DATA ANALYSIS

The data recorded by SAMS on STS–75 were processed to correct for premission bias calibration offsets and to compensate for temperature and gain related errors of bias, scale factor, and axis misalignment. The resulting units of acceleration are g's where $1\text{ g}=9.8\text{ m/sec}^2$. The data were orthogonally transformed from the five SAMS TSH coordinate systems to the orbiter structural coordinate system. The OARE data recorded during STS–75 and presented here have been compensated for temperature, bias, and scale factors¹¹ and orthogonally transformed to the orbiter body coordinate system.

After this initial data correction phase, data analyses were applied to the SAMS and OARE data to characterize the acceleration environment of the mission. Because of the inherent differences between OARE (frequency range 10^{-5} Hz to 1 Hz, sampling rate 10 samples per sec) and SAMS (frequency range 0.01 Hz to 25 Hz, sampling rate 50 to 125 samples per sec on STS–75) data, some data analysis techniques are more applicable to data from one system than the other. The particular processing technique used also depends on the type of information desired.¹⁵

8.6 COLUMBIA MICROGRAVITY ENVIRONMENT—STS–75

This section discusses the microgravity environment of the orbiter Columbia during the STS–75 mission as recorded during a specific crew activity that was performed for environment characterization, during several thruster firing events, during SPREE rotary table operations, during a Ku band antenna repositioning, during the flight control system checkout, during the Tethered Satellite System deploy and tether separation, during a waste collection system compaction operation, during a fuel cell purge, and while the orbiter was positioned in different attitudes.

8.6.1 Crew Quiet Time Test

Prior to the mission, the crew members were interested in performing specific activities to demonstrate how they could operate quietly to minimize crew-induced disturbances to the microgravity environment. Conversations with STS–75 crew members and mission planners resulted in a suite of activities that were performed during a block of time between TSS–1R operations and the USMP–3 microgravity science operations. After the mission, correlation between the SAMS data and the activities performed by the crew were determined using video tape and crew notations of the activities.

The activities were conducted from MET 006/15:00 to 006/15:37 and included normal crew actions involving the middeck lockers, galley equipment, crew equipment (bunks, footloops, and cameras), the waste collection system, crew motions, cabin air fans, and thruster operations. The crew members were basically quiet during this demonstration time. Analyses of SAMS data collected during this period indicate no apparent correlation between the crew activities and the acceleration levels. Note, however, that with the SAMS sensors located on the MPESS carriers, these data indicate how the activities of the crew in the middeck and flight deck of the orbiter affected the microgravity environment at the location of the sensitive USMP–3 experiments. The data do not represent what the environment was at the site of the activity, and we can draw no conclusions about the effects of these same activities on the acceleration environment of

the middeck, flight deck, or of a Spacelab module that may house sensitive experiments while such activities are occurring in the orbiter.

8.6.2 Attitude Adjustment and Maintenance

Orbiter attitude adjustment and maintenance is performed using the Reaction Control System (RCS) and the Orbital Maneuvering System (OMS). STS-75 provided several opportunities to investigate the effects of these systems on the microgravity environment.

Examination of the 10-sec interval average plots of SAMS data reveals a somewhat regular train of short-duration, high-magnitude disturbances most notable in the orbiter z_o -axis data and, to a lesser extent, in the x_o -axis data. Correlation of SAMS data from MET 010/04 with orbiter downlink data confirmed that these disturbances were induced when two Vernier Reaction Control System (VRCS) thrusters (F5L and F5R) were fired simultaneously as required for attitude maintenance with a 1° deadband. See reference 12 for identification of individual RCS jets. Figure 8-4 shows SAMS Unit F TSH 1B data with a 10-sec interval average calculation applied. In figure 8-4 the simultaneous firing of the two thrusters is indicated by the + markers. Note from the o markers that firing either of these thrusters individually leaves little or no evidence in the interval average data. However, when fired in tandem there is an appreciable momentary shift in the DC acceleration levels as evidenced on the x_o - and z_o -axes.

The USMP-3 MEPHISTO experiment focused on mass transport in directionally solidifying Sn-Bi alloys. Part of their experiment was a benchmark study to correlate well-defined acceleration conditions with well-controlled solidification conditions. The acceleration sources used for this study were nine primary RCS (PRCS) firings, one OMS firing, and one orbiter roll maneuver. SAMS Unit F TSH 1B data from three of the PRCS firings are shown in figures 8-5 to 8-7. Note that because the sign convention for the x and z axes are opposite for the orbiter structural and body coordinate systems, the $-z_b$ burn of figure 8-5 causes a shift in the $+z_o$ direction. Reference 13 discusses several PRCS and OMS firings that occurred during STS-75, some of which are the MEPHISTO activities. Table 8-3 compares acceleration level shifts as seen in the SAMS data to dV/dt values obtained from reference 13. While the exact provenance of the dV/dt values is unclear, the correlation shown in the table is significant.

Figure 8-8 is provided as a more detailed view of the accelerations associated with one of the MEPHISTO PRCS events. The 15-sec $-z_b$ axis PRCS 5D maneuver was performed at MET 012/12:25 using the PRCS thrusters L2D, L3D, R2D, R3D, F3D, and F4D.¹³ As seen by the six discretes at the top of figure 8-8, two of the forward thrusters (F3D, F4D) were fired for the entire 15-sec burn. The y -axis components of these two jets negated each other and the z -axis components were additive. This action translated the nose of the orbiter in the $-z_b$ direction, while the tail was translated in the $-z_b$ direction by firing four aft jets (L2D, L3D, R2D, R3D). Note that the aft jets were not fired continuously and these transients are clearly seen in the SAMS z_o data in figure 8-8.

8.6.3 SPREE Rotary Table Operations

The TSS-1R SPREE was designed to measure the charged particle populations around the orbiter. SPREE was mounted on the port side of the TSS-1R MPRESS. The sensors for SPREE were two pairs of electrostatic analyzers, each pair mounted on a motor-driven rotary table. These tables were configured to rotate at 1 r/min. During STS-75, the SPREE experiment team requested rotations during USMP-3

microgravity periods. A series of tests was performed to determine whether or not the rotations had a deleterious effect on the microgravity environment. During an orbiter free-drift period, the two rotating tables were parked and rotated at 1 r/min. The table rotation rate translates to a frequency of ~0.02 Hz. No notable accelerations are seen in the SAMS data, nor are there any evident transients in the data when the table rotations were initiated or ceased. This was analyzed by PIMS during the mission and because there were no evident accelerations related to the SPREE rotations, the USMP-3 Mission Scientist permitted SPREE operations as needed during the microgravity periods. OARE data are not available for this time period because of OARE instrument calibrations operations.

8.6.4 Ku band Antenna Repositioning

The Ku band antenna on the orbiters is used to transmit data and voice communications between the orbiters and ground stations via the Tracking and Data Relay Satellite System satellites.¹⁴ The Ku band deployed assembly is mounted on the starboard sill of the payload bay. It is deployed and activated after the payload bay doors are opened. The antenna dish is edge-mounted on a two-axis gimbal. The alpha gimbal provides a 360° roll movement around the pole of the gimbal. The beta gimbal provides a 162° pitch movement around its axis. The alpha gimbal has a stop at the lower part of its movement to prevent wraparound of the beta gimbal control cable. Periodically, the Ku band antenna beta cabling requires positioning to ensure that it does not become twisted in a way that could cause the antenna to bind. This gimbal flip is achieved by a fast slew of the antenna dish in the direction needed to unwrap the cable.

Figure 8-9 shows a spectrogram generated from SAMS Unit F TSH 1B data for a period in which the Ku band antenna was repositioned. In this figure, the 17-Hz acceleration signal characteristic of the antenna's dither frequency stops at MET 007/13:05:25, and resumes approximately 17 sec later. This break in the usually continuous 17-Hz signal is related to the repositioning activity. During fast slew operations, the 17-Hz dither is disabled.

8.6.5 Flight Control System Checkout

Approximately 1 day before scheduled re-entry, a two-part checkout procedure is performed to verify operations of the orbiter Flight Control System (FCS). The first part of this checkout uses one of the three Auxiliary Power Units (APU's) to circulate hydraulic fluid in order to move the rudder, elevons, and ailerons of the orbiter. As an APU is activated, exhaust gas is vented in the $-z_b$ direction. The result of this venting is similar in nature to a VRCS jet firing, ranging from nearly 0 to 30 lb of force. The exhaust does not vent as a steady stream, but cycles at approximately 1 to 1.5 Hz.

Part one of the FCS checkout on STS-75 lasted for approximately 25 min. Figure 8-10 is a SAMS Unit G TSH 2A spectrogram showing the extent of the first part of the FCS checkout. The activation of APU1 occurred at about 013/15:03, note the sudden change in acceleration characteristics. Of particular note is the appearance of a 1.3-Hz signal and several upper harmonics. These signals remain in the data throughout the checkout period, with slight shifts in the frequencies about 13 and 18 min into the plot. Broadband excitation of the microgravity environment about 4 min into the plot appear to be correlated with changes in APU1 turbine activity as are shorter excitations between 013/15:20 and 013/15:27. Part two of the FCS checkout procedure tests various orbiter electronics systems and did not cause a measurable disturbance to the microgravity environment.

8.6.6 TSS–1R Operations

The USMP–3 investigators were very interested in how the deployment of the TSS–1R satellite would affect the quasi-steady environment of Columbia. OARE data shown in figure 11 depict the quasi-steady environment of the orbiter at the OARE location for a 6-hour period encompassing TSS deploy operations. This plot indicates the microgravity levels prior to TSS satellite deploy, during the flyaway and deploy phases, at the time of the tether break, and after the tether separation.

From an average acceleration level of $x_b=8\times10^{-8}g$, $y_b=-1.8\times10^{-7}g$, $z_b=6.7\times10^{-7}g$ in the orbiter deploy attitude, $PYR=(210^\circ, 10^\circ, 188^\circ)$, the environment changed to $x_b=-1.8\times10^{-5}g$, $y_b=-1\times10^{-7}g$, $z_b=3.7\times10^{-5}g$ at the time of the tether separation. The shift in acceleration levels indicated here is consistent with predictions of the quasi-steady environment with the satellite deployed to 20 km.

Figures 8-12 and 8-13 are two different representations of SAMS data collected during the satellite deploy activities. Figure 8-12 shows SAMS Unit F TSH 1A data with the signal processed using a 30-sec interval average. Figure 8-13 is a spectrogram of SAMS Unit F TSH 1A data for the deploy time. Transient accelerations at about 003/01:40 and between 003/02:00 and 003/03:00 appear in figures 8-11 to 8-13. These are related to orbiter maneuvers during the TSS deploy operations. A series of transients at about 003/01:20 is caused by RCS activity, activated to compensate for TSS dynamics. In the spectrogram there is a band of disturbances that starts between 5 and 10 Hz and ranges up to about 20 Hz. These disturbances appear to correspond to the speed of the deploying TSS cable. The speed of the cable was varied during deployment for experimental investigations and because of coupled TSS and orbiter dynamics. Frequencies of about 6 Hz are consistent with calculations of disturbance frequencies using nominal values for the size of pulleys and the cable speed. Multiple pulleys of various sizes could correspond to the multiple traces in the SAMS spectrogram of figure 8-13. Figure 8-14 shows the response of SAMS Unit F TSH 1A to the break of the TSS tether. The initial response to the break is a ringing at about 9 Hz.

8.6.7 Waste Collection System Compaction

The Waste Collection System is a multifunctional system used primarily to collect and process biological waste from crew members. This system is located in the orbiter middeck. Within the waste collection system is a compactor device which is used to increase the commode capacity. Compaction is typically performed once per flight. The compactor is manually driven using a ratchet wrench. A mobile vane is rotated around on the radius of the commode. Because the compactor only collects and compacts what is already collected in the commode, compaction should not affect venting from the waste collection system vacuum vent. The waste compaction operation was performed at approximately 009/01:32 during STS–75. Analysis of SAMS data indicates that the compaction did not disturb the acceleration environment on the MPSS carriers. OARE data from that time frame indicate no apparent venting forces are associated with the compaction operation.

8.6.8 Fuel Cell Purge

The three fuel cell power plants, through chemical reactions, generate all of the 28-volt direct-current electrical power for the orbiters from launch through landing.¹⁴ The fuel cells are located under the payload bay area in the forward portion of the orbiter's midfuselage. The fuel cell power plants generate heat and water as byproducts of electrical power generation. The water is directed to the potable water storage

subsystem. If the water tanks are full or there is line blockage, the water is vented overboard through the water relief line and nozzle. This vent is indicated in figure 15 (FCP water relief) which is an overview of the orbiter onboard venting locations.

During normal fuel cell operation, it is necessary to cleanse the cells at least twice daily to purge contaminants. H_2 and O_2 purging occurs concurrently, and the venting is directed so that the only noncompensated thrust is in the orbiter y-axis direction. There were no apparent disturbances seen in the OARE or SAMS data associated with a fuel cell purge at 011/02:54.

8.6.9 Orbiter Attitude

The STS-75 mission had several primary attitudes defined for the TSS-1R and USMP-3 payloads. There were a variety of attitudes and orbiter maneuvers before the tethered satellite deployment and after the tether separation during the first 5 days of the mission. The as-flown attitude timeline should be consulted for detailed times and attitude parameters.¹³

The attitude flown for the USMP-3 payload during the majority of the last 8 days of the mission (MET 005/00:15 to 013/14:00) was a gravity gradient attitude $-xlv/+zvv$ ($pyr \sim 95^\circ, 5^\circ, 0^\circ$). This USMP-3 default attitude was chosen to minimize attitude changes, the number of thruster firings, and to reduce the possibility of orbiter debris damage. Variations in the microgravity environment due to orbiter attitudes are best seen in the OARE data. Figure 8-16 is a plot of OARE data for the entire STS-75 mission. Figure 8-17 is an example of the quasi-steady environment related to the nominal USMP-3 attitude.

Three different attitudes were flown during processing of the three AADSF samples on MET days 008, 009, and 010. These AADSF attitudes were designed to result in a quasi-steady vector in line with, against, and transverse to the crystal growth direction. The resulting quasi-steady environment associated with each of these attitudes is represented in figures 8-18 to 8-23.

8.7 SUMMARY

The microgravity environment of the Space Shuttle Columbia was measured during the STS–75 mission using accelerometers from two different instruments, OARE and SAMS. The OARE provided USMP–3 investigators with quasi-steady acceleration measurements after about a 6-hour time lag dictated by downlink constraints. SAMS data were downlinked in near real time in support of the USMP–3 investigators and recorded on board for postmission analysis.

Using a combination of data analysis techniques, the microgravity environment related to several different orbiter, crew, and experiment operations is presented and interpreted. SAMS data are analyzed to determine the effects of specific crew activities, Reaction Control System jet firings, SPREE experiment table rotations, a Ku band antenna repositioning, the FCS checkout, Tethered Satellite System deploy activities, a waste collection system (WCS) compaction, and a fuel cell purge. OARE data are analyzed for the same TSS–1R, WCS, and fuel cell purge operations and for times with different orbiter attitudes.

The specific crew activities performed in the middeck and flight deck, the SPREE table rotations, the WCS compaction, and the fuel cell purge had negligible effects on the microgravity environment of the USMP–3 MPES carriers. Of particular note in the analysis of VRCS data is that the F5L and F5R jets, when fired in tandem, caused appreciably higher magnitude accelerations than expected based on the magnitudes of single firings. The Ku band repositioning activity resulted in a brief interruption of the ubiquitous 17-Hz signal in the SAMS data.

The STS–75 microgravity environment represented by SAMS and OARE data is comparable to the environments measured by the instruments on earlier microgravity science missions. VRCS activity on this mission appears to be somewhat more frequent than on other microgravity missions with the combined firings of the F5L and F5R jets producing significant acceleration transients. Orbiter structural modes and crew exercise frequencies are typically the same among orbiters, missions, and crew members. The main differences among missions are the specific frequencies of equipment oscillations. Better coordination between PIMS and experiment and orbiter systems designers and engineers is needed to help identify the sources of all distinct characteristics of the orbiter microgravity environment. For STS–75, we have expanded our understanding of the effects of orbiter operations on the environment by investigating the Ku band antenna repositioning, WCS compaction, fuel cell purges, and FCS checkout activities. Of these, only the APU operations during the FCS checkout appeared to have a significant impact on the microgravity environment.

REFERENCES

1. Blanchard, R.C.; Hendrix, M.K.; Fox, J.C.; Thomas, D.J.; and, J.Y.: "Orbital Acceleration Research Experiment," J. Spacecraft and Rockets, Vol. 24, No. 6, pp. 504–511, 1987.
2. Blanchard, R.C.; Nicholson, J.Y.; and Ritter, J.R.: "STS–40 Orbital Acceleration Research Experiment Flight Results During a Typical Sleep Period," NASA Technical Memorandum 104209, January 1992.
3. Blanchard, R.C.; Nicholson, J.Y.; Ritter, J.R.: "Preliminary OARE Absolute Acceleration Measurements on STS–50," NASA Technical Memorandum 107724, February 1993.
4. Blanchard, R.C., Nicholson, J.Y.; Ritter, J.R.; and Larman, K.T.: "OARE Flight Maneuvers and Calibration Measurements on STS–58," NASA Technical Memorandum 109093, April 1994.
5. DeLombard, R.; and Finley, B.D.: "Space Acceleration Measurement System description and operations on the First Spacelab Life Sciences Mission," NASA Technical Memorandum 105301, November 1991.
6. DeLombard, R.; Finley, B.D.; and Baugher, C.R.: "Development of and Flight Results from the Space Acceleration Measurement System (SAMS)," NASA Technical Memorandum 105652, January 1992.
7. Baugher, C.R.; Martin, G.L.; and DeLombard, R.: "Low-frequency Vibration Environment for Five Shuttle Missions," NASA Technical Memorandum 106059, March 1993.
8. Rogers, M.J.B.; Baugher, C.R.; Blanchard, R.C.; DeLombard, R.; Durgin, W.W.; Matthiesen, D.H.; Neupert, W.; and Roussel, P.: "A Comparison of Low-gravity Measurements On Board Columbia During STS–40," Microgravity Science and Technology VI/3, pp. 207–216, 1993.
9. Finley, B.D., Grodsinsky, C.; and DeLombard, R.: "Summary Report of Mission Acceleration Measurements for SPACEHAB–01, STS–57," NASA Technical Memorandum 106514, March 1994.
10. "Summary Report of Mission Acceleration Measurements for STS–73," NASA Technical Memorandum 107269, July 1996.
11. Rice, J.E.: OARE Technical Report No. 148, OARE STS–75 (USMP–3) Final Report, CSI–9603, June 1996.

12. DeLombard, R.: "Compendium of Information for Interpreting the Microgravity Environment of the orbiter Spacecraft, NASA Technical Memorandum 107032, August 1996.
13. STS-75 Space Shuttle Mission Report, NSTS-37406, Johnson Space Center, April 1996.
14. Shuttle Operational Data Book, Vol. 1, JSC-08934, Rev. E, Johnson Space Center, Houston, Texas, January 1988.
15. Rogers, M.J.B.; Hrovat, K.; Moskowitz, M.; McPherson, K.; and DeLombard, R.: "Summary Report of Mission Acceleration Measurements for STS-75," NASA Technical Memorandum 107359, November 1996.

Table 8-1. STS-75 OARE Head Location and Orientation

OARE Sensor		Sample Rate: 10 samples/second
Location: Orbiter Cargo Bay Keel Bridge		Frequency: 0 to 1 Hz
Orientation		Location
Orbiter Structural Axis	Sensor Axis	Structural Axis
x_o	$-x_{OARE}$	$x_o = 1,153.3$ in.
y_o	z_{OARE}	$y_o = -1.3$ in.
z_o	y_{OARE}	$z_o = 317.8$ in.

Table 8-2. STS-75 SAMS Head Location and Orientation

Unit F Head 1A (TSH-1A)		Sample Rate: 50 samples/second
Serial No.: 821-19		
Location: Forward MPRESS, Forward rail		Frequency: 10 Hz
Orientation		Location
Orbiter Structural Axis	Sensor Axis	Structural Axis
x_o	$-y_H$	$x_o = 1,048.37$ in.
y_o	$+z_H$	$y_o = 4.82$ in.
z_o	$-x_H$	$z_o = 418.13$ in.

Unit F Head 1B (TSH-1B)		Sample Rate: 125 samples/second
Serial No.: 821-21		
Location: Forward MPRESS, Forward rail		Frequency: 25 Hz
Orientation		Location
Orbiter Structural Axis	Sensor Axis	Structural Axis
x_o	$-y_H$	$x_o = 1,048.37$ in.
y_o	$+z_H$	$y_o = -4.82$ in.
z_o	$-x_H$	$z_o = 418.13$ in.

Unit G Head 2A (TSH-2A) Serial no.: 821-4 Location: Inside IDGE, (aft MPESS)		Sample Rate: 50 samples/second Frequency: 5 Hz
Orientation		Location
Orbiter Structural Axis	Sensor Axis	Structural Axis
x_0	$-y_H$	$x_0 = 1,135.42$ in.
y_0	$+z_H$	$y_0 = -45.24$ in.
z_0	$-x_H$	$z_0 = 433.96$ in.

Unit G Head 2B (TSH-2B) Serial No.: 821-29 Location: Aft MPESS, Aft rail		Sample Rate: 50 samples/second Frequency: 10 Hz
Orientation		Location
Orbiter Structural Axis	Sensor Axis	Structural Axis
x_0	$-y_H$	$x_0 = 1,136.82$ in.
y_0	$+z_H$	$y_0 = -4.82$ in.
z_0	$-x_H$	$z_0 = 418.13$ in.

Unit G Head 2C (TSH-2C) Serial No.: 821-20 Location: Aft MPESS, Aft rail		Sample Rate: 125 samples/second Frequency: 25 Hz
Orientation		Location
Orbiter Structural Axis	Sensor Axis	Structural Axis
x_0	$-y_H$	$x_0 = 1,136.82$ in.
y_0	$+z_H$	$y_0 = -4.82$ in.
z_0	$-x_H$	$z_0 = 418.13$ in.

Table 8-3. Accelerations Associated with PRCS Activity

Firing	Average acceleration (from plot)	dV/dt [12]
OMS-3	46 mg	50 mg
PRCS 5D	11 mg	14 mg
PRCS 5C1	6 mg	6 mg
PRCS5C2	7 mg	6 mg

Orientation View
Scale: None

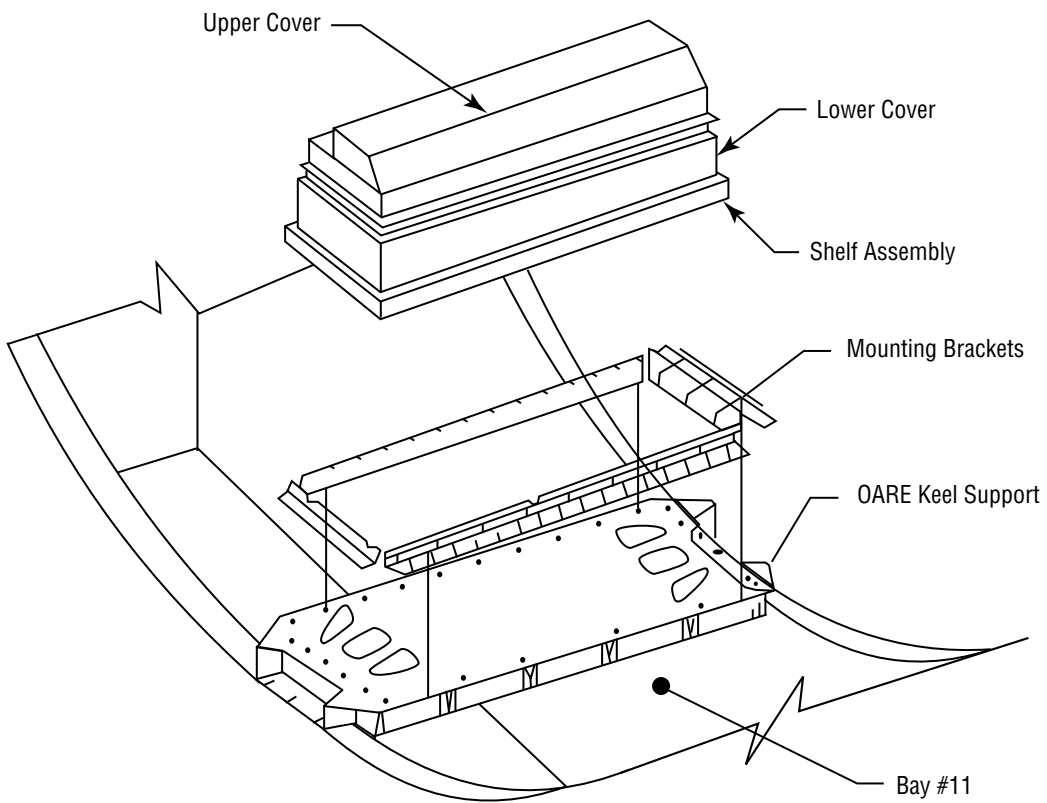
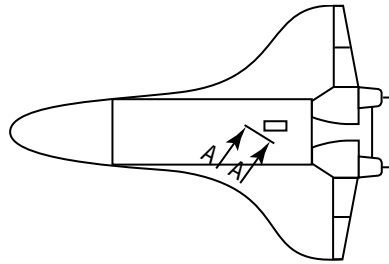
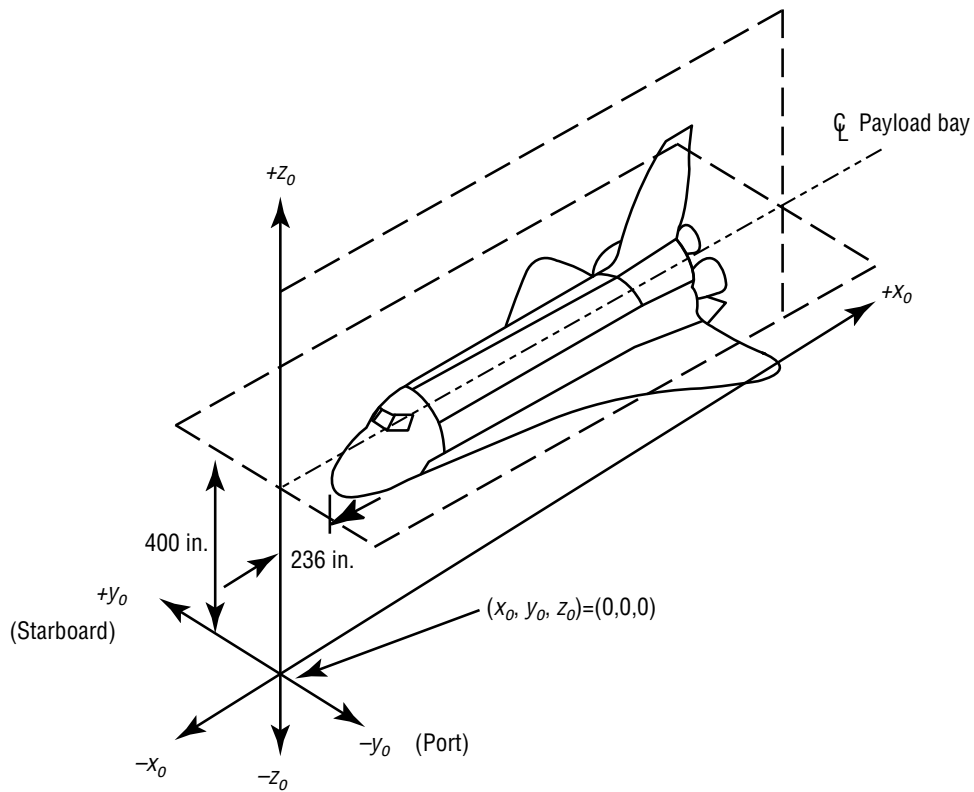
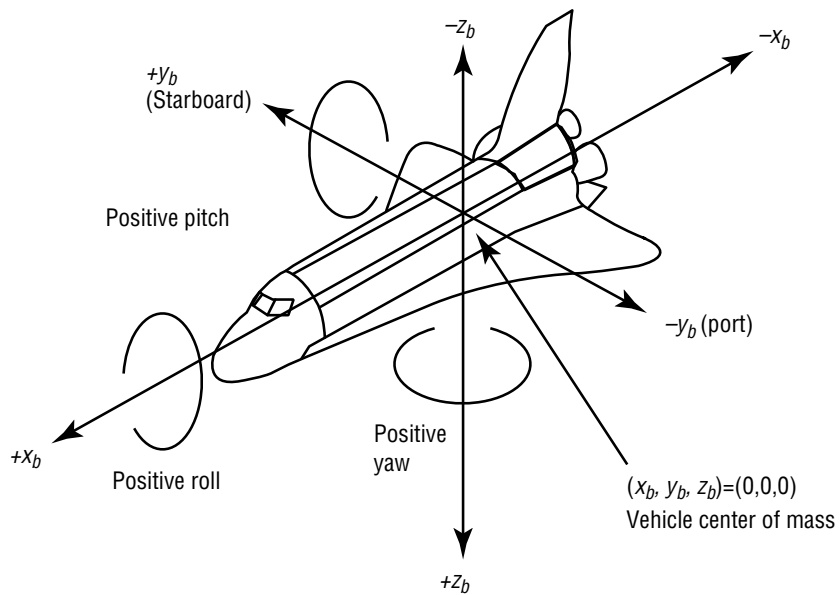


Figure 8-1. Approximate OARE instrument location on STS-75.



Orbiter structural coordinate system.



Orbiter body coordinate systems.

Figure 8-2. Orbiter body and structural coordinate systems.

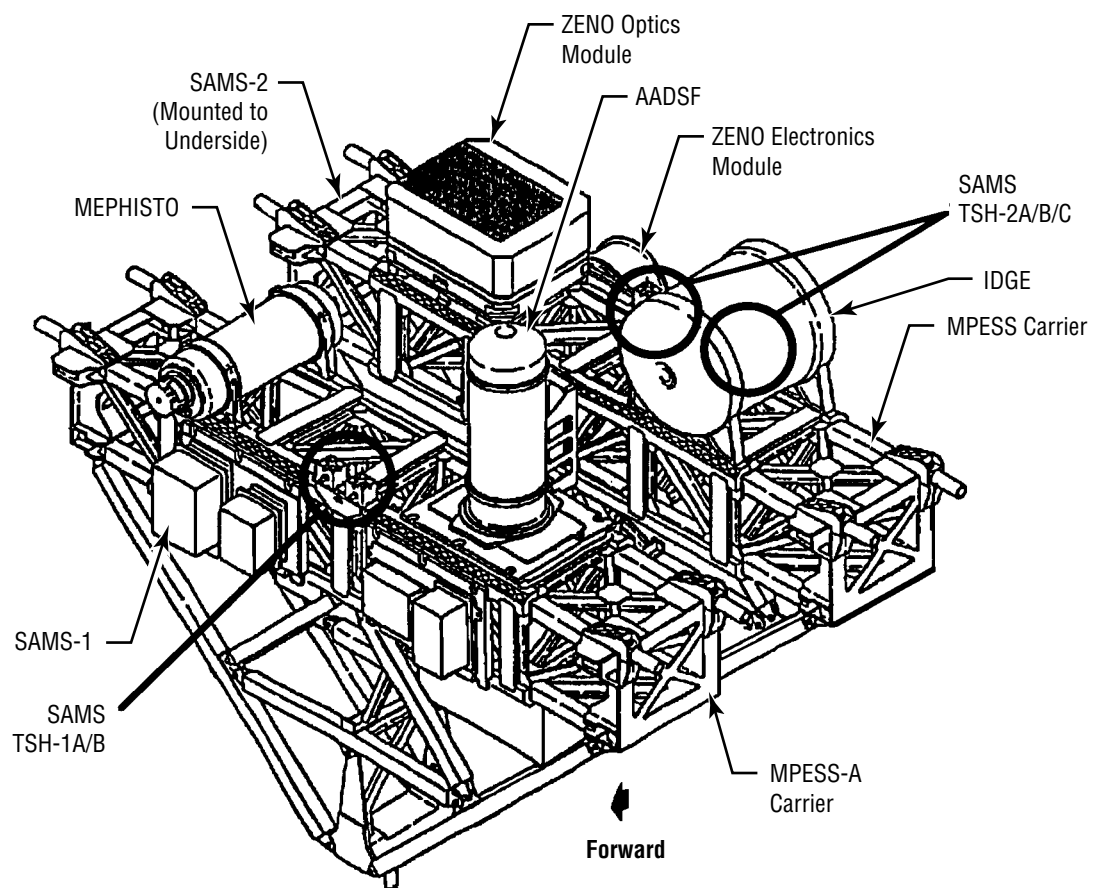
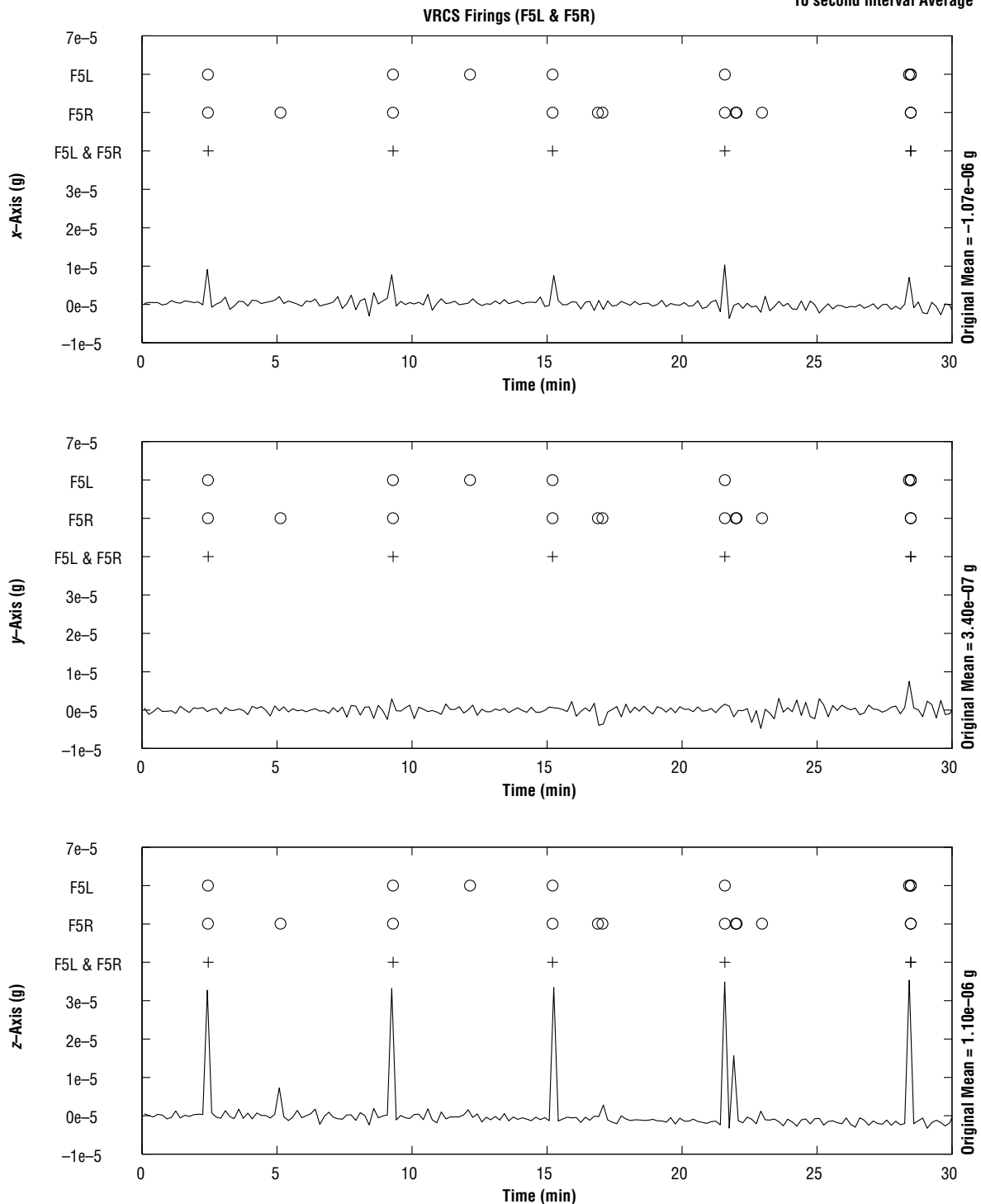


Figure 8-3. Approximate location of SAMS sensors on the USMP-3 MPRESS carriers, STS-75.

Head B, 25.0 Hz
fs= 125.0 samples per second

MET Start at 010/04:00:00.895

USMP-3F
Structural Coordinates
10 second Interval Average



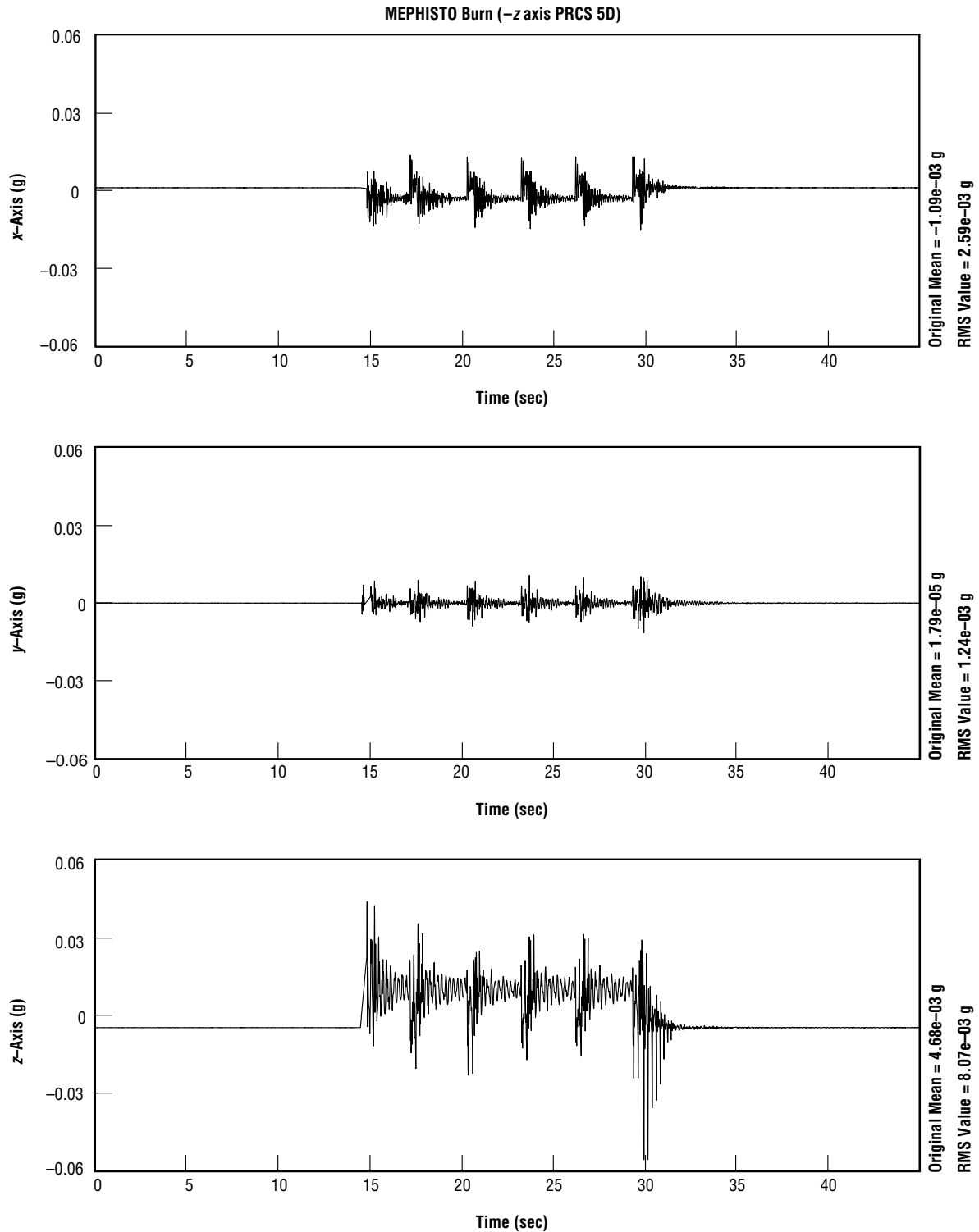
MATLAB: 28-Aug-96, 8:16 am

Figure 8-4. SAMS Unit F TSH 1B data, 10-sec interval average, showing use of F5L and F5R VRCS jets for attitude maintenance. Simultaneous F5L and F5R jet firings indicated by + markers; individual events indicated by o markers. MET start 010/04:00.

Head B, 25.0 Hz
fs= 125.0 samples per second

MET Start at 012/12:24:44.996

USMP-3F
Structural Coordinates



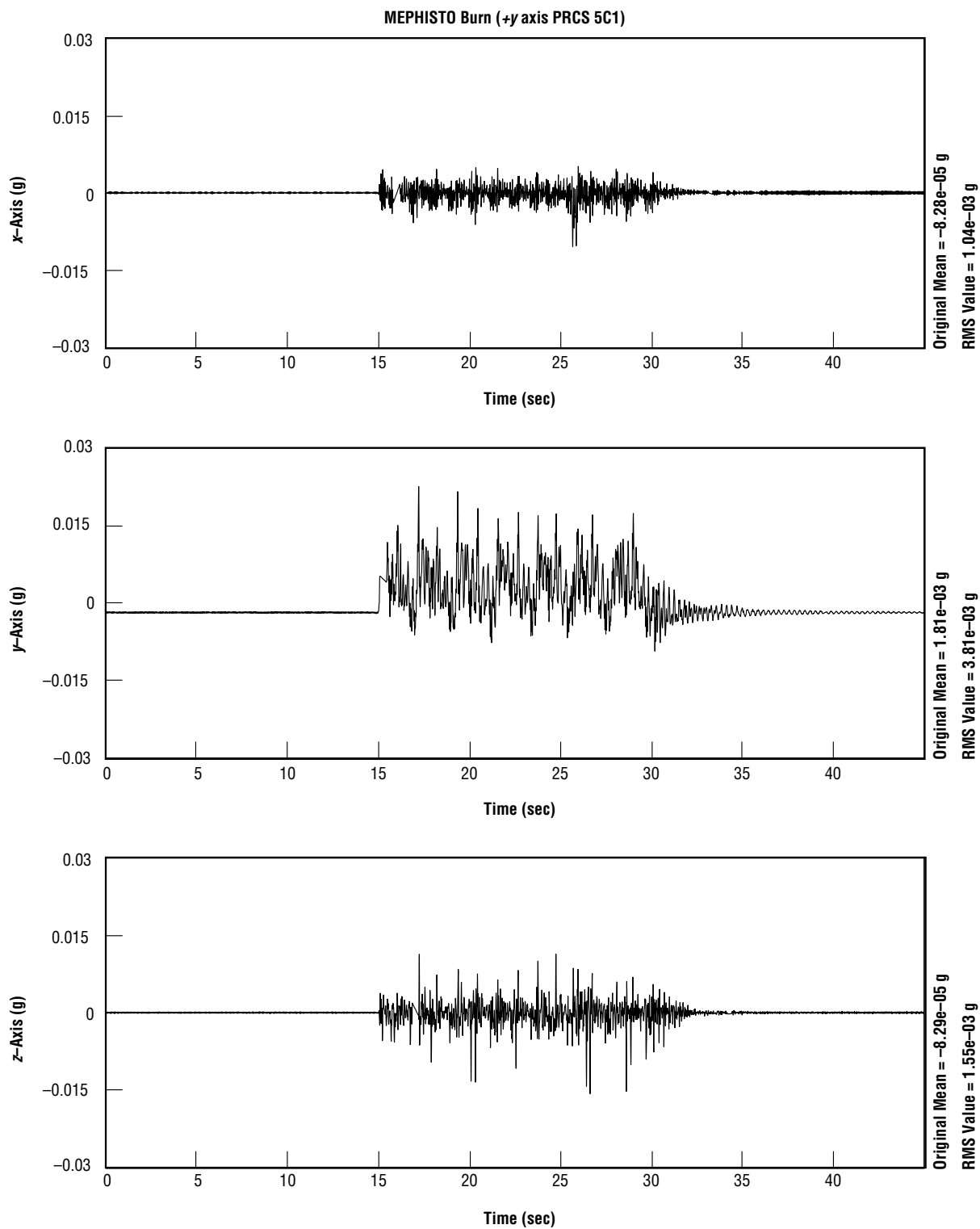
MATLAB: 6-Sep-96, 1:44 pm

Figure 8-5. SAMS Unit F TSH 1B data from MEPHISTO PRCS 5D ($-z_b$) event. MET start 012/12:24:45.

Head B, 25.0 Hz
fs= 125.0 samples per second

MET Start at 012/14:24:45.000

USMP-3F
Structural Coordinates



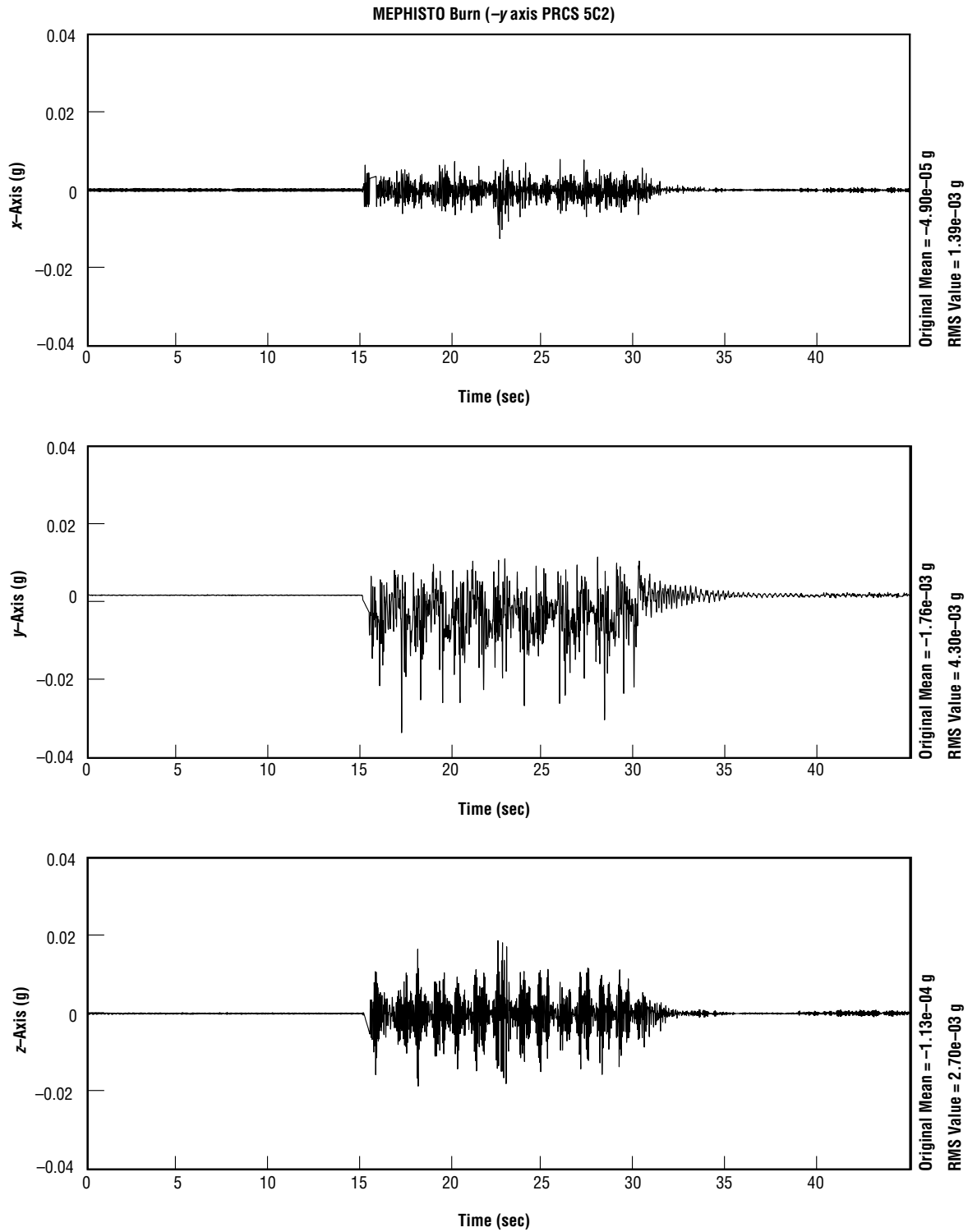
MATLAB: 6-Sep-96, 2:0 pm

Figure 8-6. SAMS Unit F TSH 1B data from MEPHISTO PRCS 5C1 (+y_b) event. MET start 012/14:24:45

Head B, 25.0 Hz
fs= 125.0 samples per second

MET Start at 012/14:27:45.000

USMP-3F
Structural Coordinates



MATLAB: 6-Sep-96, 2:12 pm

Figure 8-7. SAMS Unit F TSH 1B data from MEPHISTO PRCS 5C2 ($-y_b$) event. MET start 012/14:27:45.

Head B, 25.0 Hz

MET Start at 012/12:24:44.996

USMP-3F

fs= 125.0 samples per second

MEPHISTO Burn (-z axis PRCS 5D)

Structural Coordinates

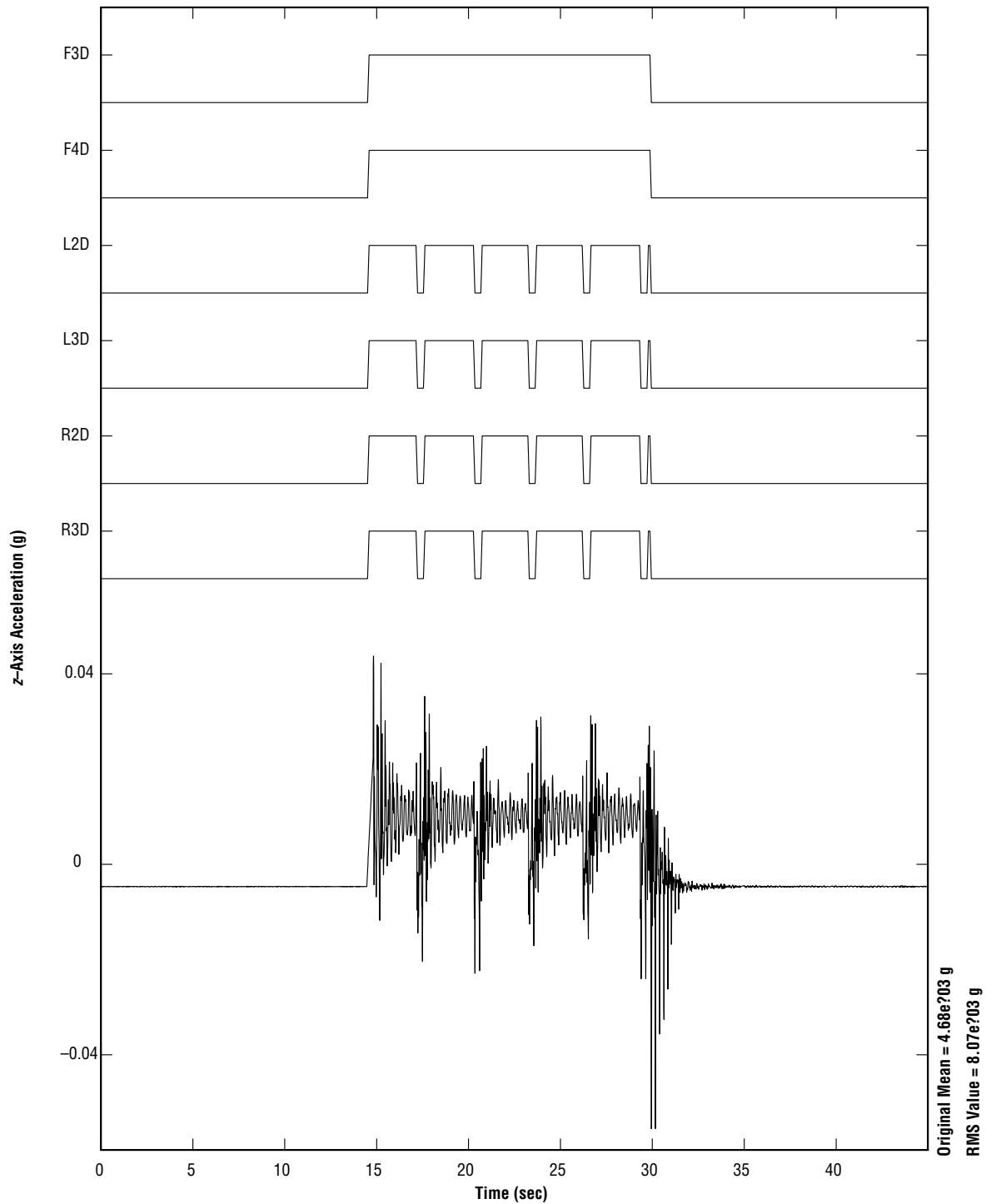


Figure 8-8. SAMS Unit F TSH 1B data from MEPHISTO PRCS 5D ($-z_b$) event, z_o axis of data shown. PRCS jet usage indicate on top section of plot. MET start 012/12:24:45.

Head B, 25.0 Hz
fs= 125.0 samples per second
dF= 0.1221 Hz
dT= 0.1365 min

MET Start at 007/13:00:11.650, Hanning k= 218
Ku-band Antenna Reposition

USMP-3F
Structural Coordinates

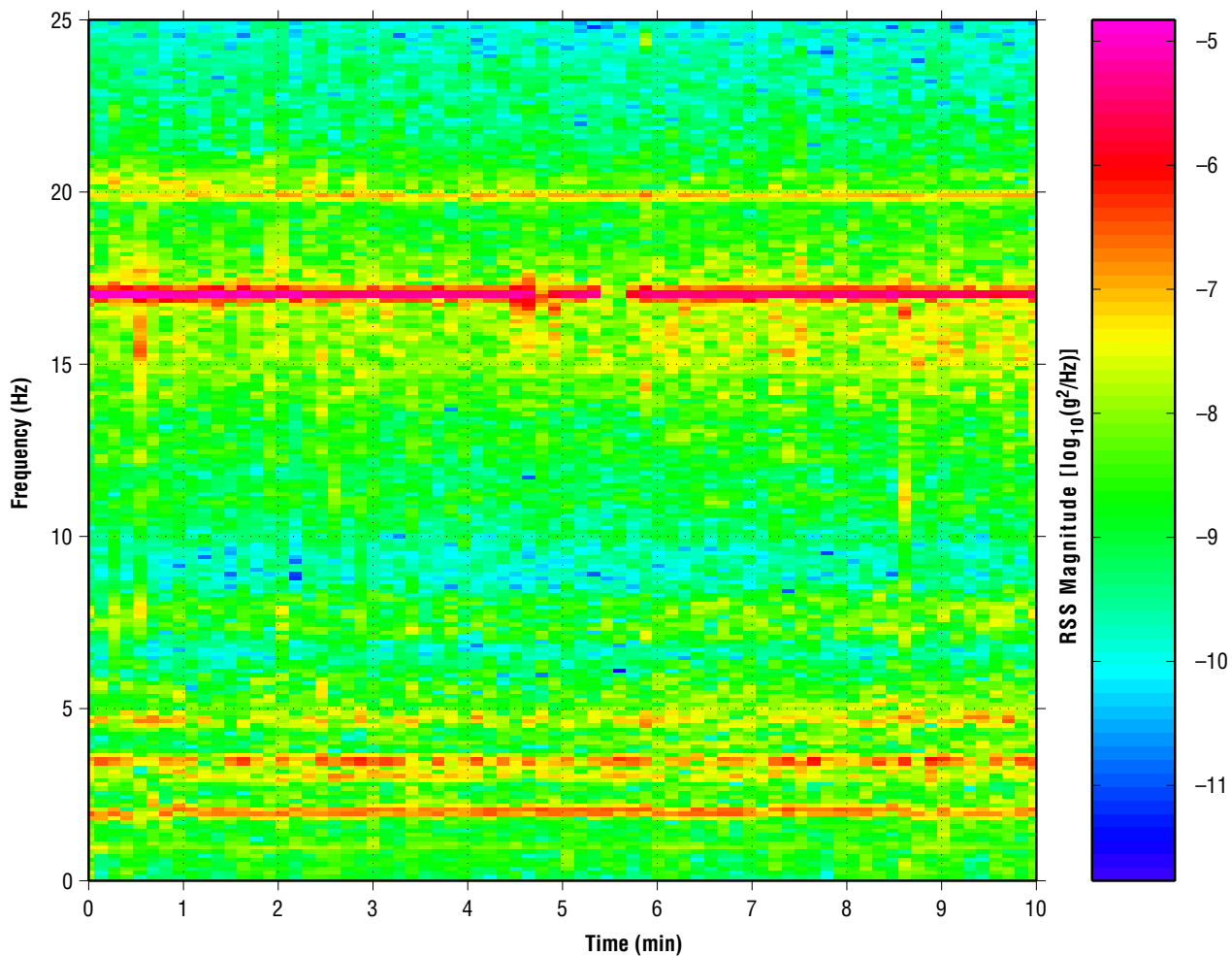


Figure 8-9. SAMS Unit F TSH 1B spectrogram showing data collected during Ku band antenna reposition. MET start 007/13:00:12. Note interruption of 17-Hz signal at 007/13:05:25 for 17 sec.

Head B, 25.0 Hz
fs= 125.0 samples per second
dF= 0.1221 Hz
dT= 0.1365 min

MET Start at 007/13:00:11.650, Hanning k= 218
Ku-band Antenna Reposition

USMP-3F
Structural Coordinates

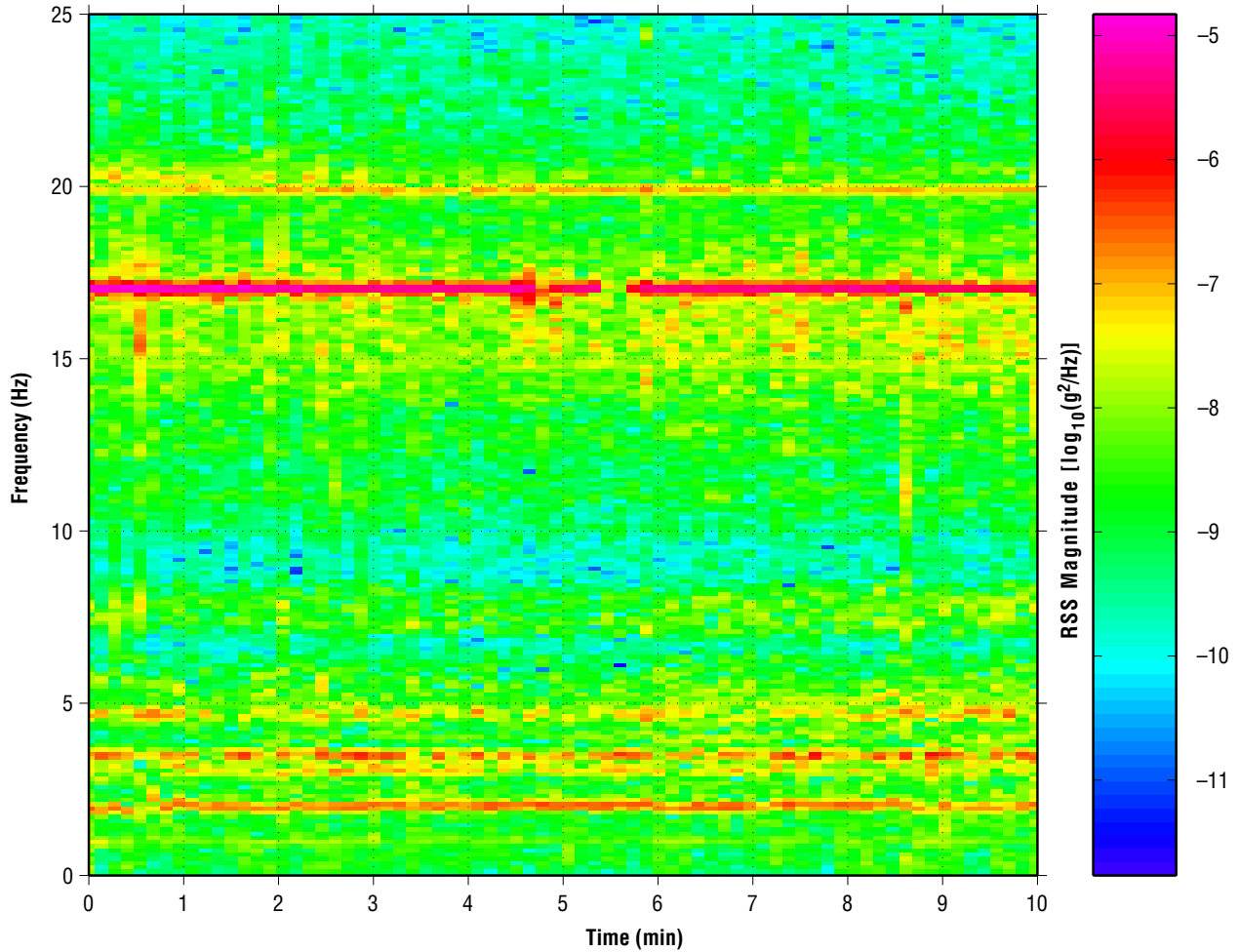
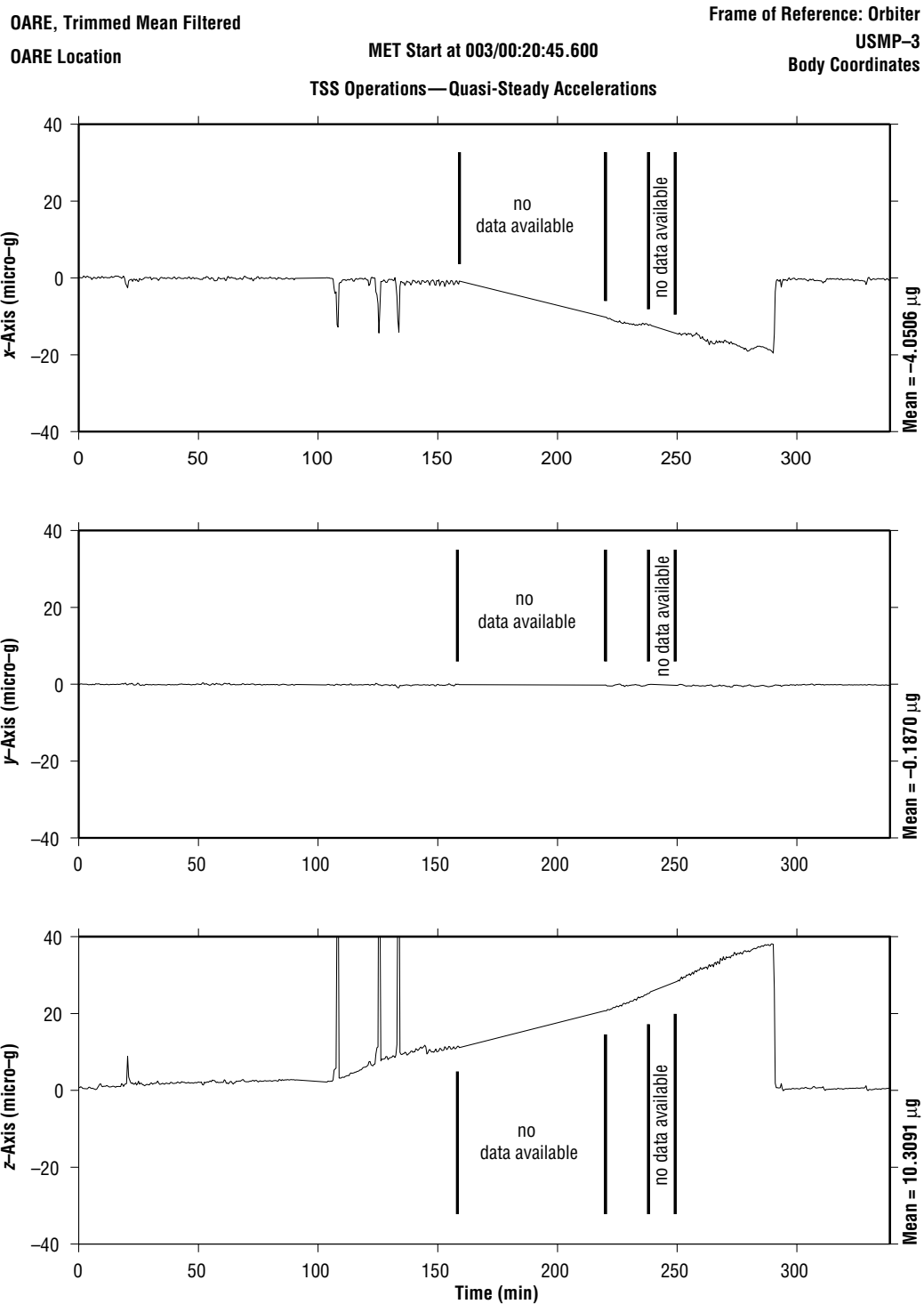


Figure 8-10. SAMS Unit G TSH 2A spectrogram showing data collected during flight control system checkout. MET start 013/15:00:00. Note change in signal character upon activation of auxiliary power unit one at 013/15:03.



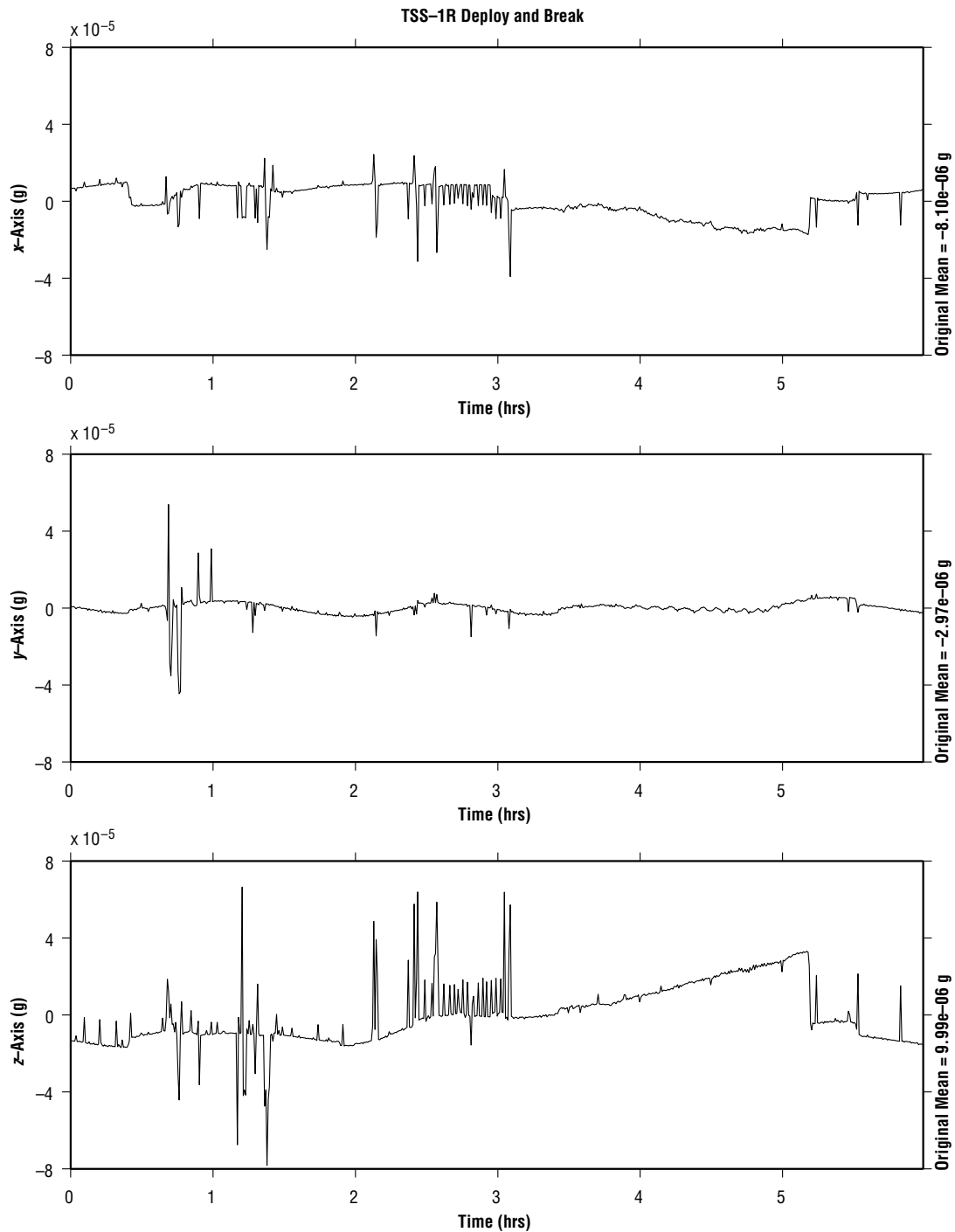
MATLAB: 25-Sep-96, 9:50 am

Figure 8-11. OARE data representing the microgravity environment at the OARE location during TSS-1R deploy operations. MET start at 003/00:00. Note TSS flyaway occurred at 003/00:27. Transient accelerations seen in the plot are due to PRCS activity to compensate for tether dynamics.

Head A, 10.0 Hz
fs= 50.0 samples per second

MET Start at 003/00:00.155

USMP-3F
Structural Coordinates
30 second Interval Average



MATLAB: 10-Sep-96, 12:35 pm

Figure 8-12. SAMS Unit F TSH 1A data representing the microgravity environment during TSS-1R deploy operations. MET start at 003/00:00. Note TSS flyaway occurred at 003/00:27. Transient accelerations seen in the plot are due to PRCS activity to compensate for tether dynamics.

Head A, 10.0 Hz
fs= 50.0 samples per second
dF= 0.0122 Hz
dT= 81.9200 sec

USMP-3F
Structural Coordinates

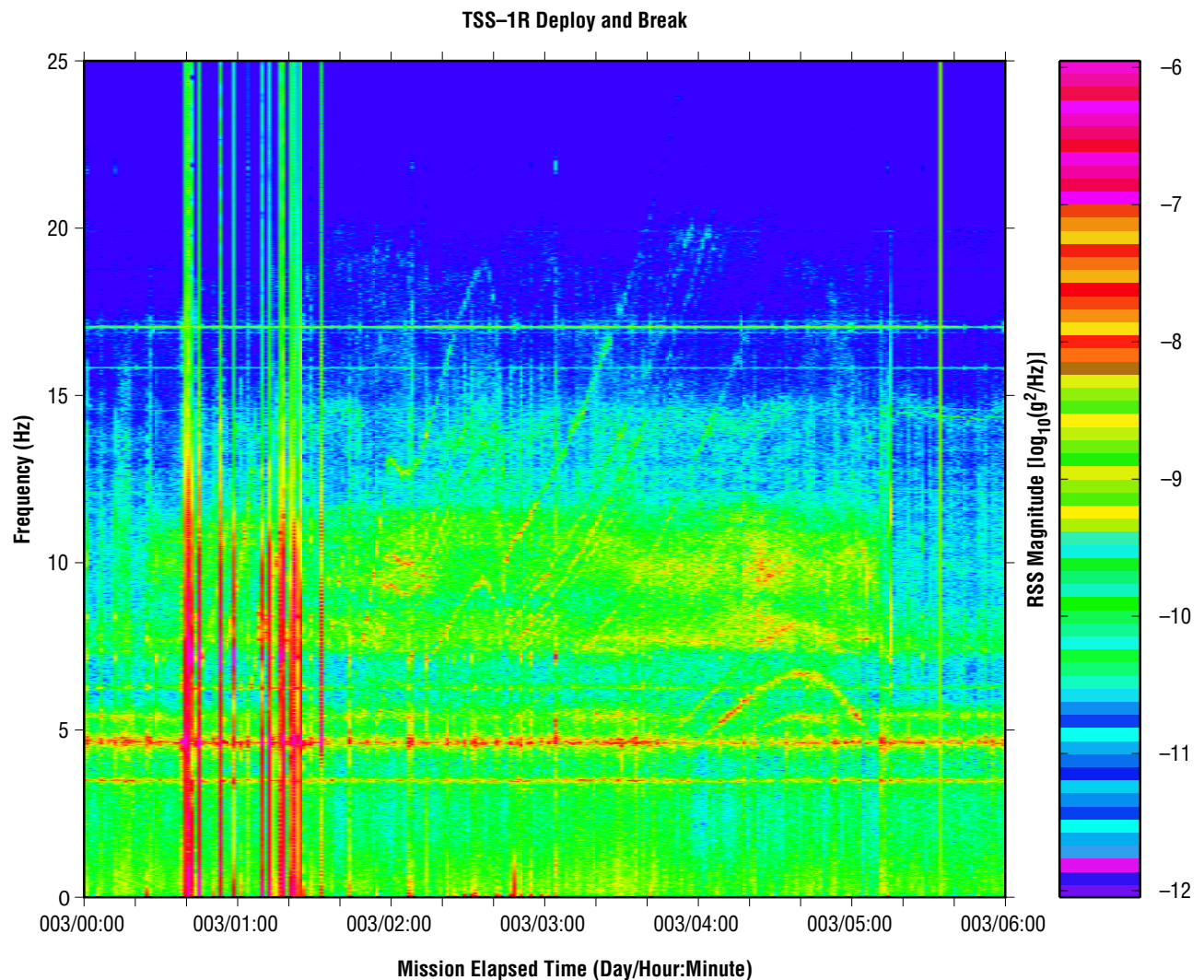
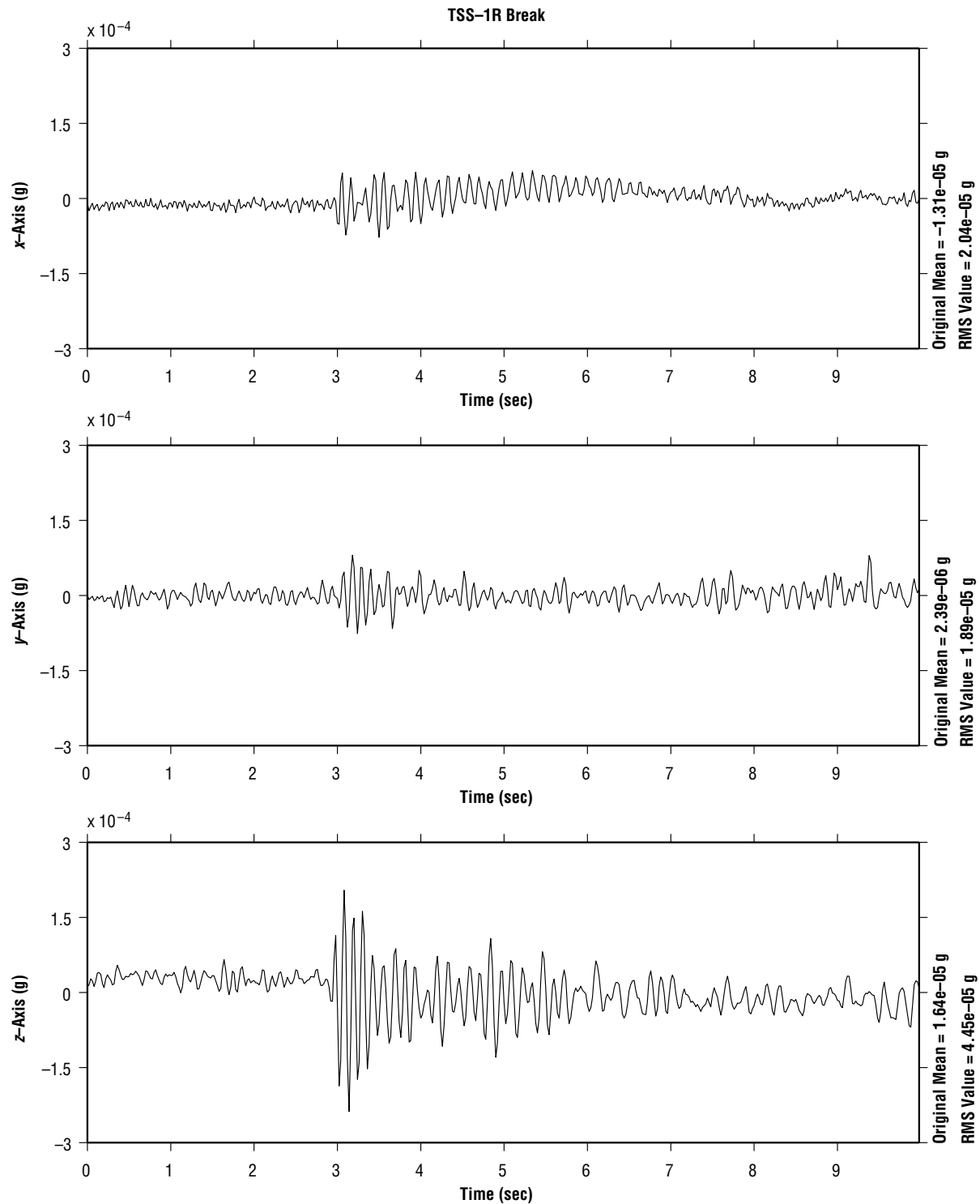


Figure 8-13. SAMS Unit F TSH 1A spectrogram showing data collected during TSS-1R deploy operations. MET start at 003/00:00. Note TSS flyaway occurred at 003/00:27. Transient accelerations seen in the plot as vertical stripes are due to PRCS activity to compensate for tether dynamics. Variable frequency traces are related to tether pulley rotations during tether deploy.

Head A, 10.0 Hz
fs= 50.0 samples per second

USMP-3F
Structural Coordinates

MET Start at 003/05:11:20.986



MATLAB: 11-Sep-96, 10:46 am

Figure 8-14. SAMS Unit F TSH 1A data from time of TSS-1R break. Note ringing of orbiter structure at about 9 Hz.

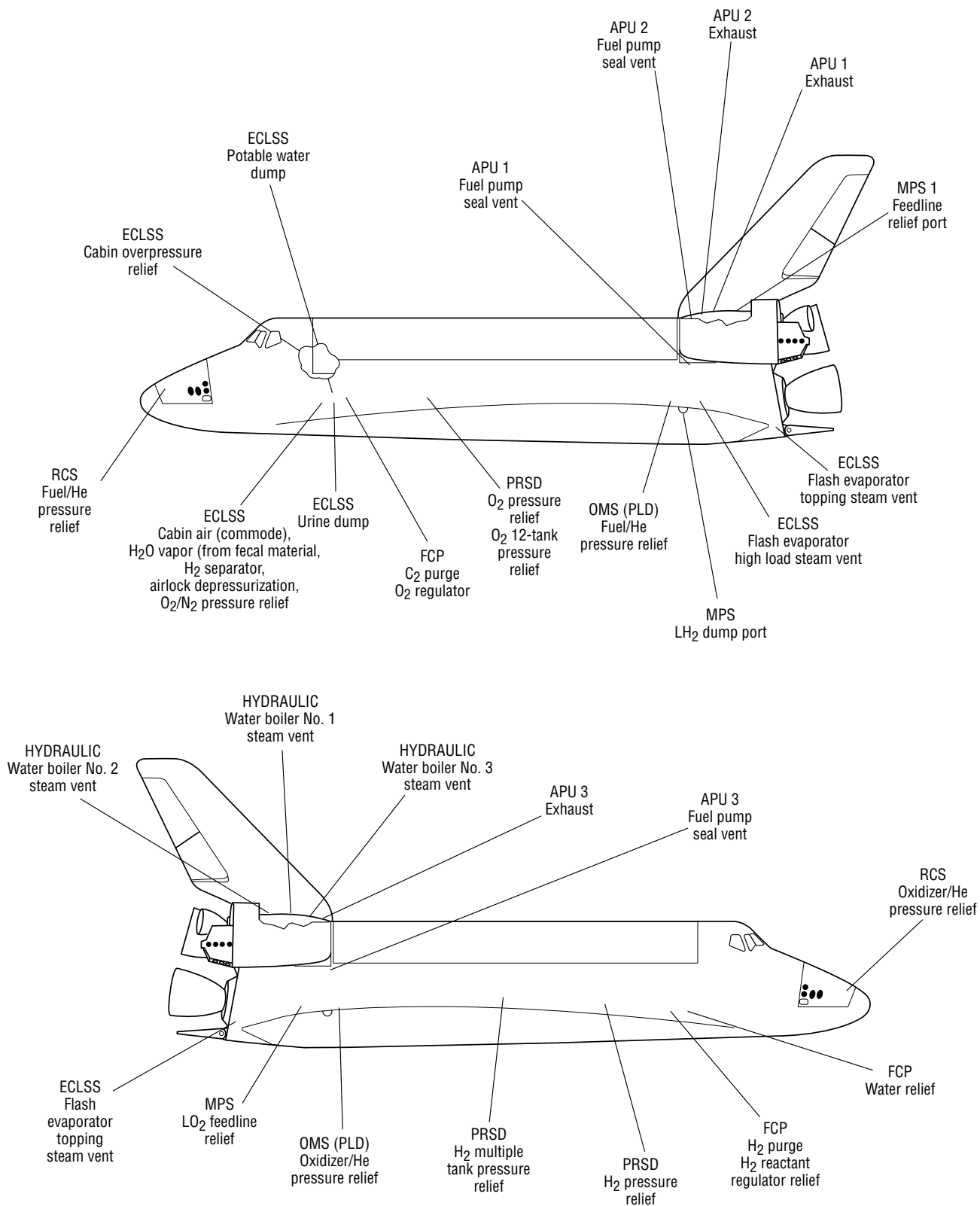


Figure 8-15. Orbiter venting location.¹⁴

OARE, Trimmed Mean Filtered
OARE Location

MET Start at 000/00:00:27.720
USMP-3 Quasi-Steady Accelerations

Frame of Reference: Orbiter
USMP-3
Body Coordinates

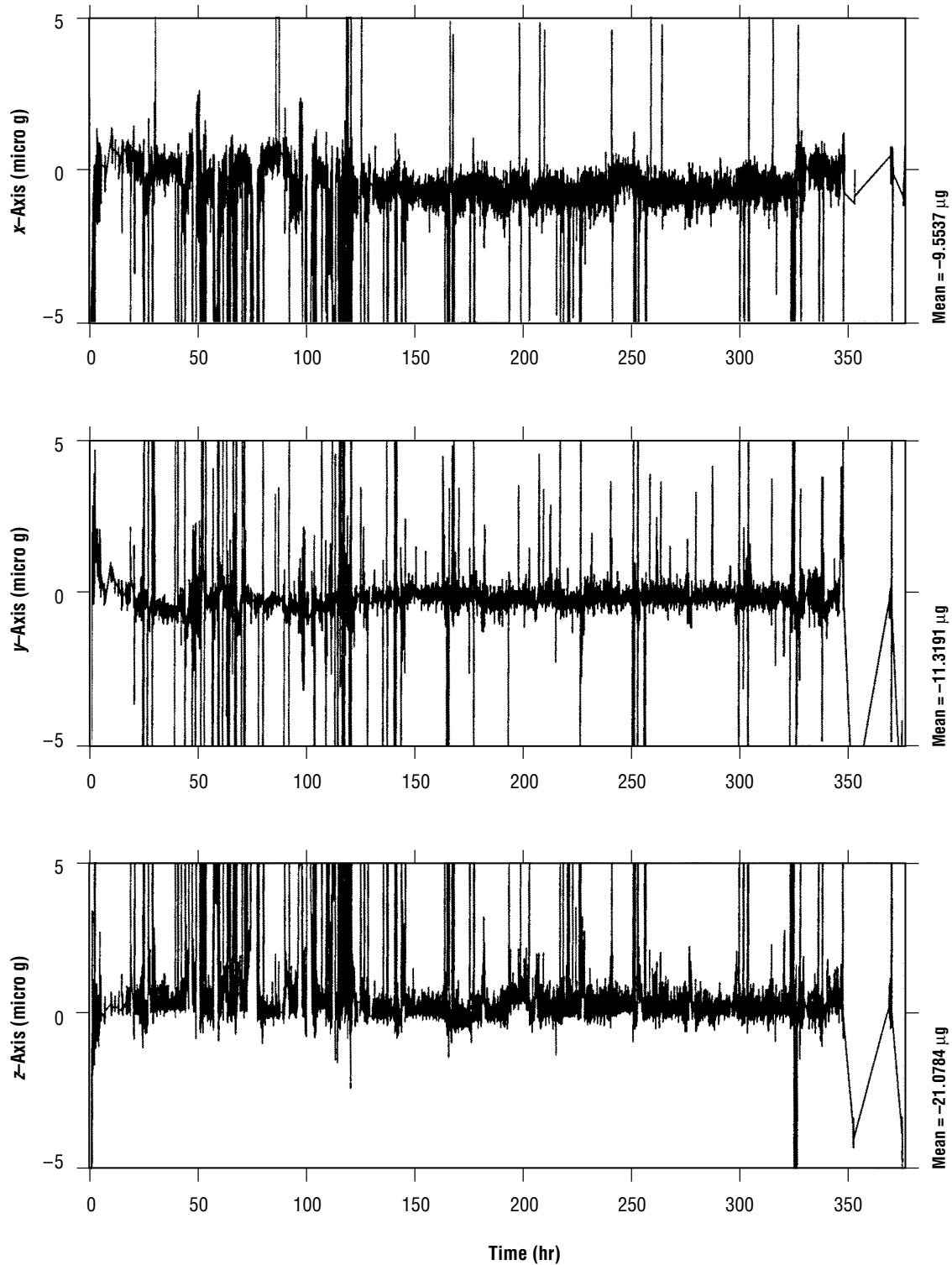


Figure 8-16. OARE data representing the microgravity environment at the OARE location during the STS-75 mission. MET start at 000/00:27.

OARE, Trimmed Mean Filtered
CG Location

MET Start at 011/00:00:26.280
USMP-3 Nominal Attitude $-x/v/+z/v$

Frame of Reference: Orbiter
USMP-3
Body Coordinates

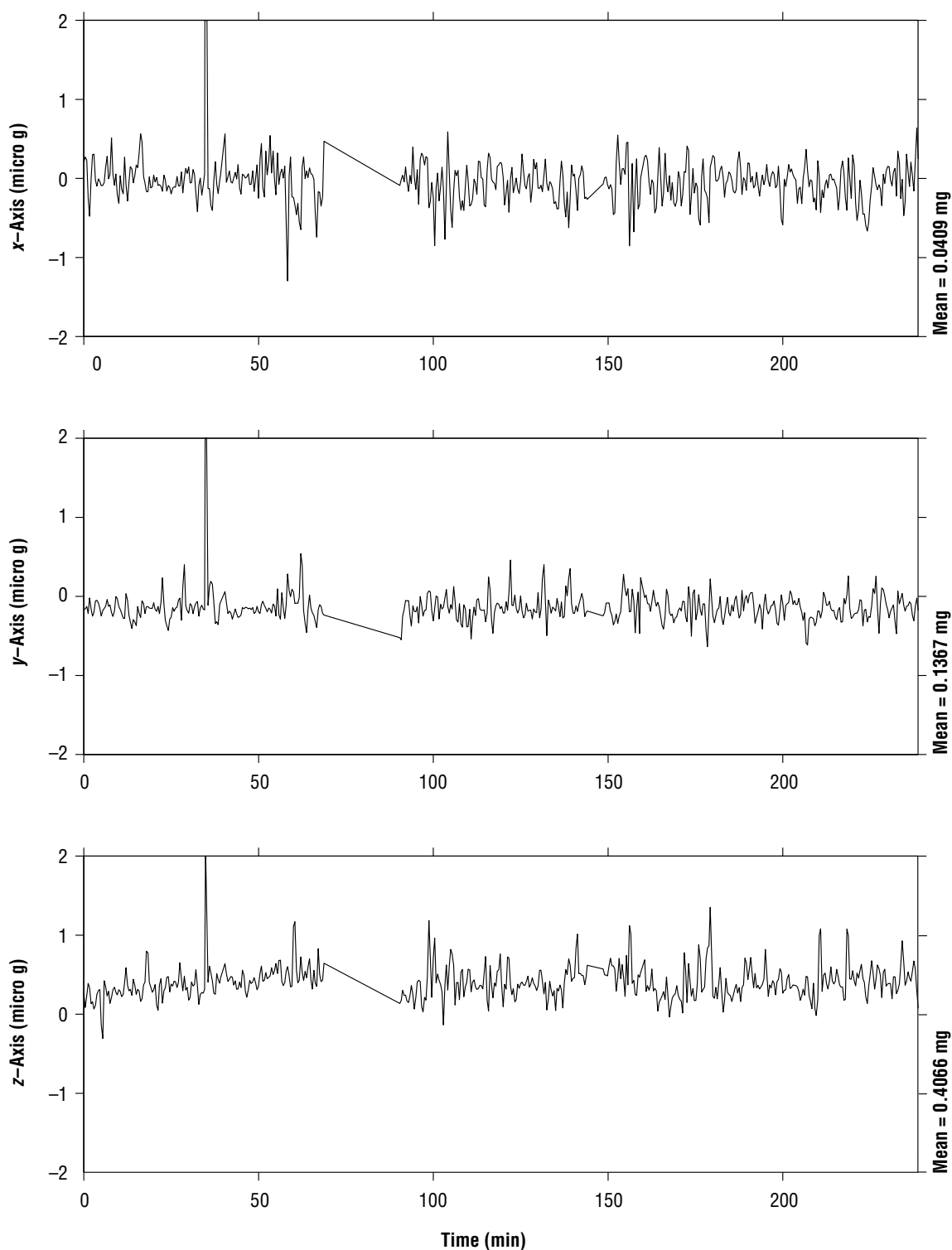


Figure 8-17. OARE data representing the microgravity environment at the OARE location while Columbia was in the nominal USMP-3 attitude. MET start at 01100:00:26.

OARE, Trimmed Mean Filtered
OARE Location

MET Start at 008/07:15:12.960
AADSF Stabilization Attitude 1

Frame of Reference: Orbiter
USMP-3
Body Coordinates

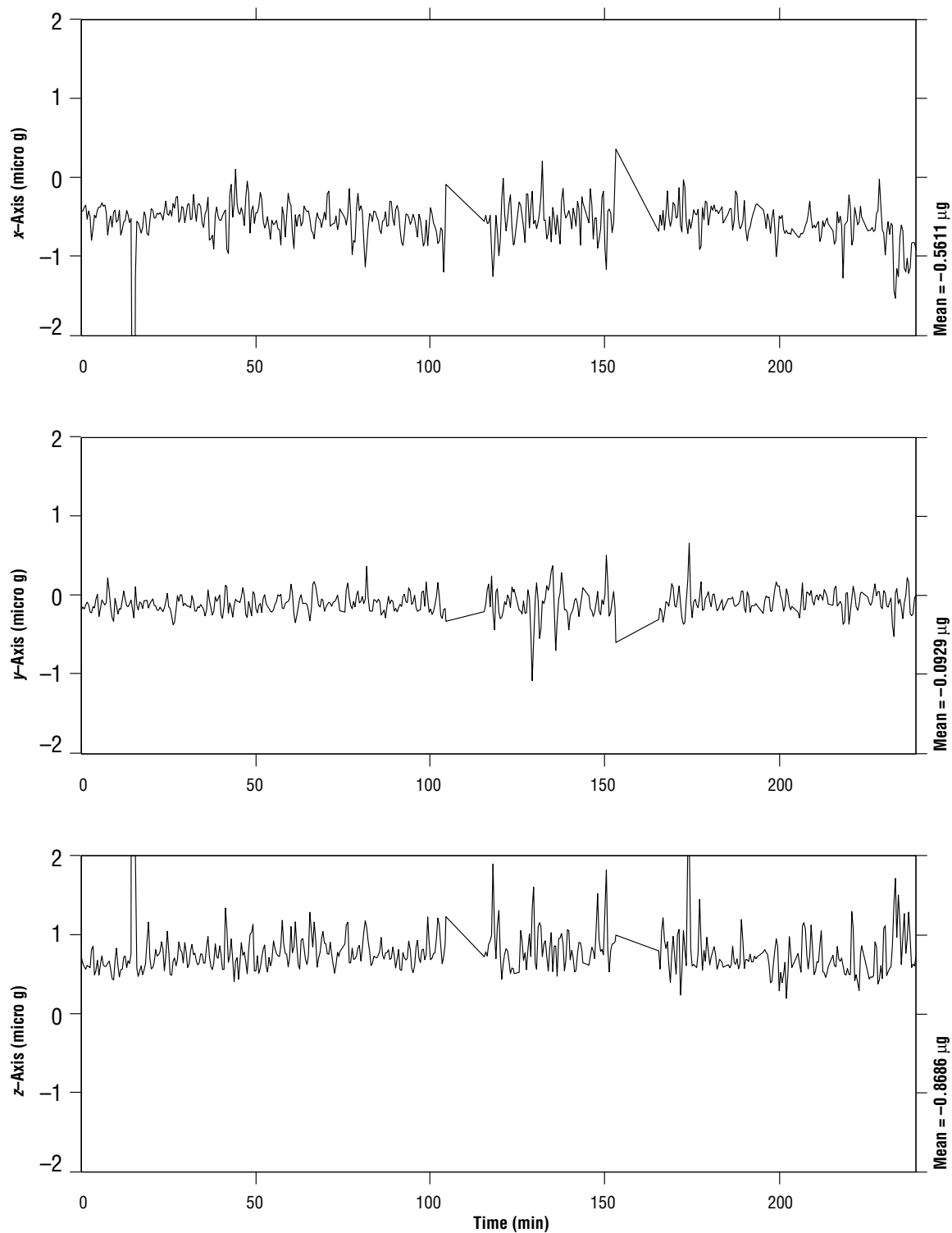


Figure 8-18. OARE data representing the microgravity environment at the OARE location while Columbia was in the AADSF 1 attitude. MET start at 008/07:15:13.

OARE, Trimmed Mean Filtered
OARE Location

MET Start at 008/02:00:47.880
AADSf Stabilization Attitude 1

USMP-3
Body Coordinates
T = 9.473 hours

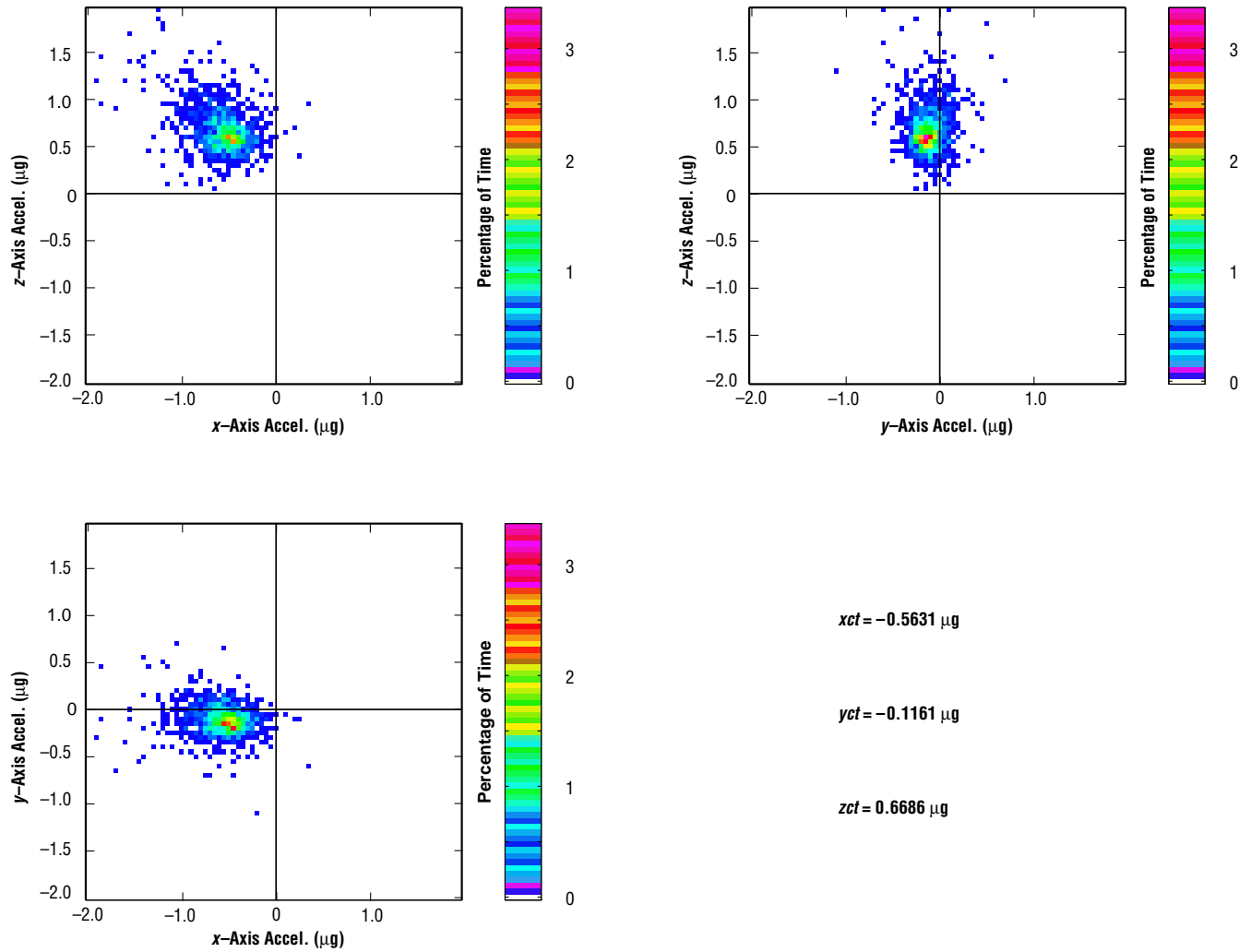
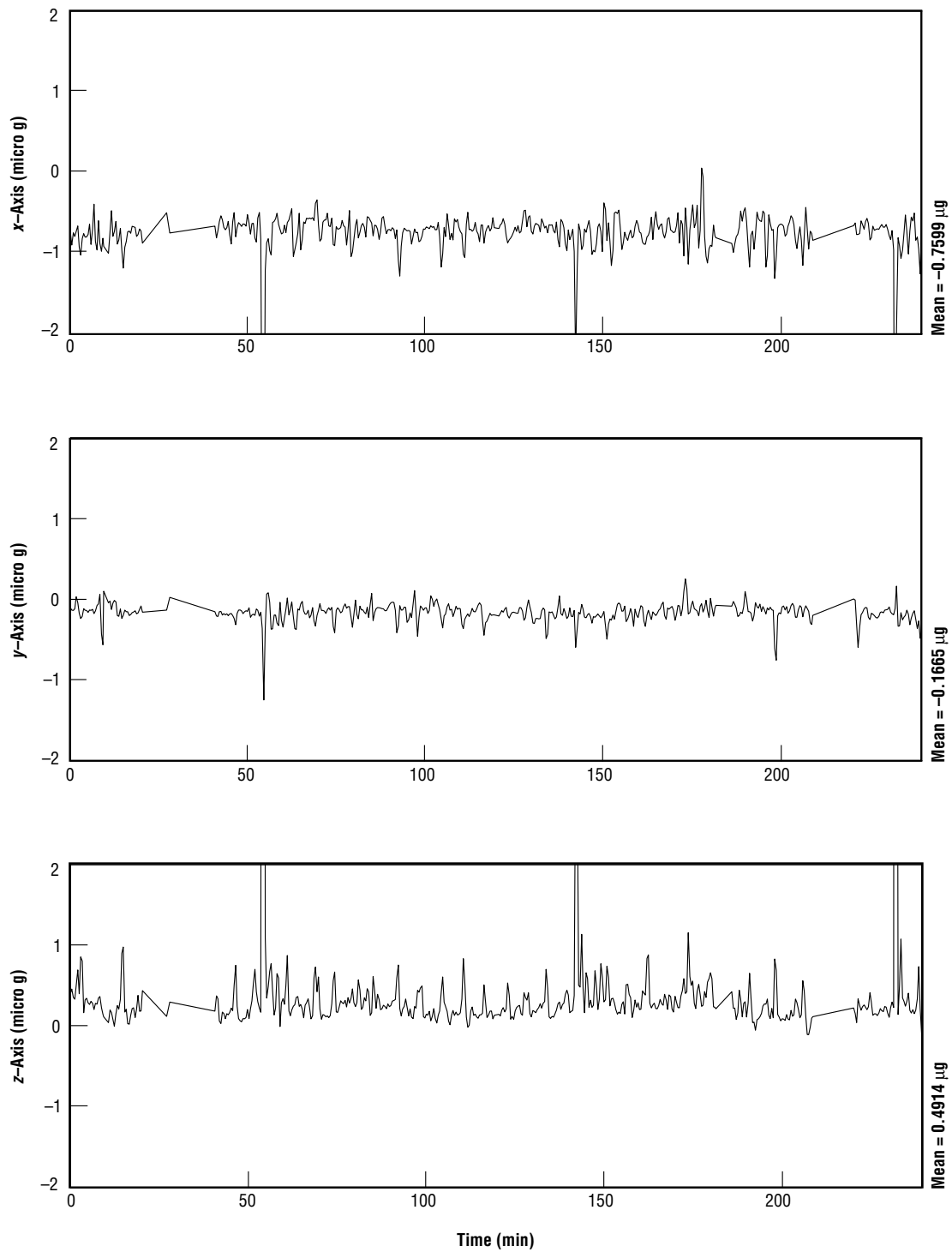


Figure 8-19. Three-dimensional projection of OARE data representing the microgravity environment at the OARE location while Columbia was in the AADSf 1 attitude. MET start at 008/02:00:47.

OARE, Trimmed Mean Filtered
OARE Location

MET Start at 009/07:00:03.600
AADSF Stabilization Attitude 2

Frame of Reference: Orbiter
USMP-3
Body Coordinates



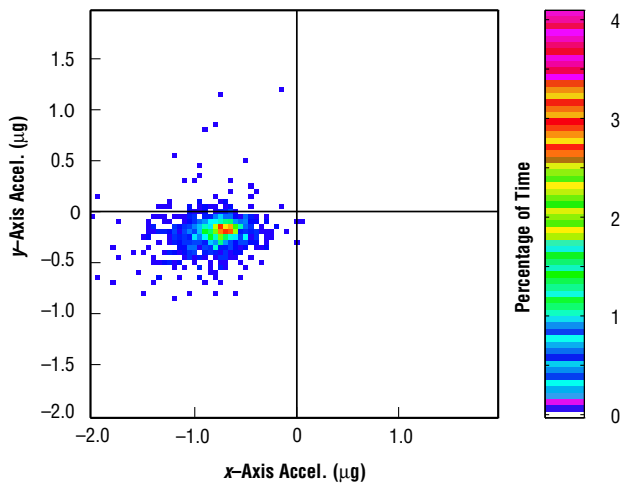
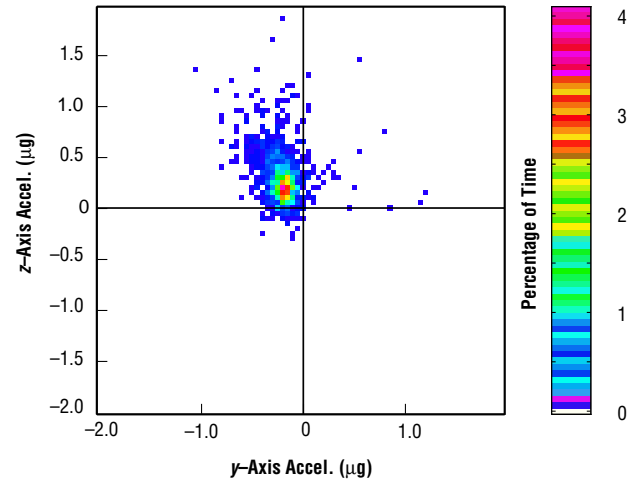
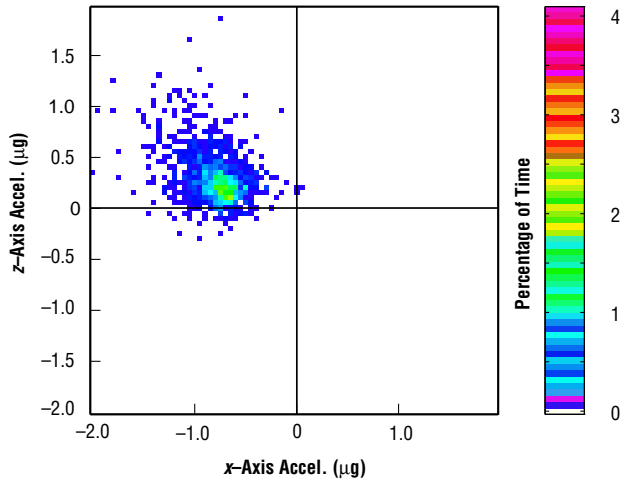
MATLAB: 3-Oct-96, 2:59 pm

Figure 8-20. OARE data representing the microgravity environment at the OARE location while Columbia was in the AADSF 2 attitude. MET start at 009/07:00:03.

OARE, Trimmed Mean Filtered
OARE Location

MET Start at 009/02:02:00.600
AADSF Stabilization Attitude 2

USMP-3
Body Coordinates
T=9.466 hours



$$x_{ct} = -0.7922 \mu\text{g}$$

$$y_{ct} = -0.2044 \mu\text{g}$$

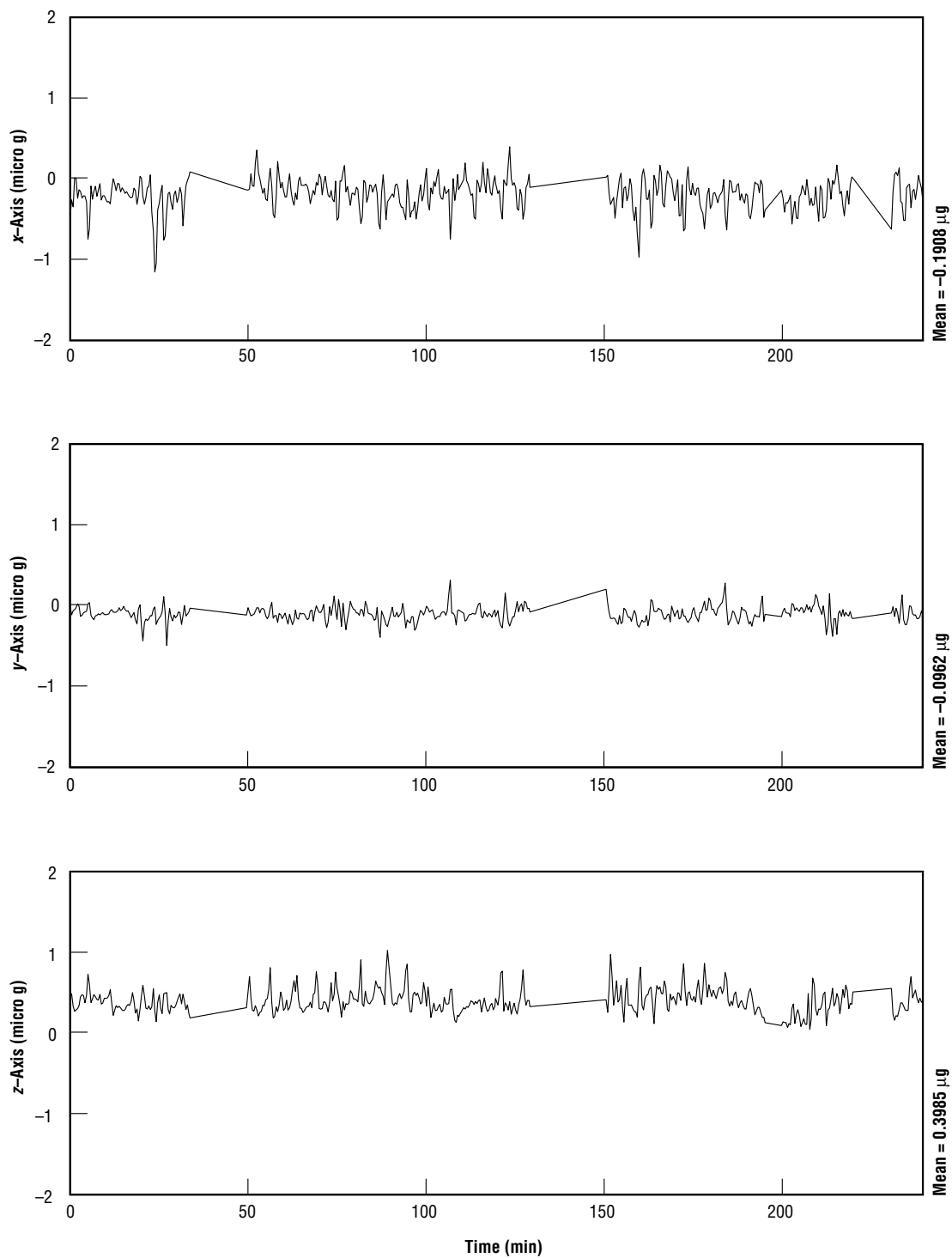
$$z_{ct} = 0.2876 \mu\text{g}$$

Figure 8-21. Three-dimensional projection of the OARE data representing the microgravity environment at the OARE location while Columbia was in the AADSF 2 attitude. MET start at 009/02:02:00.

OARE, Trimmed Mean Filtered
OARE Location

MET Start at 010/07:00:24.840
AADSF Stabilization Attitude 3

Frame of Reference: Orbiter
USMP-3
Body Coordinates



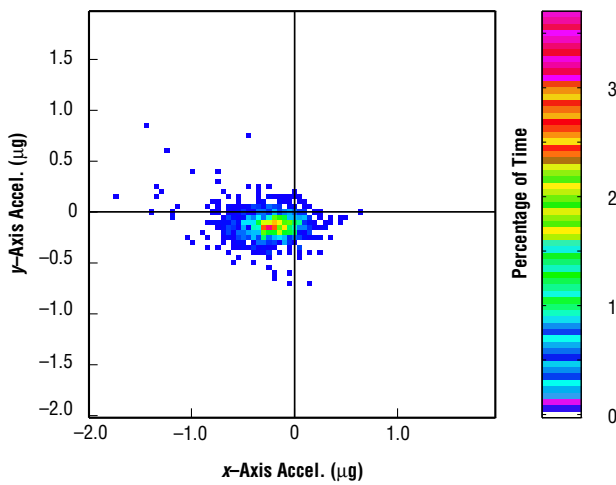
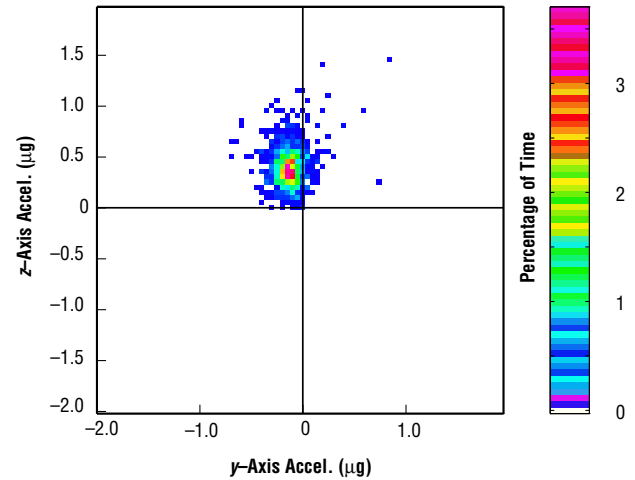
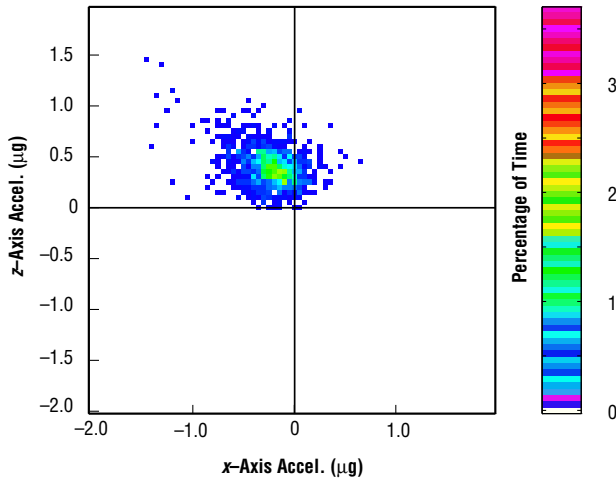
MATLAB: 3-Oct-96, 3:2 pm

Figure 8-22. OARE data representing the microgravity environment at the OARE location while Columbia was in the AADSF 3 attitude. MET start at 010/07:00:24.

OARE, Trimmed Mean Filtered
OARE Location

MET Start at 010/02:00:13.320
AADSF Stabilization Attitude 3

USMP-3
Body Coordinates
T=9.492 hours



$xct = -0.2313 \mu g$

$yct = -0.1302 \mu g$

$zct = 0.3974 \mu g$

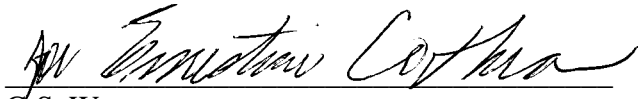
Figure 8-23. Three-dimensional projection of the OARE data representing the microgravity environment at the OARE location while Columbia was in the AADSF 3 attitude. MET start at 010/02:00:13.

APPROVAL

THIRD UNITED STATES MICROGRAVITY PAYLOAD: ONE YEAR REPORT

P.A. Curreri, D. McCauley and C. Walker, Editors

The information in this report has been reviewed for technical content. Review of any information concerning Department of Defense or nuclear energy activities or programs has been made by the MSFC Security Classification Officer. This report, in its entirety, has been determined to be unclassified.


A handwritten signature in black ink, appearing to read "G.S. Wilson", is written over a horizontal line.

G.S. WILSON
DIRECTOR, SPACE SCIENCES LABORATORY

REPORT DOCUMENTATION PAGE			Form Approved OMB No. 0704-0188	
Public reporting burden for this collection of information is estimated to average 1 hour per response, including the time for reviewing instructions, searching existing data sources, gathering and maintaining the data needed, and completing and reviewing the collection of information. Send comments regarding this burden estimate or any other aspect of this collection of information, including suggestions for reducing this burden, to Washington Headquarters Services, Directorate for Information Operation and Reports, 1215 Jefferson Davis Highway, Suite 1204, Arlington, VA 22202-4302, and to the Office of Management and Budget, Paperwork Reduction Project (0704-0188), Washington, DC 20503				
1. AGENCY USE ONLY (Leave Blank)		2. REPORT DATE April 1998		3. REPORT TYPE AND DATES COVERED Technical Memorandum
4. TITLE AND SUBTITLE Third United States Microgravity Payload: One Year Report			5. FUNDING NUMBERS	
6. AUTHORS P.A. Curreri, D. McCauley* and C. Walker**, Editors				
7. PERFORMING ORGANIZATION NAME(S) AND ADDRESS(ES) George C. Marshall Space Flight Center Marshall Space Flight Center, Alabama 35812			8. PERFORMING ORGANIZATION REPORT NUMBER M-864	
9. SPONSORING/MONITORING AGENCY NAME(S) AND ADDRESS(ES) National Aeronautics and Space Administration Washington, DC 20546-0001			10. SPONSORING/MONITORING AGENCY REPORT NUMBER NASA/TM-1998-207891	
11. SUPPLEMENTARY NOTES *D. McCauley, University of Alabama in Huntsville, Huntsville, Alabama **C. Walker, Universities Space Research Association, Huntsville, Alabama				
12a. DISTRIBUTION/AVAILABILITY STATEMENT Unclassified-Unlimited Subject Category 88 Standard Distribution			12b. DISTRIBUTION CODE	
13. ABSTRACT (Maximum 200 words) This document reports the one year science results for the Third United States Microgravity Payload (USMP-3). The USMP-3 major experiments were on a support structure in the Space Shuttle's payload bay and operated almost completely by the Principal Investigators through telescience. The mission included a Glovebox where the crew performed additional experiments for the investigators. Together about seven major scientific experiments were performed, advancing the state of knowledge in fields such as low temperature physics, solidification, and combustion. The results demonstrate the range of quality science that can be conducted utilizing orbital laboratories in microgravity and provide a look forward to a highly productive space station era.				
14. SUBJECT TERMS USMP-3, microgravity research, materials science, combustion science, low temperature physics, solidification, telescience, crystal growth			15. NUMBER OF PAGES 222	
			16. PRICE CODE A10	
17. SECURITY CLASSIFICATION OF REPORT Unclassified	18. SECURITY CLASSIFICATION OF THIS PAGE Unclassified	19. SECURITY CLASSIFICATION OF ABSTRACT Unclassified	20. LIMITATION OF ABSTRACT Unlimited	